Sapienza University of Rome
Department of Earth Sciences
Ph.D. Program in Earth Sciences
XXXVI Cycle

Multi-scale Remote Sensing geomorphological applications for updating landslide inventories supported by Artificial Intelligence

SSD: GEO/04

Ph.D. Candidate
Marta Zocchi

Tutor
Prof. Francesco Troiani

Co-tutors
Prof. Paolo Mazzanti
Prof. Gabriele Scarascia Mugnozza

2023

Declaration by Author

This thesis is composed of my original work and contains published and unpublished works produced by the Author during the three-year long Ph.D. program in Earth Sciences.

Revised by:

Prof. Francesco Zucca

Department of Earth Sciences and Environment

University of Pavia

Pavia, Italy

Prof. Thomas Oommen

Department of Geology and Geological Engineering

University of Mississippi

Oxford, MS, USA

Table of Contents

Highlights

- Up-to-date information on landslide inventories is crucial for directing appropriate land use planning and implementing mitigation solutions.

- Aim of the work: identifying high-priority areas warranting in-depth investigations for updating landslide inventories on a multi-scale basis.

- At every spatial scale, artificial intelligence supported the effective management of massive amounts of remote sensing data (*i.e.,* A-DInSAR analysis) employed for the update.

- Regional scale: landsides were semi-automatically assigned to a priority rank through a density-based aggregation method that combined geospatial constraints with displacement measures.

- Local scale: differential spatio-temporal displacement patterns of a landslide system were defined through InSAR post-processing analyses, and a Bayesian model applied to the time series.

- Multi-scale: a first InSAR screening was combined to multitemporal analyses on UAS-based products to detect early instability precursors on slopes along a highway.

- The three approaches represent a multi-scale workflow and can support local and national authorities in updating landslide inventories.

Extended abstract

Landslides are acknowledged as one of the most critical geo-hazards at the global scale, as they threaten human safety, impact social and economic aspects, and cause instantaneous and drastic changes in the landscape depending on the volume of material involved in the displacement. Considering the landslide typologies and magnitudes variability, along with the evidence that past events may likely represent the preferential path for the activation or reactivation of future instabilities, the need to record the spatial occurrence and geomorphological characteristics of such phenomena is undeniable. Landslide inventories fulfil this purpose by recording the extent and the specific morphographic and morphodynamic peculiarities of slope processes at different spatial scales. As such, they stand as a pivotal tool not only for the morphoevolution analysis of the landscape but, above all, as a fundamental step for an accurate evaluation of hazards and risks associated with these phenomena, thus playing a crucial role for authorities and decision-makers to implement development plans and prioritise mitigation measures implementation.

To ensure appropriate land use planning, information on landslide spatial and temporal distribution requires frequent and extensive updates and should be easily exploitable by government authorities. The inventory maps currently suffer from outdated, fragmented and partial records, imputable to the fact that the updating process often depends on catastrophic triggering event occurrences (*e.g.*, earthquakes and prolonged or intense precipitations) or scientific projects, limited in time. The adequate implementation, updating and use of slope processes distribution data for urban planning holds significant contemporary relevance for scientific and practical applications. Furthermore, directing planning and economic efforts in areas where predisposing factors pervasively influence the slope morpho-evolution is still challenging. This work aims to investigate the application of remotely sensed data, with specific regard to advanced satellite interferometry analysis, for updating landslide inventories from a morphographic and morphodynamic point of view on a multi-scale-basis, thus providing a clear direction on identifying high-priority areas warranting in-depth investigations at regional to local scales. Considering the challenge of investigating millions of measuring points (*i.e.*, Persistent Scatterers-PS) derived from the InSAR analysis, the support of artificial intelligence facilitated the effective management of a vast amount of data, which is hampered when applying traditional inventory methods. The implemented methodology, benefitting from the support provided by user-friendly artificial intelligence models, can be incorporated into a multi-scale workflow, offering support to authorities responsible for updating local, regional, or even national-scale landslide inventories.

On the regional scale, the landslide prioritisation was based on a clustering analysis that considered the effective interdependence of the single measuring point with its neighbours. The aggregation algorithm, namely Density-Based Spatial Clustering of Applications with Noise (DBSCAN), has allowed a robust, statistically-driven aggregation of millions of measuring points due to their density and the similarity in inherent displacement characteristics. Topological constraints incorporated in the clustering workflow favoured the correct discrimination of moving PS related to a specific process from those representing adjacent ground deformation. Moreover, outliers were effectively filtered and excluded from further analysis. The resulting PS clusters, accurately representing the extension of areas experiencing active and homogeneous deformational behaviour, were then integrated into a ranking process. The integration of this clustering procedure in a semi-automatic selection workflow proved its efficacy in the quick identification and ranking of slope processes that require a thorough evaluation of their morphographic boundaries.

At the local scale, along with a thorough examination of the morphographic and morphodynamic characteristics of the single slope process, the analysis of the displacement temporal evolution (related to the interplay of preparatory and triggering factors on the rock mass) was also considered. Specifically, the study was targeted at investigating landslide systems, where differential morphodynamics complicates the assessment of a comprehensive deformational scenario. To better depict the internal displacement heterogeneity, a post-processing analysis was conducted on the PS data to derive the bidimensional displacement vector, resulting from the combination of the measurements obtained from each orbital satellite geometry. The statistical analysis carried out on the resultant decomposed displacement vector provided substantial results in entangling the superimposition of the kinematics associated with the different sectors composing the landslide system. Furthermore, a Bayesian model was applied to the time series of the resultant vector to highlight anomalous trends and acceleration periods for each sector of the system, then compared with site-specific meteo-climatic factors. This approach allowed for a more robust correlation between accelerations in disruption rates and factors destabilising the slope (*i.e.*, preparatory and triggering). Eventually, it was possible to identify specific sectors within the landslide system that required monitoring or prioritised mitigation measures.

When nationwide transportation corridors are involved, providing a quick and accurate indication of the slope sectors susceptible to the most severe instabilities enables the subsequent planning of detailed analysis and monitoring surveys tailored to the specific criticality degree. For those cases where the interferometric technique is not feasible enough to investigate slope instability (*e.g.*, fast landslide kinematics and topographical limitations), a multi-scale approach is best suited. The first screening phase of a km-wide highway corridor was conducted through the application of interferometric analysis, which can identify active ground deformations related to slow phenomena or the displacement of debris talus derived from rockfalls and debris detachments. After selecting a few specific areas of investigation, multitemporal UAS-based high-resolution products were acquired to further analyse the slope at the local and microscale. Object-Based Image Analysis and change detection techniques were applied to multispectral and optical products: several early instability precursors and micro-landforms were identified, particularly those linked to rill erosion, that already started impacting and damaging the road infrastructure and the operating mitigation measures. The applied two-phase approach provided effective outcomes in identifying the areas of the slope most susceptible to disruption, supporting the selection of specific critical scenarios that demand immediate attention to safeguard network security and functionality and allowing for the planning of preventive measures instead of mitigation ones alone.

Plain language summary

Landslides occur in mountainous terrains worldwide: the soil or rock transported by a landslide often impacts urban settlements, causing deaths and economic damage to activities and infrastructures. Since past landslides can be reactivated over time or may initiate new failures in the vicinity because they compromise the slope stability, it is essential to record the place and extent of the phenomena that have already occurred. Landslide inventories serve this scope, as they record the extent and the specific characteristics (*i.e.*, typology, last reactivation, internal components) of landslides within maps or databases. Consequently, landslide inventories are fundamental tools for analysing landscape evolution, assessing landslide risks, and guiding authorities in development plans and mitigation measures. Information on landslide maps needs to be regularly updated and easily exploited by government authorities to ensure appropriate planning. However, outdated, fragmented, and incomplete records are common issues with the current inventory maps. This can be related to the fact that the updating process is frequently linked to the occurrence of catastrophic triggering events (such as earthquakes or heavy rainfall), which serve as the primary input for massive but short-term investigations. Thus, it is not uncommon that, between one catastrophic event and another, it can take even years before the extent and characteristics (*e.g.*, activity and intensity) of landslides can be modified and updated again. This has enormous repercussions in terms of land use and urban planning. In some areas, due to the lack of updated landslide information, there may be no restrictions imposed on building or economic activities. Therefore, this absence of restrictions may endanger both the infrastructure safety and human lives. Therefore, finding a method which allows for periodic, systematic and cost-effective updating is essential not only for scientific research purposes but also to successfully manage the problem of land use planning in those countries (such as Italy) that are exposed to very high hydrogeological risk.

This work aims to investigate the application of remotely sensed data, in particular satellite interferometric (*i.e.*, radar-based) analysis, for updating landslide inventories and provide a clear direction on identifying high-priority areas warranting in-depth investigations at regional to local scales. The support of artificial intelligence facilitated the effective management of a vast amount (several million) of measuring points derived from the interferometric analysis, which is not feasible to investigate through manual inspection. The implemented methodology, benefitting from the support provided by artificial intelligence models, can be incorporated into a consistent workflow, helping authorities to update local, regional, or even national-scale landslide inventories.

The present research project is, therefore, composed of three successive analyses, each one focusing on investigating a specific spatial scale, hence representing a workflow that can be progressively adopted when updating an inventory. Specifically, I first identified at a regional scale those slope processes warranting detailed investigations by ranking each phenomenon based on its displacement rates. The priority of a landslide to be investigated is directly proportional to its ranking; a higher class implies a higher priority. Then, depending on the specific landslide typology, a tailored local-scale investigation was applied to characterise the evolution of the process. For landslides moving at slower rates (i.e., from cm to mm per year), satellite interferometry provides valuable insights for assessing the deformational behaviour of different moving sectors of a single landslide. I also correlated each moving sector with meteo-climatic factors (like precipitation and temperature) and found potential elements that could prepare or trigger the slope to failure. For faster slope movement typologies (such as rockfalls) the combination of different platforms and sensors to properly investigate the gravitational instability is essential. In these cases, optical and multispectral sensors carried by drones can better characterise the slope to detect precursors of slope instability (e.g., initial fracturing and incision of the rock mass), allowing for preventive measures instead of mitigation alone.

List of figures

List of tables

2 Introduction

Landslides play a central role in shaping the landscape and are recognized worldwide as one of the primary geohazards impacting mountainous regions [Evans et al., 2007; Petley et al., 2007]. The quantification of the landslides' impact on both the socio-economic aspects and human lives is a subject that, despite emerging in the 1980s, remained relatively unexplored until the early 2000s [Petley et al., 2005]. According to several authors [Del Soldato et al., 2019; Gautam et al., 2021], each year landslides lead to extensive damage, including the destruction of towns and infrastructures, fatalities, injuries, and significant economic losses to national economies. Landslides exhibit discontinuity concerning their timing and geographical occurrence, and they possess an inherent variability in their magnitude even when activated by the same triggering event [Guthrie and Evans, 2007]. In light of these considerations, it becomes evident the importance of systematically gathering and preserving data on the geographical occurrence of landslides, given the interdependence between past events and the likelihood of future instability in the same or adjacent locations [Samia et al., 2017]. Landslide inventory maps serve this purpose as they document the extent of gravity-driven processes at multiple scales (from small watersheds to global scales), study the morphoevolution of landscapes dominated by mass-wasting processes, and represent the pivotal, preliminary step toward landslide susceptibility, hazard, and risk assessment [Guzzetti et al., 2000; Galli et al., 2008; Van Westen et al., 2008]. In addition, they represent indispensable tools for authorities and decision-makers to implement development plans and prioritise the funding of risk mitigation measures realisation [Corominas et al., 2014]. Despite significant technological advancements in mapping techniques and exponential growth of the availability of Earth observation data, producing a landslide inventory that is complete and accurate in both space and time is still challenging [Van Westen et al., 2008].

The present Chapter offers a first comprehensive overview of the slope instability processes and the traditional and recent techniques to produce a landslide distribution map. Eventually, I will provide the specific objectives and rationale pursued in this PhD research project.

2.1 Landslide inventories

2.1.1 Definitions

Contrary to what the term "landslide" might suggest, in a modern interpretation (referring to the last decades), this composite word refers to a more complex and profound concept of the phenomenon it strives to describe. The two words, jointly, do not limit either the geomorphological process and its landform to the narrow "land" (in the sense of a phenomenon that occurs in a subaerial environment or that involves terrain materials) or to a "sliding" movement. Within a broader context, "the movement of a mass of rock, earth or debris down a slope" can be referred to as a landslide [Cruden, 1991]. From this definition, “landslide” refers to a non-technical and all-encompassing concept of almost all types of movements and materials involved [Varnes, 1978; Cruden, 1991]. Other ordinary expressions often interchangeably used for "landslide" are "mass wasting", "mass movements", and "slope failure", neither of which includes a connotative classification meaning based on kinematics [Varnes, 1978; Highland and Bobrowsky, 2008]. Therefore, in the present work, I will use each of these terms as synonyms.

Several studies focused on understanding the various factors representing a specific landslide type. The most common classifications [Varnes, 1954, 1978; Cruden and Varnes, 1996; Hungr et al., 2014] recall a two-term combination, reflecting the different types of materials and the kinematics. The fundamental criterion originally adopted by Cruden and Varnes [1996] is based on 5+1 distinct types of movement categories, namely: 1. Falls; 2. Topples; 3. Slides; 4. Spreads; and 5. Flows (the additional category is the result of a combination of two or more kinematics, and thus referred to as "complex"). Following the update proposed by Hungr et al. [2014], a sixth category related to "slope deformation" was added. The material types considered were, in the first place, broad terms (*i.e.*, rock, debris, earth). However, not implying any geotechnical indication, Hungr et al. [2014] replaced this threefold with a list of material types that could specifically describe the mechanical behaviour of the landslide. Figure 2-1 and Figure 2-2 summarise the classification matrices respectively proposed by Cruden and Varnes [1996] and Hungr et al [2014].

TYPE OF MOVEMENT		TYPE OF MATERIAL		
		BEDROCK	ENGINEERING SOILS	
			Predominantly coarse	*Predominantly fine*
FALLS		Rock fall	Debris fall	Earth fall
TOPPLES		Rock topple	Debris topple	Earth topple
SLIDES	ROTATIONAL	Rock slump	Debris Slump	Earth slump
	TRANSLATIONAL	Rock block slide Rock slide	Debris block slide Earth block slide	Debris slide Earth slide
LATERAL SPREADS		Rock spread	Debris spread	Earth spread
FLOWS		Rock flow (deep creep)	Debris flow	Earth flow (soil creep)
COMPLEX	Combination of two or more principal types of movement			

Figure 2-1: Classification system for slope movements (modified after Cruden and Varnes, 1996).

Type of movement	Rock	Soil
Fall	1. *Rock/ice* fall[a]	2. *Boulder/debris/silt* fall[a]
Topple	3. Rock block topple[a]	5. *Gravel/sand/silt* topple[a]
	4. Rock flexural topple	
Slide	6. Rock rotational slide	11. *Clay/silt* rotational slide
	7. Rock planar slide[a]	12. *Clay/silt* planar slide
	8. Rock wedge slide[a]	13. *Gravel/sand/debris* slide[a]
	9. Rock compound slide	14. *Clay/silt* compound slide
	10. Rock irregular slide[a]	
Spread	15. Rock slope spread	16. *Sand/silt* liquefaction spread[a]
		17. Sensitive clay spread[a]
Flow	18. *Rock/ice* avalanche[a]	19. *Sand/silt/debris* dry flow
		20. *Sand/silt/debris* flowslide[a]
		21. Sensitive clay flowslide[a]
		22. Debris flow[a]
		23. Mud flow[a]
		24. Debris flood
		25. Debris avalanche[a]
		26. Earthflow
		27. Peat flow
Slope deformation	28. Mountain slope deformation	30. Soil slope deformation
	29. Rock slope deformation	31. Soil creep
		32. Solifluction

Figure 2-2: Revised Varnes classification for landslides (from Hungr et al., 2014).

Since the evolution of slope failures can occur in different modalities, timing, and intensities, thus implicating complex morpho-evolutionary scenarios and disparate effects if human settlements are involved, it has become increasingly critical to target efforts in identifying the spatial distribution of such movements. Landslide Inventory Maps (LIMs) are used for this purpose, as they record the type and extent of the phenomenon and, where known, the date of occurrence [Pašek, 1975; Carrara and Merenda, 1976; Hansen, 1984a, 1984b; McCalpin, 1984; Wieczorek, 1984; Guzzetti et al., 2000, 2012; Mondini et al., 2014; Santangelo 2015]. A further aspect to be taken into account in the classification of mass wasting processes is the representation of the state, distribution, and style of activity. The state of activity refers to the description of what is known about the timing of the process. A brief description of the different states, distributions, and styles of activity, which follows the terminology defined by Multilingual Landslide Glossary [WP/WLI, 1993], is reported hereafter.

The state of activity of a landslide can be defined as follows:

1. **Active**: landslides that currently display displacements, including both first-time movements and reactivations (in the latter case, the term **reactivated** is used).
2. **Suspended**: landslide that has moved within one annual cycle but is not moving at present.
3. **Inactive**: landslides that last moved more than one annual cycle of seasons ago. In this case, we may find: a) inactive landslide which can be reactivated by its original causes or other causes (**dormant**); b) inactive landslide no longer affected by its original causes (**abandoned**); inactive landslide which has been protected from its original causes by remedial measures

(**stabilised**); and d) inactive landslide which developed under climatic or geomorphological conditions considerably different from those at present (**relict**).

The distribution activity of a landslide broadly describes where the landslide is moving, and can be defined by the following terms [WP/WLI, 1993]:

1. **Advancing**: the rupture surface extends in the direction of movement.
2. **Retrogressive**: the rupture surface extends in the direction opposite to the movement of the displaced material.
3. **Enlarging**: the rupture surface of the landslide extends in two or more directions.
4. **Diminishing**: the volume of the displaced material is decreasing.
5. **Confined**: In a confined landslide there is a scarp but no rupture surface visible at the foot of the displaced mass.
6. **Moving**: the displaced material continues to move without any visible change in the rupture surface and the volume of the displaced material.
7. **Widening**: the rupture surface extends into one or both flanks of the landslide.

Eventually, the style of activity indicates how different movements contribute to the landslide [WP/WLI, 1993]. The simplest form is the **single** landslide, which is, intuitively, a single movement of displaced material. A **multiple** landslide shows repeated development of the same type of movement. We refer to a **complex** landslide when it exhibits at least two types of movement in sequence, while a **composite** landslide exhibits at least two types of movement simultaneously in different parts of the displacing mass. Lastly, a **successive** landslide is the same type as a nearby, earlier landslide, but does not share displaced material or rupture surface with it.
Cruden and Varnes [1996] also presented a classification based on the rate of movement of slope processes, summarised in Figure 2-3.

Velocity class	Description	Velocity (mm/s)	Typical velocity
7	Extremely rapid	5×10^{3}	5 m/s
6	Very rapid	5×10^{1}	3 m/min
5	Rapid	5×10^{-1}	1.8 m/h
4	Moderate	5×10^{-3}	13 m/month
3	Slow	5×10^{-5}	1.6 m/year
2	Very slow	5×10^{-7}	16 mm/year
1	Extremely Slow		

Figure 2-3: Landslide velocity scale (from Hungr et al., 2014).

2.1.2 Landslide inventories around the world

In contrast to the present day, during the latter half of the 20th century, landslides were regarded as geohazards of lesser significance when compared to earthquakes, floods, and volcanic eruptions. The socio-economic impact of these other natural disasters often overshadowed the damages caused by landslides. It wasn't until the 1970s that attention began to convey towards such processes, and recognizing the substantial losses, both in terms of economic repercussions and human lives, associated with them. However, early studies quantifying the damages caused by landslides remained relatively scarce during this period, as the actual extent of the landslide problem was still underestimated [Guzzetti and Cardinali, 1989a; Brabb, 1991; Howell et al., 1999].

Among the pioneering works that dealt with a preliminary identification of slope processes, we find Brabb and Pampeyan [1972], who prepared a detailed map of landslide deposits for San Mateo County, located in the San Francisco Bay. In this region, before the '70s, the landslide inventory consisted of no more than 1,200 documented phenomena in the entire Bay. It was only after the initiation of dedicated landslide mapping programs by the United States Geological Survey (USGS) that the number of identified landslide processes and deposits increased significantly, reaching approximately 70,000 mapped entities [Brabb, 1991; Howell et al., 1999]. Additional efforts followed the high-intensity storm of 1982, which triggered around 18,000 debris flows, causing at least 65$ million in damages and 25 human losses [Ellen and Wieczorek, 1988]. However, while this region was taking initial steps towards creating comprehensive maps of landslide vulnerabilities, in other parts of the world, landslide inventories still lacked adequate coverage of slope-related processes. The research conducted by Brabb and Harrod [1989] stands as a fundamental contribution to the study of landslide impacts in the United States. Their work provides a comprehensive examination of the geomorphic features of landslides, and their associated economic consequences and impact on human lives. More importantly, it has played a pivotal role in increasing awareness about the significance of creating landslide inventories and mitigating landslide risks, both on national and global scales.

In New Zealand, Crozier [1991] provided updated information regarding the widespread occurrence of landslides induced by heavy rainfall and storms, which represent significant triggers for mass movements in the country, resulting in landslide activations nearly every year [Glade and Crozier, 1996]. However, exceptional triggering events and consequent emergencies continue to represent the primary impulse for landslide mapping efforts. As a result, inventories maintain their fragmentary nature and remain applicable at the provincial or district level, contributing to the complete lack of a standardised system for maintaining a comprehensive national record of landslide phenomena up till 1990 [Glade and Crozier, 1996].

In general, examples of databases that, at a national scale, focused on collecting and storing spatio-temporal information on landslides are recorded simultaneously in various countries around the world [Glade and Crozier, 1996]. These collections predominantly included paper documents and, to a lesser extent, even initial databases of digital data in Geographic Information Systems (GIS) environments. Especially in the Alpine countries of Europe, which have shown a long history of catastrophic landslides, the conditions of altered bedrock or the presence of colluvial material and unstable glacial deposits, combined with the intensive land use, have accelerated and aggravated slope-deterioration processes [Swanston and Schuster, 1989]. Examples of databases in the alpine territories are those of France [Casale et al., 1994], Germany [Dikau et al., 1994], Austria [Kronfellner-Kraus, 1985] and Italy [Guzzetti et al., 1994]. An extensive overview of the Italian inventories will be provided in Section 2.1.4.

More recently, to obtain a more updated perspective on national landslide inventory maps in Europe, the Institute for Environmental Protection and Research (ISPRA) in Rome conducted, in collaboration with the Association of Geological Surveys of Europe (EuroGeoSurveys), a brief survey dealing with the level of detail, format, last update and other relevant information on the existing European databases [EEA, 2010]. Following this endeavour, Van Den Eeckhaut and Hervás [2012] conducted the first continental-scale effort to achieve an overview of the landslide database of 37 European countries (Figure 2-4). This work consisted of an in-depth analysis of the responses to a questionnaire distributed to each national and regional organisation, in addition to a comprehensive review of existing literature, websites, and European legislation on the subject. In both works, despite many countries currently having national landslide inventory maps, these are highly variable regarding scale and level of information. The inventories were also not always available to the public. Both works have demonstrated that not only are landslide inventories incomplete within the individual states' territory, but that a common overview of the distribution of mass wasting processes is hampered by the different levels of detail, scale and classification systems adopted [Van Den Eeckhaut and Hervás, 2012].

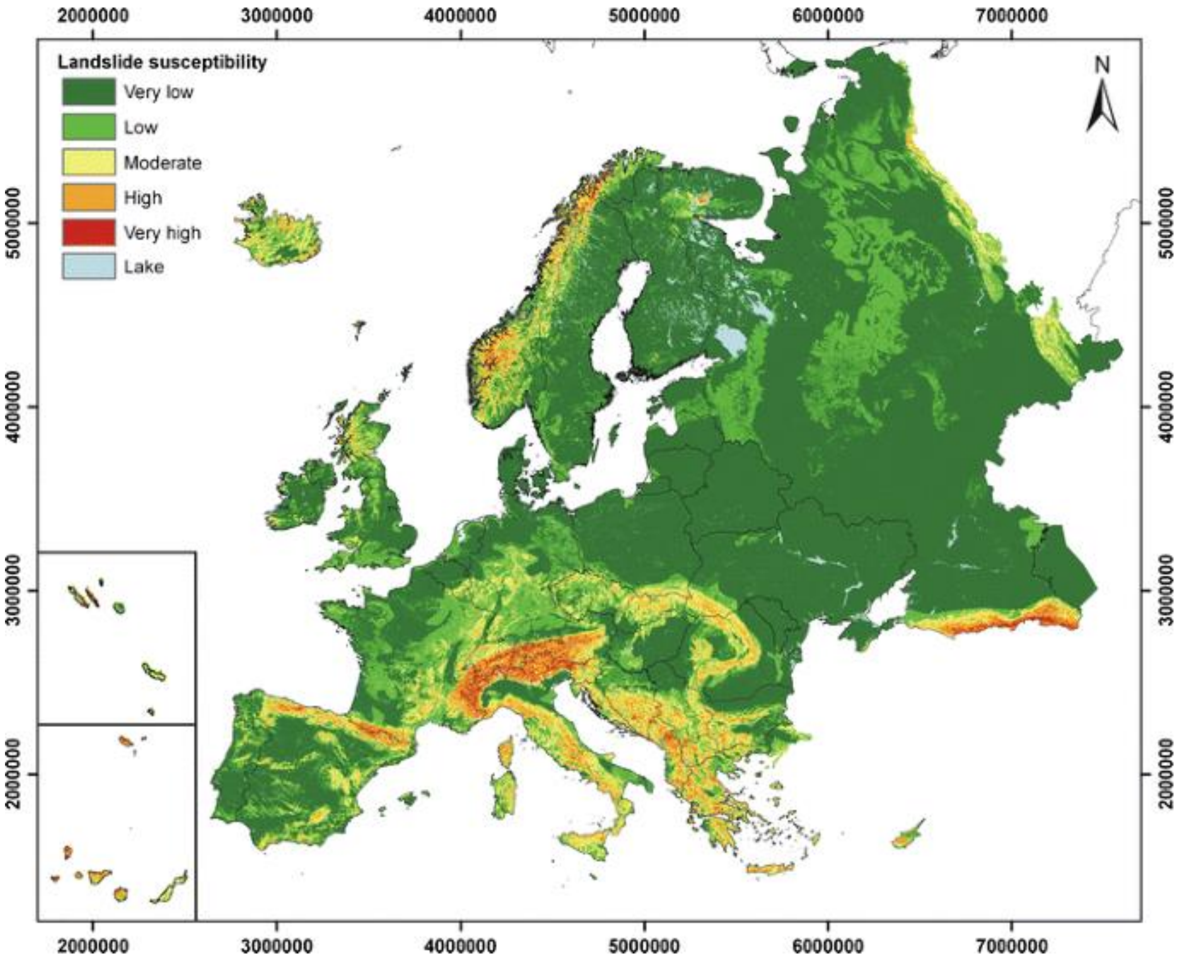

Figure 2-4: Classified landslide susceptibility map derived from the logistic regression model for the European countries. Canary, Madeira, and Azores islands are shown in the bottom left inset (from Van Den Eeckhaut and Hervás, 2012)

To date, a comparative analysis of spatial and temporal patterns of landslide occurrences worldwide using four worldwide landslide databases (i.e., International Disaster Database - EM-DAT, the Disaster Inventory System - DesInventar, the Global Landslide Catalogue - GLC, and the Global

Fatal Landslide database - GFLD) was carried out by Gómez et al., [2023]. Although characterised by different compiling criteria, description details, and spatio-temporal scales, their combination allowed to achieve a more complete insight into global landslide occurrence (Figure 2-5). However, despite the currently available technology, limitations related to the intrinsic complexity of understanding slope processes and the lack of a culture of landslide data collection still exist [Gómez et al., 2023]. Hence, the challenges associated with the production and updating of landslide inventories persist nowadays.

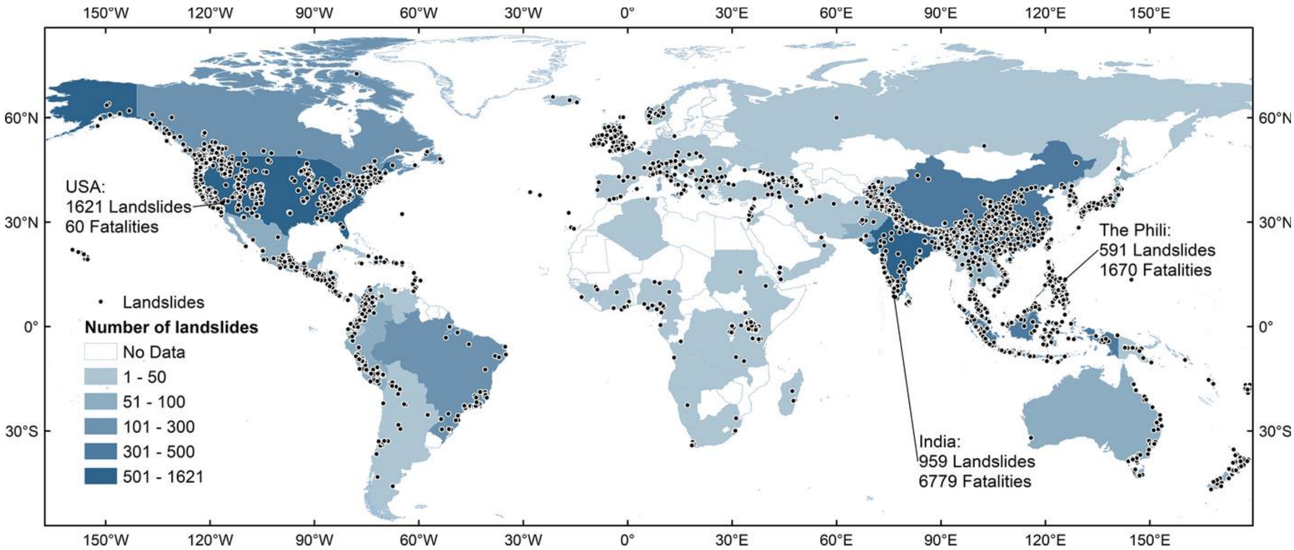

Figure 2-5: Spatial distribution of rain-triggered landslides reported in the Global Landslides Catalog (GLC 2021) (from Gómez et al., 2023)

2.1.3 Types of landslide inventory: aim and scale

Landslide inventories can belong to different classes based on the typology of mapping and, by extension, the scope of the catalogue: the two main categories are represented by i) historical; and ii) geomorphological inventories [Malamud et al., 2004; Guzzetti et al., 2012]. Collecting and storing information from archives and resources constitutes the historical inventories, which can be prepared for a specific time frame and cover local [Salvati et al., 2009; Raska et al., 2015; Piacentini et al., 2018] to national scales [Taylor and Brabb, 1986; Guzzetti et al., 1994; Reichenbach et al., 1998; Damm and Klose, 2015]. The geomorphological inventories can instead be compiled for specific time intervals (historical geomorphological inventories), showing the effects of single landslide triggering events, or representing multi-temporal datasets [Galli et al., 2008; Guzzetti et al., 2012]. In the first case, the time frame covered by such inventories may include events that have occurred over tens, hundreds, or even thousands of years [Brabb and Pampeyan, 1972; Malamud et al., 2004]. Event-based inventories are the result of a specific geomorphological survey aimed at investigating the number, type and intensity of the effects produced by one or more triggering factors, such as extreme or prolonged rainfall events [Bucknam et al., 2001; Guzzetti et al., 2004; Tsai et al., 2010; Fiorucci et al., 2018; Miele et al., 2020], earthquakes [Harp and Jibson, 1996; Fukuoka et al., 1997; Bozzano et al., 2018; Esposito et al., 2000; Lin et al., 2004; Owen et al., 2008; Gorum et al., 2011; Martino et al., 2014, 2016; Pucci et al., 2016; Ling and Chigira, 2020], and rapid snow melt [Cardinali et al., 2000; Kawagoe et al., 2009]. Eventually, multi-temporal catalogues store instability events that occurred in a specific time frame within different datasets, providing several "time-slices" of the spatiotemporal variability of the mapped landslides [Dragicévić 2004; Samia et al. 2017; Valiante et al., 2021]. In addition to the classification based on the scope of mapping, a landslide inventory can be compiled considering different mapping scales and, consequently, different methodologies. Whether small-scale inventories (> 1:200,000), which can reach national or global areas, are based primarily on the collection, synthesis, and combination of information from journals, literature, and chronicles [Kirschbaum et al., 2010, 2015; Van Den Eeckhaut et al., 2012; Mirus et al., 2020], increasing the scale involves more focused and detailed investigations. Indeed, the medium-scale inventories (1:25,000 to 1:200,000) primarily rely on the intensive interpretation of aerial and satellite imagery, with only limited field surveys conducted to verify observations made remotely [Duman et al., 2005; Calligaris et al., 2013; Conforti et al., 2014]. On the other hand, large-scale inventories (< 1:25,000) are compiled only on limited portions of the territory, with extensive field campaigns accompanied by remote sensing high and very high-resolution products (*e.g.*, digital terrain models and optical images) [Guzzetti et al., 2012].

2.1.4 Landslide inventories in Italy

As one of the European countries that is most severely and frequently hit by landslides, Italy strives to reach an up-to-date, complete depiction of the spatial and temporal distribution of slope processes over its whole territory. Favoured by its predisposing geological, geomorphological (with 75% composed of mountainous and hilly terrains), tectonic settings, and climatic conditions, the Italian territory has always been affected by slope instabilities impacting socio-economic activities and leading to a relevant amount of casualties each year (Figure 2-6), especially along the Apennines and Alpine Chains [Farina et al., 2004; Bianchi and Salvati, 2023]. Annual reports on the impact of landslides and floods on the Italian population are published each year based on the first national historical archive, called AVI (Italian Vulnerable Areas, [Guzzetti et al., 1994]). This database was prepared as part of a national inventory project to store information on sites historically affected by landslides and floods in Italy for the period 1918–2002 [Carrara and Merenda, 1976; Carrara et al., 1977; Calvello and Pecoraro, 2018]. However, it was not until 1998, following the devastating debris flow events that tragically struck the city of Sarno and claimed the lives of 137 people [Catapano et al., 2001], that the Hydrogeological Asset Plan (Piano stralcio di Assetto Idrogeologico, PAI [PAI, available at https://www.autoritadistrettoac.it/restart/glossario/PAI]) was introduced as the national-level tool for identifying hydrogeological risks for spatial planning purposes. PAI inventories represent dynamic instruments that have evolved over time. They have undergone updates by the so-called "Basin Authorities" (now known as District Basin Authorities) in response to recent research findings, investigations, emerging hydrogeological incidents, the completion of structural risk mitigation projects, or upon request from local authorities. These plans facilitate the implementation of land use restrictions and regulations as they store not only areas where landslides have already occurred but also regions susceptible to potential evolution (according to each landslide distribution activity) and areas at risk of new landslide occurrences [PAI]. Regular updates are, therefore, indispensable, as they enable the consideration of evolving instability phenomena and any newly emerging landslides. All of the PAI inventories were initially produced from preliminary recognition of the phenomena over large areas, between 1999 and 2002.

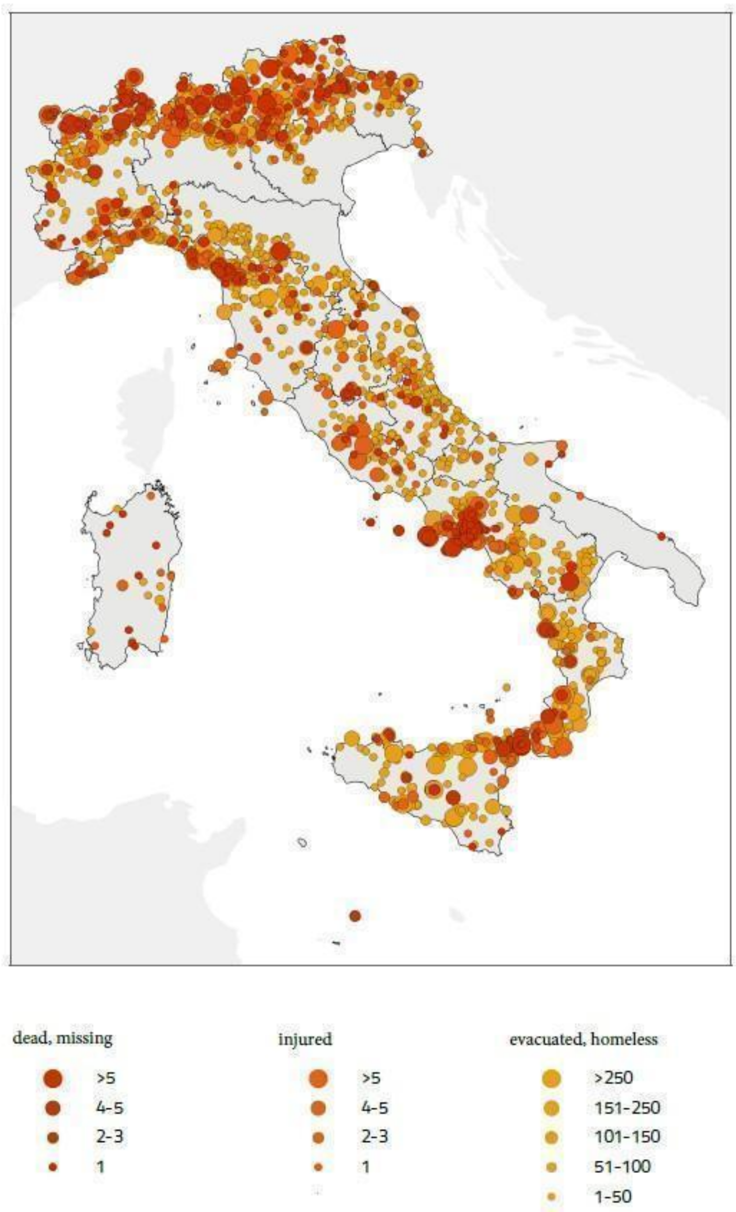

Figure 2-6: Map of landslide events with victims in the period 1971-2020 (modified after Bianchi and Salvati, 2023).

Meanwhile, the Geological Survey of Italy (part of the Land Protection and Georesources Department) launched the IFFI Project (Inventory of Landslide Phenomena in Italy), which, although started earlier (1997) with the same objectives, produced the first results in 2007, after the first adoption of the PAI [Rapporto Attività Linea A2, 2023]. Despite this, at present, the IFFI Inventory is the most complete landslide database covering the Italian territory, both regarding the adopted cartographic scale (1:10.000) and the associated parameters to slope processes. According to the last report, as of 2022, the landslides recorded in Italy are over 625,000, affecting around 8% of the national territory (Figure 2-7) [Trigila et al., 2021]. Data are collected and integrated from various sources, including national projects (*e.g.*, AVI), landslide records collected by Regions, research institutions, and universities, national and local public archives, and scientific publications and technical reports [Trigila et al., 2010]. However, even if the IFFI Inventory serves as a crucial foundational resource utilised in the PAI inventory for assessing landslide hazards, these two distinct landslide databases coexist within the same territory, frequently exhibiting disparities in their cartographic representations. During the territorial planning (*i.e.*, seismic microzonation or urban planning) landslide correspondence between the two inventories is constantly verified and updated in order to align the land-use planning to the state of fact detected on the territory [Rapporto Attività Linea A2, 2023].

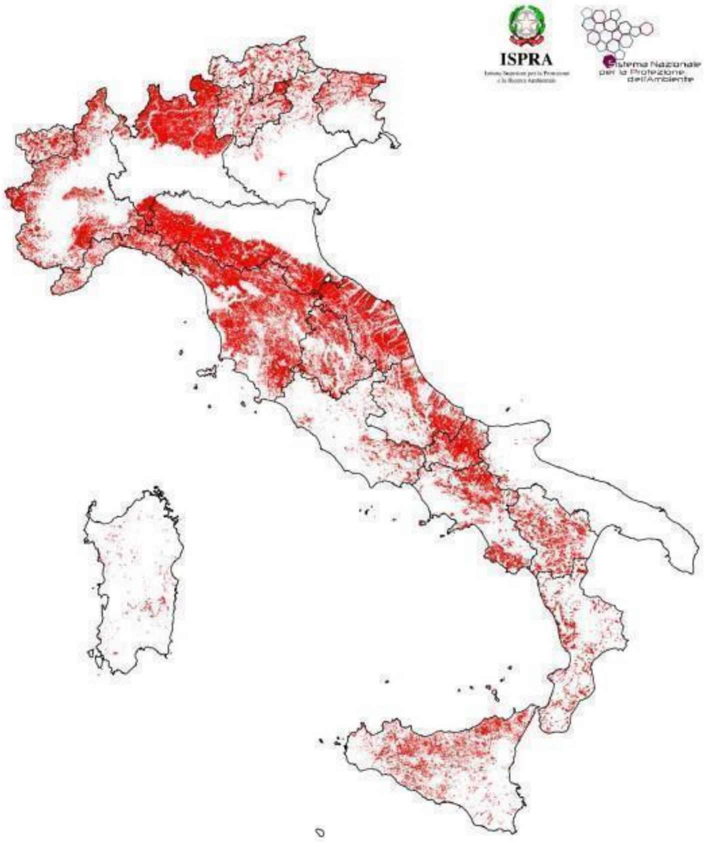

Figure 2-7: Distribution of landslides mapped and stored within the IFFI inventory. The alignment of these phenomena along Italy's two primary mountain ranges, the Alps and the Apennines, is evident (modified after Trigila et al., 2021).

Several issues such as common spatial inhomogeneity and the use of different mapping methods and classification criteria, hamper the real usefulness of national-scale inventories which, for some areas, happen to be inadequate [Fusco et al., 2023]. Therefore, to overcome these limitations, many inventories were produced at the regional level to achieve a consistent homogeneous coverage of landslide phenomena. Examples of such inventories come from several regions all over the Italian territory, such as Campania [[Fusco et al., 2023], Basilicata [Lazzari et al., 2017], Puglia [Pellicani and Spilotro, 2015; Ardizzone et al., 2023], Tuscany [Rosi et al., 2018], Umbria [Guzzetti and Cardinali, 1989b], Piedmont [Lanteri and Colombo, 2013], Liguria [Raso et al., 2019]. While the prevailing trend among these databases is to document the extent and spatial distribution of landslides, few exceptional efforts were made to include the temporal information (*i.e.*, date of occurrence or multiple reactivations). The CLOCkER catalogue (Catalogue of Landslide OCcurrences in the Emilia-Romagna Region [Piacentini et al., 2018]) includes 14,416 landslide events and their respective date of occurrence for the entire Emilia Romagna Region spanning approximately 900 years (from 1130 to 2015). Even if not applied at the regional scale, further efforts to propose the implementation of multi-temporal databases for handling complex spatiotemporal arrangements of landslides are presented in Valiante et al. [2021]. Their work applies an object-oriented classification and a hierarchical organisation of objects based on rigorous topological relations to manage spatiotemporal succession of landslides.

At the national scale, inventories that aim to combine spatio-temporal information are mainly event-based and include the spatial distribution of landslides activated or reactivated by the same trigger event (*e.g.*, precipitation, earthquake). The ITALICA (ITAlian rainfall-induced LandslIdes CAtalogue [Peruccacci et al., 2023]) catalogue includes information on the geographical location and the timing of rainfall-induced landslides. It currently lists 6312 records with information on rainfall-induced landslides that occurred over the Italian territory between January 1996 and December 2021. As for the seismic trigger, the CEDIT (Italian Catalogue of Earthquake-Induced Ground Failures [Martino et al., 2017]) inventory, based on several historical documents, is a complete collection of Landslides and Seismic-induced effects covering a period of about a millennium from 1000 AD. This database, carried on for over a decade by the Research Center for the Prediction, Prevention and Control of Geological Risks (CERI), is periodically updated and the latest version dates back to 2017, when the catalogue was not only reorganised in its architecture but also integrated with ground effects occurred during the 2016-2017 seismic sequence of the Central Apennines [Caprari et al., 2018].

2.2 Producing a landslide inventory

With the continuous expansion of globally acquired high-resolution remote sensing data and the ongoing advancements in data processing technologies, the methodologies for generating landslide inventories have undergone significant evolution. This paragraph offers a broad perspective on the diverse approaches employed in inventory production, categorised into: i) conventional or classical methods; ii) recent methodologies; and iii) new methods and future perspectives.

2.2.1 Conventional methods

2.2.1.1 Field mapping

Since field geomorphological mapping is historically the standard method for detecting signatures of slope processes, it has also erroneously perceived as a more accurate approach compared to remotely based techniques [Guzzetti et al., 2012]. Howevehoweverr, the process of identifying a landslide through geomorphological field surveys is not always as straightforward as it may appear, due to various limiting (or even precluding) factors, including:

1. **Size** of the landslide: when dealing with large landslides or gravitational deformations on slopes, it becomes challenging to observe the entire phenomenon comprehensively and map it accurately. In such cases, remote approaches can aid in identifying the actual extent of ruptures, bulging or counterslopes, and river networks' adjustments, which may be challenging to discern directly in the field [Guzzetti et al., 2012].
2. **Viewpoint** of the expert: field observers often encounter obstacles such as dense vegetation, rugged terrain, or inaccessibility, which can obscure their line of sight (Figure 2-8), resulting in an incomplete assessment of various elements of a landslide (e.g., deposit, primary or secondary scarps, flanks) [Wills and McCrink, 2002].

3. **Age** of the landslide: recognizing older landslides can be particularly challenging. In contrast to recent landslides with well-defined rupture surfaces and conspicuous deposits modifying the surrounding landscape (for example, by removing vegetation), older landslides may have smoother, less distinct features. Natural geomorphic agents and human activities in cultivated or urbanised areas can contribute to the gradual fading of failure signatures over time (Figure 2-8). Moreover, on the oldest deposits, the gradual renewal of vegetation tends to obscure the original emplacement of the landslide body [Freund et al., 2021].
4. **Time-consuming mapping**: field surveying isn't typically employed to exhaustively investigate every process within a large area. Instead, it serves to check and validate specific critical elements where the overlapping influence of multiple geomorphic processes or limitations of other remote techniques hinder accurate identification [Carrara et al., 1995].

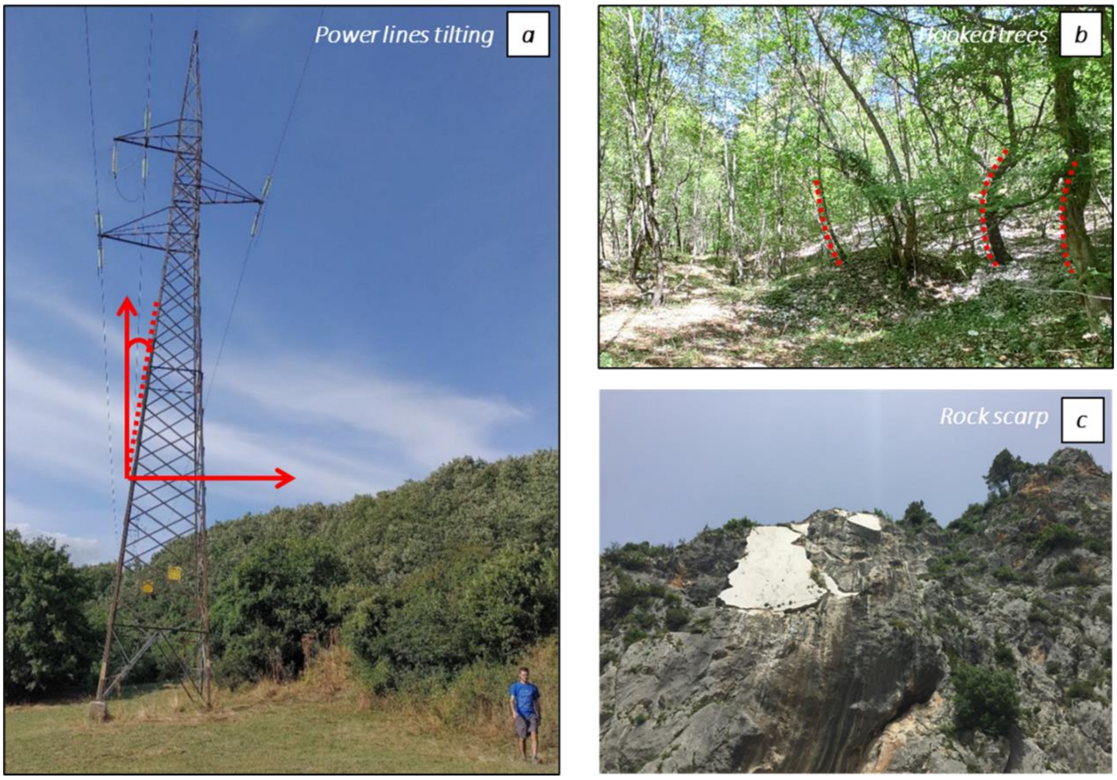

Figure 2-8: Pictures from geomorphological field surveys: sometimes it can be tricky to recognize smooth landslide features, which need to be identified through secondary field evidence (like power lines tilting and hooked trees, respectively shown in panels a and b - courtesy of Dott. Amato). The limited viewpoint of the observer may also preclude the identification and mapping of some of the landslide's components (panel c).

2.2.1.2 Visual interpretation of aerial imagery

One of the earliest applications of remote sensing techniques for landslide identification and mapping involved the visual (qualitative) interpretation of images captured by sensors mounted on aircraft. Even nowadays, interpreting imagery obtained from aerial or satellite platforms remains a primary method for information acquisition, particularly for reconstructing the multi-temporal morphoevolution of mass processes [Guzzetti et al., 2012; Napieralski et al., 2013]. In fact, for decades, various stakeholders, including national and local government agencies, research institutions, and private enterprises, have been procuring stereoscopic aerial photographs for a wide array of purposes. These invaluable resources have been accessible in numerous regions, dating back to the 1950s and, in some areas, even earlier [Guzzetti et al., 2012]. The aerial perspective offers a unique vantage point for observing and interpreting landscapes, distinct from the limited viewpoint typically available from the ground [Jensen, 2009]. Moreover, observing stereoscopic images creates a sense of three-dimensionality in two-dimensional images, making objects appear as if they have depth, volume, and spatial relationships, "*making the smallest details distinguishable with remarkable clarity due to the sensation of relief, which might pass completely unnoticed in a single photograph*" [Aber et al., 2019]. Thanks to the vertical exaggeration of the relief, a geomorphologist is aided in recognizing and mapping the topographic signatures of landslides, covering large areas with few photographs, since the average acquisition scale ranges from 1:5,000 to 1:70,000 [Pike, 1988; Guzzetti et al., 2012]. This visual recognition often takes place as an intuitive process for the interpreter. Nevertheless, several fundamental features facilitate the examination and interpretation of aerial photographs [Jensen, 2009; Aber et al., 2019]:

1. **Tone or Colour**: the distinction in grey tone (black and white) or colour is how we recognize and differentiate one object from others in the scene (*i.e.*, water, soil, vegetation, rocks), particularly when dealing with high-contrast features.
2. **Shape**: natural forms often align with the contours of the landscape, while human-made shapes tend to exhibit geometric characteristics and regular forms.
3. **Size and Height**: The absolute size and height of objects are crucial indicators that rely on the scale of the photograph, as many objects observed in aerial photos may not be as readily apparent, and determining their height can be challenging.
4. **Shadow**: Shadows serve as valuable indicators for identifying objects when viewed from an aerial perspective, continuing to depth perception in the landscape. Photographs lacking shadows can appear indistinct and challenging to interpret while, on the contrary, excessive shadowing may obscure the features of interest.
5. **Pattern**: The spatial arrangement of discrete objects can generate unique patterns, especially in the case of human-made features (*e.g.*, agricultural fields, streets) or specific natural environments (*e.g.*, drainage networks, dune fields).
6. **Texture**: Texture refers to the appearance of grouped objects that are either too small or closely spaced to form distinct patterns. Textural adjectives like smooth (uniform), intermediate, and rough (heterogeneous) are used to describe this feature. Examples include the crowns of trees within a forest canopy, or individual plants in agricultural fields. The distinction between texture and pattern is largely influenced by the scale of the photograph.
7. **Context**: The location of objects and their relationships with other objects and patterns are often critical for interpretation, as is their geographical context. Land cover and land use serve as essential clues for identifying related features within the scene, and reference to existing maps or census data can provide additional context. Interpretation often relies on common sense and experience in image analysis, as it stands as one of the elements of image interpretation with the highest complexity.

These elements of image interpretation are depicted in Figure 2-9. Since each image is composed of individual pixels with a unique colour or tone at a certain geographic location, these are the fundamental (primary) parameters upon which all other elements are based. The secondary and tertiary elements are spatial arrangements of tone and colour. The higher order elements of site, situation, and association include a higher level of complexity since they are based on the use of collateral information, convergence of evidence, and the use of the multi-concept [Jensen, 2009].

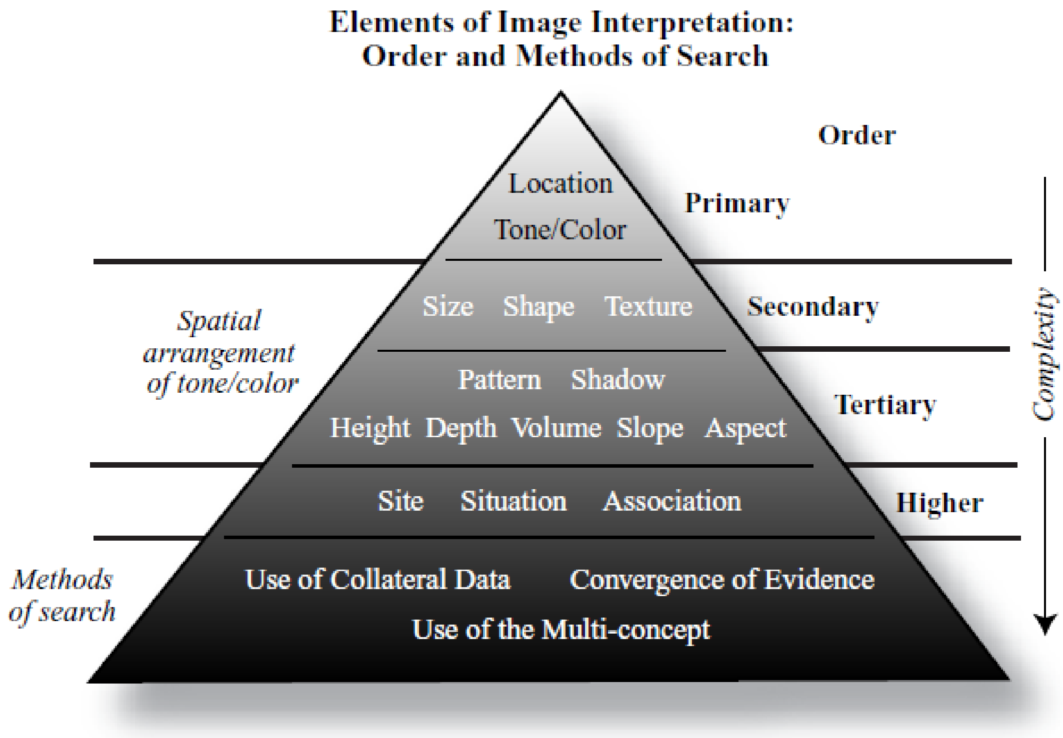

Figure 2-9: Elements of image interpretation: the first-order parameters represent the basis of the image (tone/colour), the second and third-order are spatial arrangements of the primary order parameters, while higher order corresponds to different methods of search and, therefore, higher complexity level (from Jensen, 2009).

For decades, various stakeholders, including national and local government agencies, research institutions, and private enterprises, have been procuring stereoscopic aerial photographs for a wide array of purposes. These invaluable resources have been accessible in numerous regions, dating back to the 1950s and, in some areas, even earlier [Guzzetti et al., 2012]. For example, the historical archive of the Military Geographical Institute contains over 300,000 aerial photos of the Italian territory taken between 1927 and 2010 [IGMI]. Among this impressive database, the G.A.I. (Italian Aeronautical Group) Flight, which is the first planimetric and stereoscopic covering the entire national territory for the 1954-1956 interval (Figure 2-10), and Volo Italia flights, carried out starting from 1988, are among the most used datasets to perform multi-temporal investigations of the Italian territory, including landslide morphoevolution purposes.

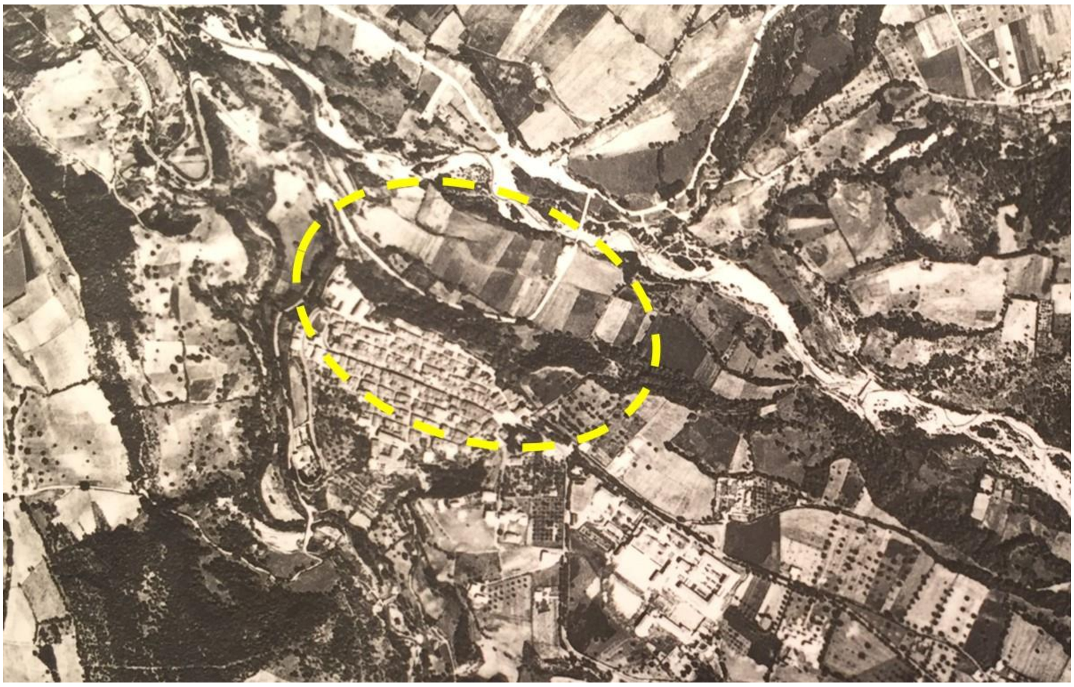

Figure 2-10: Extract of a frame of the GAI flight depicting the town of Amatrice (circled in yellow) during 1953-54.

2.2.2 Recent methods

2.2.2.1 Analysis of topographic digital datasets

The rapid progress in technology has opened up exciting opportunities for generating digital representations of the Earth's topographic surface in three dimensions, marking the natural progression from stereoscopic interpretation of two-dimensional images. Digital elevation models, commonly referred to as DEMs, are data files or databases that encompass elevation data points across a continuous geographic area [Jensen, 2009]. Depending on whether they exclusively portray the Earth's bare surface or also include above-ground objects, they are categorised as either Digital Terrain Models (DTMs) or Digital Surface Models (DSMs), respectively. Various techniques are employed to create these models, ranging from on-site field surveys and photogrammetry to the utilisation of topographic maps, laser scanning, and radar data acquisition [Jensen, 2009; Aber et al., 2019]. Indeed, the widespread availability and ease of accessibility of DEMs have marked a significant advancement in data collection within the domain of mountain geomorphology due to their global coverage and continually enhancing measurement precision. The creation, examination, and presentation of DEMs is now a standard procedure for mapping landforms [Napieralski et al., 2013]. The visualisation and interpretation of digital models can be compared to the visual analysis of aerial stereo-pairs, digitally substituted by DEM derivatives such as shaded relief of the terrain or representations of its distinctive characteristics (*e.g.*, curvature, roughness) [Guzzetti et al., 2012]. The resulting topographical products, especially in the case of shaded reliefs, support the landslide feature identification because they provide suitable lighting conditions for different slope areas by changing the shadow (Figure 2-11), thus depicting drastically different representations of the ground surface [Schulz, 2004].

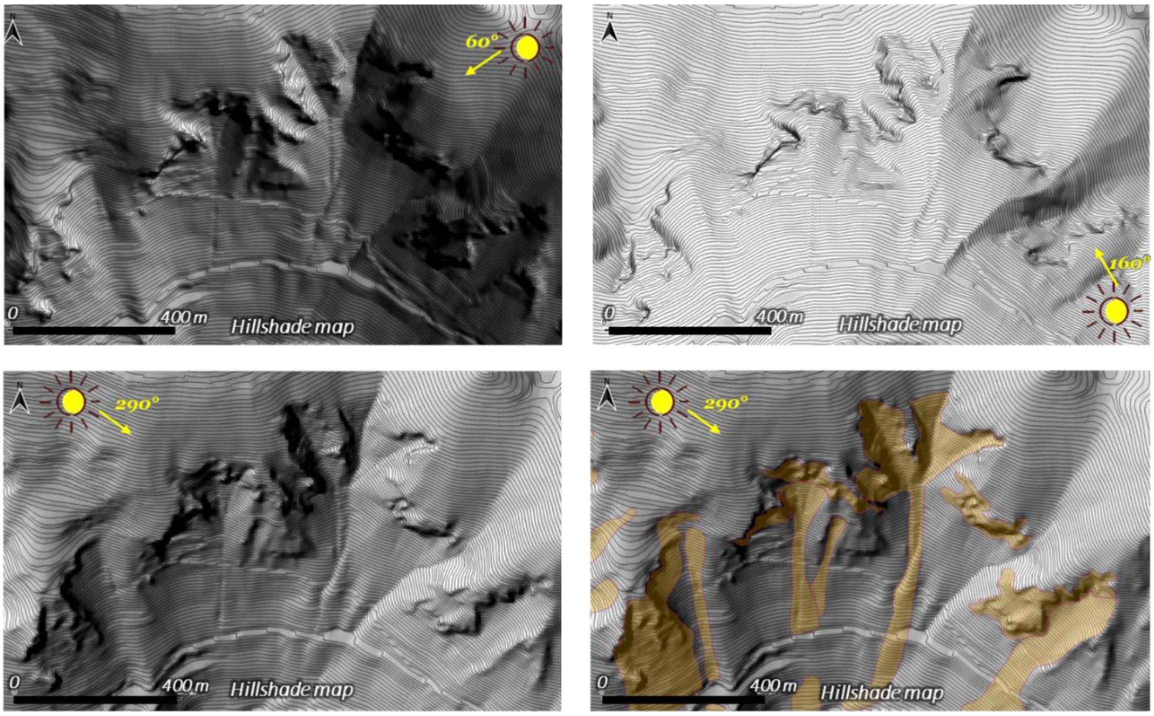

Figure 2-11: DEM-derived shaded reliefs of the same slope under changing lighting conditions. The specific sun orientation may preclude or support the landslide feature identification depending on the slope aspect and gradient: in this case, the most suitable sun azimuth is 290°.

In addition, digital models have enabled land-surface quantitative analyses (*i.e.*, geomorphometry) to address, on a specific level, the characterization of discrete surface features (*i.e.*, landforms) [Sekiguchi and Sato, 2004] or, in the general sense, to describe the continuous topography of a territory [Pike, 2009; Troiani et al., 2014]. The emergence of remote sensing technology based on Light Detection and Ranging (LiDAR) has revolutionised the collection of digital surface models and digital terrain models. LIDAR sensors achieve hundreds of thousands of points per second that already possess accurate x,y, and z coordinates and that are used both for geomorphological applications and in urban engineering [Jensen, 2009; Pawluszek, 2019]. Due to its high effectiveness in delivering precise surface topography information, today high-resolution DEMs (HRDEMs) generated from LiDAR are widespread worldwide and continue to advance rapidly [Tarolli, 2014 and references within]. Numerous examples in the literature demonstrate the various applications of HRDEMs for accurate landslide identification [Bell et al., 2012; Jaboyedoff et al., 2012 and references within; Pawluszek, 2019 and references within; Zhong et al., 2020], even in challenging environments characterised by dense forest cover [Van Den Eeckhaut et al., 2007; Chen et al., 2014], offering advantages over other investigative techniques limited by these conditions. Many countries, including Italy, have collected or are collecting national and/or regional LiDAR-derived repositories [Jaboyedoff et al., 2012], including point clouds, HRDEMs and their derivatives, giving unprecedented opportunities for landslide mapping over large areas, with potential impacts on hazard and risk evaluation or for landscape evolution modelling.

2.2.2.2 Analysis of multispectral imagery

In recent times, aerial, satellite, and unmanned aerial vehicle data (boosted by advancements in computer hardware and software, sensor capabilities, and acquisition frequency) represent the evolution of the old stereo-pairs and are currently used to evaluate the morphoevolution of the territory both through the qualitative photo-interpretation or change detection techniques. Passive optical sensors acquire images of the topographic surface in the visible and infrared domains of the electromagnetic spectrum (400 ηm - 1040 μm) in the visible and infrared domains [Jensen, 2009]. Products taken with panchromatic (single band) and multi-spectral (multiple bands) sensors are usually preferred by investigators for landslide identification, who employ both qualitative visual assessment of the landslide signatures and analytical methods (such as classification and semi-automatic detection) [Guzzetti et al., 2012].

Satellite or Unmanned Aerial System (UAS) images with high and very-high resolution enable us to identify and map landslide features at different scales and levels of detail (Figure 2-12) through the same interpretation process described in Section 2.2.1.2. Compared to traditional aerial stereoscopic images, the multitemporal and ubiquitous spatial coverage (for satellite-based images) offers the opportunity to investigate occurrences or reactivations of slope failures following major triggering events [Van Westen et al., 2006], thus keeping up-to-date event inventory maps. Additionally, the introduction of Google Earth® (Figure 2-12), offering global and multi-temporal access to VHR optical satellite imagery combined with 3D visualisation supports landslide identification [Guzzetti et al., 2012; Mohammadi et al., 2018; Cheng et al., 2021].

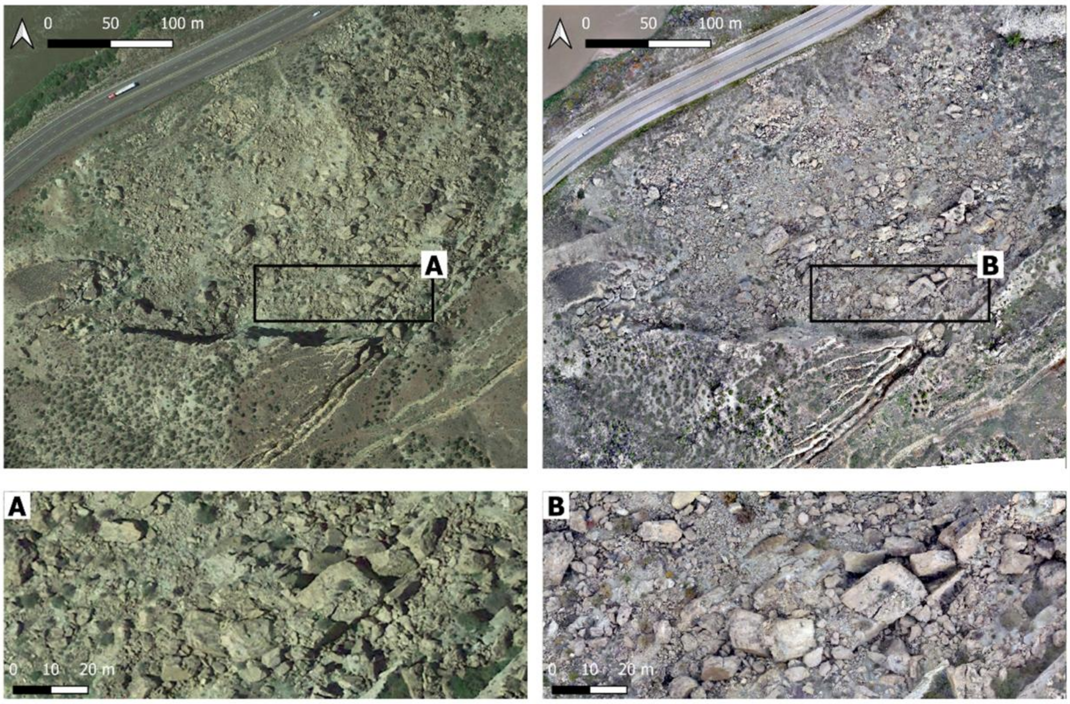

Figure 2-12: Comparison between Google Earth (left panel) and UAS-based (right panel) optical imagery of a landslide located in Colorado, USA. The zoom boxes compare the level of detail reached with images acquired at medium resolution (Google Earth, zoom A) and at very high resolution (drone image, zoom B) of the debris.

Regarding the analytical approach of satellite images, the discrimination between stable areas and areas affected by landslide-induced deformations is carried out using semi-automatic image classification techniques, which exploit the peculiar spectral information of the image. The availability of substantial volumes of medium to high-resolution imagery has made Machine Learning (ML) techniques increasingly appealing for landslide detection, training the machine to identify key landslide characteristics to "*make predictions or decisions without being explicitly programmed to do so*" [Tehrani et al., 2022]. The main approaches implemented to identify landslide features are defined as pixel and object-based, depending on whether the ML algorithm employs a single pixel or an aggregate of pixels of variable size representing the different landslide segments [Zhong et al., 2020; Tehrani et al., 2022]. In the first case, the spectral signature relative to the single pixel (whether using the single-band or a multi-band image) is analysed, disconnected from the information of the neighbouring pixels, to determine whether it is classifiable as a landslide or not. Common methods include thresholding [Hervás et al., 2003; Rosin and Hervás, 2005; Yu and Chen, 2017], change detection [Yang and Chen, 2010; Li et al., 2016; Zhao et al., 2017; Si et al., 2018], and supervised or unsupervised [Danneels et al., 2007; Lacroix et al., 2013; Siyahghalati et al., 2016] classification algorithms, whether the training pixels were assigned to user-defined labels or when the algorithm tries to find patterns in unlabelled data [Ma et al., 2020]. The limitations related to the pixel-based approach, especially related to noise and the salt-and-pepper effects which reduce the accuracy of the analysis, led to increasingly employing the Object-Based Image Analysis (OBIA) method [Blaschke et al., 2008], where the trained classification algorithm produces a class prediction for pixels on a group basis [Zhong et al., 2020; Tehrani et al., 2022]. This approach was effectively used for producing more accurate results, enabling the extraction of detailed landslides geomorphic features with various techniques [Stumpf and Kerle, 2011; Hölbling et al., 2012; Keyport et al., 2018; Amatya et al., 2021; Valiante et al., 2021].

2.2.2.3 Analysis of radar imagery

Interferometric Synthetic Aperture Radar (InSAR) has emerged as a powerful tool in the scientific literature for detecting and monitoring landslides over the last 20 years, finding several applications in landslide risk mitigation strategies at different stages and scales [Moretto et al., 2021]. The launch of several satellite missions belonging to different national and international space agencies, the improvement of satellite mission technologies, computing capabilities and processing algorithms are among the factors that contributed to the spread and development of satellite SAR interferometry worldwide. Obtaining multiple SAR images of the Earth's surface can provide valuable three-dimensional and velocity data: whenever radar images of the same ground area are captured either from different locations or at different times, enables highly accurate measurements in each image pair, even with sub-wavelength precision [Jensen, 2009]. Moreover, InSAR is particularly valuable for landslide studies due to its ability to provide frequent, wide-area coverage, and all-weather capabilities. In particular, Differential SAR Interferometry (DInSAR) is a radar-based method that exploits phase information from a minimum of two SAR images captured over the same geographic area but at different time points. This process results in the creation of interferometric differential maps, referred to as "interferograms" [Hanssen, 2001]. The advantage of these differential maps consists in the flexibility to provide qualitative information on ground displacements, even where SAR data are scarce. Nonetheless, DInSAR analyses are affected by atmospheric phase screen (APS) and residual topography [Cascini et al., 2009; Moretto et al., 2021].

Ferretti et al. [2000; 2001] achieved a breakthrough in addressing the aforementioned limitations by harnessing long acquisition sequences, specifically through the analysis of a stack of multitemporal and multi-baseline (MT/MB) interferograms. This innovative approach, known as Permanent Scatterers (PS), demonstrated its effectiveness in mitigating APS through the application of statistical filtering techniques to long-term radar sequences, resulting in highly accurate ground deformation and residual topography estimations, particularly on stable target areas [Cascini et al., 2009]. As stated by Wasowsky and Bovenga [2014], further remarkable advantage of the technique relies on the cost-effectiveness application for wide areas (hundreds and thousands of km2), maintaining high precision of measures (in the order of mm) and the availability of high-density radar targets, both in natural and urbanised areas. Therefore, the PS-InSAR technique is extremely versatile for investigating ground deformations on a multi-scale approach, from regional scale mapping [Righini et al., 2012; Bianchini et al., 2018; Frattini et al., 2018; Rosi et al., 2018; Antionielli et al., 2019; Dini et al., 2019; Xu et al., 2021], to basin scale [Sousa et al., 2010; Rocca et al., 2015; Bozzano et al., 2017a; Yazici and Gormus, 2020], up to the detailed study of processes at the local scale [Bardi et al., 2014; Eriksen et al., 2017; Pawluszek-Filipiak et al., 2019; Moretto et al., 2021](Figure 2-13).

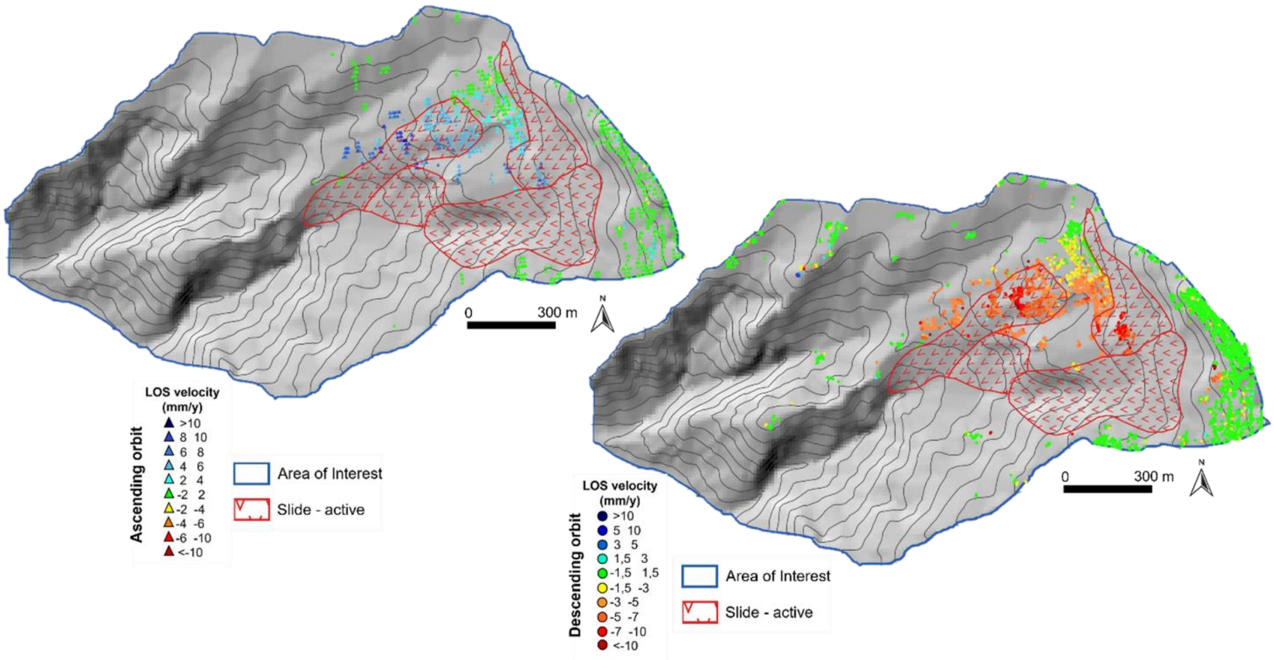

Figure 2-13: Example of PS analysis of a slope of interest located in the Marche Region, Italy. The measuring points, obtained in both orbital geometries, show severe displacements (up to 10 mm/y) within and outside the landslide extent.

Along with PS-InSAR, another popular multitemporal interferometric approach is represented by the Small Baseline Subset (SBAS) [Berardino et al., 2002], which exploits pairs of images with optimal spatial baselines (below a certain threshold). One of the main differences between PS and SBAS is that, while in the PSI analysis, each cell is dominated by a single measurement point, in the SBAS analysis no dominant element represents the resolution cell. The SBAS distributed scatterers are more susceptible to both temporal and volume decorrelation compared to PS, leading to significant variations in the number and spatial arrangement of observable targets, depending on the scattering characteristics of the ground surface [Wasowsky and Bovenga, 2014; Scaioni et al., 2014]. Nevertheless, SBAS is widely adopted for identifying and mapping landslides-related active deformations [Novellino et al., 2017; Confuorto et al., 2023] or for detailed morphodynamic characterization [Calò et al., 2014; Martins et al., 2020].

Currently, the extensive array of satellites employing different wavelengths, spatial resolution, revisiting time, and incident angles, enables comprehensive coverage of the Earth's entire surface. This availability extends back to as early as 1990 and, with ongoing advancements in sensor technology, the capacity to monitor ground deformations is steadily improving, promising even greater precision and shorter revisit times in the future [Calò et al., 2014; Wasowsky and Bovenga 2014; Moretto et al., 2021]. In particular, missions funded by the European Space Agency (ESA), from the ERS and ENVISAT satellites to the Sentinel-1A and 1B constellation, which provide nearly continuous radar information in the C-band (Figure 2-14), enable retrospective investigations into the pre-failure conditions of landslide phenomena [Barra et al., 2016; Intrieri et al., 2018; Gama et al., 2020]. L-band data provided by the Japanese Space Agency JAXA (ALOS PALSAR and PALSAR-2 missions) and the Argentinean CONAE (with SAOCOM constellations), thanks to their high capacity of penetrating vegetation canopy, are very often exploited to investigate forested areas [Jebur et al., 2014; Nishiguchi et al., 2017], managing to capture displacement information where other sensors fail. Eventually, the emergence of the "second generation" X-band SAR systems, represented by Italian COSMO-SkyMed (CSK) and German TerraSAR-X, has led to substantial enhancements in the mapping and monitoring capabilities [Herrera et al., 2011; Calò et al., 2014; Wasowsky and Bovenga 2014; Bozzano et al., 2017b], owing to their improved ground resolution and temporal sampling.

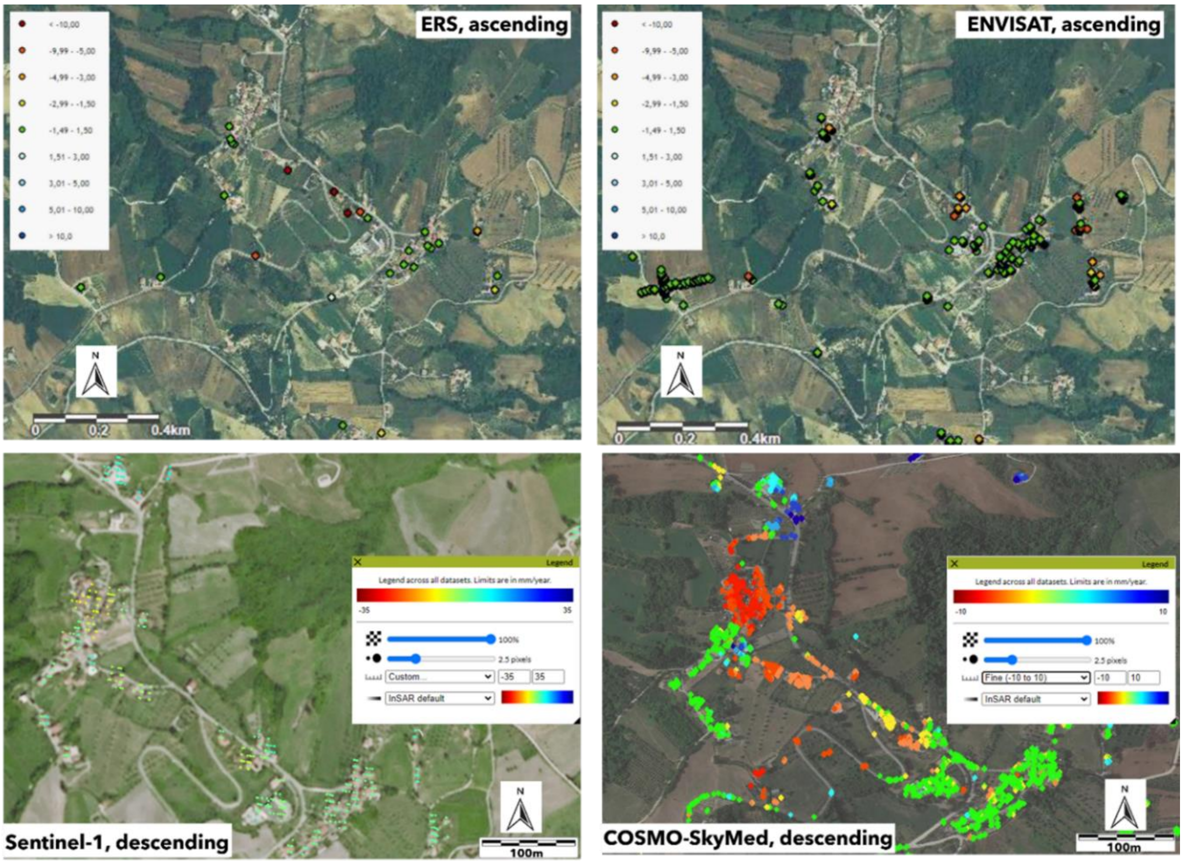

Figure 2-14: Comparison between four PS-InSAR analyses derived from C-band satellite (ERS, ENVISAT and Sentinel-1) and X-band (COSMO-SkyMed). Starting from the older sensors (i.e., ERS and ENVISAT) and depending on the band acquisition, we can observe an increase in the number of PS within the scene.

Solari et al. [2020] conducted an in-depth review on the use of interferometric analysis for the study of landslides on the Italian territory, to provide an overview of the effectiveness of this technique not only for updating national inventories purposes but also for characterisation and monitoring of the slope process in the short to long term. Figure 2-15 shows the number of published works by region: Sicily (35), Lombardy (26), and Tuscany (24) are the Regions with the highest number of applications. A conspicuous number of publications is found in the Lombardia region and generally along the Alpine arc, where the occurrence of phenomena with slow kinematics and involving large portions of slope (from Deep Seated Gravitational Slope Deformations DSGSD to large rockslides) represent the ideal context for InSAR application. In addition, works focusing on the landslide occurrence along the Apennine chain, where the InSAR technique was exploited not only for characterising and monitoring slope processes but also for mapping new landslides, especially after strong seismic events (such as Amatrice and L'Aquila) which triggered thousands of landslides.

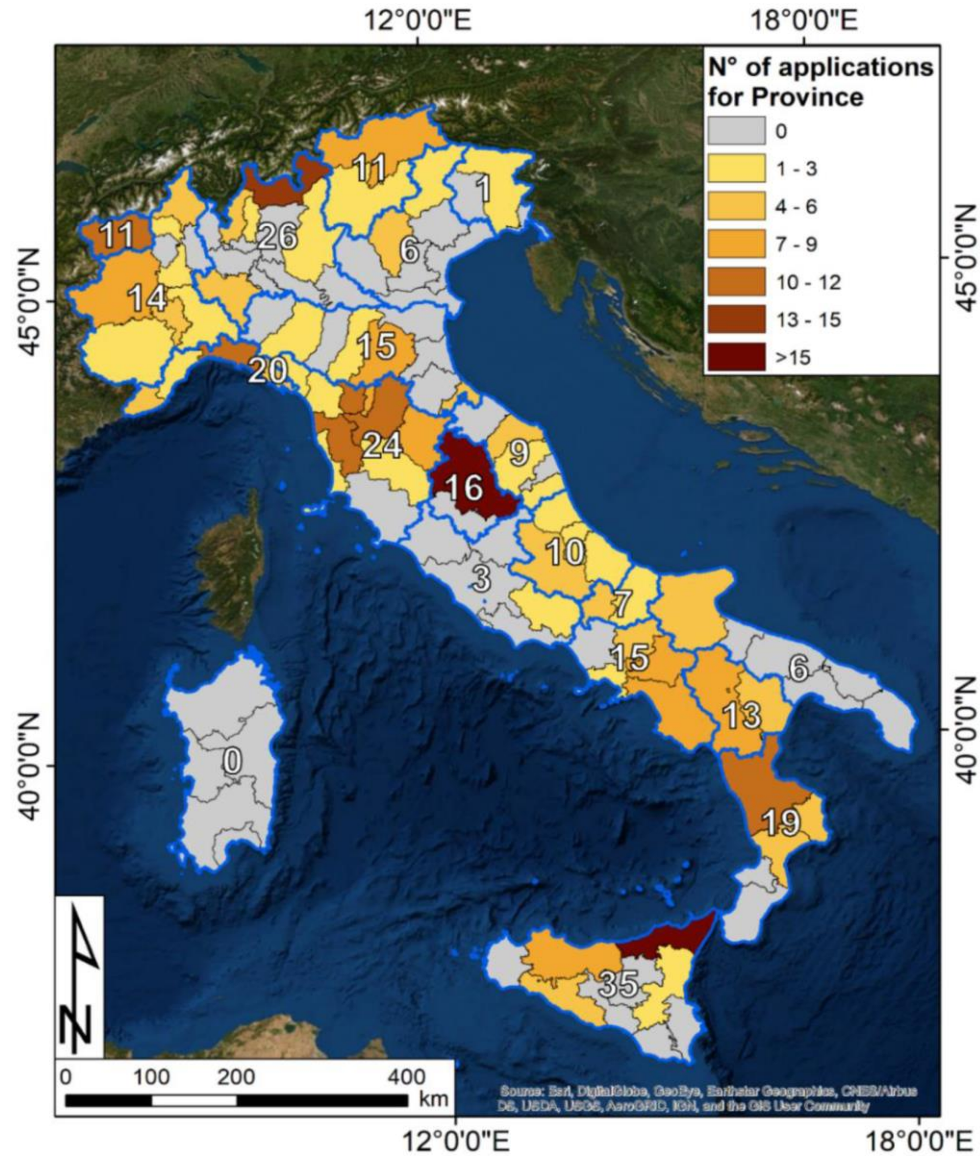

Figure 2-15: Distribution of InSAR-related applications for landslide studies in Italy during the period 1999–2019. The total number of applications for each region (apart from national-scale applications) is included (from Solari et al., 2020).

2.2.3 New methods and future perspectives

ML algorithms have increasingly emerged in the literature since they proved their capabilities in processing large data sets and finding complex patterns, which turns valuable considering the increasing availability of observational data [Tehrani et al., 2022]. Building a machine learning model involves analysing data to allow the model to discern fundamental relationships and discover insights hidden within the data set [Mohan et al., 2021]. Most ML models are predictive models, which seek to create representations of reality based on the available data (*i.e.*, training and testing datasets) [Tehrani et al., 2022]. In addition to traditional machine learning models (*i.e.*, pixel and object-based approaches), there has been a recent escalation in the adoption of Deep Learning (DL) models, which are a subset of ML. In particular, Deep Convolutional Neural Networks (DCNN) are mainly employed for landslide detection and classification using satellite data. Since 2016, the use of such models has been steadily increasing, especially for visual identification tasks mostly from optical images and, to a lesser extent, from digital elevation models [Tehrani et al., 2022]. Given the remarkable capacity of object detection demonstrated in other areas by DCNN models, the first applications to the recognition of the landslide's features have focused on identifying the signature characteristics and the contrast of the landslide body in heavily vegetated areas [Ding et al., 2016; Chen et al., 2018; Ghorbanzadeh et al., 2019]. Pre and post-event ALOS-2 and PALSAR-2 images of the 2018 Hokkaido Eastern Iburi earthquake in Japan were employed in the U-Net CNN by Konishi & Suga [2019]. So far, the only example in the literature on the use of ground-based and UAS images was presented by Catani [2021]. In his work, four well-known pre-trained CNNs (namely, GoogLeNet, GoogLeNet-Places365, ResNet.101, and Inception.V3) were exploited to use transfer learning for landslide detection.

DCNNs do not automatically outperform traditional ML models, although this is sometimes claimed. Since the performance of DCNNs strongly depends on the availability of large training datasets and optimised network architectures, many researchers use pre-trained algorithms available online, predefined parameters in solutions such as Google TensorFlow, or find the best performance through a trial-and-error approach [Zhong et al., 2020]. The future of landslide mapping holds promises for DL, despite its current limited application. To fully unlock this potential, it's crucial to gain a more profound understanding of how different design approaches impact the field, ensure the availability of sufficient training samples, and enhance our knowledge of augmentation strategies aimed at artificially increasing the pool of existing samples [Meezal et al., 2017; Zhong et al., 2020].

2.3 Aims

The information stored within the landslide inventories, however accurate they might be in both spatial and temporal terms, needs to be easily exploitable by government authorities and civil protection to ensure appropriate land use planning. Currently, the inventory updating process predominantly depends on catastrophic events occurrences, such as earthquakes or prolonged/intense precipitations, which provide the essential inputs to systematically revise a considerable number of phenomena over vast geographical regions. Along with that, despite research institutes conducting comprehensive analyses of landslides across extensive areas within the scope of scientific projects, the landslide inventory maps they produce are not maintained and updated once these projects conclude [Van Westen et al., 2006]. Unfortunately, this approach results in inventories that are fragmented, only partially exhaustive, and inevitably introduce biases that can further impact susceptibility and risk assessments. Gaining insights into the effective utilisation of the extensive data found in landslide inventories for urban planning is a topic of significant contemporary relevance, extending beyond scientific research and holding practical applications. Directing planning and economic efforts in areas where structural, geological, geomorphological and climatic settings pervasively predispose the morpho-evolution of the slope processes on the territory is still a complex topic. Furthermore, the challenge of assessing the impact of geomorphic processes at different scales [Dramis et al., 2011] involves a two-faced complexity. On one side, the need to quantify phenomena morphodynamics for precise urban planning and mitigation strategies and, on the other, the analysis of the landscape morphoevolution affected by mass wasting at larger scales, thus considering the long-term interaction with human activities. Remote sensing data, particularly interferometric methods, now stand as the pivotal technological bridge to investigate, both at the local and regional scale, ground deformations with the same accuracy. Several approaches have been implemented to update existing landslide inventories objectively and easily [Meisina et al., 2008; Barra et al., 2017; Solari et al., 2019] or to provide a landslide classification (in terms of spatial deformational pattern and state of activity) to prioritise specific phenomena over others [Bianchini et al., 2013; Cigna et al., 2013; Bonì et al., 2018] from an urban planning perspective. Although refined and effectively implemented within the scope of their project, these methods are undoubtedly limited to a single scale of investigation and do not offer a concrete possibility of being implemented within a fluid and coherent landslide updating process. Similarly, in studies confined to the site-specific process investigation, remote sensing data are often integrated with extensive field-based analysis and on-site monitoring instrumentation, economically unsustainable in the short term if several phenomena need to be covered. For this reason, the presented PhD project focuses on manipulating remote data as a cardinal tool for the prioritisation and spatio-temporal assessment of slope processes from a multiscale perspective. The tools provided, readily reproducible and user-friendly for non-experts in the field at the same time, can seamlessly become an integral component of the process for competent authorities when updating landslide inventories. The structure of the thesis reflects the adopted multiscale approach which, starting from the analysis at the regional scale, progressively leads to the local one, and even extends at the micro-scale.

Before delving into the actual description of the multiscalar methodology, in Chapter 2 I will provide a brief overview of the landslide inventory updating workflow employing traditional and recent methodologies. This validated geodatabase represents the input dataset for the work proposed in Chapter 3, involving the use of innovative techniques for semi-automatically prioritising slope processes to be updated at the regional scale.

Regional scale: Handling SAR data distribution at a regional scale poses a highly intricate challenge. The spatial dependence of the measuring points is often neglected, with only a few authors [Lu et al., 2012; Aslan et al., 2020; Festa et al., 2022] exploring the problem of PS aggregation. Most studies still rely on single-point features (*i.e.*, mean or maximum velocity) or fixed-distance buffer procedures for mapping, classifying or investigating ground deformations. In the first case, even outliers can be classified instead of being discarded, while in the second case, the fixed-distance buffer (or the buffer based on the sensor's resolution) method approximates in a regular, unrealistic way the uneven PS distribution. Therefore, in Chapter 3, I will delve into the following research question:

- Considering the irregular distribution of interferometric measurement points, how can we account for spatial dependencies and topological boundaries to highlight and prioritise critical displacement clusters for regional landslide inventory updates?

Local scale: Within the spectrum of landslide classifications in a given inventory, large slides, DSGSDs, and complex landslides are among the phenomena that present a high degree of fragmentation and internal displacement heterogeneity. Various failure mechanisms or differential morphodynamics complicate the assessment of a comprehensive scenario of the slope movement: a detailed post-processing analysis of the InSAR dataset is required to entangle the superimposition of different processes. In these cases, reactivation, and failures of one or multiple sectors of the landslide constitute a crucial element in the strategic planning of mitigation measures, which must consider a heterogeneous hazard pattern, both in the spatial and temporal domain. Chapter 4 will be dedicated to address the following questions:

- How can we obtain an accurate spatial delineation of the different kinematics of each landslide deforming sector through InSAR post-processing analysis?
- What approaches can be employed to assess the differential morphodynamics of the individual landslide bodies to facilitate the recognition of those sectors more susceptible to cyclic reactivations triggered by external forces?

Multi-scale: Transportation agencies need to prioritise inventorying landslides that impact their infrastructure networks and work on strategies to optimise the effectiveness of their monitoring tools while attenuating costs. This entails efficiently mapping and regularly updating landslide occurrences over km-long transportation corridors. For such a reason, a two-phase approach is crucial, involving an initial comprehensive screening of the entire infrastructure network, followed by a focused analysis of specific critical scenarios that demand immediate attention to safeguard network security and functionality. A multi-scale approach is best suited in these cases: identifying the most critical issues over large areas and quickly providing an indication of the location and severity of the landslides will support the mitigation strategies and economic resources management. However, transportation infrastructures are very often impacted by rockfalls which, being intrinsically characterised by very rapid kinematics and developing on steep or near-vertical rock slopes, are not investigable through InSAR. The research question to be answered in Chapter 5 is, therefore:

- Using a multiscale approach, how can we detect ongoing deformations and early indicators of future instabilities for kinematics like rockfalls that cannot be investigated using InSAR?

In the following chapters, three different case studies will be presented, each serving as an exemplary representation of the specific scale of investigation.

Chapter 3 will focus on addressing the difficulty of automating the spatial aggregation of point interferometric data at the regional scale, applying our methodology to the portion of the Central Apennines (about 8000 km^2) recently struck by the 2016-2017 seismic sequence. Through the analysis of the spatial distribution of the deformations, a prioritisation ranking was provided for the landslides of the Hydrogeological Asset Plan (PAI) inventory to be updated.

The local scale analysis, examined in Chapter 4, focuses on the study of a slope process, the DeBeque Canyon Landslide, interacting with one of the principal highways of the Colorado State (USA). The spatial and temporal deformational behaviour was parallelly analysed to highlight heterogeneous displacements of different moving sectors within the landslide and define which would likely need priority for mitigation or monitoring measures.

Eventually, Chapter 5 exemplifies the integration of different types of remote sensing data and techniques on two test sites along Highway 133, which holds strategic importance for the Colorado Department of Transportation, considering the instability processes that undermine this road segment's safety. In this case, the adopted approach has been modelled on the specific landslide type (*i.e.*, rockfalls). The method allows the transition from small-scale analysis on the entire highway via satellite interferometry, to the local scale of each test site and up to the micro-scale of specific slope sub-portions affected by early instability indicators.

3 Landslide inventory update through traditional and recent methodology: application in the Central Apennines

Following the seismic sequence that struck the Central Apennines between August 2016 and January 2017, a massive reconstruction programme has been launched for hundreds of municipalities that experienced severe damage. Among governance authorities and Civil Protection, universities and research centres were also involved in carrying out specific and detailed geo-hazards investigations. In particular, these investigations focused on updating the extent and activity of those slope processes included in the Hydrogeological Asset Plan (PAI) and interacting with urban centres and infrastructure affected by the shocks. All the selected landslides are characterised by a high or very high hazard level and, for this reason, were prioritised as their update would have concerned the reconsideration of the associated hazard and risk. Being part of the PAI inventory of the Central Apennines, landslide hazard classification at a specific level rather than another has a direct impact on the extent of limitations or potential prohibitions on the reconstruction and protection of buildings and infrastructure.

The landslides selected for the updating process are distributed over 245 slopes of interest and involve a total of 102 municipalities over the Umbria, Marche, Lazio and Abruzzo Regions (Central Apennines). Considering the high number of slope processes (over 400 phenomena) to be updated, the District Basin Authority of the Central Apennines (ABDAC), which is responsible for validating the PAI inventory) assigned to five different universities a sub-selection of landslides to accelerate the examination procedures. Within the working group related to the CERI Research Centre of the Sapienza University of Rome, I focused on the analysis, updating and validating of more than 100 instability processes in the Lazio and Umbria Regions (Figure 3-1).

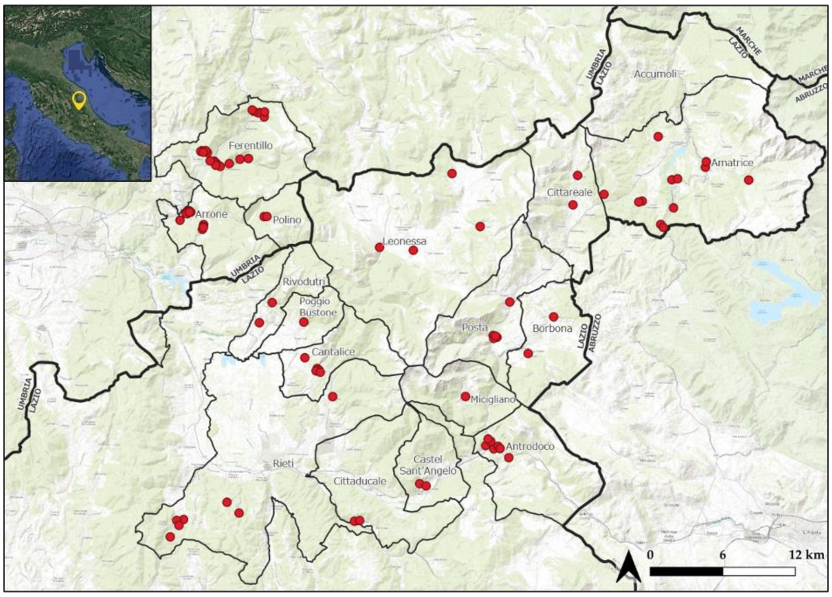

Figure 3-1: Representation of the landslides of interest (red dots) interacting with urban centres of the Umbria and Lazio Regions, assigned to the Sapienza University of Rome.

The initial database is represented by rockfalls (22%), earth/debris slides (17%), shallow landslides (19%), complex landslides (7%), debris flows (8%) and non-defined landslides (16%). Since there is neither a national or regional standard for updating landslide inventories, the preliminary phase focused on rationalising a workflow that would allow for organically and coherently revising all the deformation processes and standardising the procedure to make it as objective as possible. The implemented workflow consists of four successive steps (Figure 3-2), synthesised as follows: 1) general overview and morphological setting of the slope of interest; 2) topographical inspection and preliminary landslide extent updating; 3) multitemporal interpretation for the state of activity refining; 4) field survey validation.

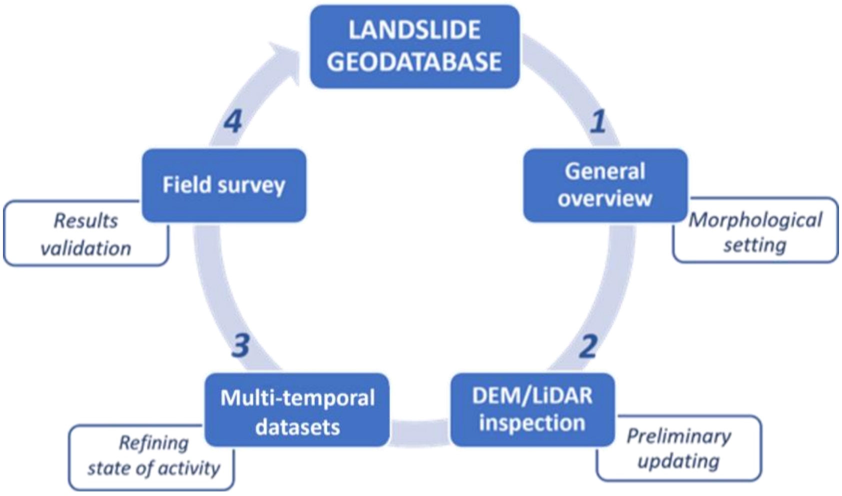

Figure 3-2: Workflow adopted for updating the PAI inventory, consisting of four progressive steps, namely: a) morphological setting of the area of interest; b) preliminary spatial extend updating through topographic inspection; c) state of activity updating through multi-temporal analysis; d) results validation through field surveys.

The first step of the workflow involved a bibliographic research phase, aimed at finding previous technical and geological reports, information on the structural, geological and geomorphological setting of each area of investigation, as well as technical documents relating to the existence of mitigation measures related to the analysed phenomena. All the geospatial and multi-temporal material found for each site was subsequently organised and stored within a georeferenced GIS database, which allowed the overlap of the different layers collected and the interpretation of the specific geomorphological context. The bibliographic information, related to distinct data types, was grouped in the following geospatial datasets: geological and lithological features; topographical features (topographical maps and medium to high-resolution DEMs); multi-temporal imagery; other pre-existing landslides inventories (*e.g.*, IFFI, earthquake-induced landslide inventories); interferometric dataset. The second step included the visual analysis and interpretation of topographical data at different spatial resolutions. Topographical maps and Digital Elevation Models (DEMs) were exploited to preliminarily map the extent of the slope process and assign them kinematics and state of activity. The Italian territory is heterogeneously covered by different elevation models, with the only exception of the TinItaly DEM (which provides full coverage of the entire territory with a 10 m pixel size) [Tarquini et al., 2023]. Therefore, the combined use of DEM at different resolutions was necessary to recognise landslide geomorphic expressions. Specifically, a LiDAR-derived DEM of 2m-resolution (where available) and a 5m-resolution DEM generated from the 1:5000 topographical map were used. Moreover, several shaded relief maps, with variable sun azimuths, were also obtained to avoid azimuth bias in the interpretation of landforms and emphasise scarps, topographic changes, and other landslide elements under different illumination effects. At the same time, the use of a multi-temporal dataset composed of optical images, both aerial and satellite, and historical interferometric information enabled, in the third phase of the workflow, the definition of the state and style of activity of the processes in the interval from the early ’50s till today. The optical dataset encompasses aerial images of flight GAI (1954-55) and Italy (1988-89), digital aerial orthophotos (1994-1998, 2000, 2006, 2008, and 2012), and recent satellite images (*i.e.*, Google Earth) displayed directly in the GIS environment. In addition, the quantitative displacement information included in the PS measuring points of the ESA satellites ERS-1 and ERS-2 (1991 - 2001) and ENVISAT (2002 -2012) was examined. The historical PS-InSAR is an open-source resource available for the entire national territory in ascending and descending geometries. The analysis of the PS time series highlighted any reactivation and acceleration of displacements, thus providing a more complete scenery of the deformation history of each phenomenon. These steps made it possible to record the information related to kinematics and states of activity of every landslide in the GIS-based geodatabase; moreover, each slope process was also assigned to a unique code, according to the ABDAC standards. In the fourth phase, field surveys were carried out in each area of interest to cross-check the results obtained through photo interpretation and interferometric satellite analysis. These surveys, along with representing an indispensable validating tool for the preliminary morphography, kinematics and state of activity records, have also allowed the registration and detail characterisation of existing mitigation measures.

After the validation obtained through the field surveys, the updated information was integrated into the database in an organic structure that includes spatial and temporal characteristics of the landslide phenomena, geological-geomorphological features of the respective slope, information on any existing mitigation measures and related state of maintenance, as well as the quantification of hazard and risk levels following ABDAC standards. Figure 3-3 portrays the different kinematics classifications between the inventory before and after the updating process.

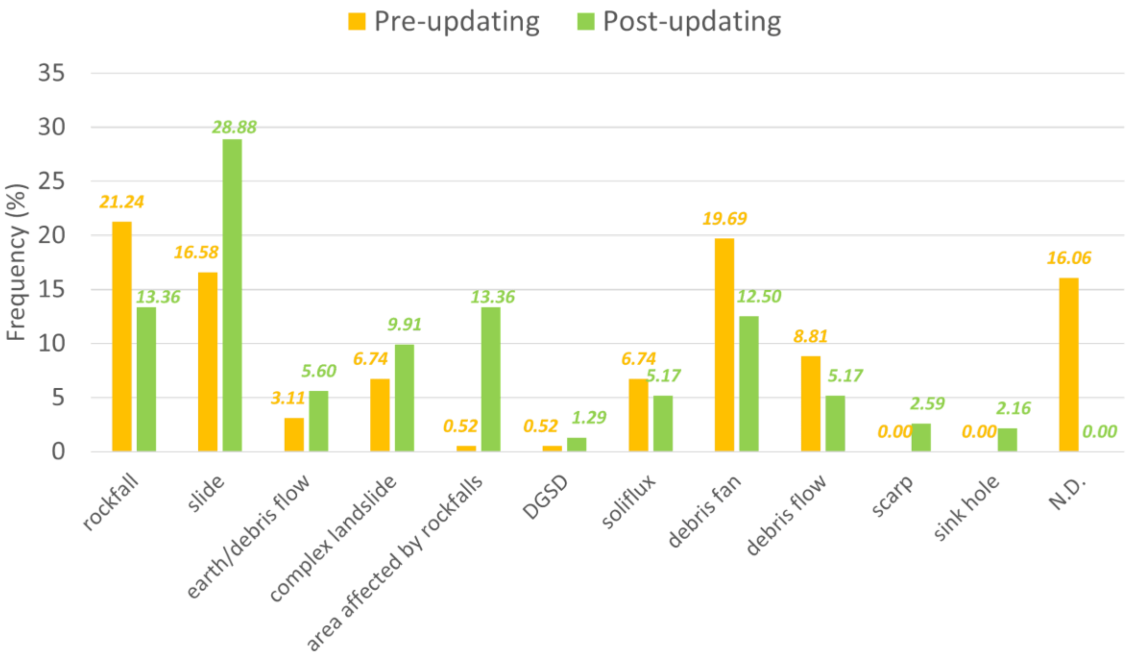

Figure 3-3: Different kinematics classifications between the inventory before and after the updating process.

Note that no landslides were categorised as non-defined, as the correct association of the slope process to a specific class is essential for the quantification of the associated risk. This updated and validated database has been used, together with the landslide geodatabases updated for the other Regions by the respective Universities (i.e., Università degli Studi di Roma "La Sapienza", Università degli Studi di Urbino Carlo Bo, Università degli Studi "G. d'Annunzio"Chieti – Pescara, Università di Camerino, Università degli Studi di Perugia), within the classification workflow described in detail in the work presented in Chapter 3.

4 Landslides Semi-Automatic Prioritisation Using Persistent Scatterers Clusters: A Regional-Scale Application After the 2016 Central Apennines Seismic Sequence

Under internal review

Abstract

Landslide inventory, together with the reconstruction of the spatial distribution of mass movements of different origin, size and state of activity, is essential for hazard assessment, risk management and mitigation, and urban planning. In addition, understanding the spatio-temporal patterns of landslides helps local and national authorities prioritize natural hazard management efforts within available economic resources, especially for planning actions to update landslide inventories, even within active seismic regions. In this context, the use of multi-temporal A-DInSAR (Advanced Differential Synthetic Aperture Radar Interferometry) techniques such as Persistent Scatterer Interferometry (PSI) is a well-established methodology for assessing and monitoring ground deformation with sub-centimeter precision over large areas (e.g., regional, and national scales). However, analyzing and extracting ground movement information from PSI-derived deformation maps on a regional or national scale can be labor-intensive due to the large number of measurement points (PS, Persistent Scatterer) generated, which range from millions to billions. As multi-sensor multi-band interferometric datasets become increasingly accessible, the need to efficiently manage this wealth of data has driven the development of post-processing methodologies designed to enhance the extraction of valuable information. This study presents a reproducible and semi-automatic post-processing analysis approach based on multi-sensor Sentinel-1 and COSMO-SkyMed PS data to evaluate priority levels associated with slope instability processes following the 2016-2017 earthquake in the Central Apennines, Italy. The methodology involves a comprehensive filtering stage to eliminate noisy data and a clustering stage to aggregate PS exhibiting similar deformation behavior within homogeneous terrain units. Landslides are automatically categorized and ranked based on successive thresholds applied to these clusters, accounting for their potential morphoevolution within the slope units. Priority for further validation through field investigations is given to landslide bodies that show deformation beyond the defined limits. The proposed methodology finds application in updating geomorphological and landslide inventory maps, as well as assessing the state of activity of landslide. This approach offers advantages over traditional methodologies, as it considers objective topological criteria when evaluating slope deformations over large areas. By establishing a standardized procedure, this study facilitates the integration of interferometric data and geomorphological characteristics for identifying areas that allocate resources for field inspections and offering a valuable tool for post-seismic reconstruction efforts undertaken by government institutions.

Keywords: Landslides; earthquake-induced landslides; PS-InSAR; post-processing; prioritisation; Central Apennines earthquake

4.1 Introduction

Among the damage caused by large and severe earthquakes, aside from the initial impact resulting from seismic shaking interacting with urbanised areas, secondary effects such as ground failures, liquefaction, and coseismic landslides must be considered [Martino and Mugnozza, 2005; Tang et al., 2016]. Especially in the case of seismic-induced landslides, the socio-economic impact, both in terms of financial resources spent on reconstruction interventions and in terms of human lives, can be dramatic [Ling and Chigira, 2020; Kallimogiannis et al., 2022]. The first scientific earthquake-induced landslide investigation was undertaken following the earthquake swarm in Calabria, Italy, in 1783 [Keefer, 2002]. Further examples of massive amounts of slope processes induced by strong seismic events were reported after the Northridge (California, Mw=6.7, [Soeters and Van Westen, 1996]), Chi-Chi (Taiwan, Mw=7.6, [Hung, 2000]), Wenchuan (China, Mw=7.9, [Yin et al., 2009]), Central Italy (Mw= 6.0, [Martino et al., 2017]) and Hokkaido (Japan, Mw= 6.6, [Zhao et al., 2020]) earthquakes. Moreover, since co-seismic first or second-generation (i.e., reactivated) slope failures represent more than 50% of the total losses due to landslides in the World [Petley, 2012], the consequence of the seismic motion on landslides deposits in the post-seismic interval can't be neglected. Indeed, mass wasting deposits stressed during seismic shocks may be more predisposed to be remobilized under the influence of subsequent triggering factors (i.e., precipitation) and be subjected to cascade failures over time [Hovius et al., 2011; Marc et al., 2015; Fan et al., 2019]. In the years following the above-mentioned seismic events, many co-seismic landslides have undergone reactivation stages as a result of rainfall and storms [Tang et al., 2016]. For such reasons, the reconstruction of a comprehensive scenario of the spatial distribution of post-earthquake mass movements is indispensable for hazard and risk assessment, and for environmental planning in urban areas [Shafique et al., 2016]. Furthermore, understanding the spatio-temporal arrangement of earthquake-induced landslides helps local and national authorities prioritise interventions for natural hazard management within the constraints of available economic resources [Martino et al., 2020]. As a well-established strategy for identifying, assessing and monitoring ground deformations over wide areas [Mondini et al., 2021], InSAR (Interferometric Synthetic Aperture Radar) techniques have been applied to tackle displacement measurements on post-earthquake mass movements [Martino et al., 2017; Polcari et al., 2017; Ramirez et al., 2020; Martino et al., 2022; Smail et al., 2022; Licata et al., 2023] which can be triggered within tens of km from the epicentre. In particular, multi-temporal InSAR processes, such as those introduced by [Ferretti et al., 2001; Berardino et al., 2002; Lanari et al., 2004], have proven to be highly effective for accurately detecting ground surface displacements at millimetre resolution. These techniques are particularly valuable for various purposes, including updating geomorphological maps and creating multi-temporal landslide inventory maps [Guzzetti et al., 2012; Rosi et al., 2018; Antonielli et al., 2019], as well as assessing and ranking the activity levels of landslides [Lauknes et al., 2010; Ciampalini et al., 2012; Solari et al., 2020]. However, analysing and extracting ground movements from InSAR-derived deformation maps at regional or national scales may result in a labour-intensive endeavour, since the Measurement Points (MPs) generated by multi-temporal processing methods might be in the order of millions to billions of points. This amount of data has undergone (and is expected to continue) to increase in terms of density due to the increasing availability of high-resolution X-Band datasets (e.g., COSMO-SkyMed)[Mazzanti et al., 2022], and freely accessible C-Band data of Sentinel-1 after the launch of the European Ground Motion Service (EGMS [Costantini et al., 2021]), which allows the exploitation of long-term ground deformations monitoring at an international scale. Nowadays, post-processing methodologies are increasingly used for gathering and optimising the displacement information from interferometric data (such as the filtering of regional scale datasets to eliminate potential noise, and the automatic identification of those areas affected by deformation that can be further validated by field investigations) [Festa et al., 2022]. Several attempts to provide easily applicable and reproducible methods for discriminating actively deforming areas within regional-scale deformation maps are found in the literature, involving the use of hot spots [Bianchini et al., 2012; Lu et al., 2012; Barra et al., 2017; Solari et al., 2019], clustering [Festa et al., 2022; Lu et al., 2012; Solari et al., 2019; Montalti et al., 2019; Tomás et al., 2019], or time-series-based [Bonì et al., 2018; Raspini et al., 2018; Aslan et al., 2020] approaches.

In this paper, we introduce a post-processing analysis based on the clusterization of InSAR data to provide a hazard level to slope instability processes updated in terms of extension and state of activity after the 2016-2017 earthquake that struck the Central Apennines, Italy. We post-processed a multi-satellite interferometric dataset for the 2017–2022-time interval, derived from the combination of Sentinel-1 and COSMO-SkyMed images, through a first filtering stage to remove noisy data, followed by a clustering stage aimed at aggregating MPs characterised by similar deformation behaviour. Landslides were assigned to a different ranking based on successive thresholds set on the moving clusters, even considering the potential morphoevolution of the landslide within its relative homogeneous terrain unit (sensu [Alvioli et al., 2016]). Such geomorphological constraints are preferable with respect to fixed distance or grid cell-based methodologies (still prevalent in the literature) since they allow considering deformations of slope processes considering real topological criteria [Pokharel et al., 2021]. We aimed to provide a reproducible methodology to semi-automatically analyse the massive quantity of data covering the territory impacted by the seismic sequence and, therefore, deliver a tool to support post-seismic reconstruction activities carried out by government institutions. This approach intends to establish a standard procedure that fills a gap in the existing literature, as it can be integrated into contexts requiring monitoring measures and the prioritisation of hazardous areas, promoting resource allocation for field inspections, and supporting territorial planning activities.

4.2 Study area

The study area corresponds to the territory affected by the Amatrice-Visso-Norcia seismic sequence, which struck the Central Apennines, Italy, from August 2016 to January 2017, involving an area of about 8000 km^2 (Figure 4-1). These events caused a dramatic amount of casualties and extensive damage to buildings, and architectural heritage in the Lazio, Abruzzo, Umbria and Marche regions [Fiorentino et al., 2018]. Moreover, considerable seismic secondary earthquake-induced effects (*i.e.*, ground fractures and landslides) were registered within a 50 km buffer from the main epicentres. In response to this emergency, a massive reconstruction plan was launched to carry out seismic microzonation studies and the comprehensive cataloguing of numerous landslides triggered or influenced by the seismic event. The field surveys revealed that the most significant deformations were related to the 2016 mainshocks [Martino et al., 2020]. Within this post-seismic reconstruction scenario, mass wasting processes located on 245 slopes of interest (shown as red dots in Figure 4-1) were investigated for extent and state of activity updating and monitoring purposes. The landslide dataset will be described in detail in Section 4.3.2.

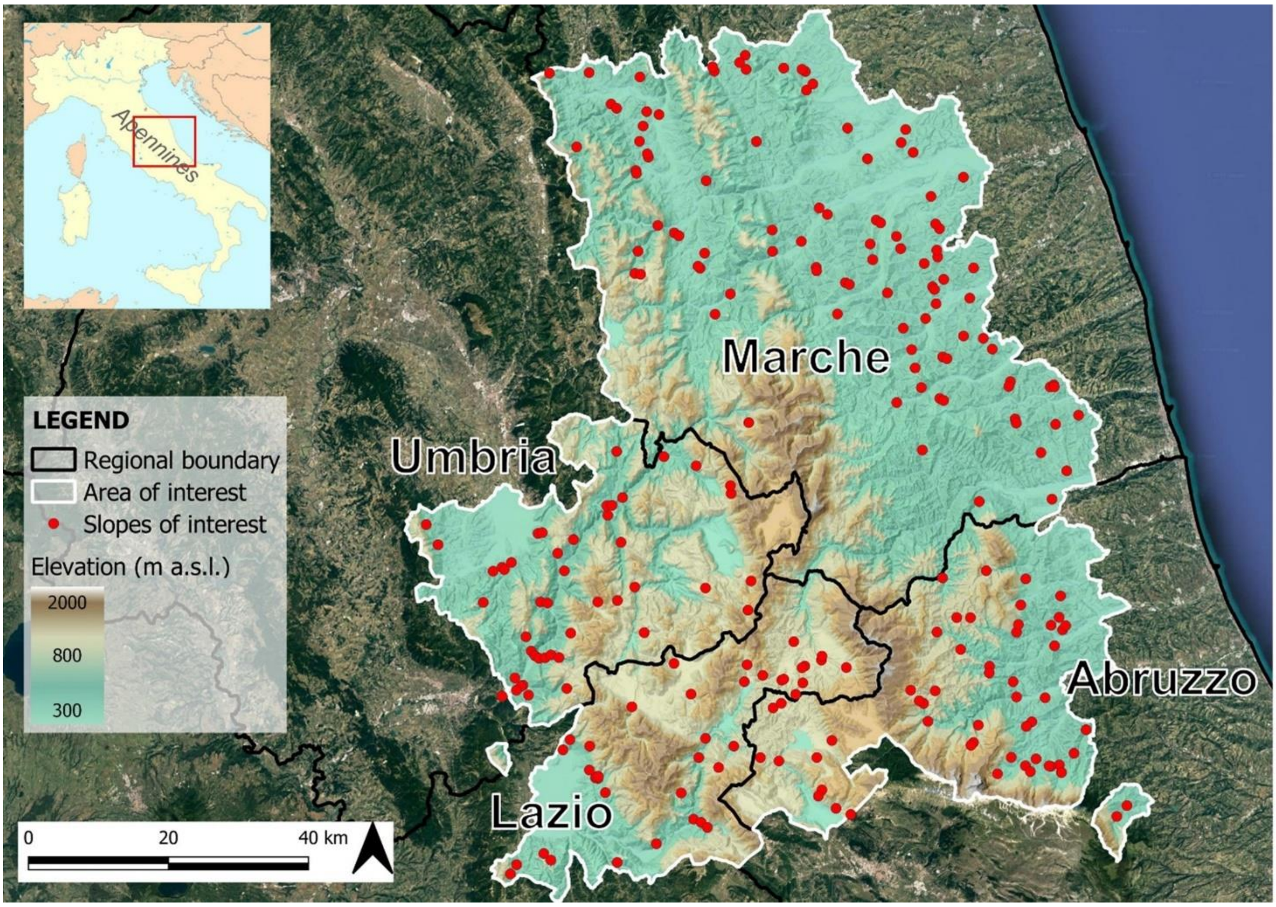

Figure 4-1: Representation of the area involved in seismic sequence in 2016-2017, which affected four distinct regions located in the Central Apennines (i.e., Lazio, Abruzzo, Umbria and Marche regions). The spatial distribution of the earthquake-induced landslides analysed in this study are displayed as red dots.

4.2.1 Geological setting

The present morpho-structural configuration of the Central Apennines is a consequence of the complex, multi-phase tectonostratigraphic evolution this area has experienced over time, which includes a first compressional phase from the Miocene to the lower Pliocene, associated with the growth and northeastward migration of the imbricate fold-and-thrust Apennines Chain, followed by the onset of an extensional tectonic wave, which began in the Late Pliocene to Early Pleistocene [Bigi et al., 2011; Pierantoni et al., 2013]. During the compressional tectonic phase, the limestones and marls sequence (Jurassic-Cenozoic) of the Umbria–Marche pelagic basin was emplaced onto limestones and dolomites of the Latium-Abruzzi carbonate platform. The eastward migration of the Apennines Chain induced the development of highly articulated foreland basin systems, filled up by thick successions of pelitic-arenaceous flysch of the Laga Formation (Upper Miocene) [Carminati and Doglioni, 2012; Marini et al., 2015]. The subsequent Quaternary extensional phase generated strike-slip and normal fault systems, which are responsible for the development of intermontane basins and include the major seismogenic sources of this sector of the Apennines [Marini et al., 2015].

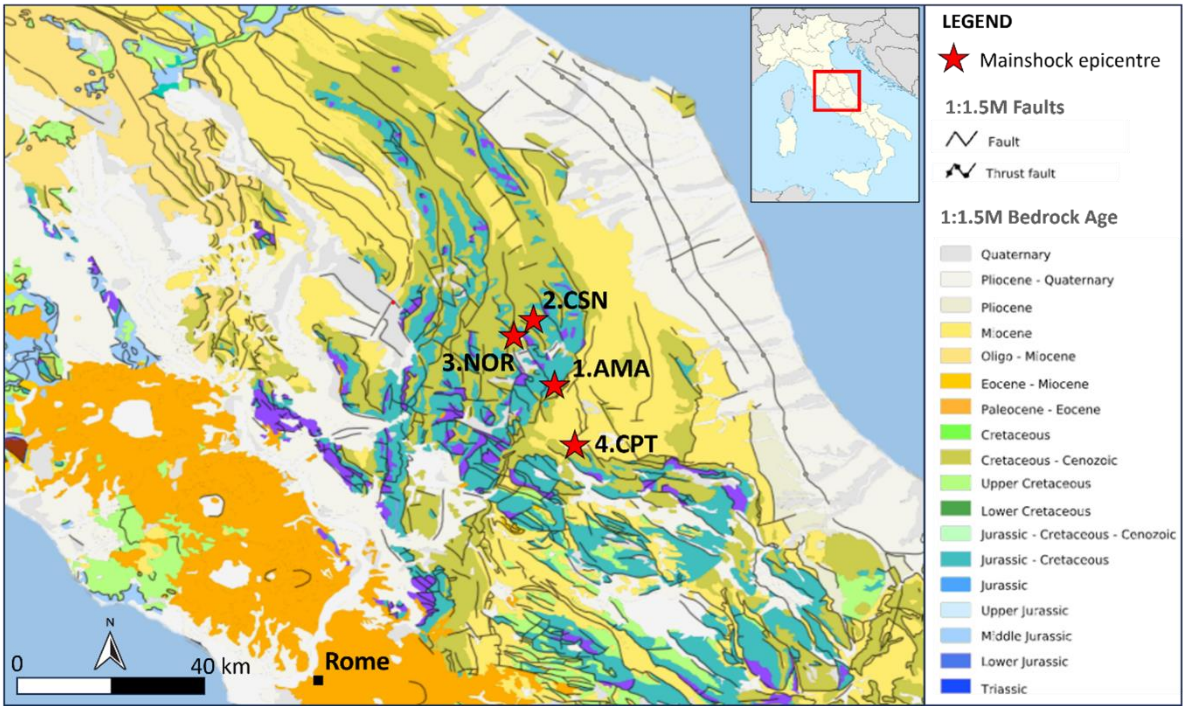

Figure 4-2: Simplified geological map of the study area in scale 1.5M modified from [OneGeology Portal]. The epicentres of the 4 main mainshocks that made up the seismic sequence of Central Italy are also reported, corresponding to: 1. Mw 6.0 Amatrice (AMA) mainshock (24 August 2016); 2.Mw 5.9 Castelsantangelo Sul Nera (CSN) mainshock (26 October 2016); 3. Mw 6.5 Norcia (NOR) mainshock (30 October 2016); 4. Mw 5.5 Capitignano (CPT) mainshock (18 January 2017).

The seismic sequence that hit the Central Apennines between August 2016 and June 2017 is the result of such a system and comprises more than 70,000 earthquakes, most of which with normal-faulting mechanisms [Martino et al., 2019; Bucci et al., 2021]. The sequence started on 24 August 2016 with the Mw 6.0 Amatrice earthquake (Figure 4-2) that destroyed the historical centres of Amatrice, Accumoli and Pescara del Tronto municipalities [Marini et al., 2015]. On 26 October 2016 the Mw 5.9 Visso earthquake (Figure 4-2), ~25 km to the north of Amatrice, severely damaged Camerino, Castelsantangelo Sul Nera, Preci and Ussita municipalities. The last mainshock of 2016 represents the largest event, the Mw 6.5 Norcia earthquake (Figure 4-2), which occurred on 30 October and was generated between the two previous mainshocks' sources. On 18 January four earthquakes with Mw > 5 were recorded near Montereale and Capitignano villages (Figure 4-2). Following each mainshock, there was a prolonged period of aftershock activity, and over subsequent months, seismic activity migrated both southward and northward.

4.3 Materials and methods

The current paragraph aims to describe the input data and the workflow (Figure 4-3) adopted to obtain a ranking of the analysed landslides of interest. The input data of the model are represented, on one hand, by a multi-sensor dataset composed of PS (Persistent Scatterer) data extracted from SAR imagery acquired by Sentinel-1 and COSMO-SkyMed satellites, which provide a surface deformation map in the study area (Section 4.3.1).

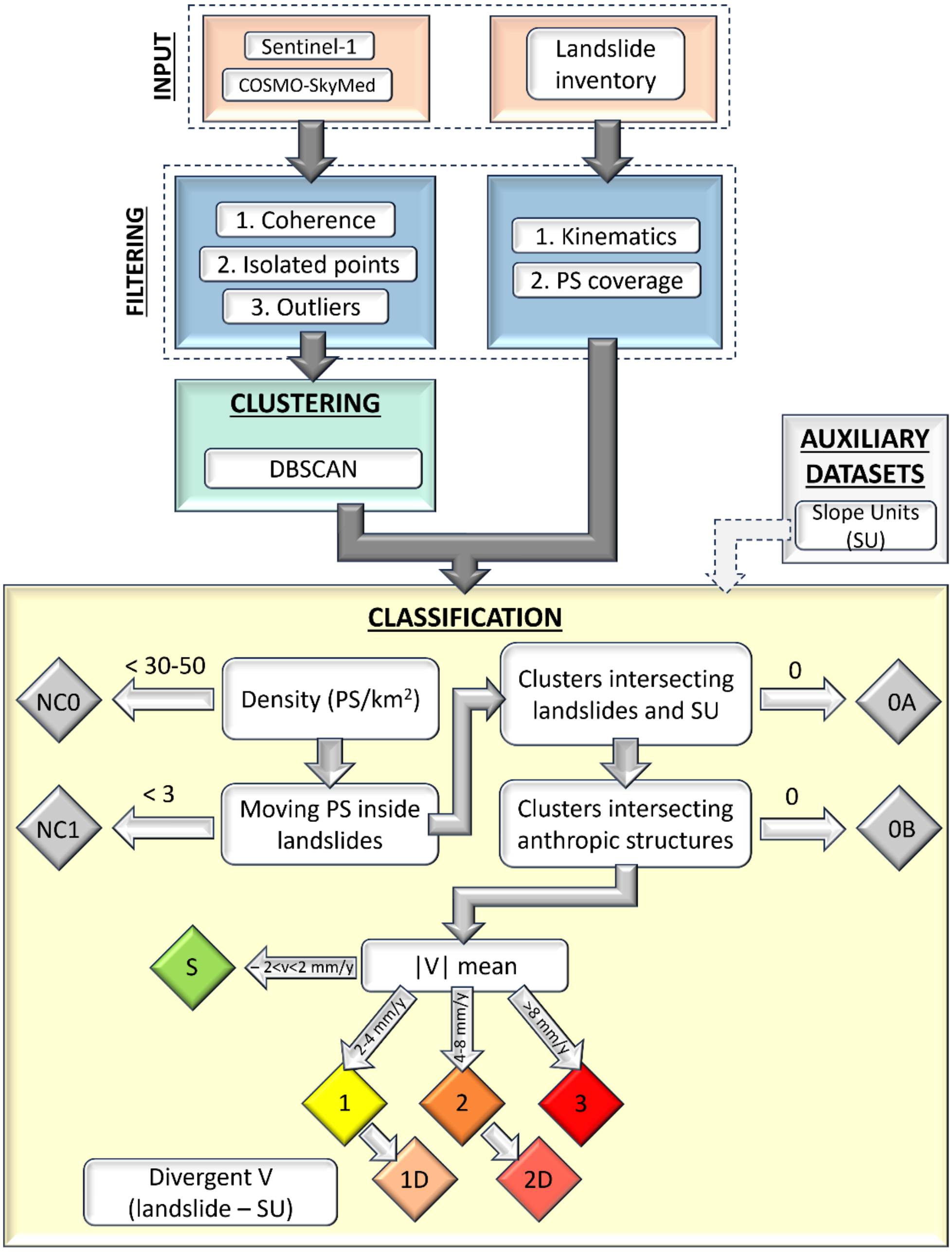

Figure 4-3: Methodological scheme for assigning a priority level to the landslides dataset based on thresholds applied to the interferometric ground deformation maps.

On the other hand, a subset of landslides from a national Italian inventory (described in Section 4.3.2) was selected to be classified and ranked for future site-specific investigations. Section 4.3.3 has been further subdivided into three subsections, respectively related to the description of the preliminary filtering of the interferometric dataset (Subsection 4.3.3.1), the spatial clustering (Subsection 4.3.3.2), and, finally, the assignment of a priority class (Subsection 4.3.3.3) based on specific thresholds applied to the interferometric data.

4.3.1 Input dataset: ground displacement map

To quantify the displacement rates occurring along the slopes of interest, the PSP IfSAR approach was employed [Costantini et al., 2008]. This method is based on considering pairs of measuring points (i.e., arcs) to identify and subsequently analyse the PS. After conducting a feasibility analysis to assess the temporal and spatial coverage of available archive images, the most feasible approach resulted in adopting a different orbital geometry for each satellite: an ascending geometry for Sentinel-1 (S1) and a descending geometry for COSMO-SkyMed (CSK). S1 comprises a pair of satellites managed by the European Space Agency (ESA) and offers ground resolution of 5x20 meters and a revisit time of 6 days due to the consecutive orbits of Sentinel-1A and Sentinel-1B, constituting the constellation [sentinels.copernicus.eu]. On the other hand, CSK offers higher ground resolution of 3x3 meters but has a longer revisit time of approximately 16 days [Torre and Capece, 2011]. The adopted solution leverages the improved temporal resolution of Sentinel-1 in ascending orbits while circumventing the scarcity of images available in the CSK archive with the same orbital configuration, which would otherwise hamper a precise analysis. The analysis was performed employing S1 images acquired in Interferometric Wide (IW) swath mode: thanks to the 250 km-wide acquisition mode, a single satellite swath was employed to cover the entire extent of the study area with data of 5m by 20m spatial resolution. Instead, considering that the HIMAGE (HI) mode of the CSK data has a 40x40 km swath at 3 by 3 m of spatial resolution, four different tracks were used to fully cover the area of interest. Further details of the acquired datasets are listed in Table 4.1. The processing allowed us to estimate the average Line of Sight (LOS) velocity for over 3M measuring points (PS) for the S1 dataset and more than 4M for each one of the CSK tracks. To maximise the information related to gravity-driven processes and exclude the contribution of the co-seismic deformation related to the 2016-2017 seismic sequence, the displacement analysis was carried out for the 2017-2022 interval.

Table 4.1: Characteristics of Sentinel-1 and COSMO-SkyMed datasets employed for the PS analysis.

	Sentinel-1	**COSMO-SkyMed**			
Orbital geometry	Ascending	Descending			
Ground resolution	5x20m	3x3m			
Radar band	C-band	X-band			
Track	117	HI_01	HI_03	HI_04	HI_05
N° of images	305	69	78	82	80
Incidence angle (°)	38.21	26.02	28.73	31.66	33.39
Heading angle (°)	12.07	-12.69	-12.68	-11.65	-11.64

4.3.2 Input dataset: landslide inventory and ancillary data

Within the framework of the reconstruction plan, a thorough study of earthquake-induced landslides was carried out after the main mainshocks. Many of the documented slope processes encompassed known phenomena already mapped in the Hydrogeological Asset Plans (Piano Stralcio di Assetto Idrogeologico, PAI) of the four Regions, which are technical inventories of geohazards that may represent constraints or limitations during urban planning actions. The hazard level assigned to PAI landslides plays a crucial role in the reconstruction perspective, sometimes leading to land-use restrictions that may prohibit all human activity except for hazard mitigation interventions, implying the relocation of buildings or settlements damaged by the earthquake. For this reason, to accelerate the operations of reconstruction, in-depth investigations were conducted to quickly update all landslides of the PAI inventory characterised by high hazard levels.

Specifically, the landslides of interest that have been the subject of such detailed investigations are distributed over 245 sites, involving a total of 102 municipalities. During 2021, detailed photo-interpretation of aerial and satellite imagery was carried out in combination with field surveys for each location: the final product comprehends an updated, comprehensive geodatabase of the slope movements extent, state of activity, anthropic structures involved in the deformational process and efficacy of eventual mitigation solutions (Figure 4-4). The following step consisted of satellite-based interferometric analysis, carried out to investigate and monitor the morphoevolution of these phenomena during the next few years. The purpose was to validate the updated inventory or else provide evidence of discrepancies between the mapping performed through photo-interpretation and field surveys, and the displacement rates recorded by satellite. In this framework, we designed a classification model to provide a ranking of those cases where inventoried processes and InSAR results diverged the most. Considering that the PS-InSAR analysis is suitable for the study of slow phenomena while, for the intrinsic limitations of the technique, rapid kinematics are undetectable, rockfalls were excluded from the dataset (Figure 4-3). All the remaining landslide typologies were used as input for the model to be assigned to a different prioritisation ranking.

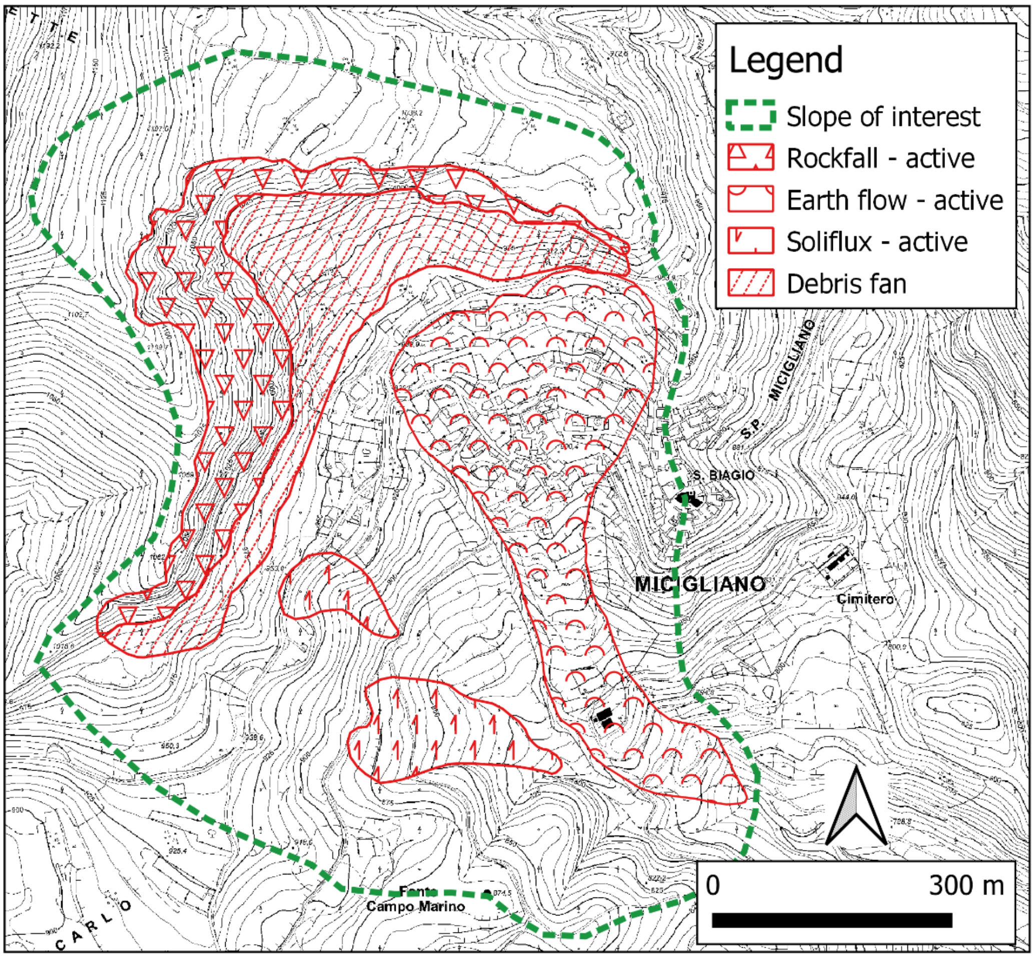

Figure 4-4: Landslide dataset interacting with the infrastructures and urban centre of Micigliano municipality, updated in the framework of the ReSTART project.

The auxiliary data introduced in the classification model are divided into topological constraints and man-made elements. The topological constraints used to analyse the spatial interaction of the moving PS with the landslide features are represented by the Slope Units (SU), which are morphologically homogeneous territorial units freely available for the whole Italian territory. The employed SU are extracted from [Alvioli et al., 2016] using the EU-DEM digital elevation model, at 25x25 meters resolution. Risk elements susceptible to the effects of gravitational processes (i.e., roads, highways, and buildings) were acquired in vector format from GeoFabrik, servings as a repository that regularly extracts and offers up-to-date, open-source data from OpenStreetMap.

4.3.3 PSI post-processing and classification workflow

4.3.3.1 Filtering phase

The filtering phase represented the essential preliminary operation of the proposed workflow (Figure 4-3) supporting the removal of noise or irrelevant information from both datasets. The filtering operations enhance the quality and reliability of the detected displacement information and, at the same time, reduce the dataset dimensions to facilitate the analysis. This process consisted of three consecutive steps, applied to remove: 1) noise; 2) isolated points; and 3) outliers. PS points that could introduce noise in the analysis were initially filtered by applying a coherence threshold of 0.6, which ensured the inclusion of reliable PS (both in space and time) while preserving over 90 percent of the valuable information within the dataset. In the second step, isolated points were removed by applying a spatial criterion that relied on an influence buffer. The buffer was designed to encompass a region where a minimum number of points, representative of the same deformation phenomenon, could be reliably considered. Several studies in the literature have focused on defining thresholds on both these parameters, which were set based on the deformational processes' extent [Solari et al., 2019], or the ground resolution of the sensor [Barra et al., 2017] and, therefore, employed an empirical criterion. In our study, considering the average dimensions of the gravity-driven phenomena of interest, we set a buffer's radius equal to 100 metres and a minimum number of 3 PS as proximity thresholds to retain interpretable clusters. In fact, while isolated PS points can still provide a correct indication of the deformations occurring in a particular portion of the territory, their reliability is affected by the absence of corroborating measuring points in their proximity. This filter was applied also to the PAI inventory, in order to retain only those landslides having more than 3 PS within a 100 m buffer. A similar scenario was considered also for the velocity parameter, along with the spatial one. The last filtering phase detected and removed outliers (i.e., inconsistent values compared to the neighbourhood displacement rates) based on the PS velocity. In this case too, if one PS within the cluster shows very different displacement values from the other measuring points, this PS would be discarded as it is considered an outlier compared to the displacement rates of that specific cluster. Therefore, in the last step, outliers were removed from each cluster to avoid introducing noise in the displacement estimation (Figure 4-3). For this purpose, we applied the outlier's removal was based on the Anselin Local Moran's Index [Anselin, 1995], a spatial statistical analysis that identifies significant clusters or velocity patterns in the dataset. Given a geospatial dataset, this statistic compares the value of each point with the values of its first three neighbours, assessing whether a PS is part of a homogeneous cluster, is a heterogeneous and randomly distributed cluster, or is a spatial outlier. As part of Moran's statistics, z-score and pseudo-p values are also calculated, expressing the statistical significance of the spatial autocorrelation in the dataset. As a result, clusters and outliers are classified into a cluster/outlier type based on the field chosen to perform the analysis (in our case, the PS velocity rates). Therefore, statistically significant clusters are distinguished in high values (HH, positive velocity rates) or low values (LL, negative velocity rates), while outliers with high or low values respectively surrounded primarily by low-value or high-value points are defined as HL and LH and filtered out. The outlier's identification allowed to remove the noise introduced during the displacement estimation.

4.3.3.2 DBSCAN

The identification and monitoring of significant clusters undergoing similar deformation patterns are essential tasks in analysing and interpreting PS data. Among the clustering algorithms, the Density-Based Spatial Clustering of Applications with Noise) [Li et al., 2015] has emerged as a powerful unsupervised machine-learning tool for identifying clusters with irregular shapes in data with varying densities. The density-based technique explores the set of ungrouped filtered PS data to detect additional outliers and extract well-separated clusters with similar deformation behaviour (i.e., dense regions) without any preliminary information about the number of groups existing in the dataset [Lv et al., 2016]. Two input parameters are required to define clusters by linking neighbouring points: the eps radius and the MinPts density threshold. The radius determines the maximum distance between two data points that can be regarded as part of the same cluster, whereas the density specifies the minimum number of data required within the neighbourhood to form a core point [Starczewski et al., 2020]. Points that fail to meet these criteria are deemed outliers to the sample. The PS datasets are clustered by considering the boundaries given by the SU they belong to. In the context of the clustering process, ground displacement operated as a critical factor for categorising PS data into clusters. When dealing with multivariate datasets it is crucial to recognize only significant variations within the same cluster. Therefore, we employed a standardisation procedure to bring the velocity values to a common scale. In particular, we assigned a value of -1 for displacement rates indicating motion towards the satellite LOS and a value of +1 for those showing movement away from the LOS direction. Finally, we allocated a value of 0 for PS considered stable (with velocities ranging from -2 and +2 mm/y). This process avoids affecting the performance of the clustering algorithm due to the broad range of the velocity feature, enabling the DBSCAN to effectively operate on the datasets. We performed the unsupervised clustering, implemented with Python from the Scikit-learn library [scikit-learn.org], by applying a MinPts value equal to 3. The optimal radius (eps) was automatically determined inside each Slope Unit to ensure the adaptability of the clusterization to local conditions. The dynamic estimation involved the extraction of the knee point in the k-distance graph, which represents the distances between data and their three-nearest neighbours (Rahmah and Sitanggang, 2016). The adopted approach ensured that clusters within each Slope Unit were based on the local density of deformation patterns, handling variations of spatial distribution across different regions of the area of interest. The employed methodology assigned a unique cluster number attribute for each point within the designated area of interest, enabling the extraction of deformation clusters.

4.3.3.3 Classification workflow

Once the PS data filtering and clustering processes were concluded, the aggregated groups of points were used in the implemented ranking model to assign a different prioritisation value to landslides of interest. The implemented prioritisation pipeline and the output classes were reported in Fig.3. The first step was to evaluate the presence of PS inside the investigated landslide bodies. The threshold set on the density was obtained from the literature [Barra et al., 2017; Solari et al., 2019], taking into account the different spatial resolutions of the S1 and CSK sensors. In particular, landslides showing a PS density less than 30PS/km2 (for S1 data) and 50PS/km2 (for CSK data) were assigned to the not-classified (NC0), according to the poor spatial coverage of PS-InSAR data (Figure 4-3). Similarly, slope processes without at least 3 moving PS (hence, at least one cluster of displacement) were considered not-classified (i.e., NC1, Figure 4-3). The NC1 class has been assigned to this category because the absence of moving clusters does not necessarily imply a lack of active deformation of the slope process but rather a potentially unfavourable slope orientation compared to the satellite LOS, which would prevent an adequate movement assessment. The following steps involved the ranking of all the slope processes not exhibiting moving clusters between the body of the landslide and the slope unit (well-mapped, 0A) or moving clusters crossing both the landslide perimeter and the relative SU, but not interacting with human structures or infrastructures (not-interacting, 0B, Figure 4-3). In the 0A class, all observed phenomena seem to be accurately mapped (by PS-InSAR measurements) since the clusters of deformation fall within the mass process limits. In the 0B class, these instability processes, while presenting moving PS outside the mapped polygon (but still within the topological boundary marked by the relative SU), do not affect man-made structures, hence related to a low priority level based on the aim of our study. To assign a priority ranking that could be easily interpreted by non-experts and used for in-depth investigation, the following ranking classes were based on thresholds set on the average LOS velocity of clusters. Thresholds based on the average LOS velocity were assigned for moving clusters located within landslide boundaries, in-between landslides and SU, or clusters located in the SU and within a specific distance from the landslide body. The specific distance, already included in the PAI inventory, varies for each landslide, as it considers the potential evolution of the distribution activity of each process (e.g., advancing, retrogressive, enlarging, [WP/WLI, 1993]). Although in several works the landslide classification is implemented based on the velocity projected along the steepest slope gradient (Vslope), the major disadvantage of such a procedure relies on the assumption that the landslide kinematics is purely translational, otherwise, the retrieved displacement is underestimated. This implies that the Vslope is not feasible when considering a landslide inventory including the full spectrum of kinematics, hence the average LOS velocity was considered as the best option for our analysis. The thresholds set on the absolute mean value of the cluster velocities are the following:

- $|v| < 2$ mm/y: stable, class S
- $2 < |v| < 4$ mm/y: Low- priority, class 1;
- $< |v| < 8$ mm/y: Medium- priority, class 2;
- $|v| > 8$ mm/y: High- priority, class 3.

We also accounted for the possibility that clusters moving between landslide polygons and the SU might exhibit a gradient in the displacement rates, indicating zones with a differential deformation pattern. Consequently, we introduced two additional classes, denoted low-priority differential (1D) and medium-priority differential (2D), to acknowledge this differential movement between clusters. This distinction is crucial, as it can exacerbate the expected level of damage by introducing complexity into the deformation scenario for human structures.

4.4 Results

4.4.1 Multi-sensor deformation maps

The multi-sensor dataset allowed us to obtain good coverage of displacement data in the area of interest despite the presence of densely vegetated and cultivated areas. Considering that the objective of the present work is to provide a classification of the gravitational phenomena interacting with anthropic structures and that the latter constitute excellent radar signal reflectors (and, consequently, high-coherent PS), in most cases, the obtained information was representative of deformation processes of interest. As mentioned in Section 4.3.1, the total number of PS obtained for the area of interest is around 2M for S1 and just under 15M for CSK (about 4M for each track). Figure 4-5 shows the data coverage for both orbital geometries used.

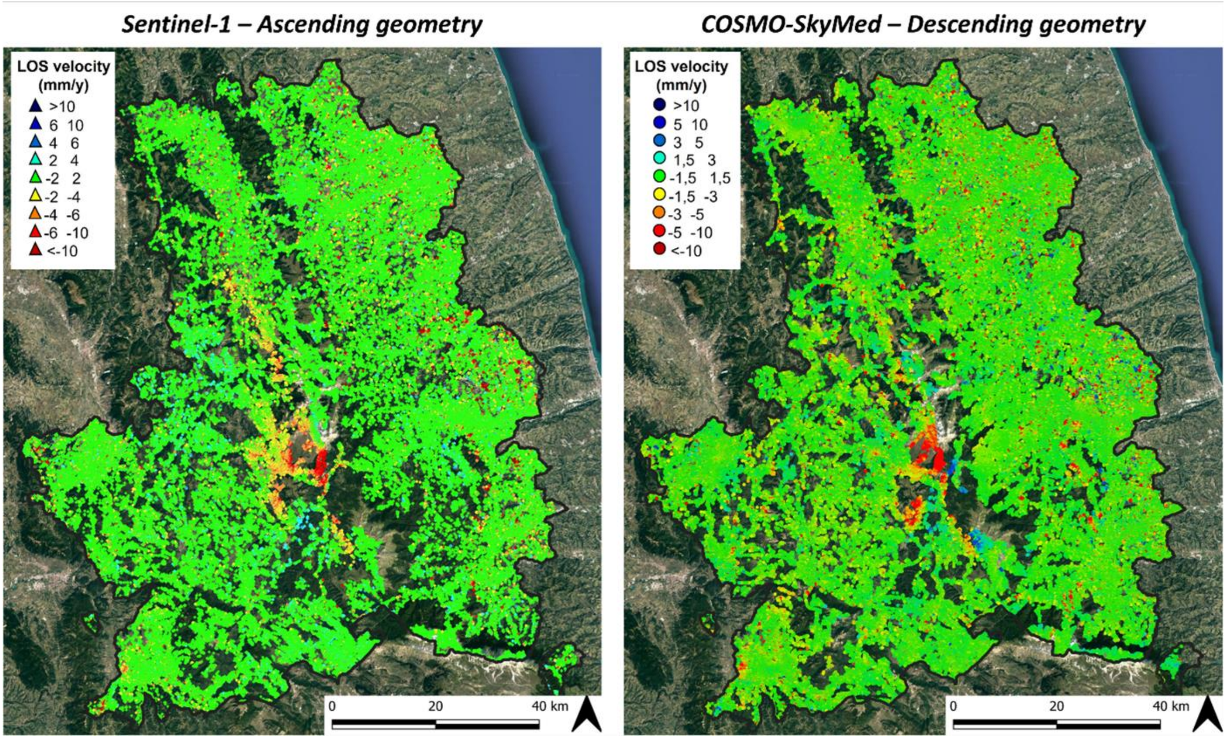

Figure 4-5: Deformational maps at the regional scale for the study area. The panels display the displacement rates measured in the ascending orbit from the Sentinel-1 satellite (left panel), and the deformations retrieved from COSMO-SkyMed for the descending geometry (right panel).

From the comparison between the two orbital geometries, the different resolutions of the S1 and CSK sensors significantly affected the ability to identify PS. In the descending orbit, the measurement points are much denser and provide better data coverage throughout the study area. Nevertheless, in both cases, the areas surrounding the epicentre of the 2016-2017 seismic sequence and along the active faults' system lack displacement measures. This is probably due to the intense co-seismic deformations affecting the analysis of ground displacements. While the signal is completely decorrelated in the proximity of the epicentre, residues of the co-seismic deformation are detected up to about 10 km moving away from this area. To ease the filtering, clustering, and classification tasks, we exclude those PS outside of the slope units comprising the landslides of interest, which were considered as the minimum morphological boundaries to discriminate between adjacent instabilities.

4.4.2 Priority assignment

The application of the proposed workflow allowed us to assign each of the over 500 landslides to one of the 10 classes for obtaining a different prioritisation level (Figure 4-6). Considering the higher spatial coverage of the CSK dataset, the number of landslides for which the use of the InSAR technique was effective support for field activities is much higher than S1. During this process, despite the presence of measuring points, areas of interest which did not show sufficient distribution of displacement information to study and classify the landslide phenomenon were discarded. In this first phase, we discarded 3% of the areas poorly covered by S1 data and less than 5% of the landslides of interest covered by CSK, classified as NC0. The subtle difference is linked to the fact that, given the higher ground resolution of the CSK sensor, the PS density threshold set is higher (50 PS/km2) than that decided for S1 (30 PS/km2). In the following step, a much higher number of phenomena (45-50%) without enough moving PS was discarded and classified as NC1.

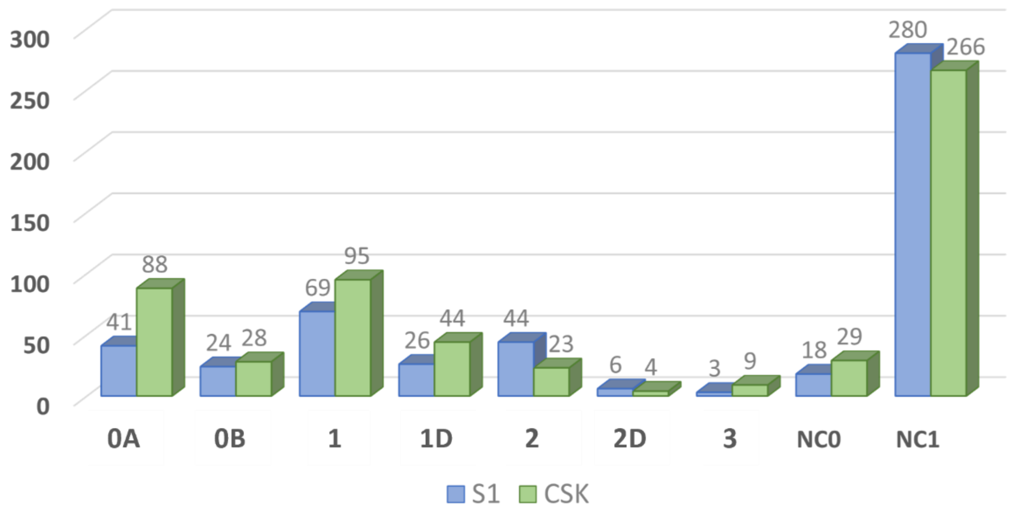

Figure 4-6: Overview of the landslide classification in nine ranking classes.

The last steps before the priority class assignment consisted of the filtering of Classes 0A and 0B, respectively representing landslides showing non-overlapping moving PS clusters with Slope Units, or with infrastructure and urban areas. Regarding class 0A, when considering the slope units associated with it, dataset S1 had approximately half the number of landslides without any significant movement clusters compared to those excluded when using CSK data (41 landslides in S1 versus a total of 88 landslides in CSK). On the other hand, the count of non-interacting clusters involving anthropic structures was noticeably lower, resulting in a reduction of less than 30 landslides for both datasets. Eventually, the crucial parameter for distinguishing the priority levels among the remaining landslides was the average velocity calculated for each moving cluster. This criterion differentiated, in terms of velocity rates, those landslides with adequate distribution of the ongoing displacements, significant enough to impact vulnerable anthropic elements, and whose actual deformation's extent was underestimated. Out of the initial set of landslides considered for classification, approximately 148 polygons from S1 and 175 from CSK successfully passed through the selection process and were assigned to 5 different priority levels (Figure 4-6).

Among the five proposed levels, classes with low priority (specifically, class 1 and 1D) encompass the highest proportion of landslides. Approximately 19% of the instabilities were categorised as low priority when considering the S1 data, while this figure increased to about 23% when using CSK data. Figure 4-7 shows the cases of the municipalities of Moscano (panel a), ranked as class 1, and Borgiano (panel b), whose landslides are ranked instead as class 1D, located in the Marche Region. For a better visualisation of the deformation maps, the unmoving PS are not shown.

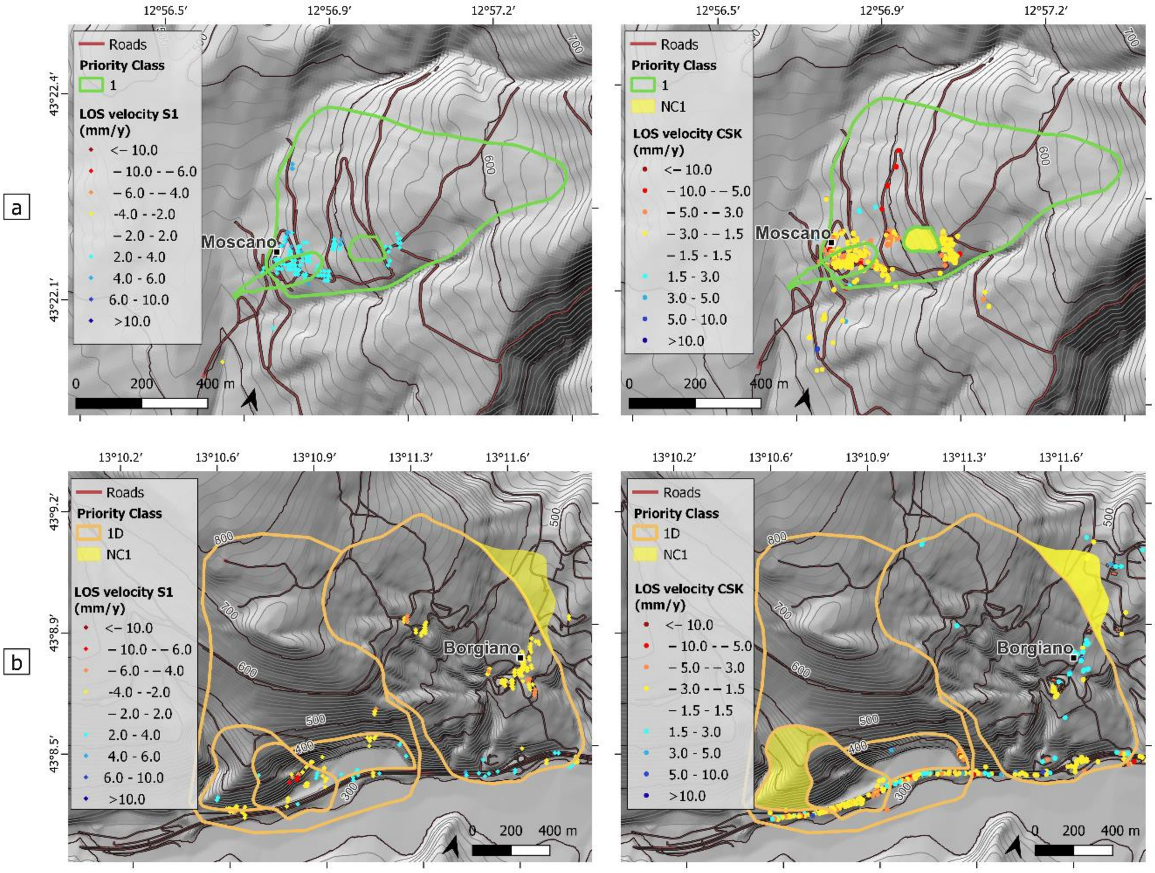

Figure 4-7: Example of two case studies ranked with a low priority level (i.e., class 1 and 1D). Panel a) represents the gravitational instability processes and the relative deformation rates affecting the municipality of Moscano. Panel b) shows the displacement rates of landslides interacting with the anthropic structures of the municipality of Borgiano. In this case, differential deformational patterns can be measured over the landslide bodies, leading to the assignment in the 1D category. Given the high concentration of PS, information from the measuring points that are considered stable (velocity ranging between -1.5 and 1.5 mm/y) was omitted for better interpretation of the analysis.

The landslide that affects the town and the infrastructure of Moscano, and is classified as a quiescent complex landslide, is well characterised in the southern sector, along its foot. In both geometries, the displacement clusters display an average velocity of |3| mm/y, with a displacement direction towards the southwest (approaching the sensor in the ascending geometry and moving away from the descending one). In both cases, small clusters outside the perimeter of the landslide body indicate that this instability process affects a slightly larger area, deforming with the same average velocities. In panel b of Figure 4-7, a heterogeneous displacement pattern is recorded on the landslide bodies affecting the town of Borgiano and the anthropic structures located along the valley floor. In both orbital geometries, the movements measured in the central-eastern area of gravitational instability show a displacement component along the maximum slope direction.

Indeed, S1 clusters displaying negative velocity (approximately -3mm/y on average) move away from the ascending sensor, while the PS (averaging +3mm/y) recorded in the descending orbit move away from the sensor (light blue shades). The deformational measures, although remaining in the order of about |3| mm/y, abruptly change their motion direction, which is opposite to the one described above at the foot of the two landslides. In this sector, the national highway SS7 that runs along the valley floor and, in some parts, even the quarry located at the foot of the western gravitational phenomenon, exhibit opposite displacement direction with respect to the upper part of the slope, which can be potentially related to bulging.

Almost 70 landslides intersecting clusters with average displacement rates ranging between 4 and 8 mm/y were assigned a medium priority level (i.e., class 2). When compared to their respective totals, the number of landslides categorised with medium priority is higher by exploiting S1 data (amounting to 44 landslides out of 511), as opposed to the classification using CSK (Figure 4-6). Two case studies of landslides resulting as category 2 from the classification process are located respectively in the Marche and Lazio regions (Figure 4-8).

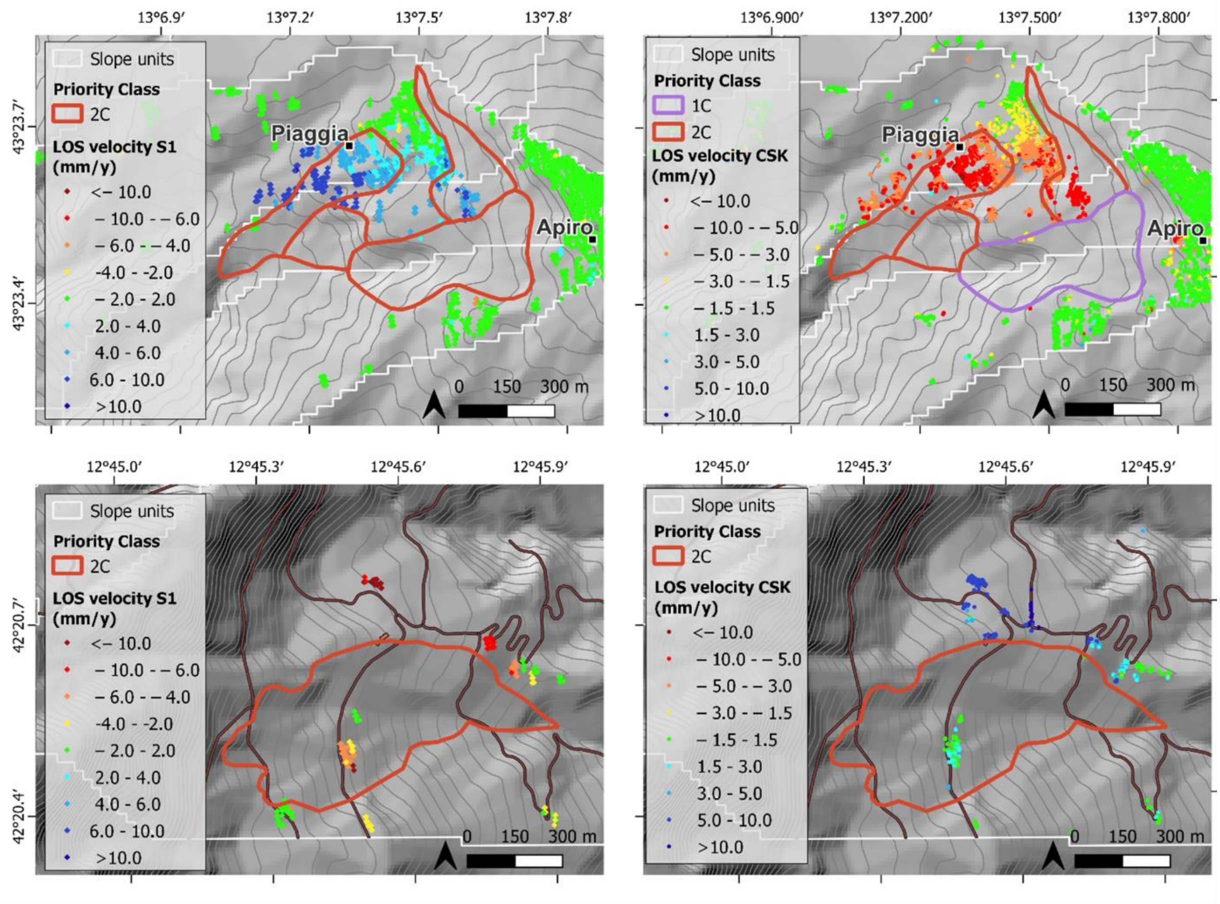

Figure 4-8: Example of two case studies ranked with a medium priority level (i.e., class 2). Panel a) represents the gravitational instability processes and the relative deformation rates affecting the village of Piaggia (municipality of Apiro, Marche). Panel b) shows the displacement rates of landslides interacting with the anthropic structures of the village of Poggio Perugino (municipality of Rieti, Lazio).

The first example (panel a) involves the instability processes affecting the village of Piaggia (municipality of Apiro). This example vividly illustrates how a substantial number of measurement points displaying significant movement (with displacement rates on the order of approximately ±7/8 mm/year) are entirely omitted in the mapping of deformation phenomena. In this way, different commercial structures and some houses, although involved in rather conspicuous deformations, are not affected by landslides inventoried in the PAI. Similarly, although with more fragmented information due to the uneven distribution of stable scatterers to the ground, the township of Poggio Perugino (municipality of Rieti) shows several moving clusters of PS, indicating deformation rates of about +-7mm/y in both geometries (panel b of Figure 4-8). In any case, a direct correlation between the clusters excluded from the mapping and the landslide of interest is not, in this case, so obvious. Only the PS cluster located at the foot of the landslide appears to be near the deformation, whereas a couple of separate groups in the northern sector of the area may be associated with a distinct phenomenon.

Finally, landslides classified with a medium-high (i.e., class 2D) and high priority level (i.e., class 3) are the least numerous. A comparable number of landslides belong to class 2D for both S1 (6 landslides) and CSK (4 landslides) while, in the high-priority class, the number of landslides classified with CSK data (9 phenomena) is much higher than those classified using S1 (only 3 landslides). Figure 4-9 illustrates the instability processes affecting the municipalities of Montemartano and Offida.

In the case of Montemartano, there is a significant contrast in the spatial distribution of deformations observed in the ascending and descending geometries. This difference is substantial enough to lead to the classification of the landslide into two distinct priority levels. On one hand, utilising S1 data, displacement rates of about -4.5mm/y above the gravitational process boundary were obtained, at about 740 m a.s.l. This part of the slope falls within the geomorphological limit of the slope unit related to this landslide, thus potentially indicating a further extension of the instability to those sectors (Figure 4-9a). In the central portion of the landslide body, the severe deformations measured in the municipality of Montemartano and along a section of the provincial road reach average displacement rates of about -20 mm/y, thus raising the classification to a priority level 3 (Figure 4-9a). On the other hand, the deformation cluster acquired with the CSk data is well concentrated in the urban centre, and entirely enclosed by the perimeter of the landslide, which then, according to the classification model, is "well mapped" (class 0A, Figure 4-9a1).

The last case taken as representative of the prioritisation model concerns the municipality of Offida. Once again, the model returned two different priority classes based on the different interferometric datasets used, although not as divergent as the example described above. A considerable portion of the town of Offida, along with the primary and secondary roads, is under intense deformations, which are appreciated with both orbital geometries. Due to the considerable density of buildings and infrastructures, we can appreciate a gradual transition in the displacement pattern. From displacement rates in the order of about +-7mm/y, located towards the top of the landslide, to peaks of over 18 mm/y recorded with CSK, and over 20mm/y recorded with S1 is noticeable. Isolated clusters with lower deformation rates (less than 4mm/y) are recorded just above the inventoried landslide crown, identifying a wider extension of the process than the mapped portion. Moreover, thanks to the data acquired in descending geometry, it is possible to highlight how, within the slope unit that includes the mapped phenomenon (and in the neighbouring slope units as well), there is an evident inversion of the recorded velocities, shifting in the orientation from southwest (away from the sensor for the PS in yellow and orange shades) to northeast (approaching the sensor for the PS in blue shades) measured in the body of landslide. In the ascending geometry, this inversion is not recorded. For this reason, if in the case of S1, the landslide is classified as priority level 3, in the case of CSK the phenomenon is assigned a 2D priority level.

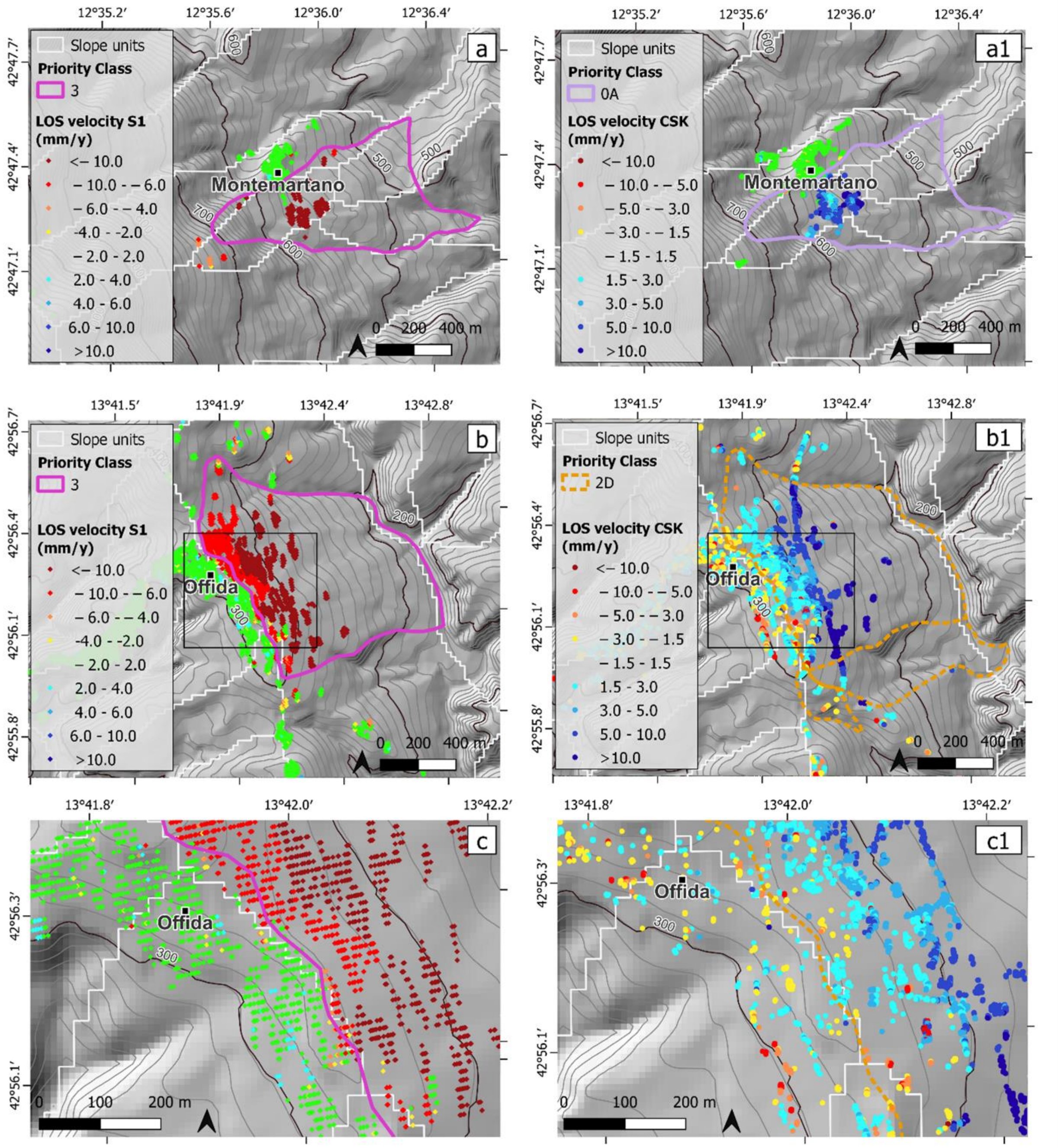

Figure 4-9: Example of two case studies ranked with a medium-high (i.e., class 2D) and high priority level (i.e., class 3). Panels a) and a1) represent the gravitational instability processes and the relative deformation rates affecting the village of Montemartano (municipality of Spoleto, Umbria). Panels b-b1) show the displacement rates of landslides interacting with the anthropic structures of the municipality of Offida (Marche). In panels c) and c1) details of the moving clusters exceeding the boundaries of the mapped phenomenon are illustrated for both orbital geometries. Given the high concentration of PS in the urban centre of Offida, information from the measuring points that are considered stable (velocity ranging between -1.5 and 1.5 mm/y) was omitted for better interpretation of the analysis.

4.5 Discussion

We successfully exploited the PS displacement rate information to assign a different priority level to the landslides of interest. Out of the input data (over 500 landslides from PAI inventory), we found that at least 30% (for both orbital geometries) exhibit moving clusters closely extending beyond their boundaries and, therefore, potentially associated with the same gravitational process.

The subdivision into the five priority subclasses remains consistent for both the S1 dataset and the CSK dataset. The distribution of phenomena within each category is generally similar, except for minor variations that can be attributed to the use of different sensors and varying resolutions. When examining the distribution of landslide occurrences across each class, a noticeable decreasing trend emerges, beginning from the lowest priority class (i.e., class 1), which accounts for 13% in the case of S1 and 16% with CSK, to the highest priority class (i.e., class 3), accounting for S1 and CSK 0.6% and 1.5%, respectively.

At the local scale, the selected case studies shown in the results section have also allowed us to analyse in detail the correct assignment of the phenomenon to each priority class, confirming that some areas, already examined in the literature with local-scale investigations, are worthy for further reconstruction of the phenomena morphodynamics. The landslide that affects the town of Borgiano, which has been assigned a level of medium-low priority, has already been documented in the literature as a small DGPV (specifically, a deep-seated block slide, Aringoli et al., 2010). This landslide, owing to its interaction with critical anthropogenic structures like the primary connecting road, a quarry, and a water production reservoir, is subjected to ongoing monitoring through a specialised GPS monitoring system. Furthermore, geophysical surveys have been conducted to examine the active deformation characteristics. The displacement rates obtained by ascending and descending PS, averaging around 3 mm/y, perfectly match the phenomenon classification (sensu Cruden and Varnes, 1996), corresponding to the slow or very slow category. From the geomorphological surveys and the geophysical analyses, it clearly emerges how the DGPV basal part, which affects the state road, is effectively subjected to bulging, as confirmed by the InSAR displacement measures. A small counterslope located south of the town of Borgiano expresses the same deformational behaviour. The instability appears to extend, as suggested by geophysical cross-section interpretations [Aringoli et al., 2010], even beneath the lake's bottom, where the limitations of the InSAR technique prevent the detection of displacements. The prioritisation process for both the Borgiano landslide (already documented in literature) and the Moscano landslide (so far unexplored) proved its effectiveness. This process highlighted the significant impact on anthropogenic structures, particularly those of strategic importance. It also facilitated the displacement rate measurement for both phenomena and found that the current boundaries should be extended.

In the cases of mass processes classified with medium ranking, we obtained excellent results. The case of Piaggia is perhaps the most exemplary, as it is well characterised by dense measuring points in correspondence with the inhabited and industrial areas. The perimeter of gravitational phenomena does not take into account large portions of this inhabited centre, which however exhibit intense deformation. Similarly, the landslide of interest located in the town of Poggio Perugino stands as a critical case study, since the mapped slope instability does not comprehend some areas that show quite significant displacements (rates of about 5-7 mm/y). In this case, the deformation clusters excluded from the perimeter of the landslide are located in portions relatively distant on the slope, and may therefore not be part of the landslide of interest, but rather related to new slope failures not yet identified in the PAI inventory. In any case, it is important to stress that these deformations insist on several sections of the primary road network leading to the residential area. Whether it's an extension of the same landslide or new gravitational phenomena that haven't been identified yet, the ranking model accurately recognised a problematic zone that warrants additional investigation. If such instabilities were to affect the primary road network, they could disrupt and even preclude any connection in the event of future emergencies. Similarly, a redefinition of the landslide system in the Piaggia district should be reconsidered, as should a more detailed examination of the varying displacement rates observed by satellite measurements.

The varying performance of different sensors and ground resolutions became evident through the cases of Montemartano and Offida, which received different rankings depending on the satellite employed. The InSAR measurements obtained in the descending geometry confirmed displacement rates observed between 2011 and 2014 with CSK by [Di Matteo et al., 2023]. Such displacements are retrieved exclusively in correspondence with the inhabited centre: thus, the Montemartano landslide does not exhibit deformation sectors outside the mapped perimeter and was correctly classified as "well mapped" (class 0A). On the contrary, in the ascending geometry, we report a deforming area in the upper portion of the slope (between 750 and 800 m a.s.l.), which is partly covered by vegetation. The different radar bands related to the two satellites likely affected the ability to record movements in this area. Sentinel-1 C-band sensor, less influenced by the vegetation and with a greater penetrative capacity than the X-band sensor, succeeded in identifying a moving cluster in a challenging area, with few scattering elements surrounded by shrubs. Detailed geological surveys (Licata et al., 2023), pointed out that this specific portion of the slope is covered by unconsolidated debris talus, which easily experiences movements uncorrelated with the complex landslide below. In this case, therefore, although the ability of the model to identify mapping criticality, the attribution of such a high-priority class is to reconsider in the light of field evidence. Similarly, a slight discrepancy is also observed for the Offida landslide ranking. The finer ground resolution of CSK provided an exceptional level of detail in measuring the differential displacement rates within the urban centre, not comparable with that achieved by S1. The city develops on a watershed, on which the crown of the landslide body has been identified. The difficulty in distinguishing movements related to the phenomenon under study or other strains insistent on the opposite side can in this case be facilitated by the use of interferometric information, which can support a more correct delimitation of the process in an urban context, which can always be challenging.

4.5.1 Novelties, limitations and future perspectives

This study stands as one of the first applications of PS-InSAR analyses in the Central Apennines since, compared to other Italian regions, there has been a notable absence of regional-scale studies [Solari et al., 2020]. Our work has addressed this gap in the context of the complex geomorphic dynamics of the Central Apennines, an area known for its pervasive presence of landslides [Trigila et al., 2021]. We introduced a spatial statistical approach (*i.e.*, clustering analysis) as a novel instrument for evaluating and assessing a priority ranking to landslides, so far poorly explored with respect to hot-spot and buffer analyses, which still represent very popular approaches. The application of the DBSCAN method allowed us to assign measuring points with similar deformational behaviour to the same cluster in a way resembling the interpretation an expert would perform. By doing so, the spatially aggregated information enabled us to obtain a more robust interpretation key that better mirrors the actual deformation patterns. While a mere interpolation or hotspot creation might result in an overestimation of the deformation rates extent in an area (assumed that they don't display a linear deformation pattern), a more precise approach as the DBSCAN involves focusing solely on the cluster within an active deformation zone and a limited relative buffer. The comparison depicted in Figure 4-10 highlights that, based on the PS mean velocity (Figure 4-10a), the clustering analysis carried out through the DBSCAN algorithm (Figure 4-10b) yields more reliable results compared to the hotspot analysis (Figure 4-10c). In Sector I, the interpolation fails to distinctly identify a deformation cluster due to the mixing of displacement values with nearby stable velocity values, leading to an attenuation of the deformation signal. Conversely, DBSCAN effectively isolates and delineates the deformation area, strictly connected to the deformation identified further north, thus supporting the interpretation of the process. Sectors II and III demonstrate DBSCAN's efficacy in identifying outliers within the dataset, simplifying filtering operations. In the hotspot analysis, outliers are either integrated into the interpolation process, resulting in small areas of apparent deformation (Sector II), or categorized as stable areas if nearby speed values exhibit opposite signs (Sector III).Future implementations should also incorporate the temporal dimension, considering, together with the spatial distribution of the velocity rates, also the PS time series trends, to obtain a more reliable aggregation of similar PS representing the same slope process. Furthermore, by incorporating geomorphological constraints (such as Slope Units) into our analysis, we were able to substantially enhance our ability to identify clusters potentially attributable to the same geomorphic process (*i.e.*, excluding moving clusters separated by drainage divides or ridges). However, the current main limitation of Slope Units as geomorphological constraints is their spatial resolution, which is still limited to 25 metres pixel size, unreliable for analysing the extension of small phenomena. The authors are currently working on further implementation of the Slope Units resolution, starting from high-resolution digital models to obtain more accurate slope subdivisions into homogeneous terrain units.

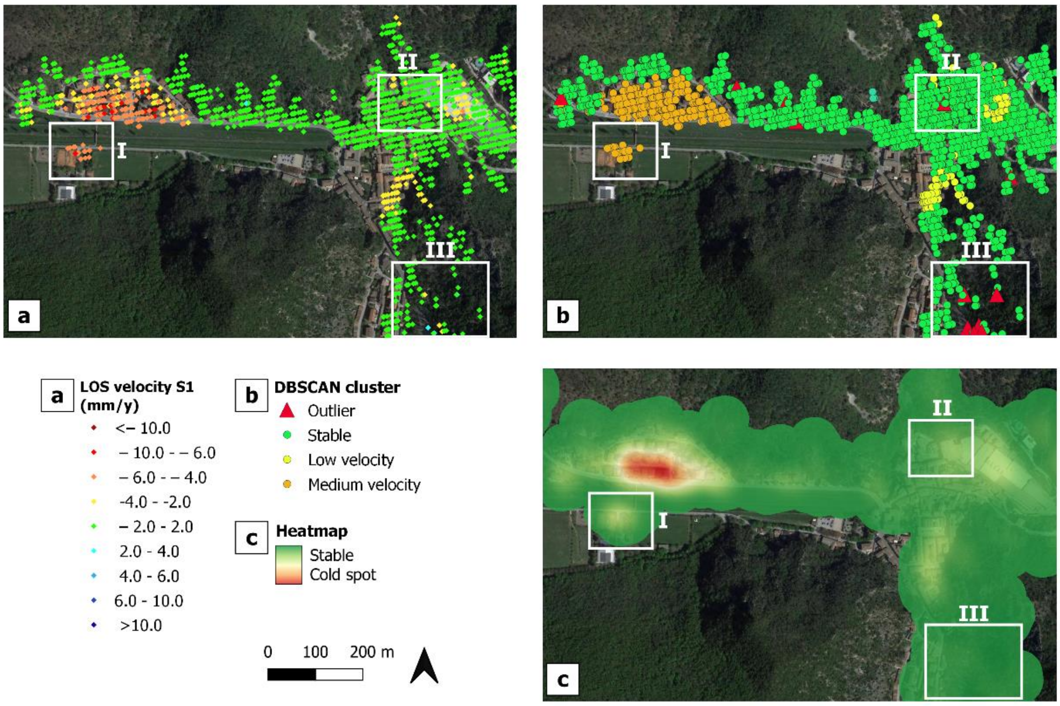

Figure 4-10: Comparison between the results obtained through the DBSCAN-based aggregation model and the classic hotspot analysis-based techniques. The panel on the left shows the deformation map generated with the Sentinel-1 dataset on a test area. The top right panel displays the DBSCAN algorithm performance: PS aggregated in separate moving clusters are effectively highlighted more accurately through this procedure than through the hot-spot-based analysis (bottom right panel).

4.6 Conclusions

In regions with historically frequent seismic activity, it is of paramount importance to thoroughly investigate the interplay between slope instability and urban development. The impact of severe seismic motions, like the Central Apennines sequence, can extend over vast areas, reaching up to several tens of kilometres from the epicentre. Consequently, their interaction with slope instability phenomena within the seismic area can multiply exponentially, leading to the reactivation or triggering of hundreds to thousands of landslides. In addition to conducting comprehensive field investigations targeted at assessing earthquake-induced landslides, it is equally vital to provide tools that can facilitate large-scale monitoring and updating of gravitational deformations. For this purpose, our work provided valuable and easily reproducible methodologies to support the cataloguing of the actual extent and current state of activity of landslides at the regional scale, ensuring spatio-temporal up-to-date information for urban planning and risk management instruments (*i.e.*, PAI inventory). This methodology, designed to be adopted by both expert and non-expert users, is targeted to plan detailed investigations based on the results of prioritisation of different areas of study. A central aspect of our study revolves around the synergistic use of interferometric data aggregation algorithms (*i.e.*, DBSCAN), wherein the motion of individual Persistent Scatterers is interpreted based on the deformation patterns in their immediate vicinity, and the geomorphological constraints represented by the Slope Units, which delimit this aggregation according to topological criteria. Moreover, by exploiting different radar bands and spatial resolution, albeit with the limitation of one orbital geometry available per sensor, we obtained distinct information that demonstrated the advantages of reduced sensitivity to vegetation (resulting in a less noisy analysis, as observed with Sentinel-1) or enhanced capability to measure differential deformational patterns (as evidenced by COSMO-SkyMed). In the near future, with the advent of freely accessible and regularly updated Europe-wide interferometric products like EGMS, there will be a growing demand for the standardisation of procedures related to the identification and classification of active deformational areas. Additionally, it will be imperative to explore innovative tools for efficiently handling the vast volume of data generated by these sources.

5 PS-InSAR post-processing for assessing the spatio-temporal differential kinematics of complex landslide systems: a case study of DeBeque Canyon landslide (Colorado, USA)

Under review on Earth Surface Processes and Landforms

Abstract

The complex superimposition of different kinematics and nested sectors within landslide systems amplifies the challenge of interpreting their heterogeneous displacement pattern and targeting effective mitigation solutions. As an example of such peculiar spatio-temporal behaviour, the DeBeque Canyon Landslide (Colorado, USA) is emblematic of the application of interferometric post-processing analysis for a detailed, remotely based investigation. We employed a multi-geometry Persistent Scatterers (PS) InSAR dataset to provide continuous information on the spatio-temporal scale and achieve a solid representation of the segmented kinematics and timings. From the updated geomorphological map of the landslide system and its internal components, a bi-dimensional decomposition of the PS dataset was performed to derive, for each sector, the respective displacement orientation and inclination. Statistical-based analyses carried out on the displacement vector descriptors and time series lead, respectively, to the spatial characterization of the landslide system segmented style of activity, and the assessment of trend abrupt changes related to preparatory and triggering factors. A clear differentiation of the rotational or translational kinematics within the landslide system was accomplished solely using surface displacement measures. Moreover, the application of a Bayesian model on the bi-dimensional vector time series lead to the identification of significant differences in the deformational behaviour of each sector with respect to precipitation and temperature factors. Our approach represents a replicable method for local-scale characterization and monitoring of landslides exhibiting complex spatio-temporal displacement patterns and providing an effective, low-cost solution for transportation agencies from a risk-reduction perspective.

Keywords: Landslide system; InSAR post-processing; PS-InSAR; landslide kinematics; multi-geometry combination; time series decomposition.

5.1 Introduction

Landslides significantly impact mountain environments worldwide, reshaping the topography but also affecting human activities, thus posing a threat to urban settlements [Bozzano et al., 2010; Agliardi et al., 2012; Crosta et al., 2013; Raspini et al., 2017; Herrera et al., 2018]. The interplay of litho-structural factors and hydro-climatic conditions controls their differential erosion and sediment redistribution, affecting the long-term morphoevolution of the slopes [Crosta et al., 2017; Preisig et al., 2016; Della Seta et al., 2017; Riva et al., 2018; Delchiaro et al., 2019; Marmoni et al., 2023]. Under the ongoing effect of such factors, rock masses accumulate stress and experience a slow yet persistent deformation, which may result in complex spatiotemporal arrangements of landslides, derived from the internal segmentation and mobilisation of nested bodies [Lopez Saez et al., 2012] or the superimpositions of different types of movements [Bossi et al., 2015; Valiante et al., 2016; Wang et al., 2020]. The term landslide system [Valiante et al., 2021 and references therein] describes such arrangements of gravity-driven morphotypes derived, over the long term, from the same slope deformation. Assessing this segmentation through an extensive spatial kinematic characterization, including the quantification of distinct displacement rates and mechanisms, as well as the identification of nested bodies and secondary failures, is crucial for understanding the complex morphodynamics of these phenomena [Bigot-Cormier 2005; El Bedoui et al., 2009; Crosta et al., 2017; Delchiaro et al., 2023; Dong et al., 2023].

The factors controlling landslide system history can be long-term static, as in the case of predisposing ones (e.g., bedding, lithology), or dynamic as in the case of the preparatory ones (e.g., temperature, river incision, glacial debuttressing). In addition, short-term triggering factors (e.g., earthquakes, extreme rainfall events) can lead the slope to the ultimate failure. In this regard, precipitation events play a decisive role both in the short term, acting as triggers when heavy rainfall or sudden snowmelt occurs [Grøneng et al., 2011; Del Ventisette et al., 2012; Nishii et al., 2013; Crosta et al., 2014] and, along with temperature, as preparatory factors, whenever prolonged rainfalls and seasonal changes undermine the slope marginal stability over the mid and long term [Popescu 2002; Ibsen and Casagli, 2004; Scheevel et al., 2017; Steger et al., 2022].

The interplay between the aforementioned factors impacts the temporal displacement evolution and may lead to the differential reactivation of the landslide system's internal sectors and even to a generalised failure [Del Ventisette et al., 2012; Wang et al., 2020]. From a geotechnical perspective, mitigation measures planning and construction become challenging due to the high spatio-temporal displacement variability, especially when strategic infrastructures are involved. An overall analysis is often carried out through traditional geotechnical and geophysical techniques that allow acquiring accurate localised measurements [Crosta and Agliardi, 2002]. However, given their spot-like peculiarity and the high cost of pervasive positioning, they fail to provide a comprehensive perception of the heterogeneous displacement pattern of the landslide, likely underestimating the actual fragmentation of the system.

To achieve a robust yet persistent interpretation of the spatio-temporal evolution of landslide systems, Interferometric Synthetic Aperture Radar (InSAR) and Light Detection and Ranging (LiDAR) can be effectively employed for a thorough investigation as they provide high spatio-temporal resolution, and extensive measurements coverage [Singhroy and Molch, 2004; Gischig et al., 2011; Ciampalini et al., 2016, Vick et al., 2020; Xu et al., 2021]. Combining these two techniques is ideal for investigating slow-moving phenomena in mountainous and hilly terrains. Whereas LiDAR data in the form of Digital Elevation Models (DEMs) are often employed for a detailed morphometric characterization of landslide signatures on rugged topography [Glenn et al., 2006, Ardizzone et al., 2007; Kasai et al., 2009; Jaboyedoff et al., 2012], InSAR techniques proved optimal detection of subtle ground deformations moving within the specific sensor's detection capability (i.e., from several centimetres to a few millimetres per year) [Wasowski et al., 2014; Mazzanti et al., 2015]. From the traditional differential interferometry method [Tarchi et al., 2003; Dong et al., 2018; Crippa et al., 2020; Reyes-Carmona et al., 2023] to advanced multi-temporal methodologies based on Small

Baseline Subsets [Berardino et al., 2002] and Persistent Scatterers - PS [Moretto et al., 2021], InSAR-derived displacements are essential for the landslide's deformational pattern quantification and mapping purposes [Bozzano et al., 2017a; Di Martire et al., 2017; Bordoni et al., 2018; Antonielli et al., 2019; Bonì et al., 2020]. The PS-InSAR technique has found widespread application in analysing the spatial displacement patterns associated with slow deformation processes, providing valuable insights for investigating landslide systems' segmented and heterogeneous kinematic behaviour [Crippa and Agliardi, 2021] and considering their interaction with man-made structures [Frattini et al., 2013]. In addition, PS displacement time series can be correlated with external meteorological forcings. In this case, examining the historical temporal deformation pattern of the slope process can allow us to highlight the relationship between reactivations and sudden accelerations in the displacement trend, triggered by high-intensity, short-duration events, or influenced by medium and long-term seasonal trends.

Nevertheless, the motion assessment through PS-InSAR applications is heavily affected by the intrinsic characteristics of the technique, which retrieves the ground deformation velocity along the satellite line-of-sight (LOS) and therefore fails to record the real tridimensional components of the displacement vector [Eriksen et al., 2017; Crippa et al., 2021]. Moreover, considering the complexity of examining multiple deforming sectors nested in a larger disrupted rock mass, the present literature still offers rare studies that aim to address this challenge in the spatial domain [Eriksen et al., 2017; Crippa et al., 2021] and, to the best of the author’s knowledge, none in the temporal one.

Therefore, the purpose of this study is to exploit PS-InSAR analysis to examine the spatial kinematic variability and temporal dynamics of a landslide system. The first part of the methodological section is dedicated to the description of the exemplary case study used in the present work. Then, we described how we estimated the two-dimensional displacement vector and employed it as an alternative to the LOS velocity for further displacement analysis. We used the combination of the multi-geometry Sentinel-1 dataset acquired between 2014 and 2019 considering it with respect to the LiDAR-derived local topography to derive the bidimensional vector. The spatial and temporal outcomes of the InSAR post-processing analysis are described in the two main subsections of the results. First, we delineated the spatial deformation pattern of the selected landslide exploiting the decomposed displacement vector to obtain a clear distinction of the peculiar kinematics of each sector composing the system. Eventually, from a temporal point of view, we correlated the decomposed velocity to the meteo-climatic data, identifying a correlation between displacement acceleration phases and precipitation and temperature factors, acting both as triggering and preparatory.

5.2 Materials and Methods

The methodology presented in the current section is tailored to investigate the spatial variability and morphodynamic evolution of the DeBeque Canyon Landslide system, described in Section 5.2.1. This system was used as an exemplary test site to investigate the heterogeneous deformational behaviour of a slow-deforming slope threatening Interstate 70, one of the major highways of the United States. Detailed mapping of the geomorphological features of the landslide was carried out through visual interpretation of a high-resolution digital topographic model (Section 5.2.2) as a preliminary step for further quantitative investigation on a multi-geometry interferometric dataset

(Section 5.2.3). We differentiated the heterogeneous spatial pattern by considering, in the first place, the decomposed velocity vector distribution over the landslide's sectors. Subsequently, we also examined the vector's time series for each zone of the landslide to retrieve specific timings and correlations with preparatory and triggering factors.

5.2.1 The DeBeque Canyon case study

The study area is located in the northern part of Mesa County in Colorado (USA): here, channelised surficial waters belonging to the Colorado River system represents the main morphogenetic agent, incising the extensive plateau in the form of deep canyons and playing a crucial role in disrupting the slope stability along its banks (Figure 5-1). A critical example of this interaction is the DeBeque Canyon Landslide (DCL) at milepost 51 of Interstate 70, a landslide system that has historically impacted the road, thus representing an area of concern for the Colorado Geological Survey [White et al., 2003].

This test site is in the western portion of the Upper Colorado River Basin, which is characterised by an arid to semi-arid climate [Kopytkovskiy et al., 2015] and can be referred to as BSk based on the Köppen climate classification [Zepner et al., 2020]. Summers are typically hot and dry, with temperatures reaching an average of 26°C in July, while winters are cold, with an average temperature below 0°C in December-January, as represented in the climate chart reported in Figure 5-1. Precipitations are scarce, averaging around 235 mm per year (Figure 5-1). Future projections of climatic trends draw attention to the progressive increase of drought periods, where liquid and solid precipitation are likely to decline while temperatures are expected to increase 2-4°C [Ficklin et al., 2013; Kopytkovskiy et al., 2015]. Such temperature increase is linked with the anticipation of snowmelt and runoff timing during Spring, thus potentially influencing the deformational trend of mass movements in the area [Ficklin et al., 2013].

Historically referred to as the "Tunnel Landslide", the DCL showed first signs of activity before 1910 (the precise date is unknown), when a 300 m-long, 90m-high sandstone slab partially dammed the Colorado River that deviated its path towards the opposite bank [White et al., 2003]. Two other historic paroxysmal events were recorded before the last catastrophic failure occurred in April 1998. As reported by White [2005], the landslide movement caused the permanent diversion of the Colorado River channel and the Old Highway 6 destruction in 1924, which was subsequently relocated but disrupted again in 1958. The last paroxysmal failure occurred in April 1998: a section of the newly built Interstate 70, located at the foot of the landslide, was laterally shifted 3 m and pushed up around 7 m. Ongoing displacement of these sectors is currently recorded and monitored by the Colorado Department of Transportation and Colorado Geological Survey using in-situ instruments and repeated LiDAR scanning [Gaffney et al., 2002; White, 2014; Weidner and Walton, 2020]. The first conceptual model of the geology, subsurface geometry, and the interaction of the different failure mechanisms involved in the DCL system was proposed by White [2000] and White et al. [2003], who reconstructed the model by means of a photogrammetric study based on aerial stereo-pairs available for the landslide site. Field mapping and wire-line core borings were also performed to reconstruct structural and stratigraphical information. The deformational area is divided into three main sectors (Figure 5-2) based on the surficial expression of the distinct failure mechanisms affecting the slope, namely the Upper Block, Rubble Zone, and West Disturbed Block [White, 2000; White et al., 2003; Weidner and Walton, 2020].

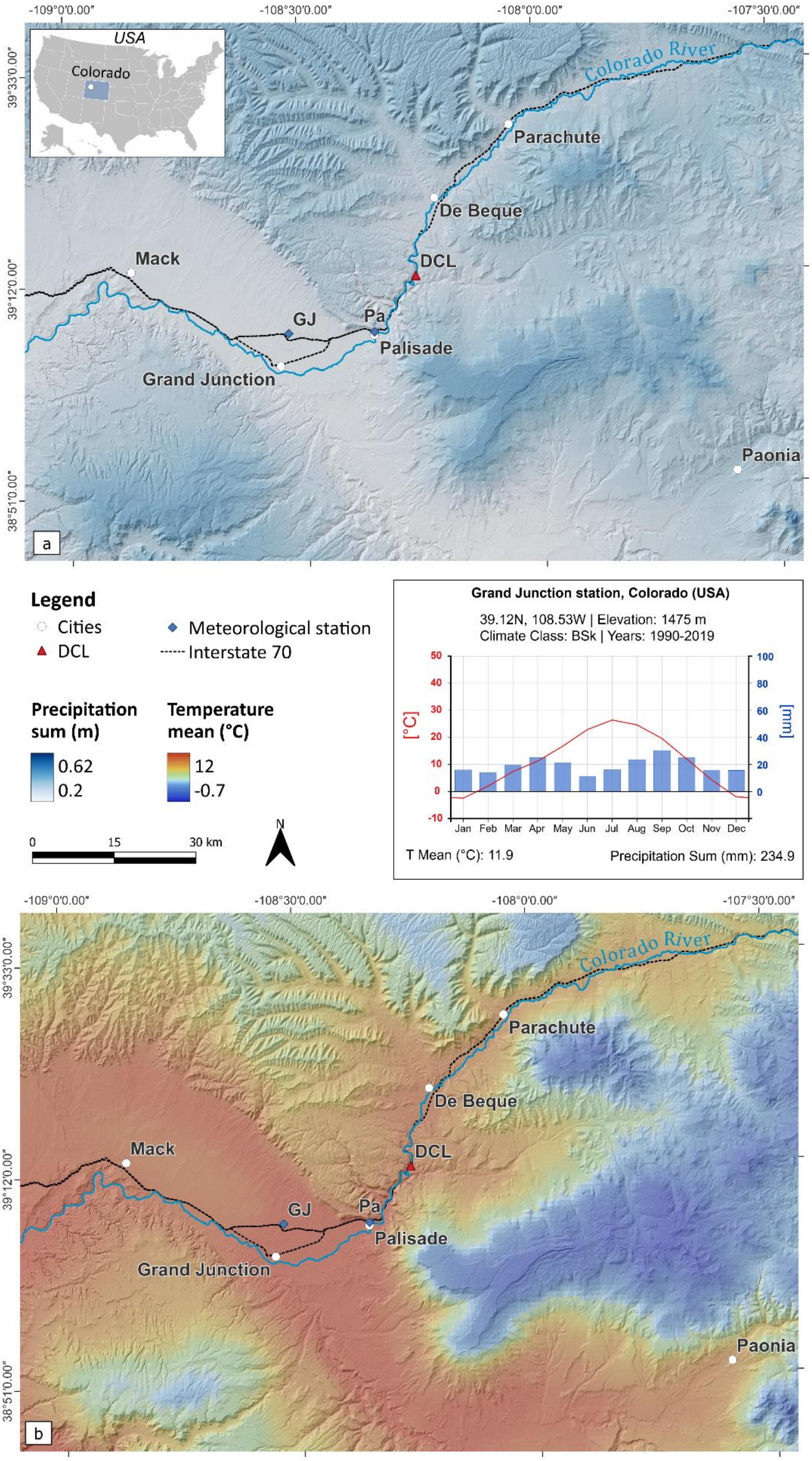

Figure 5-1: Geographical setting of the study area. The map shows the sum of the average annual rainfall (a) and average annual temperature (b) for the western portion of the Colorado basin [Fick et al., 2017], where the DeBeque Canyon Landslide (red triangle) is located. The blue rhombus indicates the location of two meteorological stations near Grand Junction (GJ) and Palisade (Pa), whose data were extracted and analysed in combination with the displacement time series (see Section 5.2.3). A representative climate chart is available for the GJ station, the closest station to the study area [Zepner et al., 2020].

The Upper Block is a wedge-shaped block delimited by an active cliff face on the right side and by a set of fractures and tension cracks, part of a shear zone along the upper side, which promotes its sliding. The material supplied by the retreating cliff accumulates in the Rubble Zone, where it translates to the rotational area located at the toe of the landslide system, thus constituting the "Rotational Failure Engine" model proposed by White et al. [2003]. Eventually, the West Disturbed Block represents a transitional sector that undergoes both the creep movements of the above Upper Block and the lateral shifting of the main rotational area of the Rubble Zone (Figure 5-2) [Weidner and Walton, 2020].

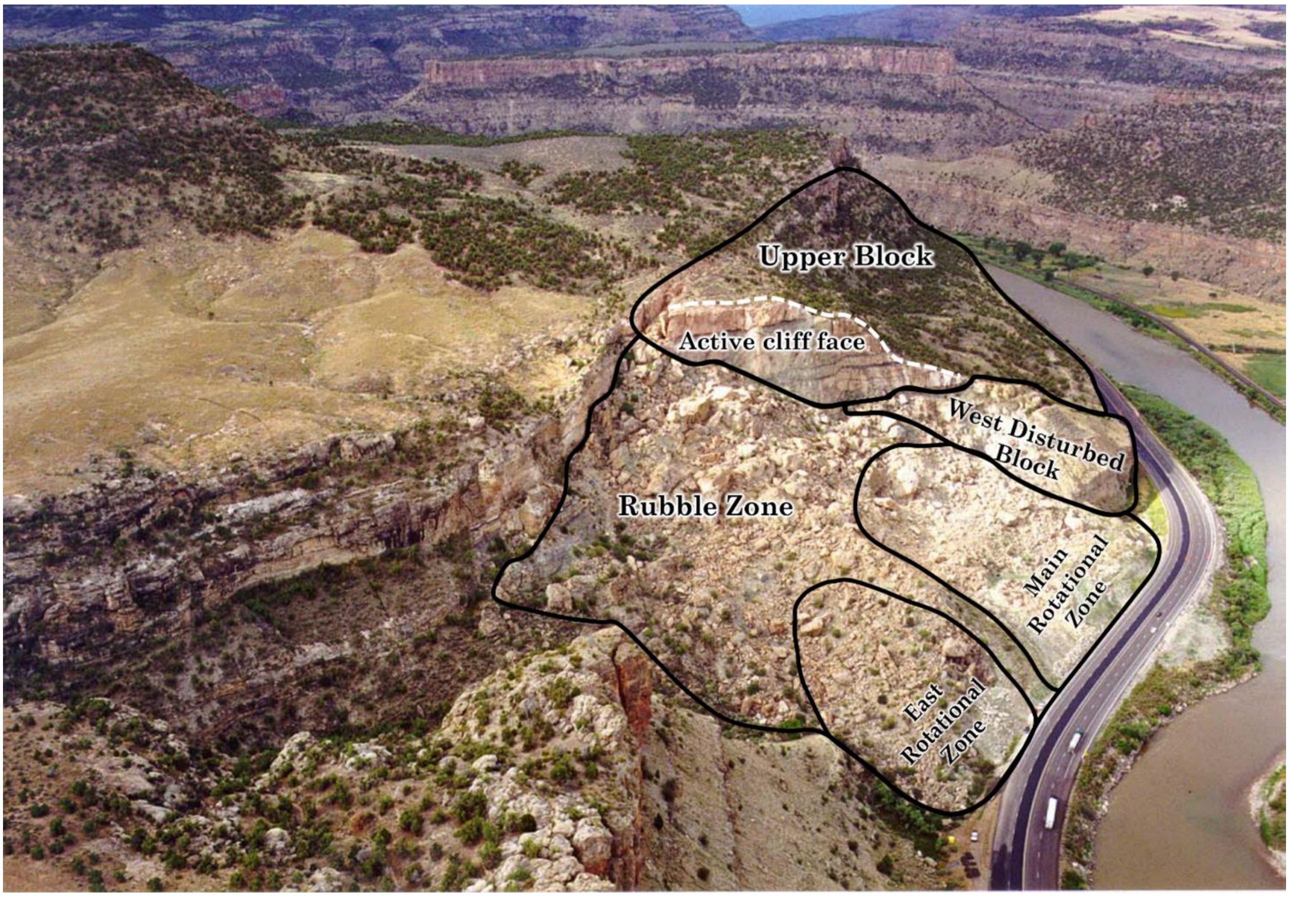

Figure 5-2: Oblique aerial view of the DCL (photo taken pointing to the west direction). The landslide system is divided into different sectors, each one characterised by distinct failure mechanisms (modified after White et al., 2003).

The geology of the DeBeque Canyon, located in the depositional basin of the Colorado Plateau, consists of the upper Mesa Verde Group, a Late Cretaceous sedimentary sequence (Figure 5-3a). This sequence was deposited in a coastal plain environment and is mainly composed of nearly horizontal interbedded layers reflecting the sea level oscillations during the transgressive and regressive cycles of the western Cretaceous Seaway shoreline [Hettinger and Kirschbaum, 2002].

The lithological alternation of prominent massive sandstone beds (up to 30 m) interbedded with less competent, thinner shale and siltstone layers [Gaffney et al., 2002; White et al., 2003; Weidner and Walton, 2020] gives the slope its peculiar step-like morphology. As reported by White et al. [2003], the stability of the DCL system appears to be significantly conditioned by the different geomechanical properties of the less competent layers overlying the sandstone bed outcropping in the proximity of Interstate 70 (Figure 5-3a). Figure 5-3b shows the geological section from the Upper

Block, intensely disrupted by a set of vertical fractures, through the Rubble Zone (characterised by a translative component of the deformations) and eventually to the Main Rotational Zone. Moreover, a fault running parallel to the headscarp contributes to compromising the rock mass stability [White et al., 2003].

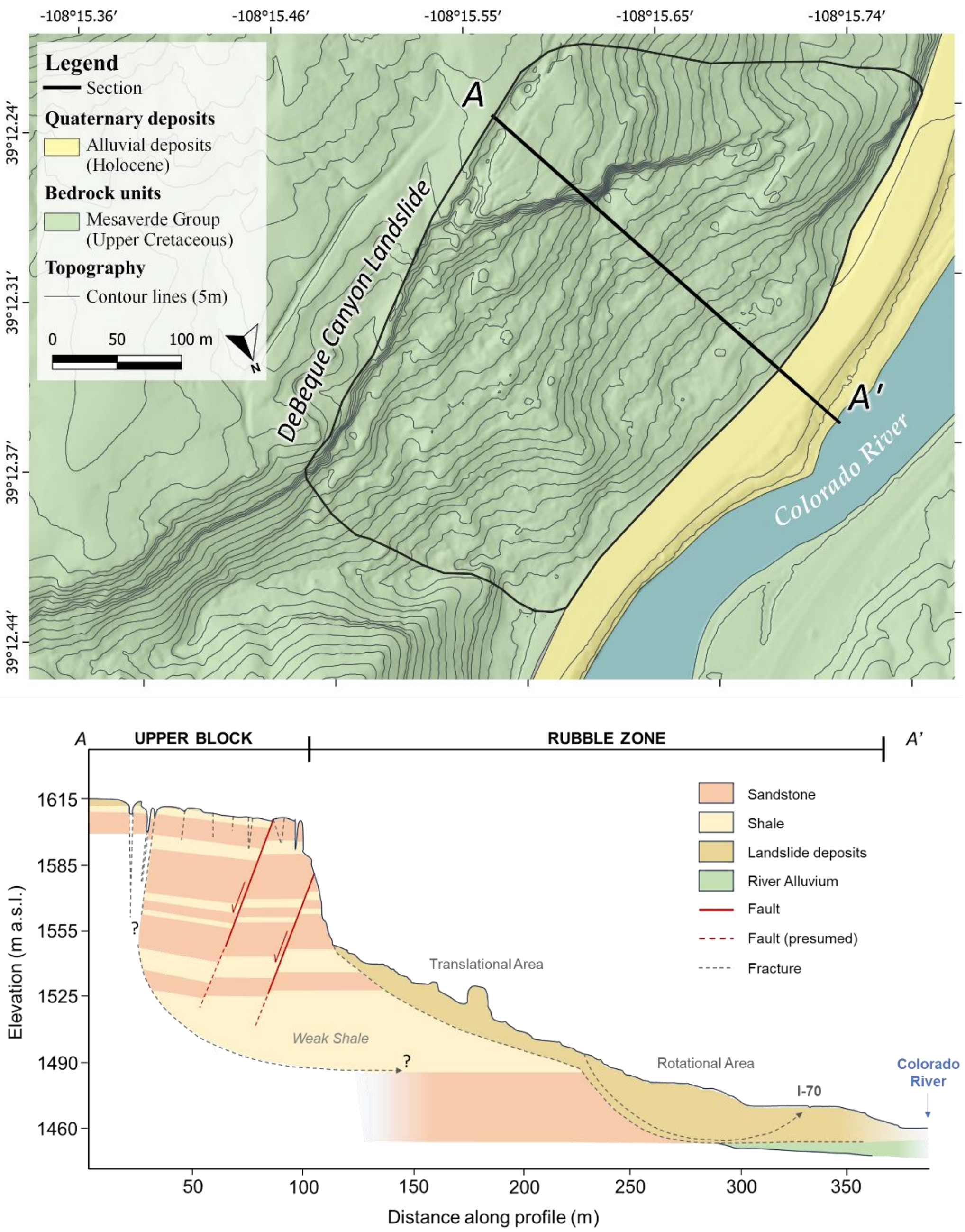

Figure 5-3: The upper panel represents the portion of the geological map at a scale of 1:100.000 (modified after Ellis and Gabaldo, 1989) relative to our study area, along with the extent of the DCL (missing in the original geological map) and mapped accordingly to White et al., 2003 and White et al., 2007. The lower panel illustrates the geological cross-section of the western part of the landslide (modified after White et al., 2003).

5.2.2 Terrain visual analysis

In this study, terrain analyses were carried out using a Digital Terrain Model (DTM) with a ground resolution equal to 1 m derived from a LiDAR survey performed within the framework of the 3D Elevation Program (3DEP). This program provides freely downloadable bare-earth models over the United States territories [U.S. Geological Survey, 2019]. The DTM used for our study area was derived in 2016. Preliminary recognition and mapping of the landforms and processes occurring along the slope were supported by the visual interpretation of hillshade maps, realised with varying sun azimuth angles, and 1 m and 5 m intervals contour lines maps, both of which were extracted using the geomorphological tools available in the QGIS 3.22 software. In addition to the DTM interpretation, freely available GoogleEarth images [GoogleEarth Pro, 2016] supported the visual recognition of the main landslide characteristics (e.g., primary and secondary scarps, reverse slopes, convex foot, surficial drainage modifications) that are clear evidence of a disrupted rock mass.

5.2.3 InSAR analysis

The quantification of the deformational motion occurring along the slope of interest has been performed through an Advanced Differential Interferometric SAR analysis (A-DInSAR). Specifically, we used the Persistent Scatterers Interferometry approach [Ferretti et al., 2001], one of the most common multi-temporal processing methods. The assessment of surficial deformations is based on the information achieved by high-coherent pixels of every acquired SAR image, including those images with large baselines [Kampes, 2006]. The fundamental improvement of this procedure is that for each high-stability pixel, called Persistent Scatterer (PS) after Ferretti et al. [2000] and Ferretti et al. [2001], the atmospheric contribution can be precisely estimated and removed, thus reducing both spatial and temporal decorrelation issues [Mazzanti et al., 2021; Moretto et al., 2021]. The dataset analysed in the SARPROZ (the SAR processing tool by Perez) software [Perissin et al., 2011] includes 129 ascending and descending Sentinel-1 imagery, spanning the 2014-2018 time interval.

The processing allowed us to estimate the average LOS velocity and the displacement time series for more than 3000 PS over the entire landslide area. Before carrying out the post-processing analysis, we filtered the dataset based on a coherence threshold fixed at 0.75 to retain only reliable and accurate measurement points. The aim of the post-processing step consisted of the in-depth characterization of the DCL system's spatio-temporal evolution. It is necessary to deepen the manipulation of the interferometric data since the display of the LOS mean velocity and its spatialization alone can offer a preliminary, partial insight.

A preliminary evaluation of the radar sensor's capability for recording displacements is decisive for assessing the ground displacement morphodynamics. Since the displacement recorded by the SAR sensor is the unidimensional average velocity along the satellite LOS projection, the actual tridimensional movement of the landslide is considerably underestimated or else, in the most unfavourable scenario, not detectable should the motion occur orthogonally to the satellite LOS. Through the C-factor computation, we can represent the percentage of ground displacement that can be recorded along the slope, taking into account both the radar signal characteristics and the terrain site-specific morphology [Notti et al., 2014].

It is calculated as follows:

$$C=[N*\cos(S)*\sin(A-1.571)]+ [E*(-1* \cos(S)*(\cos(A-1.571))+(H*\sin(S))] \tag{1}$$

where: $N = \cos(1.571-\alpha)*\cos(3.142-\theta)$;
$E = \cos(1.571-\alpha)*\cos(4.712-\theta)$; $H = \cos(\alpha)$

SAR orbital parameters are represented by the LOS velocity angles for the vertical, North and East directions (namely H, N and E), and azimuth (θ) and incidence (α) angles, while S and A represent the slope and aspect derived from the DEM. Every parameter is expressed in radians.

Starting from the combination of the ascending and descending orbital geometries, we resolved the real displacement vectors along the horizontal (East-West, Vh) and vertical (Up-Down, Vv) directions [Raspini et al., 2012; Tofani et al., 2013; Notti et al., 2014] (Figure 5-4) using the GIS-based PS-Toolbox, an A-DInSAR post-processing software developed by NHAZCA S.r.l.

The vectorial decomposition plugin needs two distinct layers for both geometries and their respective orbit parameters (i.e., heading and incidence angles) as input data. The PS are then spatially joined based on the geometric distance between neighbours and resampled into synthetic points distributed on a regular grid. Considering the ground resolution of Sentinel-1 data, we set the cell size equal to 15 m to avoid misrepresenting the effective vector motion and to avoid incorporating the contribution of PS too distant from each other. The final multi-look combination output consists of two separate layers of synthetic points regularly distributed over the study area, representing the derived Vh and Vv components. Moreover, for each synthetic PS, we obtained the bidimensional vector Vt (Fig.4), resulting from the combination of the decomposed velocity in the up-down and east-west directions according to the following formula:

$$Vt = \sqrt{Vh^2 + Vv^2} \quad (2)$$

Its respective angle τ, was also derived as:

$$\tau = \cos^{-1}(Vh/Vt) \quad (3)$$

and it represents the displacement gradient of the investigated phenomenon. Relating τ to the local slope as a difference (τ-σ), we extrapolated the local Δ gradient, which indicates the landslide's displacement direction with respect to the slope: negative values describe a displacement "out" of the slope (bulging), while positive values indicate a movement "into" the slope (subsidence). When Δ approximates to 0 (τ = slope), the landslide displacement occurs along the direction parallel to the slope (translative movement). The progressive shift from translational to rotational dynamics can be evaluated analysing the statistical distribution of the Δ gradient on the different zones [Crippa et al., 2021]. Furthermore, the differential DCL system kinematics were examined by projecting the vector Vt along profiles that intersected the most significant geomorphological elements.

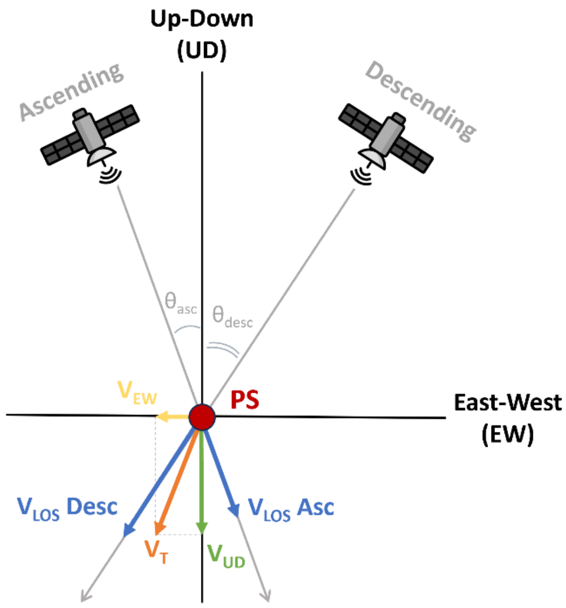

Figure 5-4: Schematic representation of the decomposed radar signal starting from the two LOS velocities (blue arrows) along the ascending and descending orbits. The vertical and horizontal components of the movement are represented in yellow and green, respectively, while the resultant Vt vector is displayed in orange.

The PS displacement time series has been utilised to assess the style of activity of the landslide and gain insights into the process temporal evolution considering its response to potential triggering and preparatory factors (i.e., precipitations and temperature variations).

For this purpose, time series displacement for the 2014-2018 period were examined using the Bayesian Estimator of Abrupt change, Seasonality and Trend (BEAST) analysis package [Zhao et al., 2019]. Time series and unidimensional data sequences are decomposed into their underlying components, such as trend or seasonal variations, and residual or random fluctuations. While conventional methods seek the best model to estimate the parameters related to seasonality and trends, the Bayesian model averaging algorithm analyses data using multiple competing models, assigning each one a probability to be the true estimator and then deriving an averaged model representing the best fit [Zhao et al., 2019]. In our analysis, the output consisted of a set of variables related to the trend's abrupt changes and their corresponding probabilities of representing authentic variations in the temporal displacement pattern.

Then, the landslide motion retrieved from the vector Vt was analysed alongside the liquid precipitation and temperature recorded by the Palisade station [Colorado Climate Center, n.d.] located in the homonymous city (Figure 5-1), and evaluated as the nearest and more complete station for the comparison between displacement and local hydrologic conditions.

The comparison of meteo-climatic and displacement datasets was conducted on two different timescales for each internal sector of the landslide and eventually to highlight differing geomechanical responses to the same predisposing and triggering factors. First, the meteorological and PS recorded movements were aggregated on weekly timesteps to assess subtle variations in the limited temporal interval covered by the interferometric analysis. Moreover, the climatic control on the rock mass was also evaluated extending the investigated period, spanning several decades and available for the Grand Junction weather station (Figure 5-1) [Zepner et al., 2020]. We thus considered the average rainfall and temperature values over the past 30 years to address the influence of the climate's long-period impact and identify potential changing trends.

5.3 Results

The present section describes the results obtained after the visual terrain analysis targeted to map the landslide's features (Section 5.3.1). Outcomes derived from the spatial and temporal PS-InSAR post-processing are examined in Section 5.3.2.

5.3.1 Geomorphological mapping

The visual interpretation of optical images and high-resolution DTM was fundamental in identifying those morphotypes related to each landslide sector. Figure 5-5 depicts a few examples of the mapped features, from a general overview of the entire system (Figure 5-5a) to specific portions of the Rubble Zone (Figure 5-5b), West Disturbed Block (Figure 5-5c) and Upper Block fissures and trenches (Figure 5-5d). As reported in Fig.6, we defined the actual delimitation of each internal sector, modifying the overall extent of the landslide body already mapped by previous authors. One of the most significant changes includes the precise delimitation of the Upper Block zone of influence, whose western border had so far been underestimated or drawn as an uncertain limit [White et al., 2003; Weidner et al., 2020]. Furthermore, the surficial geomorphological evidence of the disruption was also corroborated by the satellite SAR measurements, which captured movements in an area previously overlooked. This interpretation enabled the expansion of the Upper Block area (Figure 5-6), influenced by an ongoing and persistent deformation. Right above the landslide crown, two shaded linear features were also recognized from DTM and defined as a retrogressive scarp and a fracture. Their positioning reveals the active displacement of this part of the slope, where PS are scarce or cannot register any movements and corresponds to the retrogressive evolution of the slope instability.

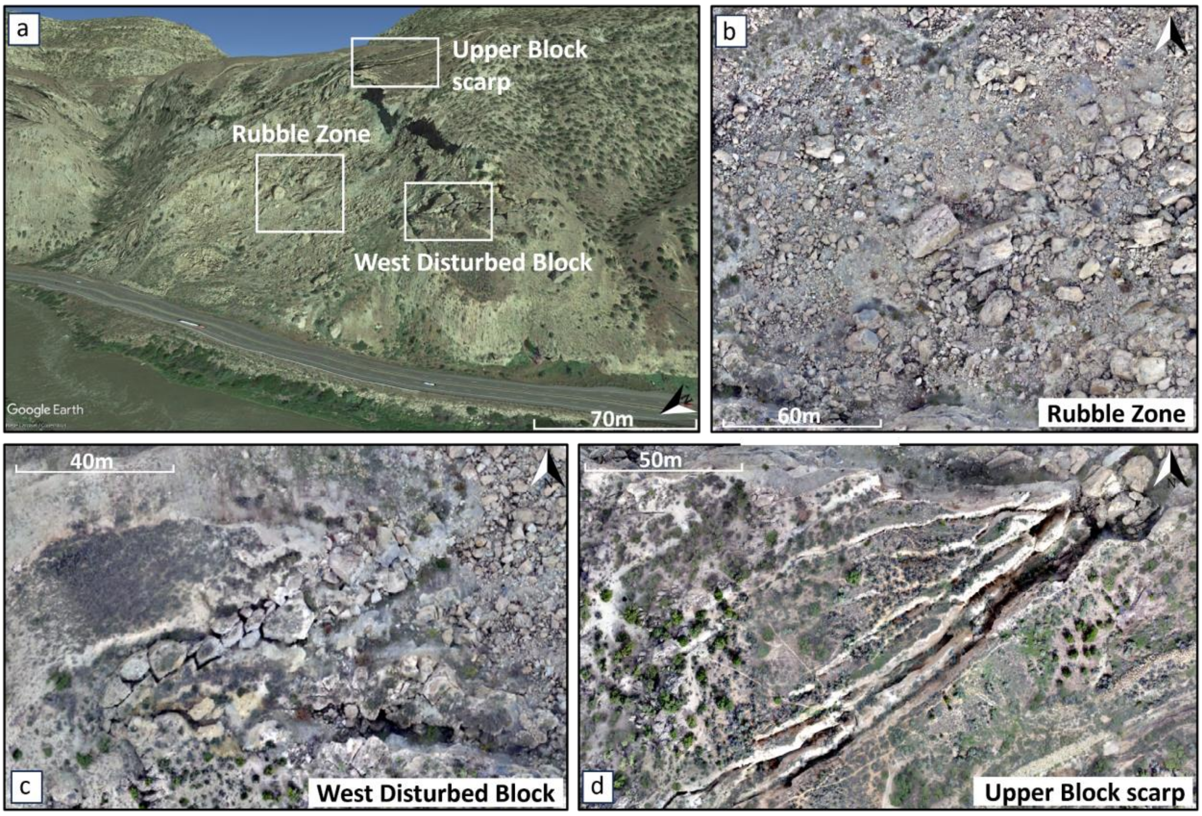

Figure 5-5: Oblique view of the DCL (panel a, image taken from GoogleEarth) and details of its surficial deposit and geomorphological features in correspondence with the Rubble Zone (b), West Disturbed Block (c) and Upper Block scarp (d).The latter three panels were modified after White et al. [2014].

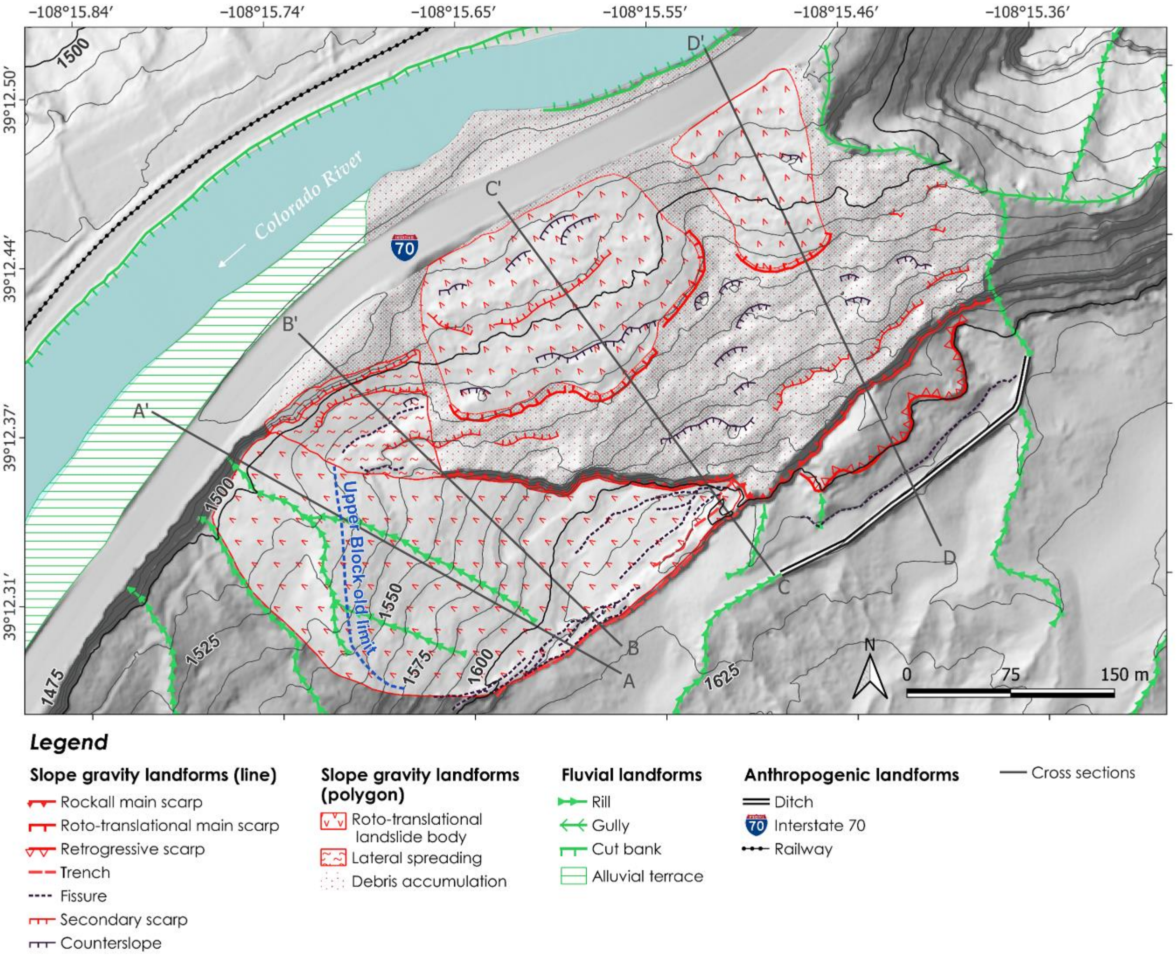

Figure 5-6: Geomorphological map of the DCL, including the previous limit (blue dotted line) of the Upper Block. Geodetic coordinate system for World (EPSG: 4326).

5.3.2 InSAR analysis

The preliminary evaluation of the recordable displacement percentage related to each of the DCL system's internal sectors is displayed in Figure 5-7 in the form of C factor mean values. The obtained C values differ depending on the acquisition orbital geometry and are lower in ascending geometry than in descending one. Considering that the resulting values range on average above 60%, the surficial deformation could be considered close, even if not entirely, to the total movement recordable by the satellite SAR sensor.

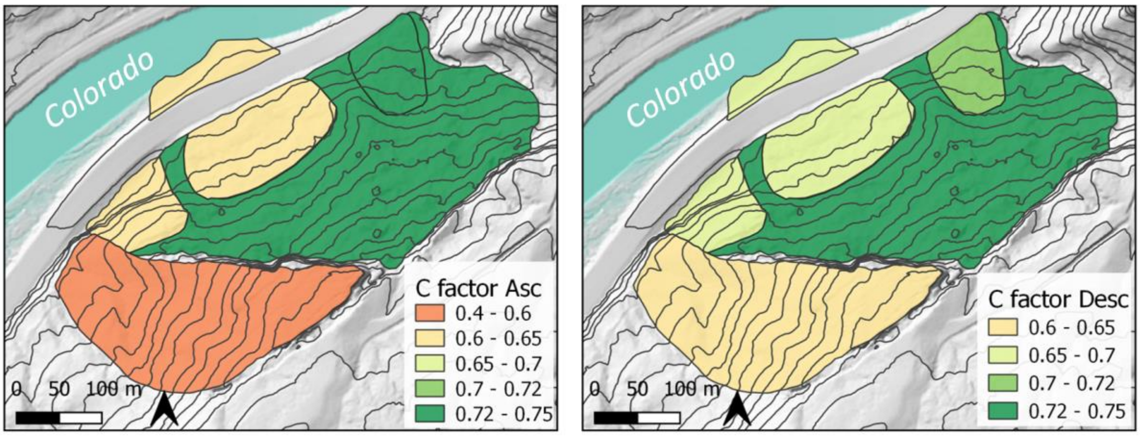

Figure 5-7: Maps showing C-factor calculated for the ascending (left panel) and descending (right panel) geometries. Each landslide's sector is coloured based on the averaged C-factor, expressed in percentage, for the respective area.

Figure 5-8a and Figure 5-8b demonstrate how incorporating ground motion information from PS data assisted in identifying different kinematics associated with each of the internal sectors of a landslide system. The analysis revealed that a significant portion of the slope is involved in the progressive deformation of the rock mass and that this actively deforming area is broader compared to what previous literature reported.

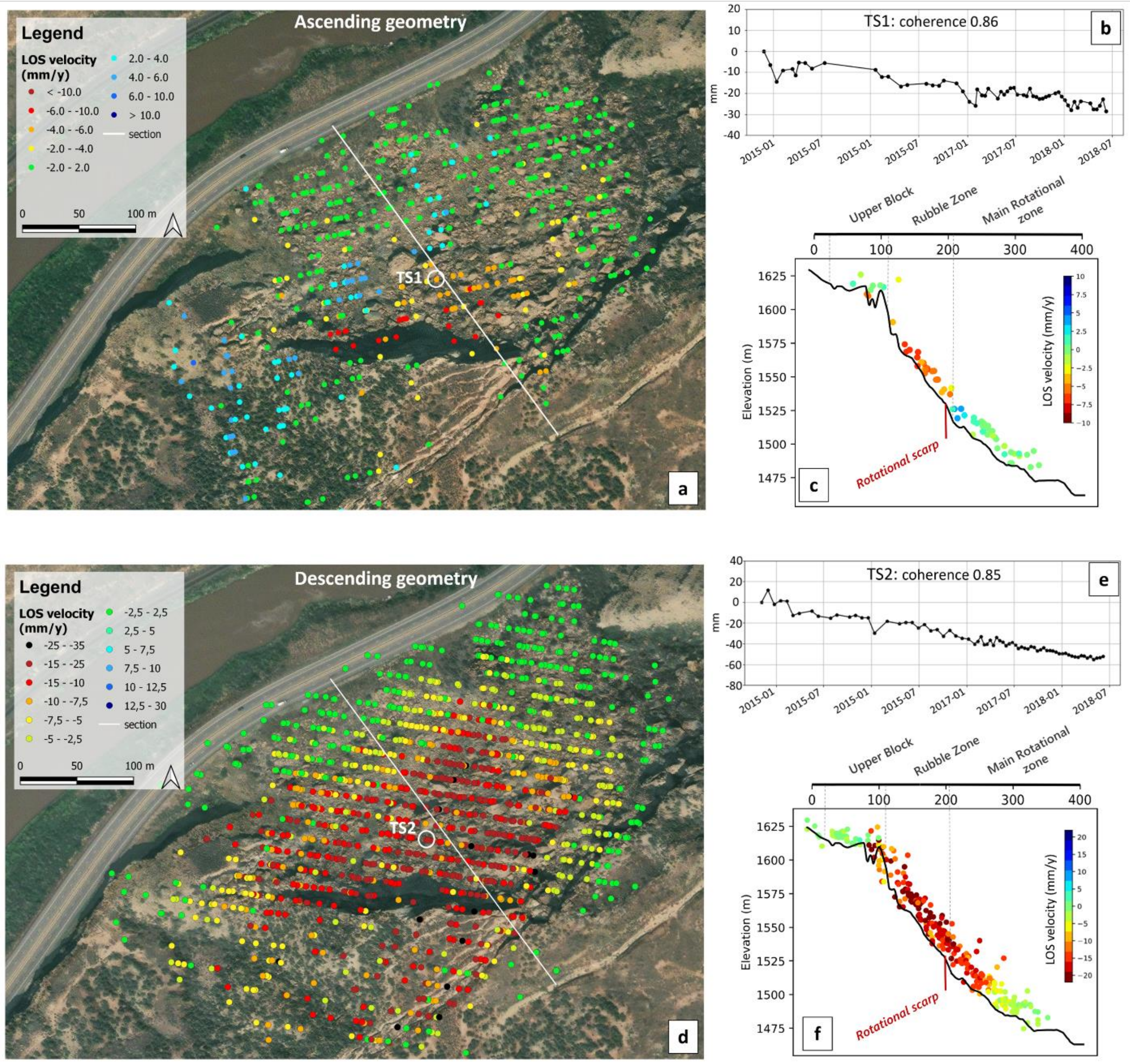

Figure 5-8: Panels a) and d) represent the PS distribution over the DCL extension for the ascending geometry and descending geometries. Each one of these two main panels is accompanied by a representative time series (panels b and e) and cross section (c and f), the latter one displaying the PS projected along the topographic profile and the landslide body sections of Upper Block, Rubble Zone and Main Rotational Zone.

The recorded velocity ranges for the ascending geometry is significantly lower compared to the descending one. The Rubble Zone is predominantly characterised by negative displacement values, ranging between -5 and -7.5 mm/y, and locally measuring velocities up to 10 mm/y at the bottom of the Active cliff face of the DCL. The negative values of this cluster undergo an abrupt trend shift in correspondence with the Main Rotational scarp, where the velocity values switch to +5 mm/y. The same trend is recorded along the Upper Block's body, even if the presence of vegetation partly disguises the rock outcrop, thus reducing the PS density with respect to the contiguous areas. Moreover, considering the lower values of the C factor in the ascending geometry, the LOS velocity information measured in the descending geometry was preferred to avoid underestimating the actual extent of the deforming area. Displacements recorded in the latter orbit cover a greater area and are characterised by larger ranges than the ascending one, where peaks of over 25 mm/y are observed. Displacement values range on an average of -10/-15 mm/y, principally covering the central portion of the Rubble Zone and the top of the Upper Block. Clusters of -15 to -25 mm/y characterise the eastern part of the Main Rotational Zone and the Rubble Zone. This heavily deforming core gradually fades towards lower displacement values through the Main and East Rotational bodies, as well as at the Upper Block's foot.

The time series of PS, representative of the landslide central sector's displacements and visualised (Figure 5-8b and Figure 5-8e), exhibits a trend without clear evidence of sudden accelerations or abrupt changes in both geometries. Specifically, in the ascending geometry, during the interval covering the second half of 2016, the available images are limited and display significant temporal gaps. Conversely, the time series in the descending geometry shows a more evenly distributed set of images throughout the entire temporal interval, with no significant interruptions.

The PS data has been further refined through a meticulous post-processing analysis aimed at discriminating, from a spatial point of view, the kinematics of the distinct gravitational processes superimposed within the landslide system. The vectorial decomposition outcomes are illustrated in Figure 5-9a and Figure 5-9b.

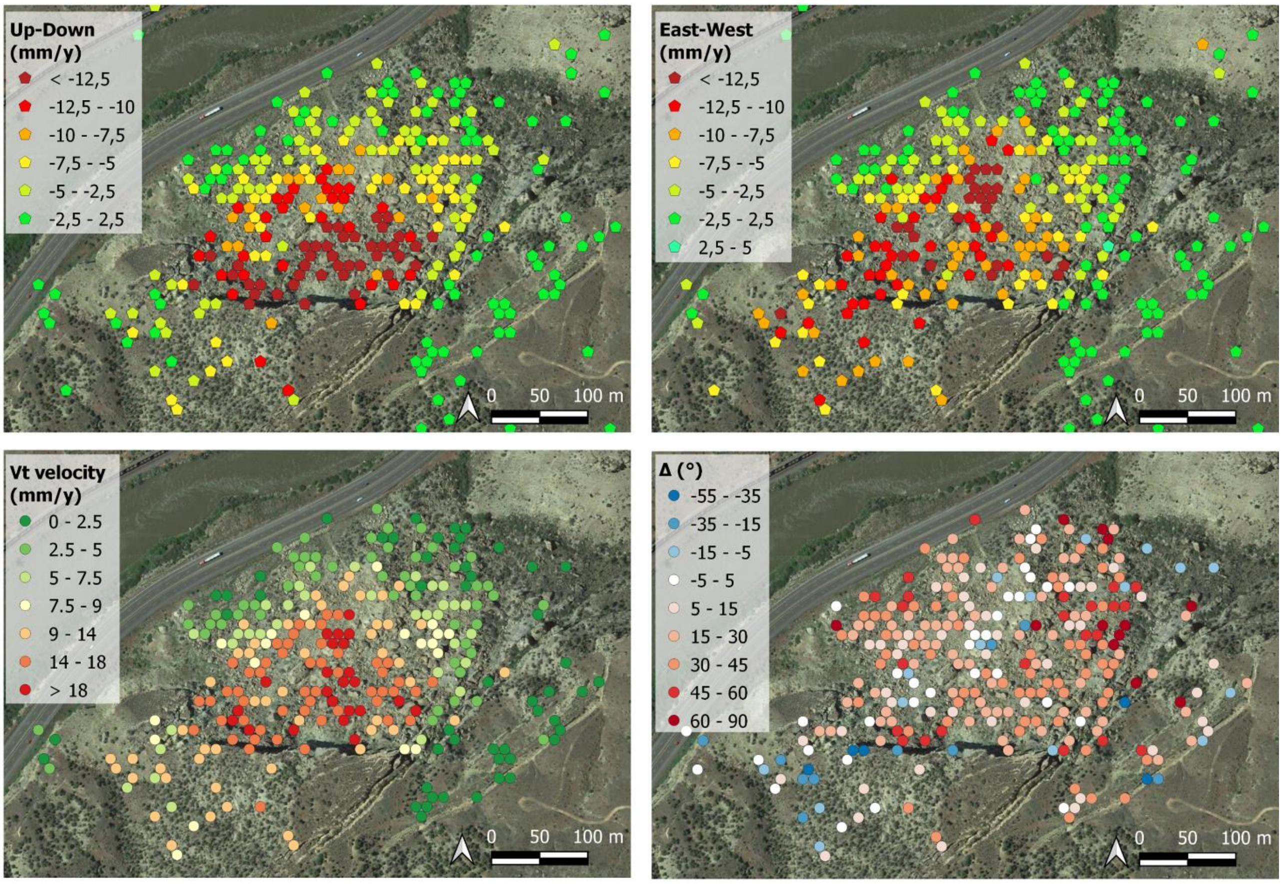

Figure 5-9: PS-InSAR velocity decomposition. a) Visualization of the decomposed velocity along the vertical direction (colours towards red shades represent subsiding movement); b) Visualization of the decomposed velocity along the horizontal direction (colours towards red shades represent movement to the east, light blue to west); c) representation of vector Vt; d) representation of the difference between vector Vt and local slope gradient as Δ (expressed in degrees).

The Rubble Zone shows a strong vertical component (<-12.5 mm/y) and minor displacement rates towards the east direction (recorded movements reach up to -12.5 mm/y for a few synthetic points). Similarly, the East and Main Rotational Zones' deformation is greater along the vertical direction than the horizontal one, except for two point clusters located at the opposite eastern and western boundary of the latter area, recording velocities exceeding -12 mm/y. The Upper Block is the only sector experiencing marked horizontal displacements. From the combination of the decomposed multi-geometry datasets, we obtained the bidimensional vector Vt and the related delta gradient, expressing the connection between the landslide movement and the local topography (Figure 5-9c). We can notice how the Δ distribution changes over the DCL, shifting from negative and null ($-5° < \Delta < 5°$) values retrieved in the Upper Block to predominantly positive values through the rest of the sectors. Almost the entire DCL body exhibits a strong downward movement, while the Upper Block is the only isolated sector displaying movements parallel to the surface topography and, in its lower part, with a bulging component (Figure 5-9d).

The frequency distribution examination led to a more precise assessment of the multimodal distribution of the LOS velocity, with respect to that previously estimated through visual analysis. Whenever the distribution displays a relevant peak, a distinct PS cluster is identified for that specific velocity interval; a marked segmentation of the process kinematics thus corresponds to several peaks in the distribution curve. The frequency distribution of the ascending geometry is strongly peaked around zero, yet showing a slight asymmetry towards negative velocity values, where a second, modest peak is located at -10mm/y (Figure 5-10a). At approximately +-4 mm/y, two other inflections are detected, identifying the clustering of the PS around these velocity values. On the contrary, the descending frequency distribution shows an unequivocal multimodal curve (Figure 5-10b), including two peaks at around -4 and -18 mm/y, and a less evident inflection centred at -10 mm/y. To isolate each contribution of the overlapping kinematics and integrate the information of the multi-geometry InSAR analysis, we exploited the displacement rate vector Vt and its correlated angular parameters. As different roto-translational dynamics produce peculiar surface geomorphic expressions, the relationship between recorded displacement rates and local topography must be considered. For this purpose, we evaluated the Δ gradient distribution for the Rubble Zone, Upper Block, and Main and East Rotational zones (Figure 5-10c). Since Δ represents the difference between the phenomenon movement direction and the local slope inclination, its value is a straightforward expression of translative kinematics, whether they include bulging or subsiding components or are perfectly parallel to the slope. Figure 5-10c illustrates the four distinct distributions along with the averaged DCL curve. From the statistical analysis of Δ we can notice that the frequency curves are all centred between 20 and 40° except for the Upper Block, which diverges from the other zones exhibiting a peak around zero.

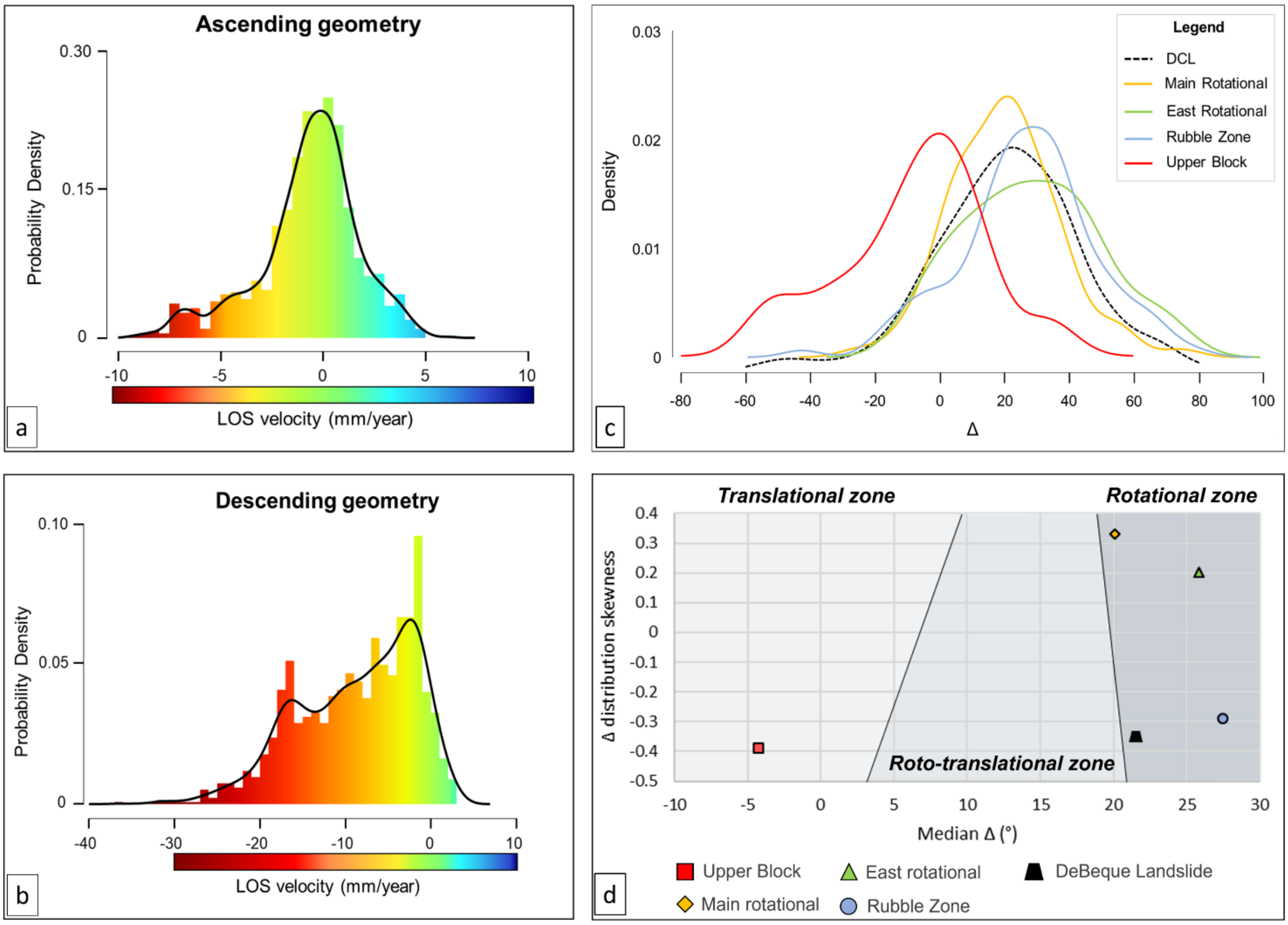

Figure 5-10: Results from the spatial post-processing analysis for the differential kinematic characterisation of the DCL are shown in this picture. Panels a) and b) display the distribution of the ascending and descending LOS velocity for the whole DCL area. Panel c) Δ distribution; panel d) landslide sectors' classification based on Δ skewness and median parameters (boundaries separating translational and rotational zones based on Crippa et al., 2021).

The diverging trend implies that the Upper Block is the only zone that is represented by a plain translational movement due to Δ values approximating zero (and therefore retaining more frequent motions along the slope inclination). Surprisingly, along with the Main and East Rotational Zones, the Rubble Zone itself displays an evident rotational kinematic component, even if another smaller inflection is identified around zero along the left tail. To discriminate the predominant failure mechanism among the full spectrum of kinematics, ranging from translational to rotational movements, we exploited the median and skewness parameters as a measure of the Δ distributions' diversity (Figure 5-10d). Negative values of both median and skewness parameters isolate the Upper Block in the translational domain of the chart, while purely rotational phenomena occupy the first quadrant of the diagram. Instead, despite falling within the rotational domain, Rubble Zone and DCL share high median values (greater than 20°) and asymmetric curves (negative skewness).

In addition to the statistical analysis of Δ, we examined the displacement bidimensional vector Vt for each of the landslide's sectors for better visualising the differential kinematics throughout the whole instability extent. The inclination and absolute value of Vt were projected considering four 30m-wide swath profiles crossing the aforementioned zones (Figure 5-11).

The majority of the synthetic PSs projected along the Upper Block's swath profile (Figure 5-11a) displays an along-slope movement direction, confirming the predominance of the translative component of the displacement.

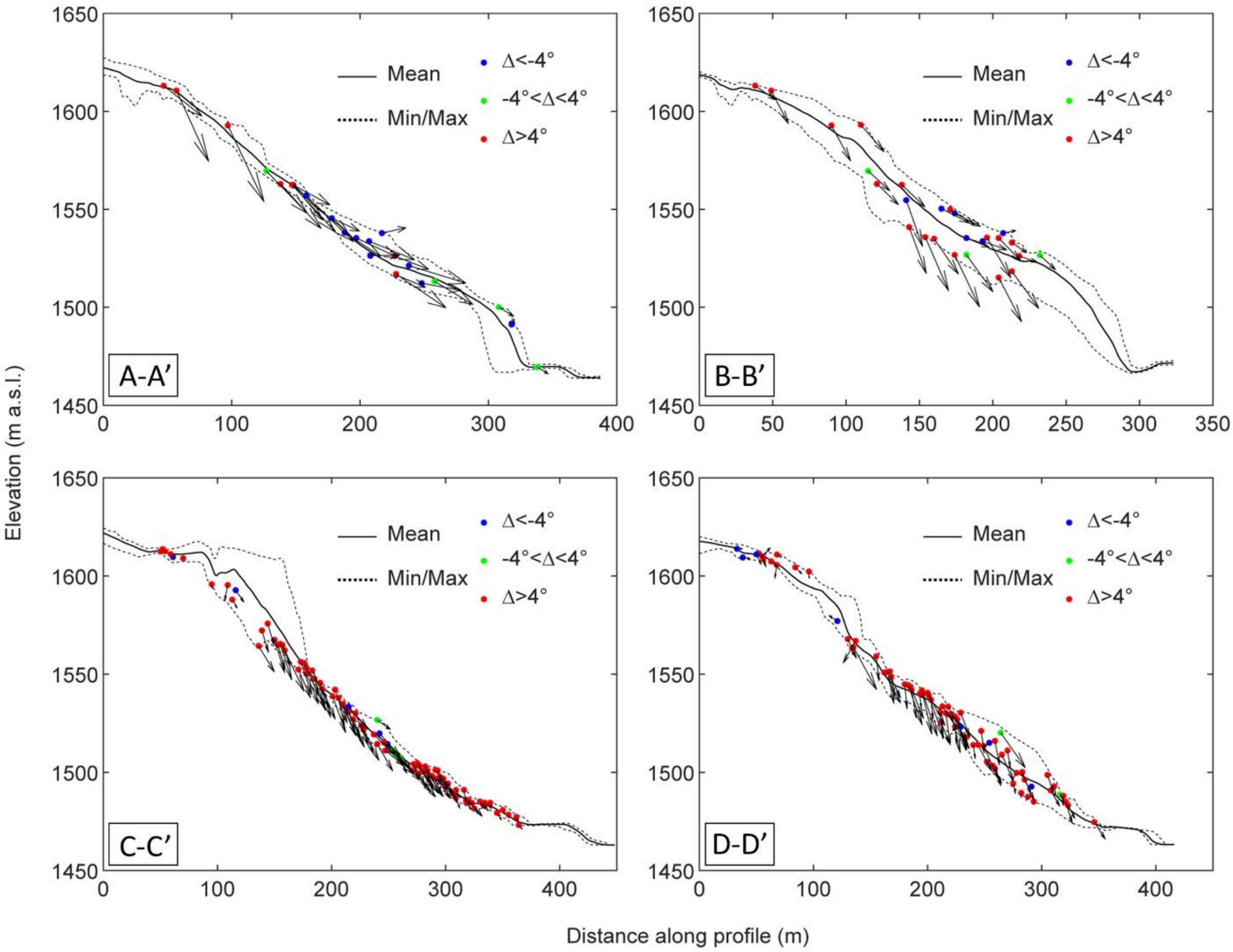

Figure 5-11: Projection of the synthetic PS along four different mean (black continuous lines), minimum and maximum (dotted) topographic profiles displayed in Fig.5 and intersecting: a) the Upper Block; b) the Upper Block and West Disturbed Block; c) the Main Rotational Zone; and d) the East Rotational Zone. For each synthetic point, its bi-dimensional vector Vt and Δ values are respectively displayed by an arrow (whose length is proportional to Vt modulus) and categorised with respect to negative (<-4°), positive (>4°) and circa null Δ values (-4°< Δ <4°).

The profile of Figure 5-11b, starting from the top of the Upper Block and crossing the West Disturbed Block, exhibits a bimodal trend of Vt gradients, with a sharp shift localised at around 150 m distance along the profile. Even if the synthetic points are scarce, we can notice that the upper portion still preserves an along-slope (or slightly inward) orientation, typical of the Upper Block dynamics. The turning point of the vector orientation is located around half the cross-section, where the arrows start dipping in the slope (positive Δ). The last two cross-sections represent the Main (Figure 5-11c) and East Rotational Zones (Figure 5-11d), respectively. The two representations show that most points share positive delta values, strongly dipping inward in the upper and central part of the slope. Instead, at the foot of the two landslides delta values gradually decrease and the Vt vector orientation becomes almost parallel to the slope.

Figure 5-12 shows the results of the temporal characterisation of the landslide system deformational pattern.

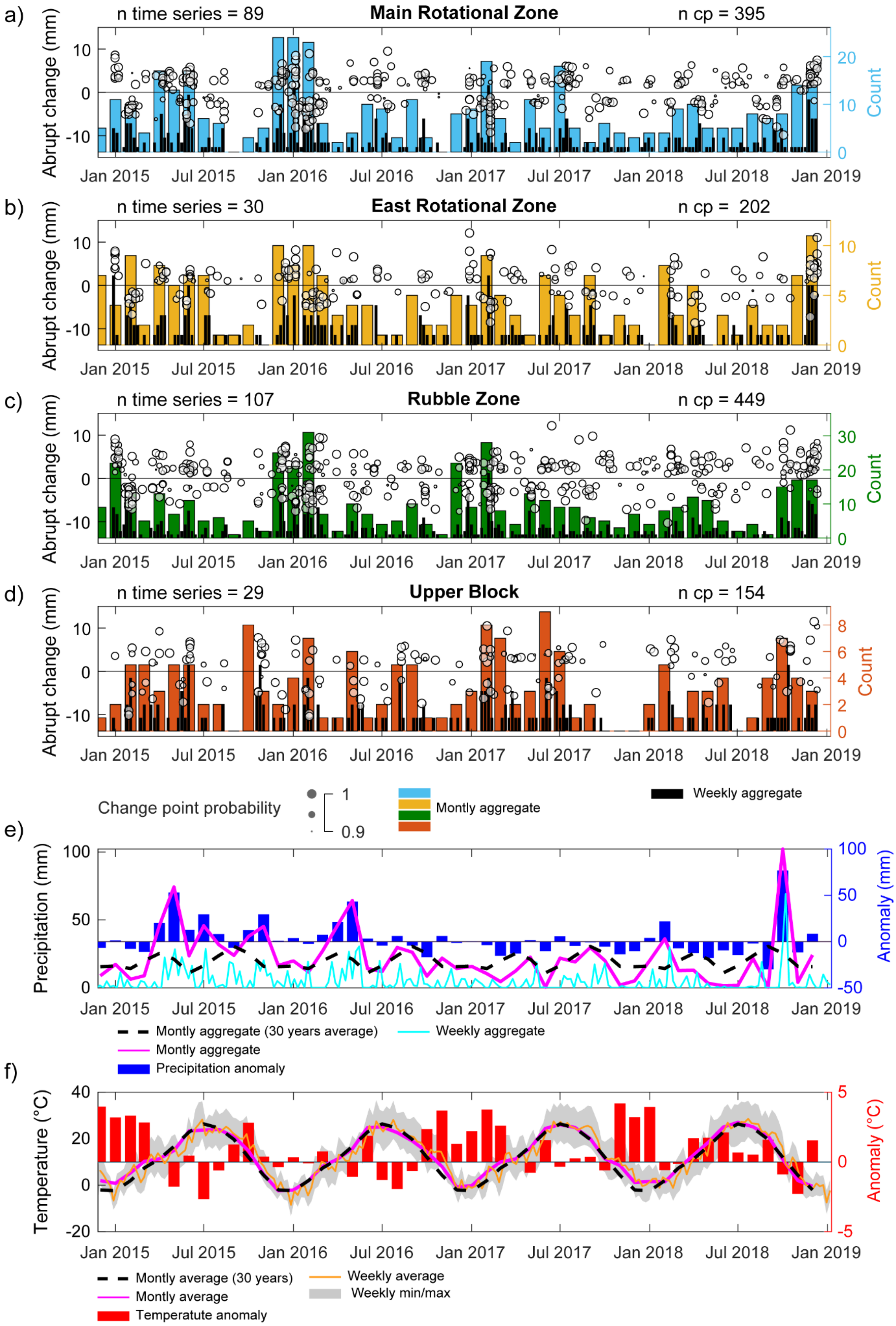

Figure 5-12: Trend change detection results for the four different sectors of the landslide system (panels a-d). For each time series, abrupt changes exceeding a 0.9 probability of occurrence threshold are displayed as black circles, while abrupt change counts are represented on a weekly (black bars) and monthly basis (colored bars). Daily precipitation and temperature values are shown as weekly and monthly aggregate or average, respectively, in panel e) and panel f), along with their respective 30-year trends and related anomalies (blue and red bars).

Specifically, a-d plots refer to different system sectors and display abrupt changes with a probability of occurrence greater than 90% and relative counting (on a weekly and monthly basis) for the analyzed time interval (2015-2018). Considerable clustering of such abrupt changes reveals that most time series records acceleration trends with similar timings.

A comparative examination of the plots revealed similar trends for the Main Rotational, East Rotational, and Rubble Zones. In particular, all three zones exhibit changes in the displacement rate during the December-February interval of 2016, 2017, and 2019 years and, to a lesser extent, also in the same period of 2015. In these periods (December-March), the average temperature over 30 years fluctuates between +4°C and -2°C. No clear correspondence with the positive temperature anomalies observed during 2015, 2017, and 2018 was observed.

Conversely, the Upper Block displays abrupt changes recorded in the trend at the end of winter (February-March) of the same years except for 2019. During these time frames, the average temperature over 30 years fluctuates between +2°C and -2°C. In addition to the mentioned acceleration stages, other occasional variations within the trend were recorded in correspondence with exceptionally rainy months. For instance, during the April-June 2015 and 2016 rainfall anomalies, all sectors indicated displacement evidence, especially the Upper Block. Similarly, during the June-July 2017 period, significant acceleration is noticed even without monthly precipitation anomalies as those recorded in 2015 and 2016. Moreover, the Upper Block displayed abrupt trend changes during the October-November period of 2015 and 2018. October 2018 is the month when the most intense rainfalls occurred (and, consequently, the one with the highest recorded anomaly), followed by May 2015 and May 2016. For each of these periods, the Upper Block exhibits significant displacements, less pronounced in the other sectors.

5.4 Discussion

When approaching landslide systems characterization, it is critical to consider the single contribution of every phenomenon composing this aggregation. Even if the disruption caused by these mass movements has slow displacement rates, the persistent deformation of the slope and the progressive evolution of depletion and accumulation zones need to be considered. By post-processing the InSAR information, we have shown that we can discriminate the variability of the displacement pattern that characterizes the different sectors, highlighting the intrinsic spatial heterogeneity and asynchronous response to external stresses (both impulsive and prolonged in time).

In this regard, the opportunity offered by the satellite multi-looking combination granted the accurate investigation of each cluster's displacement component along the actual movement direction instead of the sensor's line of sight. Few attempts in literature focused on unravelling landslides' heterogeneous morphodynamics based on SAR multilooking displacement decomposition. However, these methodologies have thus far been exclusively applied for spatial analysis, overlooking temporal information and neglecting implications related to the examination of preparatory and triggering factors. Crippa et al. [2021] quantified the landslide internal heterogeneity for regional-scale classification purposes implying the necessity of embracing a more generalized assumption when considering landslide segmentation across extensive areas. Conversely, Eriksen et al. [2017] exploited the vectorial decomposition for identifying complex deformations displacement patterns at the local scale yet avoiding proposing a detailed internal subdivision of the processes constituting the landslide system.

5.4.1 DeBeque Landslide System case study

New insights on the classification of the DCL's different failure mechanisms were derived from a remote perspective from both the spatial and temporal points of view. We show how different dips of the displacement vector with respect to the slope gradient reflect the shift from translational (i.e., the Upper Block) to rotational slides (i.e., Main and East Rotational Zone). The Upper Block is the only example of a translational landslide within this system, and for which the Vt vectors indicate a marked displacement component parallel to the slope, except for the rock wedge located in its upper portion, bounded by trench and fractures. This peculiar behaviour is detectable even along the B-B' profile (Figure 5-11b): from an almost parallel (or at least slightly inclined) motion along the slope, the deformation direction shifts to dipping inward the slope when reaching the West Disturbed Block, for which the displacement has a considerable vertical component (Figure 5-11b).

Moreover, our data suggests a different interpretation of the Rubble Zone kinematics with respect to the model adopted up to this point [White et al. 2005, Weidner 2020, Weidner et al., 2020]. Indeed, the authors indicate a translational movement along a 30 m deep shear zone parallel to the slope, while surface displacements exhibit a marked subsiding component, discernible through the Vt projection along the cross-sections (C-C′ and D-D′). The Rubble Zone's vectors are strongly oriented inside the slope instead of lining up parallel to it (such as for the Upper Block). In these two profiles, the vectors of the Rubble Zone maintain an orientation very similar to those located within the Main and East Rotational landslide, characterised exclusively by a rotational kinematic component, and for which the vectors gradually become less inclined due to the bulging effect towards the foot of the landslides. We can infer the peculiar behaviour of the Rubble Zone even from the Δ gradient diagram (Figure 5-7d), which share more similar statistical parameter to the whole DCL landslide system than to one of the two end-members of the spectrum (i.e., pure translational or rotational behaviour). We could interpret this outcome as a suggestion that the Rubble Zone kinematic could fall within a "transition domain" with fuzzy thresholds, and thus be represented by a mix of roto-translative components.

Furthermore, we delved into the temporal aspect of the Vt vector by comparing displacement time series with meteorological and climatic factors. There seems to be a notable correlation between the temperatures during the coldest months (December-March) and the displacements, particularly in the Main, East, and Rubble Zones. Conversely, the deformation response in the Upper Block aligns more closely with precipitation anomalies. This distinctive system response can be interpreted as a consequence of varying deformative evolutionary stages: the Main, East, and Rubble Zones exhibit advanced evolution, while the Upper Block is still experiencing ongoing deformation. Specifically, rock mass fracturing, more pronounced in advanced evolutionary stages, plays a significant role during thermal expansion-contraction cycles that induce both the growth of pre-existing cracks and the genesis of new ones [Grechi et al., 2021]. Nevertheless, to substantiate this hypothesis, a more comprehensive study is essential to gain a detailed understanding of the underground dynamics of the system.

5.5 Conclusions

Assessing the internal segmentation that slow-moving landslide systems experience under persistent stress and differential deformation can lead to the identification of potential collapse scenarios of one or more sectors that are part of this system. In addition, understanding the impact of conditioning factors on each sector of the main landslide is valuable for evaluating the heterogeneous displacement pattern from a temporal perspective. Both assessments represent a critical point in the design of mitigation measures when considering the potential asynchronous reactivation of different portions of the landslide and, therefore, carefully planning solutions to be adapted to individual dynamic and temporal evolution.

The combination of high-resolution topographic information and satellite data allowed us to precisely update and delimit the actual deformational extent of the entire landslide, so far partially underestimated. We presented a reproducible method that can be used in combination with in-situ measurements or as a self-stand method for the assessment of the heterogeneous spatio-temporal displacement pattern of landslide systems. Our findings demonstrate how interferometric data can discriminate between the different processes involved in the progressive destabilisation of the DCL, characterised by dynamic disruptions with differential movements and seasonal acceleration timing. The fundamental conclusions are summarised as follows:

1. Precise identification of different kinematics characterising the landslide system was accomplished through SAR-derived bidimensional displacement components, obtained by exploiting the satellite multi-look acquisition mode. In particular, statistical variables associated with the 2D vector were analysed to distinguish rotational or translational components of the landslide movement solely using surface displacement measures.
2. The 2D vector time series were decomposed through a Bayesian model and correlated with meteo-climatic factors (i.e., precipitation and temperature) to identify changes in the deformational trend of each sector. Main acceleration stages were found for the Rubble Zone, Main and East Rotational Zones mainly during winter periods, while the Upper Block acceleration stages seem more correlated to precipitation anomalies.

Finally, a more detailed understanding of the spatial and temporal dynamics of landslide systems lays the foundation for more accurate multi-hazard scenario studies.

6 Multi-Sensor and Multi-Scale Remote Sensing Approach for Assessing Slope Instability along Transportation Corridors Using Satellites and Uncrewed Aircraft Systems

Extracted from *Zocchi et al. Multi-Sensor and Multi-Scale Remote Sensing Approach for Assessing Slope Instability along Transportation Corridors Using Satellites and Uncrewed Aircraft Systems. Remote Sensing,* ***2023****, 15.12: 3016.*

Abstract

Rapid slope instabilities (i.e., rockfalls) involving highway networks in mountainous areas pose a threat to facilities, settlements, and life, thus representing a challenge for asset management plans. To identify different morphological expressions of degradation processes that lead to rock mass destabilisation, we combined satellite and uncrewed aircraft system (UAS)-based products over two study sites along the State Highway 133 sector near Paonia Reservoir, Colorado (USA). Along with a PS-InSAR analysis covering the 2017–2021 interval, a high-resolution dataset composed of optical, thermal, and multispectral imagery was systematically acquired during two UAS surveys in September 2021 and June 2022. After a pre-processing step including georeferencing and orthorectification, the final products were processed through object-based multispectral classification and change detection analysis for highlighting moisture or lithological variations and for identifying areas more susceptible to deterioration and detachments at the small and micro-scale. The PS-InSAR analysis, on the other hand, provided multi-temporal information at the catchment scale and assisted in understanding the large-scale morpho-evolution of the displacements. This synergic combination offered a multi-scale perspective of the superimposed imprints of denudation and mass-wasting processes occurring on the study site, leading to the detection of evidence and/or early precursors of rock collapses, and effectively supporting asset management maintenance practices.

Keywords: rock slope instabilities; UAS; InSAR; multi-scale; instabilities; early precursors; erosion processes; asset management plan

6.1 Introduction

Slope instabilities, especially along transportation corridors in mountainous areas, pose a threat to facilities, settlements, and life [Agliardi et al., 2003; Martino et al., 2009]. According to the United States Geological Survey (USGS), the destruction caused due to landslides, in general, results in 25 to 50 deaths per year and costs an excess of $1 Billion in damages in the United States alone, [Landslides 101, USGS]. With the increasing population and demand for advanced infrastructure, it is crucial to assess mass wasting hazards and manage the associated risks for maintaining transportation corridors safety [Lato et al., 2015; Arpin and Arndt, 2016]. Among the recurrent mass movements involving highway networks, rockfalls are among the most hazardous types. Despite the often limited volumes of rockfalls, their high energy and velocity, as well as their frequency, make them a major cause of mass wasting fatalities [Guzzetti, 2000; Crosta and Agliardi, 2003;

Piacentini et al., 2014]. Several geomorphic processes (including thermic cycles, progressive weathering of rock materials and water infiltration) control the mechanical properties and the degradation state of the rock mass, therefore influencing its overall stability [Crosta and Agliardi, 2003, Moore and Sanders, 2009; Karir et al., 2022]. Conventional methods of rockfall hazard assessment involve rigorous fieldwork where quantitative measurements (e.g., spacing, density and orientation of fractures) and qualitative evaluations (e.g., recent detachments and potential sources of future failures) are addressed [Arpin and Arndt, 2016]. Although these in-situ point measurements can effectively assist the prediction of slope stability with high precision, they are time-consuming, have limited spatial extent, and can be expensive. Unprecedented opportunities derive from the extensive use of remote sensing methods, which facilitate an efficient, cost-effective and safe assessment of the slope pre-failure conditions. Remote sensing-based data come in a wide range of platforms (*e.g.*, spaceborne and airborne), spatio-temporal, and radiometric resolutions [Khorram et al., 2012]. At a large scale, satellite Synthetic Aperture Radar Interferometry (InSAR) enables the precise monitoring of ground deformations over tens of square kilometres. InSAR analysis thus represents one of the best instruments for creating regional-scale slope instabilities inventories [Rosi et al., 2018; Dini et al., 2019] and relative susceptibility maps ([ussain et al., 2021; Yuan and Chen, 2022]. However, due to the line-of-sight acquisition mode of the satellite sensors, geometric distortions like shadowing effects may limit the capacity of this method to effectively investigate vertical slopes. Recent developments in Uncrewed Aircraft Systems (UAS) include their capacity of carrying multiple sensors, fly on-demand at specific times, orient the sensor's look angle based on the topography characteristics, and the possibility to achieve ultra-high-resolution information (1-20cm) for precise morphodynamic characterization of processes and landforms [Lucieer et al., 2013]. These practical advantages are optimal for the rockmass stability evaluation, and were successfully exploited by previous studies through classification systems such as the Slope and Rock Mass Rating [Wang et al., 2022; Ismail et al., 2022a; Filice et al., 2022]; realisation of tridimensional models for mapping geomechanical properties [Robiati et al., 2019; Stead et al., 2019; Devoto et al., 2020; Ismail et al., 2022b] or for stability analysis, hazard and risk modelling [Gantimurova et al., 2021; Konstantinidiset al., 2021; Udin et al., 2019; Wang et al., 2019; Robiati et al., 2023]; exploitation of multispectral and hyperspectral sensors for landslide susceptibility assessment and detailed analysis of the slope's lithological and moisture conditions [Lin et al., 2016; He and Barton, 2019; Frodella et al., 2017]. In particular, the scientific community is dedicating its efforts to identifying early precursor signals indicative of instability events or studying the temporal morphoevolution of block and debris detachments exploiting topographic models and quantitative geomechanical characterization of the rock masses. The progressive creep, deformation and micro-tremors are clear indicators of the ongoing disruption of the slope stability, therefore standing as the primary goal for a comprehensive assessment of rockfall hazard. Most of the previous literature so far lies with the application of terrestrial-based technologies, such as Terrestrial Laser Scanner (TLS) [Abellán et al., 2010; Royán et al., 2014; Kromer et al., 2015; Farmakis et al., 2020; Núñez-Andrés et al., 2023] or Terrestrial InSAR platforms (TInSAR) [Carlà et al., 2019; Romeo et al., 2021] to identify pre-failure information. Despite the numerous advantages and exceptional precision of these techniques, however, several challenges arise due to the high costs and logistical constraints (linked to the positioning of the instrumentation and the lack of data in shaded areas). Also in this case, the versatility of UAS sensors and platforms renders them an efficient (yet far from being fully exploited) alternative for evaluating the early precursor of rock destabilisation through topographic models [Graber and Santi, 2023]. Several authors [Sarro et al., 2018; Francioni et al., 2020; Gallo et al., 2019; Žabota et al., 2023] analysed the predominant discontinuities through UAS-based structure from motion (SfM) photogrammetry techniques to estimate average block sizes and determine their simulated run-out. A multi-scale approach consisting of the creation of different Digital Surface Models of the slope along a road was adopted by Migliazza et al. [2021]. Statistically representative geometrical data for the discontinuities of the rock mass were obtained to eventually define the possible kinematic mechanisms and volumes of potentially detachable blocks. To determine potentially unstable rock volumes and provide the magnitude of future rockfalls, geometrical and geomechanical properties of the main sets of discontinuities and joints of the rock mass were extracted by Rodriguez et al. [2020] and Caliò et al. [2023], respectively using photogrammetry point clouds alone or a combination of thermal images and photogrammetric cliff model. These applications, however, are limited to accounting for the discontinuities' properties as the sole factor influencing the slope stability, disregarding the progressive alteration and fragmentation driven by water infiltration and erosion. In this framework, our study represents one of the few applications of UASs for detecting local to micromorphological signatures of the initial stages of slope disruption. Furthermore, we consider the multi-scale imprint of denudation and mass-wasting processes, along with their respective preliminary indicators, exploiting a synergic combination of satellite and drone-based data can offer an in-depth characterization of landforms and geomorphic agents [Liu et al., 2021; Ma et al., 2021; Hu et al., 2022; Liu et al., 2022]. In this study, the morphological features, and radiometric differences, associated with significant change detection over the study area are investigated. We applied a multi-scale and multi-sensor approach integrating satellite-based InSAR analysis with UAS-based data to assess mass wasting processes on two study sites located along State Highway 133 near Paonia Reservoir in Colorado, USA.

6.2 Geographical and geological settings

The Paonia Reservoir area is part of the southern sector of the Piceance Basin, a structural and sedimentary basin formed during the late Cretaceous–Paleocene Laramide orogeny. The exposed stratigraphic sequence, representing this Cretaceous–Tertiary boundary, mainly consists of the white rocks of the Ohio Creek Member and the variegated rocks of the Wasatch Formation (Figure 5.1), both deposited in a non-marine environment. The first unit was considered by many stratigraphers as a separate formation because of its distinctive white/light-grey colour but was eventually reduced in rank to the Ohio Creek Member of the Mesaverde Group by Johnson and May [1980], who described it as a deep paleo-weathered kaolinitic zone undistinguishable in age (late Cretaceous) from the underlying rocks of the Mesaverde group. The lithological composition varies from light-grey or white conglomeratic sandstone with well-rounded chert pebbles in the lower and upper part, to interbedded layers of sandstone, siltstone and shale with some thin coal lenses in the middle sector [Godwin, 1968; Johnson and May, 1980; Johnson, 1989]. This lithological alternation finds expression in slope morphology, where thick and resistant sandstone ridges intermingle with more erodible siltstone and shale layers. The white-weathering Ohio Creek member is unconformably overlain by lower Cenozoic rocks of the Wasatch Formation. At this location, the

Wasatch Formation deposition is characterised by non-kaolinized, mottled maroon medium- to coarse-grained conglomeratic sandstones [Godwin, 1968; Johnson and May, 1980; Johnson, 1989].

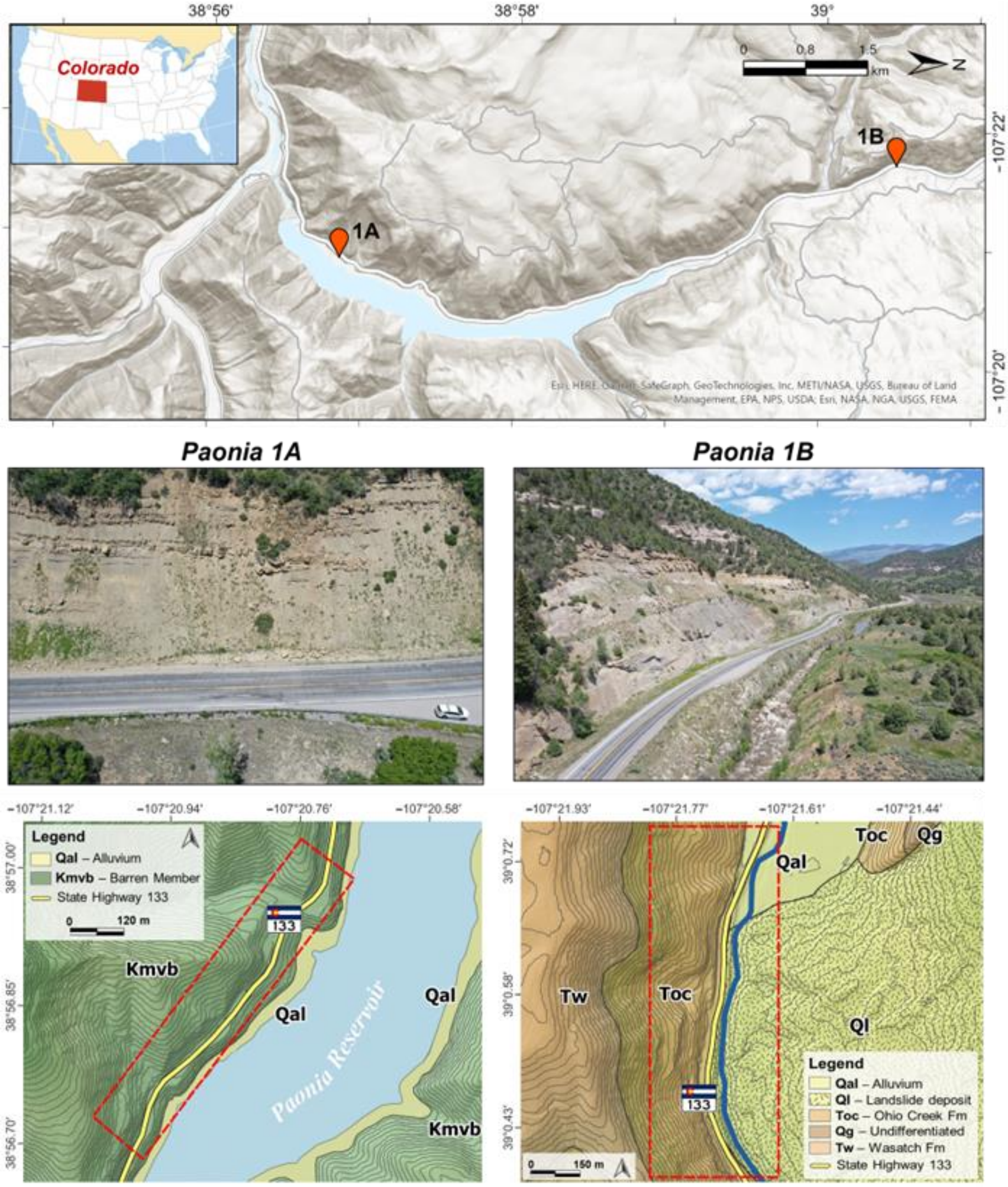

Figure 6-1: Location of the study areas along State Highway 133 (upper panel). The oblique view of the slopes of interest and their geological setting is reported in the bottom panels, respectively for Paonia 1A (left panels) and Paonia 1B (right panels). The figures were realised using ArcGIS Pro 3.0.4 and QGIS 3.22.14.

The area of interest referred to as Paonia 1A is located along the western side of Paonia Reservoir and around 500 m north of Paonia Dam (from MP 24.7 and 25.0 of State Highway 133, Figure 1). The slope reaches the highest values of steepness (up to 65°) along the upper part, where the bedrock unit of the Mesaverde Group outcrops. In this part, light brown and light tan sandstone beds (a few metres thick) are interbedded with thinner grey mudstone and shale layers, corresponding to the Barren Member of the Mesaverde Group (Figure 6-1) [Dunrud, 1989]. The lowest part of the slope, with a mean steepness value around 35–40°, is mainly composed of an unconsolidated deposit fed by mass wasting due to the mechanical and chemical weathering of the bedrock outcropping in the upper part. The resulting scree slope is constituted by small-sized rocks (a few cubic centimetres). At the same time, massive boulders are more likely to accumulate along the foot of the slope and inside the roadside ditch.

The second area of interest (hereafter called Paonia 1B) is located two miles north of Paonia Reservoir on the west side of SH133 (from MP 29.9 to 30.2), just north of the confluence of West Muddy Creek into East Muddy Creek and along the south-eastern slope of the Bull Mountain (Figure 1). This sector of SH133 aligns with the foot of a slope characterised by a mean steepness value of about 40°, sharply interrupted by a flatter area (less than 10°) located in its middle portion. A concave-shaped landslide scar isolates several morphological steps in the northern sector of the area, which could be kinematically due to the roto-translational landslide mechanism.

6.3 Materials and Methods

This section includes two main subsections, for the interferometric synthetic aperture radar analysis (InSAR) and the UAS-based acquisition and processing techniques adopted in the present work. The first analysis was performed at the catchment scale: the scope was detecting large deformation processes and considering their interaction on portions of SH133 wider than those included in the actual study areas. Downscaling the investigation, the UAS-based products were used to identify signs of slope instabilities at the small and micro-scale. In particular, different radiometric sensors (i.e., optical, thermal and multispectral) were combined to highlight morphological variations related to erosion or accumulation processes.

6.3.1 Satellite-Based (InSAR) Analysis

Advanced differential interferometric synthetic aperture radar (A-DInSAR) is a multi-image process that provides high-resolution measurements over large areas [Aswathi et al., 2022]. Specifically, the persistent scatterers (PS) technique [Ferretti et al., 2001] is capable of identifying and measuring the displacement of millions of ground points, thereby providing a much more detailed and comprehensive understanding of ground deformation (and its association with geological processes) over time. PSs represent the time-coherent pixels retrieved in the stack of differential interferograms, thus corresponding to phase-stable objects in the scene [Funning et al., 2007]. For the present study, medium-resolution Sentinel-1 data were used for the 2017–2021 time interval. The European Space Agency’s two-satellite constellation has the main advantage of high temporal coverage (revisit time of up to 6 days) over the same area. The dataset was analysed in the SARPROZ software 2022 (the SAR processing tool by Perez [Perissin et al., 2011] and allowed to estimate both the average line-of-sight (LOS) velocity and the displacement time series (TS) for the PS over the two study areas. The essential steps of the processing consist of co-registering all of the images to the one chosen as the master. Subsequently, two radar parameter maps are generated to estimate the quality of the persistent scatterer candidates (PSCs): these maps respectively represent the multi-temporal amplitude value for each pixel (reflectivity map) and the coefficient of the amplitude variation (amplitude stability index map). The next step relates to the detection and removal of the atmospheric phase screen (APS) for estimating each persistent scatterer (PS) and the velocity values along the line-of-sight (LOS) relative to a reference point identified in a stable region [Antonielli et al., 2021; Moretto et al., 2021]. At the end of the PSI workflow, PSs having a low temporal coherence threshold (<0.5) were discarded. Of the two available orbital geometries, only the results from the ascending geometry analysis were reliable enough to be interpreted. Geometric distortions due to the off-nadir angle of the descending geometry, in particular shadow effects, heavily affected the spatial coverage of the data.

6.3.2 UAS-Based Acquisition and Processing

The multi-temporal UAS-based data acquisition aimed to create high-resolution products to assess a comprehensive deterioration model of the rock mass, including seasonal moisture condition variations, structural changes and lithological characterization. For this purpose, two UAS flight campaigns were carried out in September 2021 and June 2022; the flights were operated from traffic pullouts along Colorado SH133 (Figure 6-2a) in adherence to Federal Aviation Administration (FAA) regulations regarding drone visual-line-of-sight (VLOS), maximum flight altitude relative to ground level, and flights over traffic. Moreover, visual observers selected from the field team helped UAS pilots ensure air space safety.

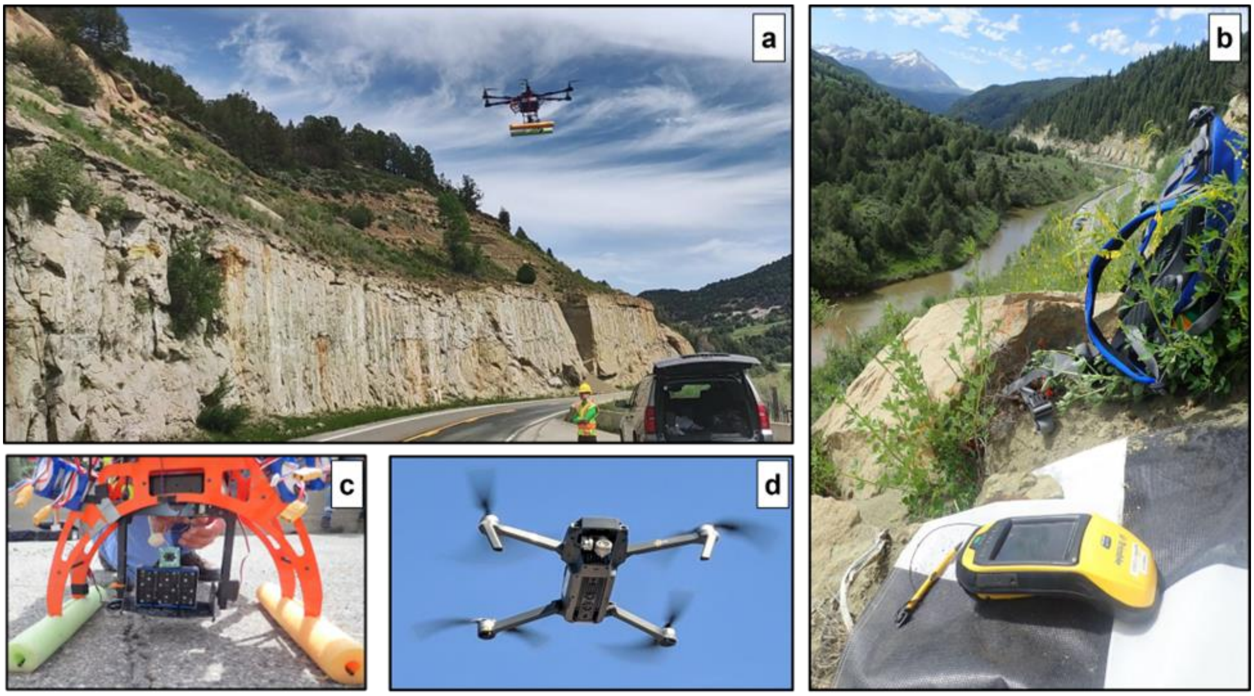

Figure 6-2: Examples of drones, instruments and sensors used during the field operations. Panel (a) Bergen Hexacopter flying over Paonia 1B site; (b) AeroPoint and Trimble 3 GPS unit placed at Paonia 1A site; (c) Tetracam multispectral camera; (d) Dual optical and thermal cameras.

To accurately georeference drone-derived image products, together with cloth photogrammetry targets, we placed ten ground control targets (Figure 5.2b) throughout the planned study area. Each AeroPoint already includes built-in GNSS and Wi-Fi systems that allow a level of accuracy of down to 3 cm during the imagery georeferencing process. The flights were planned with overlaps of 70% along the flight line and 60% at the sides and were manually carried out at the same time of the day to cover the study sites under similar lighting conditions each year. A set of multi-sensor cameras were flown as payload on three different UASs to capture and analyse complementary and interconnected environmental conditions that contribute to the rock instabilities of the area. More than ten flights per survey were necessary to acquire nadir and oblique-oriented images to represent the near-vertical slopes accurately. The Tetracam multispectral camera (Figure 5.2c) was flown as payload on the Bergen Hexacopter at each study site. This sensor can capture detailed information about the spectral characteristics of the landscape, which can reveal potential changes in moisture content and mineral composition.

The M2EA (Figure 5.2d), equipped with dual optical thermal integrated cameras, was used to capture radiometrically calibrated thermal imagery over each site. In Table 5.1, we summarise both the drones' specifications and the type of sensors flown as payload.

Table 6.1: The characteristics of the drones used for the study

Characteristics	DJI Mavic 2 Pro	DJI M2EA	Bergen Hexacopter
Camera	Integrated 20mp	Integrated dual optical (12/48mp) thermal (640x480 radiometric 30hz)	Tetracam Micro-MCA6
Maximum take-off weight (kg)	0.907	0,11	4.5
Flight range (min)	25	25	15
Flight altitude (m)	45-60	30-60	30-70
Maximum horizontal speed (km/h)	72	72	30
N° of images (nadir)	2000	3500 thermal	Tetracam: 700 (6 bands)
N° of images (oblique)	800	900 thermal	Tetracam: 500 (6 bands)

6.3.2.1 Pre-processing

Prior to drone flights, the ground control, in the form of cloth photogrammetry targets and AeroPoints, were evenly placed throughout the planned study area (Figure 5.2b). The AeroPoints continuously logged their position while the cloth photogrammetry targets were surveyed using a Trimble 3 GPS unit, with both methods providing coordinates with centimetre-level accuracy. These ground control targets, appearing within the field of view of the drone camera, provided geolocation information for accurately positioning the drone-based orthoimage products.

For the optical imagery collected by the DJI Mavic 2 Pro, the software Agisoft Metashape v.1.8.1 was used to align and find tie points between photos, producing image-based dense clouds, orthophotos, and DEMs. Ground control position information collected for each target was required for this processing to produce accurately geolocated products.

For the thermal imagery collected by the DJI M2EA, the raw images were processed into per-pixel true-temperature radiometric images using AethaGlobal's ThermoConverter software v.1.3.14.0. The true-temperature images were then processed into a true-temperature orthophoto using the image processing software Pix4Dmapper v.4.7.5. The orthophoto was geo-referenced using the ground control present in the orthoimage.

For the 6-band multispectral imagery collected by the Tetracam Micro-MCA6, raw images were processed using Tetracam's proprietary 'PixelWrench2' software v.1.2.4.9 to convert raw images into multi-band tiff images. The tiff images were then more precisely aligned using intensity-based image registration techniques available within MATLAB. The resulting aligned images were then processed using Agisoft Metashape to create a 6-band orthoimage for the study site. Ground control target GPS data were used as inputs during Metashape photogrammetry processing to create a georeferenced product.

6.3.2.2 Processing: Classification analysis

The georeferenced 6-band Tetracam orthoimage was classified into several soil or rock types (e.g., sandstone, arkosic sandstone), vegetation (i.e., living or dead), and other classes (e.g., shadows, road) using the software Trimble eCognition v.10.3 [Trimble, 2022]. To create this classification, the orthoimage was first segmented in eCognition using a multi-resolution segmentation best-fitting neighbour algorithm that groups pixels into objects by minimising or optimising the average heterogeneity of image objects [Trimble, 2022]. In this process, pixels were grouped into segments based on the spatial and spectral characteristics of the pixels and their neighbours, using all six bands of the Tetracam orthoimage. Desired mean segment size parameters were input by the user to affect the number of segments, the size of segments (which impacts the final classification), and the file size of the segmented image. Segmenting the image allowed the user to perform object-based image analysis (OBIA), which can be an improvement over pixel-based image classification for representing landscapes [Blaschke, 2010]. Pixel-based image classification solely uses the spectral information of the image bands in the classification. Grouping these pixels into objects using multi-resolution segmentation created an object-based classification that was based on both the spectral and spatial characteristics of the 6-band orthoimage. After the image was segmented, a supervised classification hierarchy was created, containing the distinct mapping classes. Based on observations made in the field (ground truth information), and visual observations of the image itself, the eCognition user then assigned individual segments as samples to each desired class in their class hierarchy. The user might use both ground-truth information and their own visual observations of the orthoimage to discern different vegetation types and assign samples to unique vegetation classes (e.g., living and dead vegetation classes). After some samples were assigned to each class in the class hierarchy, the analyst then used a nearest neighbour classification algorithm [Trimble, 2022] to assign each image object (segment) in the image membership to a class based on the spectral information of the samples. The classified orthoimage was then exported in a Geotiff format to be interpreted in a GIS environment together with other analyses.

6.3.2.3 Processing: Change Detection analysis

Change detection techniques involve the comparison of multi-temporal datasets to assess the temporal effects of a specific process and quantify changes due to natural phenomena or anthropogenic activities [Hussain et al., 2013]. Significant changes identified between at least two images lead to the generation of a change map. Asokan and Anitha [2019] provided a comprehensive review of different change detection techniques, addressing issues and challenges of performing change detection on remotely acquired images. For this study, the algebra-based change detection approach was followed, which consists of the application of mathematical operation on each pixel to retrieve the difference image. The DEM generated using the orthoimages from the 2021 and 2022 data collection, after preprocessing, were coregistered and the algebraic operation of subtraction was performed on them in ArcGIS Pro 3.0.1. The 2022 image was subtracted from the 2021 image to monitor changes that occurred after the 2021 data collection. The differences that were reflected after the change detection task were mostly due to elevation changes between the two acquisitions. While the DEM comparison allowed the extraction of information related to changes in elevation, the orthoimages acquired from the Mavic 2 Pro were processed to assess any variation in terms of radiometric characteristics. The change detection analysis that was implemented on IRIS software v.23.0, developed by NHAZCA S.r.l. [Photomonitoring.com], involves the use of the Structure Similarity Index Method (SSIM) algorithm [Wang et al., 2004], a function of the brightness, contrast and structural component of pixels and determined by constructing a moving window around each pixel for both images. The SSIM is defined as follows:

$$SSIM(x,y) = \frac{(2\mu_x \mu_y + C_1)(2\sigma_{xy} + C_2)}{(\mu_x^2 + \mu_y^2 + C_1)(\sigma_x^2 + \sigma_y^2 + C_2)} \quad (1)$$

where μx and μy represent the luminance for the two image signals, σ represents the contrast and C represents a constant to ensure stability when the denominator is very close to zero. This equality index represents the radiometric variation between the image selected as the master (i.e., 2021 orthoimage) and the one selected as the slave (*i.e.*, 2022 orthoimage) on a scale from 0 to 1 [Cosentino et al., 2022]. The closer the index is to 1, the more the two images are similar: an index equal to 1 means that no changes were identified over the observed time interval [Mazzanti et al., 2022].

6.4 Results

This section summarises the results obtained through the PS-InSAR analysis, visual interpretation of UAS-based products, and the classification and change detection analyses carried out on them. The results were divided into two subsections for Paonia 1A and Paonia 1B, respectively.

6.4.1 Paonia 1A

Regarding the UAS-based analysis, it has been decided to present the primary outcomes of two specific sectors that are representative of the processes observed throughout the entire area of interest. These sectors, shown in Figure 5.3, are located along SH133 in the central part of the study area. Sector I stretches nearly to the northern boundary of the slope of interest: Figure 4 illustrates the same area in different panes, each representing a specific analysis carried out on the site of interest. As evident from the orthophoto captured through the DJI Mavic 2 Pro optical sensor (Figure

5.4a) in June 2022, the slope appears almost entirely uniform, with sedimentary rocks in a tan shade and dotted with patches of vegetation in the central part. However, a linear pattern of slightly lighter colour can be observed in the upper part of the slope, corresponding to the exposed rock strata.

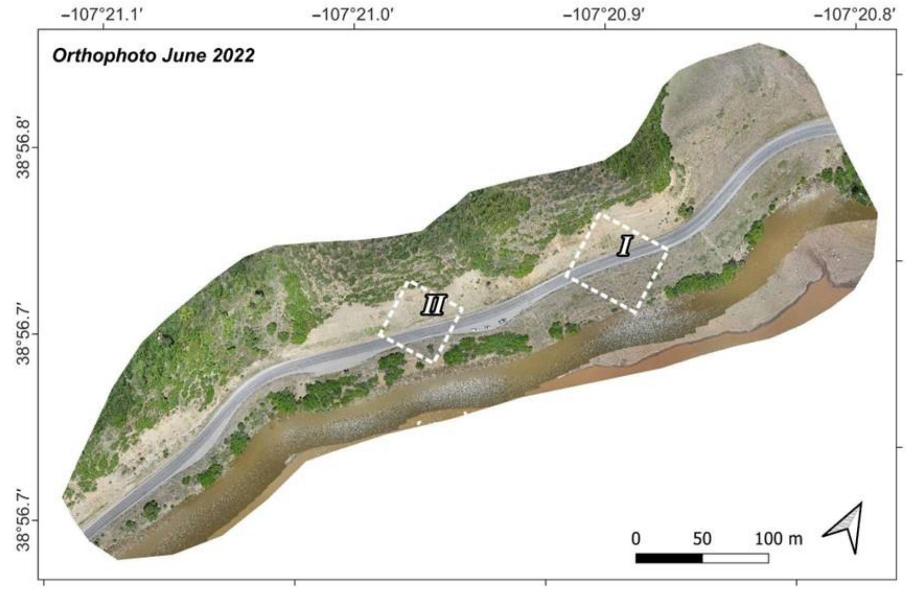

Figure 6-3: Location of the two most representative Sectors for Paonia 1A study site, respectively referred to as Sector I and Sector II. The figure was realised using QGIS 3.22.14.

On the contrary, the per-pixel temperature visualisation of the thermal image returns improved discrimination of the slope, enabling the identification of distinct patterns and textures distinguished by varying temperature values (Figure 5.4b). The slope region near SH133 shows the highest temperature values, with an average of around 50 °C. This area becomes more homogenous heading north, while the southern and central portions of the sector exhibit a more granular texture and colder temperatures, which drop by up to 32–33 °C. Particularly in the central part, the slope continuity is interrupted by clusters of lighter colours that match the vegetation already identified in the orthophoto. The summit section of the slope, which has a finer texture, displays uniformly distributed temperatures with an average of 45 °C. A distinct central band separates the two regions, which features a linear pattern with alternating areas of cooler temperatures (around 38 °C) and warmer temperatures (around 55 °C), characterised by a coarse texture.

Figure 4c represents the outcome of the DEM-based change detection between the two data collections in September 2021 and June 2022. The elevation difference is represented with a red-to-blue colour scale, where shades of red represent positive values (≥0.15 m) while shades of blue represent negative values ≤ 0.15 m). Areas showing negligible or no changes were left uncoloured for better interpretability of results. Except for the portion along the roadside, showing an evident decrease, a rise in elevation values between the two years is registered throughout the slope. The values indicating an elevation increase of around 30–40 cm appear to form fan-like shapes, which align along the lower section of the slope and are separated from each other by areas exhibiting minimal variation in height.

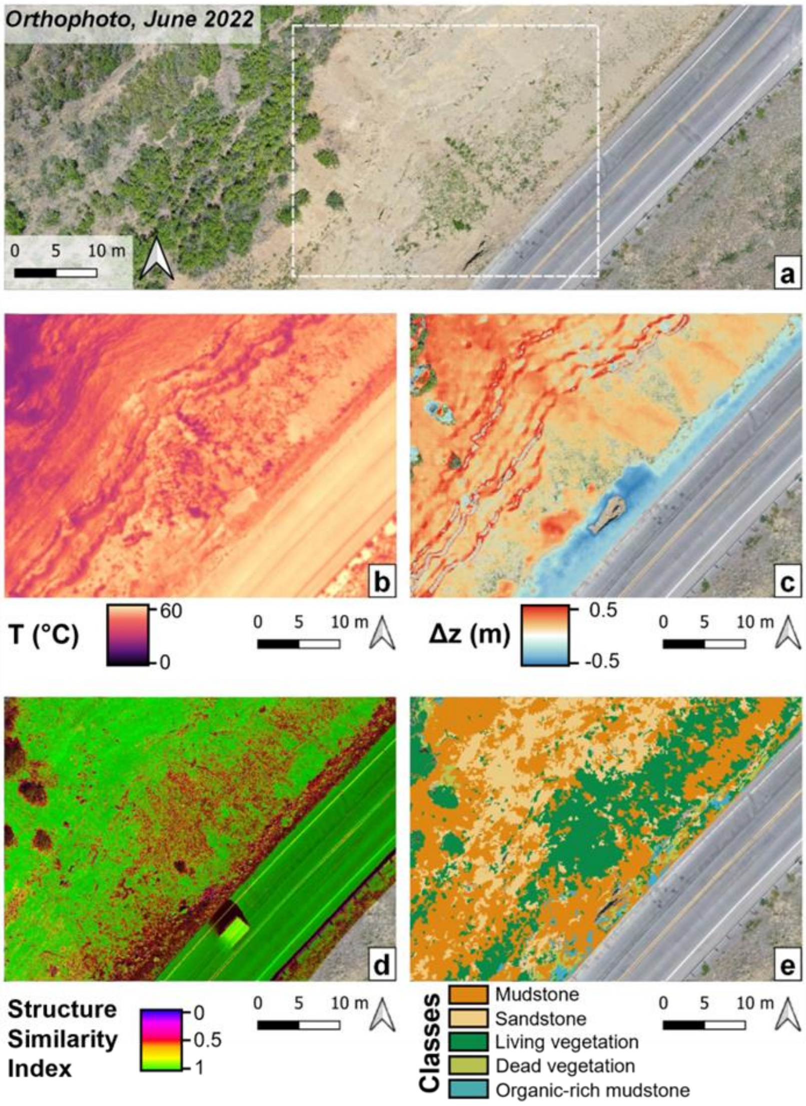

Figure 6-4: The results obtained for Sector I of the Paonia 1A study area are presented in 5 panels, corresponding to: (a) orthophoto acquired in 2022; (b) per-pixel temperature thermal image; (c) DEM-based change detection; (d) optical-imagery-based change detection; and (e) classes resulting from the classification analysis. The figures were realised using QGIS 3.22.14.

For the change detection analysis performed between the orthophotos, choosing a four-pixel window size emphasised even slight radiometric variations. A major part of the scene depicted in Figure 4d has an SSI value close to one, indicating that the 2021 and 2022 images look very similar in terms of radiometric characteristics. The most notable changes are concentrated in the basal and central regions of the slope, where a decrease in SSI (around 0.5) values corresponds with changes in debris accumulation (especially along the roadside) and vegetation presence, the latter of which has a significant impact on the analysis. The final panel of Figure 5.4 displays the results of the multispectral image classification. In Sector I, the classification analysis has identified five distinct classes, two of which correspond to the vegetation present in the scene (distinguished as living or dead), while the other three relate to the sedimentological properties of the rocks. These three classes correspond to samples of sandstone and mudstone (with lower or higher organic matter content) that were recognized during the field operations and used as training data. However, the most representative classes in this area are only sandstone, mudstone, and living vegetation, whereas small scattered patches of dead vegetation and organic-rich debris constitute a minimum part of the scene. The debris accumulation, mainly composed of mudstone, develops along the foot of the slope and on the sandstone bedding plane, whose heads (in beige) are well recognizable in the summit portion.

The same comparative criterion adopted for Sector I is also applied to the results for Sector II, reported in the subsequent panels of Figure 5.5 to facilitate the visual interpretation of the data.

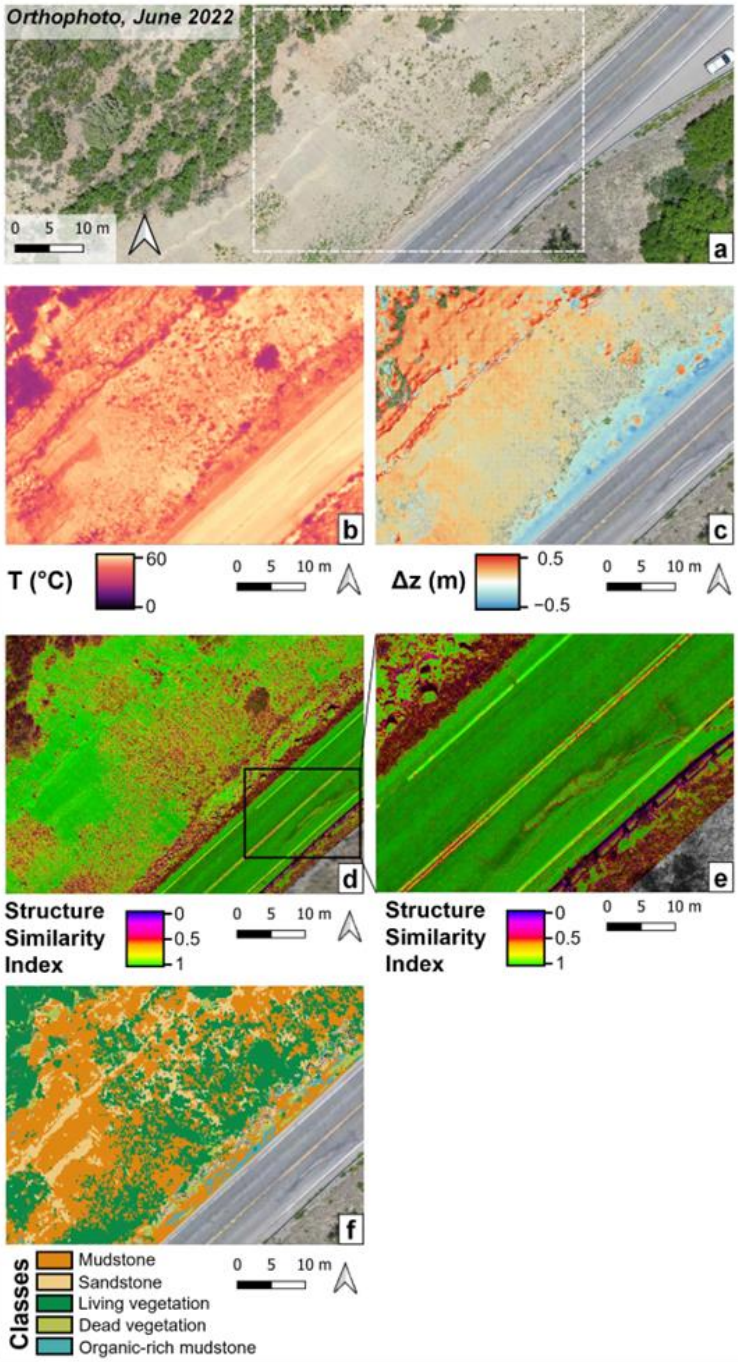

Figure 6-5: The results obtained for Sector II of the Paonia 1A study area are presented in 6 panels, corresponding to: (a) orthophoto acquired in 2022; (b) per-pixel temperature thermal image; (c) DEM-based change detection; (d,e) optical-imagery-based change detection at various scales and (f) classes resulting from the multispectral classification analysis. The figures were realised using QGIS 3.22.14.

In this case, as well, the sandstone banks that appear in the optical image (Figure 5.5a) in a slightly lighter shade of beige than the rest of the outcrop emerge clearly in the thermal visualisation

(Figure 5.5b), being marked by lower temperature values (around 40 °C) than the sediments (more than 50 °C). The classification analysis validates this finding by clearly differentiating the beige, linear pattern of the sandstone from the more diffused brown of the mudstone, enabling the recognition of the sandstone stratification throughout the entire extent of the scene (Figure 5.5f). Below these banks, there is a distinct area with sporadic bushes and vegetated spots that can be easily identified through both optical image and object-based classification (Figure 5.5a,f). These areas correspond to the living vegetation class.

The results of thermal and change detection also confirm the presence of these areas, where the thermal image highlights cooler and potentially more moist zones with temperatures below 40 °C (Figure 5.5b), while the change detection analysis (Figure 5.5d) yields an SSI value of 0.5, indicating significant changes over the two years. It is worth noting that the variations detected in the change detection analysis do not exhibit a chaotic structure like the one shown in Figure 4d, but rather present a linear pattern that converges towards the base of the slope. Moreover, subtle changes in the fractures constituting a semicircular road crack, located right below the convergent linear pattern, were highlighted by the analysis.

Similarly to Sector I, the DEM-based change detection for Sector II reveals a significant material accretion near the road edge. Besides the uniform accumulation of debris in this region (15–30 cm), large blocks, which are predominantly sandstone blocks (Figure 5.5f), can be also found near the road pitch.

For the Paonia 1A site of interest, the results of the PS-InSAR analysis show a few sparse measurement points, which are not representative of significant deformations affecting the slope.

6.4.2 Paonia 1B

The PS analysis allowed us to investigate the deformations occurring on the slope of interest at Paonia 1B, considering its morphoevolution on a larger scale. The measurement points, derived from 250-km-wide imagery (i.e., interferometric wide swath, IW), cover the slopes that develop along the hydrographic right and left banks of East Muddy Creek. Average velocities ranging from −4 to −10 mm/y were recorded in the southernmost part of the slope of interest, forming a small deformation cluster moving away from the sensor and thus indicating a downslope movement (Figure 5.6a). On the opposite slope, apart from a stable PS cluster located along the foothill, a clear movement with displacement rates of over 4 mm/year is measured towards the east direction (Figure 5.6b). The analysis provided important clues to the recent displacement rates of a landslide phenomenon already well identified in the historical maps of the area [Godwin, 1968; Stover, 1986], but whose state of activity was investigated only by Lowry et al., [2020]. This landslide is part of the broader "East Muddy Creek Landslide Complex", which consists of three distinct phenomena located on the western flank of the Ragged Mountains and that was mapped through the visual interpretation of the one-metre LiDAR-based DEM produced within the framework of the 3D Elevation Program (3DEP) [U.S. Geological Survey] and the PS-InSAR results.

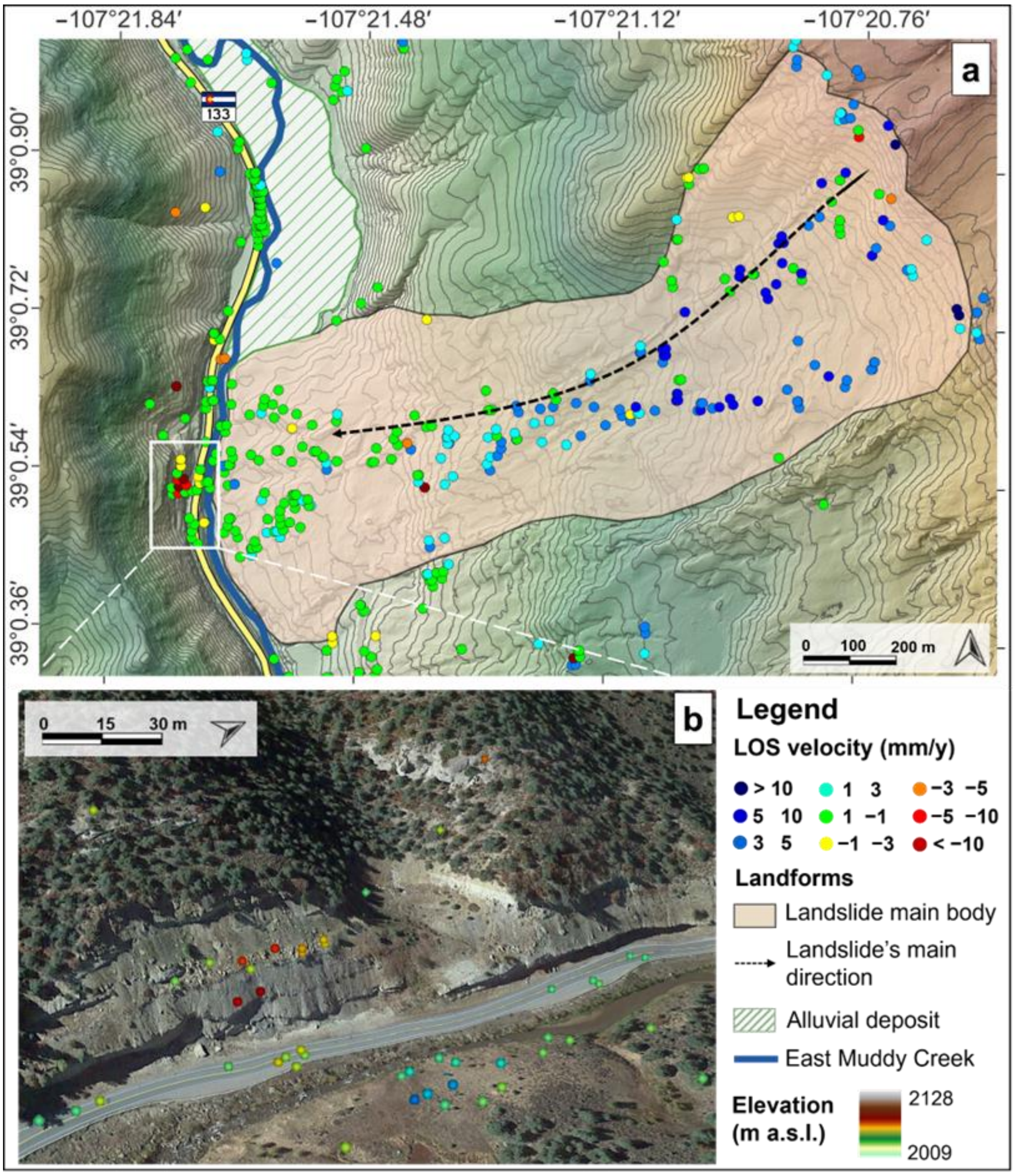

Figure 6-6: PS-InSAR results for Paonia 1B site. In the upper panel (a) the catchment scale ground deformations are shown. The massive landslide phenomenon retrieved by the PS-InSAR analysis displays displacement rates of up to 10 mm/year. At a smaller scale (panel (b)), a well distinct cluster with 3–10 mm/year displacement rates is visible on the opposite bank. The figures were realised using QGIS 3.22.14

Similarly to Paonia 1A, distinctive sectors of Paonia 1B (Figure 5.7) were chosen to represent landforms and processes occurring on the slope. Sector I covers the left flank of the concave-shaped landslide scar which interrupts the continuity of the strata. A massive sandstone bank, lighter in colour, bounds a flat area where greyish and brownish debris accumulates (Figure 5.8a). A more detailed differentiation of the slope features is captured by thermal (Figure 5.8b) and multispectral sensors (Figure 5.8c).

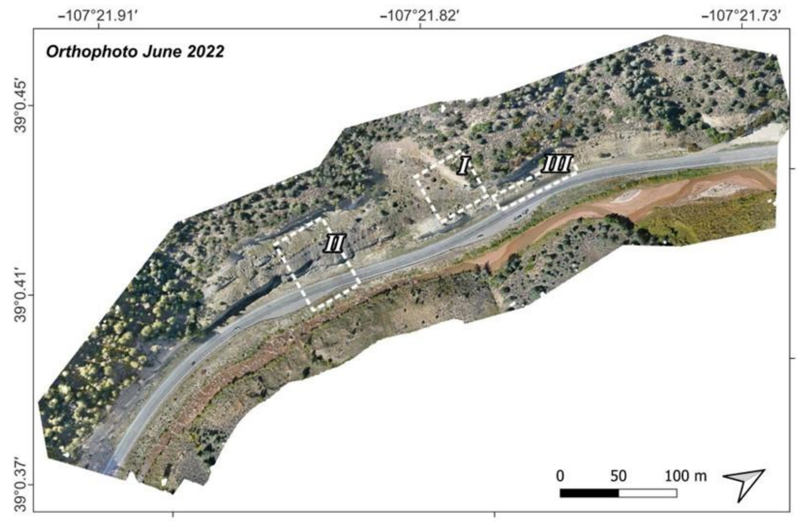

Figure 6-7: Location of the three most representative Sectors for Paonia 1B study site, respectively referred to as Sector I, II and III. The figure was realised using QGIS 3.22.14.

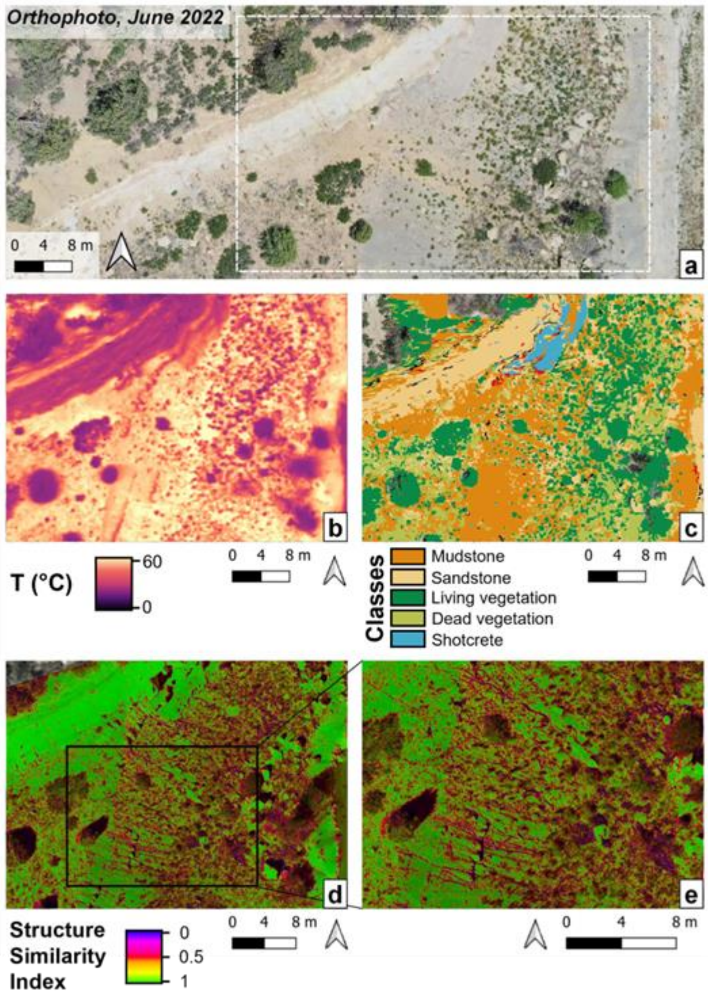

Figure 6-8: The results obtained for Sector I of the Paonia 1B study area are presented in 5 panels, corresponding to: (a) orthophoto acquired in 2022; (b) per-pixel temperature thermal image; (c) classes resulting from the classification analysis; (d,e) optical-imagery-based change detection at various scales. The figures were realised using QGIS 3.22.14.

The overhanging sandstone bank is still well distinguished from the surroundings in terms of lower temperature, appearing as a continuous red/purple band and dividing the vegetated top of the slope from the warmer soil and debris area (temperature up to 50 °C). Just below the sandstone outcrop, the multispectral classification identifies shotcrete covering the slope, contrasted by sandstone's higher temperature values and the unconsolidated material's lower values. Scattered features, corresponding to low-growing vegetation (dead and living) and trees, allineate along the eastern section of the slope, while the mudstone class is found in its central area. The radiometric change detection highlights significant changes (SSIM < 0.5, Figure 5.8d), mostly in correspondence with the vegetated spots but, where the mudstone class outcrops, a linear pattern with similar low values of SSIM is also identified, developing along the steepest part of the central area. Figure 8e focuses on the aforementioned linear pattern, clearly visible between the vegetation.

Sector II is located slightly to the south and includes a portion of a stepped slope, where vertical sandstone strata alternate with erodible layers, forming gentler morphologies. Few reliable persistent scatterers, in the upper part of the slope and specifically on the less steep portions (Figure 5.9a), recorded an average velocity of up to 10 mm per year in the LOS direction (i.e., downslope). The thermal visualisation of the scene shows quite similar temperature values ranging between 42 and 50 °C (Figure 5.9b). The only exceptions are represented by the lower temperatures of the vertical slope faces and three warmer spots (more than 55 °C) along the roadside. The two yellow spots located in the northern part of the scene present a fan-shaped morphology, with the apex in the vicinity of the vertical road cut, whereas the third one is more distributed. In the last panel of Figure 5.9, the DEM-based change detection outcomes are shown.

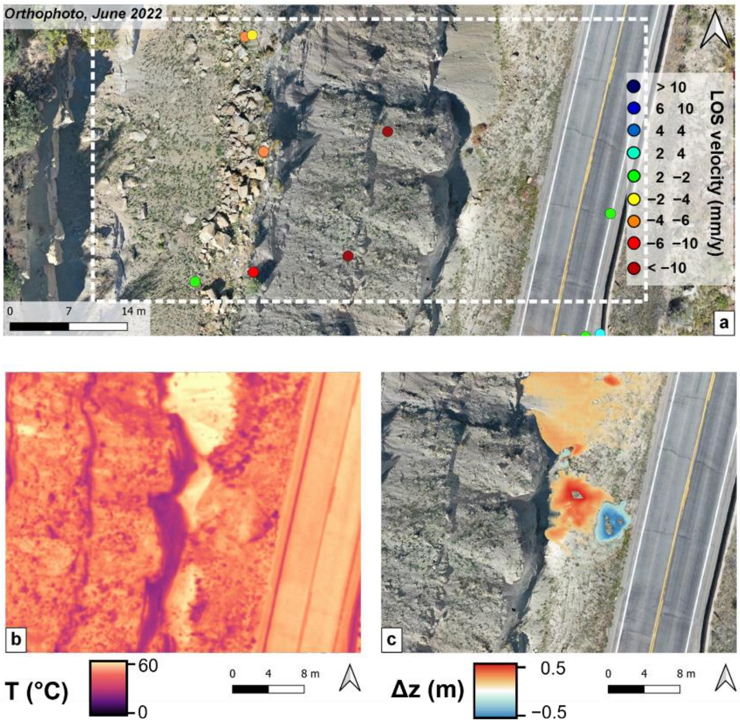

Figure 6-9: The results obtained for Sector II of the Paonia 1B study area are presented in 3 panels, corresponding to: (a) orthophoto acquired in 2022 and PS-InSAR analysis; (b) per-pixel temperature thermal image; (c) DEM-based change detection.

A diffuse increase of about 30 cm in height matches the fan-shaped spot in the northern part, with very limited incrementations of more than 50 cm along its boundaries. A sharp change in elevation values can be also noticed in the central part of the scene, where two adjacent areas show differential movements in opposite directions (blue and red areas in Figure 5.9c): in both cases, the elevation change reaches 50 cm.

The third and last sector analysed for the Paonia 1B area was chosen to represent the analysis carried out on a vertical surface like a road cut. In the orthophoto (upper panel of Figure 5.10) the surface predominantly appears in two shades of greyish beige. The darker shade is predominant on a small portion on the left and in the upper part of the cut, while the lighter shade of beige is along the base and at the edges of the image. This slight colour difference is, on the contrary, well perceivable in the multispectral classification (Figure 5.10, lower panel), and respectively corresponds to the Sandstone (blue) and Weathered Sandstone (yellow) classes.

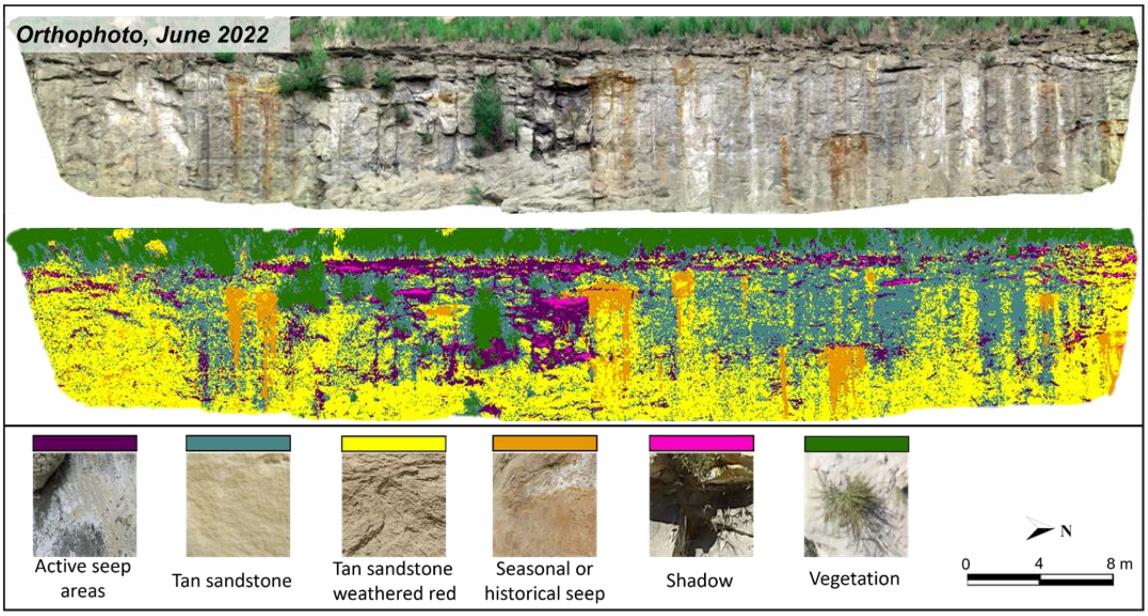

Figure 6-10: Sector III: multispectral image classification of the road cut. The figures were realized using QGIS 3.22.14.

A definite purple layer is interpreted as an area of active seep that stretches right under the vegetation covering the top of the surface and can also be found in the central part of the outcrop, along with minor shadowed areas. Inactive seep areas, corresponding to the orange vertically elongated features in the orthophoto, perfectly match the orange category of the classification analysis.

6.5 Discussions

This study aims to examine the ability of different sensors to identify evidence and early precursors of slope instabilities. Two drone flight campaigns carried out one year apart, along with satellite-based interferometric analysis, served this purpose by highlighting processes of intense and persistent denudation of the slopes of interest in the study areas.

In the Paonia 1A area, signs of erosion phenomena mainly related to surface and concentrated runoff dynamics are clearly visible in both sectors. In the central parts, the presence of vegetation indicates an accumulation or stagnation of water and, specifically for Sector I, it is located just downstream from what appears to be a slight concavity in the stratification, well recognizable from the thermal image (Figure 5.4b). Sediment accumulation processes occur in these concentrated runoff rills and lead to the formation of diffuse (Figure 5.5c) or fan-shaped (Figure 5.4c) debris accretion, defined by an increase in height values in the change detection analysis. Due to this considerable sediment production, the maintenance activities, such as the accumulated debris removal, are particularly noticeable, as shown by the blue band in Figure 5.4c and Figure 5.5c, indicating a decrease in elevation between 2021 and 2022. However, a minor part of this decrease is to be addressed to the vegetation changes between September 2021 (when the foot of the slope was covered by both living and dead vegetation) and June 2022. While in Sector I, the denudation processes seem to affect only the slope, in Sector II, we observe a more mature scenario of water erosion and infiltration that has led to the road surface's initial disruption. The micro-scale geomorphic features, both anthropic and natural, were pointed out by the change detection performed with IRIS software v. 23.0 (Figure 5.5d). Rills and gullies, formed after the precipitation event occurred on 19th September (Weatherwx.com), identify the area most prone to degradation. Moreover, a wide convex road crack is the morphological evidence of this severe and persistent erosion that would possibly cause the partial failure of the highway. In this case in particular, but also for Sector I, the multispectral analysis is proof of how the slope is influenced by differential moisture conditions, which stand out immediately thanks to the presence of vegetation.

For the Paonia 1B area of interest, the results of the InSAR analysis (Figure 5.6) provided substantial information to study displacements occurring at the catchment scale and contribute to understanding the large-scale morpho-evolution of this area. Displacement values recorded by the PS confirm those from Lowry et al. [2020], delineating a complex scenario where the evolution of the Central East Muddy Creek Landslide Complex is highly interconnected to the opposite slope's instability asset and fluvial incision. The Central Landslide, due to its differential displacement pattern and annual velocity rates, still represents a critical condition for the risk assessment of SH133. Its activity style, characterised by discontinuous reactivation phases [Lowry et al., 2020], defines a major threat to Colorado State Highway 133 (already damaged in 1986–1987). However, investigating this phenomenon, including its interaction with fluvial incision rate and mass-wasting processes on the opposite slope, would have required a proper modelization and was therefore not extensively carried out since it goes beyond the specific purpose of this work. On the other hand, the point measurements forming a cluster on the Paonia 1B slope of interest led to the identification of localised instabilities (Figure 5.9a). The movement can be correlated with unconsolidated materials sliding along the slope and then aligning in debris fans (clearly visible in the thermal product, Figure 5.9b) right below the PS cluster. This consistent waste deposit supply resulted in the complete occlusion of a drainage ditch (increase in height, Figure 5.9c), eventually cleaned during maintenance work (decrease in height, Figure 5.9c). As for the other study site, a clear example of the effects of intense denudation affecting specific portions of the hillslope is represented in the panels of Figure 5.8. Here, concentrated erosion processes drove the disruption of the shotcrete applied for stabilising the prominent banks. The shotcrete is abruptly interrupted in the southern part of the sandstone banks (Figure 5.8c), where a dense linear pattern of rills engraves the more erodible mudstone layers (Figure 5.8d,e). The Sector III example was provided to demonstrate the capacity of the sensors to identify not only the ongoing mass-wasting processes but also to point out early indicators of future instabilities. In this case, the multi-spectral information was essential to mark seeping areas where block detachment or collapses may easily occur (Figure 5.10).

The advantages of combining several sensors that could provide complementary information made it possible for an extensive investigation of different processes from a multi-scale perspective. Different landforms overlaying the slopes make it difficult to discern the corresponding process imprint and, therefore, to give a comprehensive representation of the territory's complexity (Schmidt and Andrew, 2005). Each of the applied sensors, with its specific spatial resolution, facilitated this task, enabling the extraction of one or more landform signatures and the relative forming process. Table 5.2 summarises the scale of processes and related landforms detected through our multi-sensor approach. At the sub-catchment scale, the satellite-based InSAR analysis was the only medium-resolution technique that could measure the deformations with an accuracy comparable to the other methods. Gradually downscaling the investigation at the decametric and metric scales, thermal imagery and DEM-based analysis provided the most suitable results for delineating debris fans, blocks detached from the massive sandstone layers and areas subjected to concentrated runoff features. Eventually, micro-morphotypes were investigated by exploiting optical image-based change detection and multispectral classification. The micro-scale topographic landforms (i.e., road cracks and centimetre-scale rills) and subtle moisture variations (*i.e.*, seep areas) respectively depicted by those methods can be correlated to early instability indicators. The regional-scale satellite-based products were effective in identifying possible areas of instability, while further downscaled investigations of those areas with drone-based high-resolution products provided significantly better outputs for the decision-making and mitigation processes of asset management plans. This multiscale approach was successful in identifying both the evidence and the early precursors of rock mass instability impacted by intense deterioration processes.

Table 6.2: Comparison between sensors, type of products and respective type of processes or landforms investigated at different scales.

Sensor	**Type of Product**	**Scale**	**Type of Process or Landform**
Satellite Radar (C band)	PS-InSAR analysis	Catchment or sub-catchment scale	Large landslides and deformations
Mavic 2 Pro integrated 20 mp	DEM-based change detection	Hillslope scale	Sediment accumulation and erosional processes
M2EA thermal	Thermal imagery	Hillslope scale	Humid zone and rock differentiation
Mavic 2 Pro integrated 20 mp	Optical imagery	Sub-hillslope scale	Small-scale topographic features
Mavic 2 Pro integrated 20 mp	Optical imagery-based change detection	Micro-topography scale	Rills and road crack formation or opening
Tetracam Micro-MCA6	Multispectral analysis	Sub-hillslope scale	Small-scale rock and soil differentiation
		Micro-topography scale	Seep area identification

Although the combination of the aforementioned remote sensing techniques provided crucial insights into the slope deformation processes, some limitations in their applicability to our case study need to be considered. Despite the great advantage of free and open data, Sentinel C-band sensors are significantly affected by vegetation coverage, causing decorrelation issues that could reduce the quality of the interferometric measurements and limit the accuracy and reliability of PS-InSAR for slope monitoring. Further improvements could be accomplished by employing sensors with longer wavelength characteristics (*i.e.*, L-band sensors), better suited for monitoring slope movements in dense vegetation contexts due to their large penetration depths into canopies [El Hajj et al., 2019]. On the other hand, even if UAS-based data can be successfully employed for detecting and monitoring subtle or localised deformations, they are often impacted by weather and environmental conditions and can experience data processing challenges. Even slight illumination conditions can affect the reliability of thermic acquisition and optical analysis such as radiometric change detection, which in some cases faced shadowing issues. Therefore, well-planned UAS surveys are necessary (but not always easy to accomplish) for obtaining reliable results.

Within the framework of assessing rockfall hazards along transportation corridors, it is crucial to ensure the safety and functionality of these vital infrastructure networks. Debris and block detachments pose significant risks to motorists, leading to accidents, road closures, and costly maintenance operations. Transportation agencies are therefore tasked with identifying and prioritising the most dangerous slopes that require immediate attention and allocation of resources. However, with extensive highway networks spanning vast areas, it becomes crucial for transportation agencies to adopt an effective yet rapid approach to evaluate and rank the hazardous slopes. The traditional field-based methods, while reliable, can be time-consuming, labour-intensive, and often limited in scope. In the current trend of implementing identification and rating systems for slopes affected by instability along infrastructures, previous studies [Sarro et al., 2018; Francioni et al., 2020; Rodriguez et al., 2020; Gallo et al., 2021; Migliazza et al., 2022; Žabota et al., 2023; Caliò et al., 2023; Graber and Santi, 2023] have predominantly focused on characterising local-scale discontinuities within rock masses. The recognition and characterization of families of discontinuities, extensively studied in the literature, are necessary to understand the potential kinematics of block or debris detachment. However, it is fundamental to recognize that these factors alone are not the sole contributors predisposing a slope to collapse. Fluctuations in the temperature and water content, as well as the differential erosion affecting the sandstone and siltstone alternation, influence the weathering of rock slopes [Draebing, 2021; Birien and Gauthier, 2023]. In this context, our study addresses the pressing need for an improved and replicable methodology that takes advantage of remote sensing data to facilitate the rapid quantification of those factors influencing rock mass stability. The approach employed in our study demonstrates that combining various remote sensing techniques enhances the identification of geomorphic processes and their impacts at different spatial scales. These outcomes provide valuable and practical insights that can be considered by transportation agencies when ranking slopes and assessing rockfall hazards through rockfall hazard rating systems (RHRS) [Santi et al., 2009]. The rationale of this engineering procedure is to classify high-risk slopes along transportation corridors, assigning a score based on several criteria, including factors such as ditch effectiveness, differential erosion rates and water presence. The traditional field-based RHRS encounters limitations due to time-consuming on-field measurements and potential underestimation of these factors, often addressed qualitatively. These limitations arise from restricted view angles, challenges in accessing certain sections of near-vertical or highly inclined slope surfaces, and the difficulty of investigating parameters at different scales while achieving a comprehensive understanding of the interconnected degradational processes [Oommen et al., 2017]. With its multiscale, remotely sensed perspective, our study highlights the significance of providing a methodical and repeatable procedure to be implemented in the current rating systems for monitoring the sites and updating the assigned rating considering the spatio-temporal morphoevolution of the slope conditions. Furthermore, it takes into account the spatial variability and influence of pre-failure factors by employing different sensors and processing analyses.

6.6 Conclusions

Due to the mountainous topography of Colorado, much of the State Highway network has been developed through cut slopes. Along with predisposing factors such as the lithological asset and the road cuts, denudation processes play a fundamental role in destabilising the unconsolidated material and the deterioration of the exposed rocks. The investigation approach adopted in the present work succeeded in efficiently detecting the instabilities affecting the two slopes of interest along the Colorado SH133. In particular, the key findings of our work can be summarised as follows:

1. The combination of different platforms (satellite or UAS) and sensors, along with their respective products at varying spatial resolutions, was essential to identify several superimposed processes. Each informative level (i.e., multispectral and SAR analysis, thermal and optical products, terrain models), enabled distinguishing the specific geomorphic expression of the different degradation processes. In doing so, we shed light on the landform's multi-scale characteristics, thus interpreting their potential to differentially disrupt the slope stability. Moreover, the examples of retrogressive erosion and rill initiation retrieved in both study areas represent early predictors of future rock failures or road collapses.
2. The fourth dimension (i.e., time), explored through the use of multi-temporal data collections, provides a significant amplification of the potential of a single remote sensing survey. Change detection and interferometric analyses allowed the quantitative assessment of the dynamics of morphological features (e.g., road crack propagation, areas more susceptible to depletion or sediment accumulation) and a preliminary forecast of their morphoevolution.
3. Unusual processing solutions, such as optical-based change detection, can lead to new opportunities for micro-morphotype detection and characterization. This technique could serve as a primary step for a more quantitative assessment of the slope erosion rates and geostructural stability.
4. Remote sensing data can provide a detailed model of the slope's mechanics and conditions at a specific time. This information is particularly beneficial for monitoring highway networks and transportation corridors, supporting asset management practices from a predictive maintenance perspective.

7 Conclusions

The primary aim of this study was to investigate the application of remotely sensed data, specifically satellite interferometry information, for updating landslide inventories from a morphographic and morphodynamic point of view, and subsequently providing a clear direction on identifying high-priority areas warranting in-depth investigations. At every scale, from regional to local mapping, the support of artificial intelligence facilitated the effective management of a vast amount of data that can be challenging to handle through traditional inventory methods. Utilising machine learning algorithms tailored to the specific needs and goals of each presented work, we achieved an objective recognition of spatial and temporal displacement patterns that is challenging to attain with methods dependent on the operator's judgement, which undoubtedly introduces a bias related to his own experience and sensitivity during the analysis.

At the regional scale, the implemented procedure effectively aggregates interferometric data by combining geospatial criteria with velocity measurements of data points, accounting for the spatial dependence of the single measuring point with respect to its surroundings. Therefore, resulting PS clusters, aggregated according to a robust statistical criterion, accurately represent the real extension of areas experiencing active deformation, outperforming aggregation based on fixed-distance buffers. Moreover, incorporating topological constraints (*i.e.*, Slope Units) in the clustering process, favoured the correct discrimination of moving points pertaining to a specific process from those related to adjacent ones. By doing so, we avoid incorporating measuring points extending beyond physical boundaries, such as watershed limits or valleys, where aggregation would not be appropriate. Integrating this clustering process in a semi-automatic selection workflow proved its high efficacy for quickly identifying and classifying landslides that required a careful evaluation of their morphographic boundaries.

At the local scale, I achieved precise delineation of the actual deformation area of the phenomenon, including sections of the landslide where substantial displacement rates were observed, some of which had previously been excluded or remained uncertain during field operations. Additionally, for phenomena with complex kinematics or heterogeneous deformational behaviour, it became crucial to identify specific sectors within the landslide extension that required monitoring or prioritised mitigation measures. In Chapter 3 case study, the innovative utilisation of InSAR post-processing, involving a two-dimensional displacement decomposition, enabled the accurate delimitation of the various kinematics constituting the landslide system and the detection of the intervals of anomalous time trends in the displacement series. The Bayesian model applied to time series derived the probability of occurrence of abrupt changes based on the analysis of hundreds of displacement measurements, thus strengthening the correlation analysis between accelerations in disruption rates and external triggers (*i.e.*, precipitation). The resulting temporal deformation pattern of each different landslide sector did not reveal differing timings under the same preparatory and triggering factors in the specific case study. Nonetheless, it can be applied as a valuable tool in similar cases for assessing how the slope process responds to external forcings.

For those cases where the interferometric technique is not feasible to investigate slope instability, one must rely on supplementary tools capable of providing displacement measures. In the case study presented in Chapter 4, several UAS-based surveys were performed on the rock slopes susceptible to rockfalls after a large-scale InSAR screening of the slope processes affecting the sector of interest of the highway. The multispectral and optical images captured by the UAS were analysed using Object-Based Image Analysis (OBIA) and Change Detection techniques, and numerous early indicators of instability, particularly those linked to embryonic erosion, were identified. These erosional phenomena had damaged several areas, affecting at the same time the road infrastructure and the operating mitigation measures. Furthermore, the very-high ground resolution provided by the sensors mounted on the drones played a crucial role in identifying micro-scale landforms at a sub-centimetre level, from fractures along the road to rills on the slopes, which would have otherwise remained undetectable through satellite imagery. While InSAR data undeniably proved valuable in recognizing movements related to debris sliding along the slope (and potentially impacting the road in the future) or to large-scale phenomena that impacted the infrastructure in the last decades, it is the multispectral and optical information that emerges as the primary tool for identifying the areas of the slope most susceptible to disruption.

The three presented works can be considered a progressive, analytical workflow to be adopted when updating a landslide inventory. Supported by artificial intelligence models, we first identified at a regional scale those slope processes warranting detailed investigations. Then, depending on the specific landslide typology, a tailored local-scale assessment to characterise the morphoevolution of the landslide is pursued. For slow kinematic landslides, satellite interferometry provides valuable insights into both the spatial deformational patterns and, crucially, the morphodynamic response in relation to external factors like precipitation and temperature, acting as preparatory or triggering elements. For fast kinematic slope movements (such as rockfalls), or in cases where the interferometric technique is inadequate for a thorough investigation (*i.e.*, unfavourable slope orientation, geometric distortions), it becomes essential to combine the use of different platforms and sensors to properly investigate the gravitational instability. In such cases, optical and multispectral sensors carried by UAS can better perform the slope characterization to identify micro-scale landforms and detect precursors of slope instability, allowing for preventive measures instead of mitigation alone. The application of established AI models, well-documented in the literature, can be seamlessly incorporated into this multi-scale workflow, offering support to authorities responsible for updating local, regional, or even national-scale landslide inventories.

7.1 Limitations and future perspectives

The traditional machine learning techniques described in Section 2.2.2.2 are well established in the literature for identification and classification tasks. Despite the significant contribution that these techniques have and continue to have in handling vast amounts of data, there are still several limitations in terms of automation of slope process recognition. Most of the models rely on user experience for the thresholds, parameters and input datasets selection, often selecting these factors after a trial-and-error process. Furthermore, the exponential availability of spatial and temporal high-resolution data, heavily hamper the performance of ML algorithms for feature extraction tasks. For instance, the EGMS project (European Ground Motion Service) providing open-source advanced interferometric data at the European-scale spatial coverage, offers unprecedented opportunities for governments, research institutions, universities and societies to exploit such a massive and continuously updated database. Managing a database of such magnitude, especially for large-scale studies, will be one of the biggest challenges of the coming years. Future research endeavours will be dedicated to implementing increasingly automatic methods to derive morphography, morphodynamic and morphoevolution of the entire spectrum of ground deformation processes (*e.g.*, landslides, subsidence, volcanoes). These techniques will serve inventorying purposes, but, more importantly, they will enable continuous monitoring and regular updates of these phenomena. Although it is currently largely employed for object detection in optical and multispectral satellite images, Deep Learning applications will be directed towards the identification of deformational patterns both at the spatial level through the classification of PS clusters and at the temporal one, possibly predicting upcoming failures from the interferometric time series. The foremost disadvantage related to the use of Deep Learning on interferometric datasets remains the almost absence of training datasets that can contribute to adequate training of the models. It is likely that in the next few years, we'll witness the emergence of labelled interferometric data repositories, which will be increasingly exploited to train and improve the recognition performance of these models. At the same time, it will become compulsory to enforce the automatic incorporation of such open-source data into civil protection frameworks and long-term monitoring strategies to act for forecasting, prevention and emergency stages. Across the different phases of risk management (*i.e.*, pre and post-crisis), the InSAR information can serve as an effective operational tool, even if the monitoring and especially prevision of upcoming failures will represent a critical challenge in the forthcoming decade.

8 References

1. Abellán, A.; Calvet, J.; Vilaplana, J.M.; Blanchard, J. Detection and spatial prediction of rockfalls by means of terrestrial laser scanner monitoring. Geomorphology 2010, 119, 162–171, doi:10.1016/j.geomorph.2010.03.016
2. Aber, J. S., Marzolff, I., Ries, J., & Aber, S. E. W. (2019). Small-format aerial photography and UAS imagery: Principles, techniques and geoscience applications. Academic Press. https://doi.org/10.1016/B978-0-12-812942-5.00010-0
3. Agliardi, F., & Crosta, G. B. (2003). High resolution three-dimensional numerical modelling of rockfalls. International Journal of Rock Mechanics and Mining Sciences, 40(4), 455-471. https://doi.org/10.1016/s1365-1609(03)00021-2
4. Agliardi, F., Crosta, G. B., and Frattini, P. (2012). 18 Slow rock-slope deformation. In J. J. Clague & D. Stead (Eds.), Landslides: Types, Mechanisms and Modeling (pp. 207–221). Chapter, Cambridge: Cambridge University Press.
5. Agliardi, F., Scuderi, M. M., Fusi, N., & Collettini, C. (2020). Slow-to-fast transition of giant creeping rockslides modulated by undrained loading in basal shear zones. Nature communications, 11(1), 1352. https://doi.org/10.1038/s41467-020-15093-3
6. Alvioli, M., Marchesini, I., Reichenbach, P., Rossi, M., Ardizzone, F., Fiorucci, F., & Guzzetti, F. (2016). Automatic delineation of geomorphological slope units with r. slopeunits v1. 0 and their optimization for landslide susceptibility modeling. Geoscientific Model Development, 9(11), 3975-3991. https://doi.org/10.5194/gmd-9-3975-2016
7. Amatya, P., Kirschbaum, D., Stanley, T., & Tanyas, H. (2021). Landslide mapping using object-based image analysis and open source tools. Engineering Geology, 282, 106000. https://doi.org/10.1016/j.enggeo.2021.106000
8. Anselin, L. (1995). Local indicators of spatial association—LISA. Geographical analysis, 27(2), 93-115.
9. Antonielli, B., Mazzanti, P., Rocca, A., Bozzano, F., & Dei Cas, L. (2019). A-DInSAR performance for updating landslide inventory in mountain areas: An example from lombardy region (Italy). Geosciences, 9(9), 364. https://doi.org/10.3390/geosciences9090364
10. Ardizzone, F., Cardinali, M., Galli, M., Guzzetti, F., & Reichenbach, P. (2007). Identification and mapping of recent rainfall-induced landslides using elevation data collected by airborne Lidar. Natural Hazards and Earth System Sciences, 7(6), 637-650. https://doi.org/10.5194/nhess-7-637-2007
11. Ardizzone, F., Bucci, F., Cardinali, M., Fiorucci, F., Pisano, L., Santangelo, M., & Zumpano, V. (2023). Geomorphological landslide inventory map of the Daunia Apennines, southern Italy. Earth System Science Data, 15(2), 753-767. https://doi.org/10.5194/essd-15-753-2023
12. Aringoli, D., Gentili, B., Materazzi, M., & Pambianchi, G. (2010). Deep-seated gravitational slope deformations in active tectonics areas of the Umbria-Marche Apennine (Central Italy). Geogr. Fis. Dinam. Quat, 33(2), 127-140.
13. Arpin, B., & Arndt, B. (2016). Comparison of 2D and 3D rockfall modeling for rockfall mitigation design. In 67th Highway Geology SymposiumHighway Geology Symposium.
14. Aslan, G., Foumelis, M., Raucoules, D., De Michele, M., Bernardie, S., & Cakir, Z. (2020). Landslide mapping and monitoring using persistent scatterer interferometry (PSI) technique in the French Alps. Remote Sensing, 12(8), 1305. https://doi.org/10.3390/rs12081305
15. Asokan, A.; Anitha, J.J.E.S.I. (2019). Change detection techniques for remote sensing applications: a survey. Earth Sci. Informatics, 12, 143–160. https://doi.org/10.1007/s12145-019-00380-5.

16. Aswathi, J.; Binoj Kumar, R.B.; Oommen, T.; Bouali, E.H.; Sajinkumar, K.S. (2022). InSAR as a tool for monitoring hydropower projects: A review. Energy Geosci., 3, 160–171. https://doi.org/10.1016/j.engeos.2021.12.007.
17. Bardi, F., Frodella, W., Ciampalini, A., Bianchini, S., Del Ventisette, C., Gigli, G., ... & Casagli, N. (2014). Integration between ground based and satellite SAR data in landslide mapping: The San Fratello case study. Geomorphology, 223, 45-60. https://doi.org/10.1016/j.geomorph.2014.06.025
18. Barra, A., Monserrat, O., Mazzanti, P., Esposito, C., Crosetto, M., & Scarascia Mugnozza, G. (2016). First insights on the potential of Sentinel-1 for landslides detection. Geomatics, Natural Hazards and Risk, 7(6), 1874-1883. https://doi.org/10.1080/19475705.2016.1171258
19. Barra, A., Solari, L., Béjar-Pizarro, M., Monserrat, O., Bianchini, S., Herrera, G., ... & Moretti, S. (2017). A methodology to detect and update active deformation areas based on Sentinel-1 SAR images. Remote sensing, 9(10), 1002. https://doi.org/10.3390/rs9101002
20. Bell, R., Petschko, H., Röhrs, M., & Dix, A. (2012). Assessment of landslide age, landslide persistence and human impact using airborne laser scanning digital terrain models. Geografiska Annaler: Series A, Physical Geography, 94(1), 135-156. https://doi.org/10.1111/j.1468-0459.2012.00454.x
21. Berardino, P., Fornaro, G., Lanari, R., & Sansosti, E. (2002). A new algorithm for surface deformation monitoring based on small baseline differential SAR interferograms. IEEE Transactions on geoscience and remote sensing, 40(11), 2375-2383. https://doi.org/10.1109/TGRS.2002.803792
22. Bianchi, C., & Salvati, P. (2023). Rapporto Periodico sul Rischio posto alla Popolazione italiana da Frane e Inondazioni. Anno 2022, Istituto di Ricerca per la Protezione Idrogeologica (IRPI), Consiglio Nazionale delle Ricerche (CNR) (in Italian). https://doi.org/10.30437/REPORT2021.
23. Bianchini, S., Cigna, F., Righini, G., Proietti, C., & Casagli, N. (2012). Landslide hotspot mapping by means of persistent scatterer interferometry. Environmental Earth Sciences, 67, 1155-1172. https://doi.org/10.1007/s12665-012-1559-5
24. Bianchini, S., Herrera, G., Mateos, R. M., Notti, D., Garcia, I., Mora, O., & Moretti, S. (2013). Landslide activity maps generation by means of persistent scatterer interferometry. Remote Sensing, 5(12), 6198-6222. https://doi.org/10.3390/rs5126198
25. Bianchini, S., Raspini, F., Solari, L., Del Soldato, M., Ciampalini, A., Rosi, A., & Casagli, N. (2018). From picture to movie: Twenty years of ground deformation recording over Tuscany region (Italy) with satellite InSAR. Frontiers in Earth Science, 6, 177. https://doi.org/10.3389/feart.2018.00177
26. Birien, T.; Gauthier, F. (2023). Influence of climate-dependent variables on deformation and differential erosion of stratified sedimentary rocks. Geomorphology, 421, 108518. https://doi.org/10.1016/j.geomorph.2022.108518
27. Bigi, S., Casero, P., & Ciotoli, G. (2011). Seismic interpretation of the Laga basin; constraints on the structural setting and kinematics of the Central Apennines. Journal of the Geological Society, 168(1), 179-190. https://doi.org/10.1144/0016-76492010-084
28. Bigot-Cormier, F., Braucher, R., Bourlès, D., Guglielmi, Y., Dubar, M., & Stéphan, J. F. (2005). Chronological constraints on processes leading to large active landslides. Earth and Planetary Science Letters, 235(1-2), 141-150. https://doi.org/10.1016/j.epsl.2005.03.012
29. Blaschke, T., Lang, S., & Hay, G. (Eds.). (2008). Object-based image analysis: spatial concepts for knowledge-driven remote sensing applications. Springer Science & Business Media.
30. Bonì, R., Bordoni, M., Colombo, A., Lanteri, L., & Meisina, C. (2018). Landslide state of activity maps by combining multi-temporal A-DInSAR (LAMBDA). Remote sensing of environment, 217, 172-190. https://doi.org/10.1016/j.rse.2018.08.013
31. Bonì, R., Bordoni, M., Vivaldi, V., Troisi, C., Tararbra, M., Lanteri, L., ... & Meisina, C. (2020). Assessment of the Sentinel-1 based ground motion data feasibility for large scale landslide monitoring. Landslides, 17, 2287-2299. https://doi.org/10.1007/s10346-020-01433-3

32. Bordoni, M., Bonì, R., Colombo, A., Lanteri, L., & Meisina, C. (2018). A methodology for ground motion area detection (GMA-D) using A-DInSAR time series in landslide investigations. Catena, 163, 89-110. https://doi.org/10.1016/j.catena.2017.12.013
33. Bossi, G., Cavalli, M., Crema, S., Frigerio, S., Quan Luna, B., Mantovani, M., ... & Pasuto, A. (2015). Multi-temporal LiDAR-DTMs as a tool for modelling a complex landslide: A case study in the Rotolon catchment (eastern Italian Alps). Natural Hazards and Earth System Sciences, 15(4), 715-722. https://doi.org/10.5194/nhess-15-715-2015
34. Bozzano F., Gambino P., Prestininzi A., Scarascia Mugnozza G. & Valentini G. (1998): Groundeffects induced by the Umbria Marche earthquakes of September-October 1997, Central Italy.Proc. 8th Cong. IAEG, Vancouver, 2, 825-830.
35. Bozzano, F., Mazzanti, P., Prestininzi, A., & Scarascia Mugnozza, G. (2010). Research and development of advanced technologies for landslide hazard analysis in Italy. Landslides, 7, 381-385. https://doi.org/10.1007/s10346-010-0208-x
36. Bozzano, F., Mazzanti, P., Perissin, D., Rocca, A., De Pari, P., & Discenza, M. E. (2017a). Basin scale assessment of landslides geomorphological setting by advanced InSAR analysis. Remote Sensing, 9(3), 267. https://doi.org/10.3390/rs9030267
37. Bozzano, F., Caporossi, P., Esposito, C., Martino, S., Mazzanti, P., Moretto, S., ... & Rizzo, A. M. (2017b). Mechanism of the Montescaglioso landslide (Southern Italy) inferred by geological survey and remote sensing. In Advancing Culture of Living with Landslides: Volume 2 Advances in Landslide Science (pp. 97-106). Springer International Publishing. https://doi.org/10.1007/978-3-319-53498-5_12
38. Brabb, E. E., & Pampeyan, E. H. (1972). Preliminary map of landslide deposits in San Mateo County, California (No. 344). US Geological Survey. https://doi.org/10.3133/mf344
39. Brabb, E. E., & Harrod, B. L. (1989). Landslides: extent and economic significance: proceedings of the 28th international geological congress: symposium on landslides, Washington DC, 17 July 1989.
40. Brabb, E. E. (1991). The world landslide problem. Episodes Journal of International Geoscience, 14(1), 52-61. https://doi.org/10.18814/epiiugs/1991/v14i1/008
41. Brabb, E. E. (1995). The San Mateo County California GIS project for predicting the consequences of hazardous geologic processes. In Geographical information systems in assessing natural hazards (pp. 299-334). Dordrecht: Springer Netherlands.
42. Bucknam, R. C., Coe, J. A., Chavarría, M. M., Godt, J. W., Tarr, A. C., Bradley, L. A., ... & Johnson, M. L. (2001). Landslides triggered by Hurricane Mitch in Guatemala–inventory and discussion. US Geological Survey Open File Report, 1.
43. Caliò, D.; Mineo, S.; Pappalardo, G. (2023). Digital Rock Mass Analysis for the Evaluation of Rockfall Magnitude at Poorly Accessible Cliffs. Remote Sens, 15, 1515. https://doi.org/10.3390/rs15061515.
44. Calligaris, C., Poretti, G., Tariq, S., & Melis, M. T. (2013). First steps towards a landslide inventory map of the Central Karakoram National Park. European Journal of Remote Sensing, 46(1), 272-287. https://doi.org/10.5721/EuJRS20134615
45. Calò, F., Ardizzone, F., Castaldo, R., Lollino, P., Tizzani, P., Guzzetti, F., ... & Manunta, M. (2014). Enhanced landslide investigations through advanced DInSAR techniques: The Ivancich case study, Assisi, Italy. Remote Sensing of Environment, 142, 69-82. https://doi.org/10.1016/j.rse.2013.11.003
46. Calvello, M., & Pecoraro, G. (2018). FraneItalia: a catalog of recent Italian landslides. Geoenvironmental Disasters 5: 13. https://doi.org/10.1186/s40677-018-0105-5
47. Caprari, P., Della Seta, M., Martino, S., Fantini, A., Fiorucci, M., & Priore, T. (2018). Upgrade of the CEDIT database of earthquake-induced ground effects in Italy. Italian Journal of Engineering Geology and Environment, 18(2), 23-39. https://doi.org/10.4408/IJEGE.2018-02.O-02
48. Cardinali, M., Guzzetti, F., & Brabb, E. E. (1990). Preliminary maps showing landslide deposits and related features in New Mexico (No. 90-293). US Geological Survey. https://doi.org/10.3133/ofr90293

49. Cardinali, M., Ardizzone, F., Galli, M., Guzzetti, F., & Reichenbach, P. (2000, October). Landslides triggered by rapid snow melting: the December 1996–January 1997 event in Central Italy. In Proceedings 1st Plinius conference on Mediterranean storms (pp. 439-448). Bios: Cosenza.
50. Carlà, T.; Nolesini, T.; Solari, L.; Rivolta, C.; Dei Cas, L.; Casagli, N. (2019). Rockfall forecasting and risk management along a major transportation corridor in the Alps through ground-based radar interferometry. Landslides, 16, 1425–1435. https://doi.org/10.1007/s10346-019-01190-y.
51. Carminati, E., & Doglioni, C. (2012). Alps vs. Apennines: The paradigm of a tectonically asymmetric Earth. Earth-Science Reviews, 112(1-2), 67-96. https://doi.org/10.1016/j.earscirev.2012.02.004
52. Carrara, A., & Merenda, L. (1976). Landslide inventory in northern Calabria, southern Italy. Geological Society of America Bulletin, 87(8), 1153-1162. https://doi.org/10.1130/0016-7606(1976)87<1153:LIINCS>2.0.CO;2
53. Carrara, A., Pugliese Carratelli, E., & Merenda, L. (1977). Computer-based data bank and statistical analysis of slope instability phenomena; Computer-based data bank and statistical analysis of slope instability phenomena. Zeitschrift fur Geomorphologie, 21(2). https://doi.org/187-222. 10.1127/zfg/21/1977/187
54. Carrara, A., Cardinali, M., Guzzetti, F., & Reichenbach, P. (1995). GIS technology in mapping landslide hazard. In Geographical information systems in assessing natural hazards (pp. 135-175). Dordrecht: Springer Netherlands. https://doi.org/10.1007/978-94-015-8404-3_8
55. Casale, R., Fantechi, R., & Flageolet, J. C. (1994). Temporal Occurrence and Forecasting of Landslides in the European Community - Final Report. European Community - Programme Epoch (Ct. 90 00251), 957.
56. Cascini, L., Fornaro, G., & Peduto, D. (2009). Analysis at medium scale of low-resolution DInSAR data in slow-moving landslide-affected areas. ISPRS Journal of Photogrammetry and Remote Sensing, 64(6), 598-611. https://doi.org/10.1016/j.isprsjprs.2009.05.003
57. Catani, F. (2021). Landslide detection by deep learning of non-nadiral and crowdsourced optical images. Landslides, 18(3), 1025-1044. https://doi.org/10.1007/s10346-020-01513-4
58. Catapano, F., Malafronte, R., Lepre, F., Cozzolino, P., Arnone, R., Lorenzo, E., ... & Maj, M. (2001). Psychological consequences of the 1998 landslide in Sarno, Italy: a community study. Acta Psychiatrica Scandinavica, 104(6), 438-442. https://doi.org/10.1034/j.1600-0447.2001.00512.x
59. Chen, W., Li, X., Wang, Y., Chen, G., & Liu, S. (2014). Forested landslide detection using LiDAR data and the random forest algorithm: A case study of the Three Gorges, China. Remote sensing of environment, 152, 291-301. https://doi.org/10.1016/j.rse.2014.07.004
60. Chen, Z., Zhang, Y., Ouyang, C., Zhang, F., & Ma, J. (2018). Automated landslides detection for mountain cities using multi-temporal remote sensing imagery. Sensors, 18(3), 821. https://doi.org/10.3390/s18030821
61. Cheng, L., Li, J., Duan, P., & Wang, M. (2021). A small attentional YOLO model for landslide detection from satellite remote sensing images. Landslides, 18(8), 2751-2765. https://doi.org/10.1007/s10346-021-01694-6
62. Christensen, N.S., Wood, A.W., Voisin, N. et al. (2004). The Effects of Climate Change on the Hydrology and Water Resources of the Colorado River Basin. Climatic Change 62, 337–363. https://doi.org/10.1023/B:CLIM.0000013684.13621.1f
63. Ciampalini, A., Cigna, F., Del Ventisette, C., Moretti, S., Liguori, V., & Casagli, N. (2012). Integrated geomorphological mapping in the north-western sector of Agrigento (Italy). Journal of Maps, 8(2), 136-145. https://doi.org/10.1080/17445647.2012.680775
64. Ciampalini, A., Raspini, F., Frodella, W., Bardi, F., Bianchini, S., & Moretti, S. (2016). The effectiveness of high-resolution LiDAR data combined with PSInSAR data in landslide study. Landslides, 13, 399-410. https://doi.org/10.1007/s10346-015-0663-5

65. Cigna, F., Bianchini, S., & Casagli, N. (2013). How to assess landslide activity and intensity with Persistent Scatterer Interferometry (PSI): the PSI-based matrix approach. Landslides, 10, 267-283. https://doi.org/10.1007/s10346-012-0335-7
66. Colorado Climate Center, n.d. Providing information and expertise on Colorado's complex climate. https://climate.colostate.edu (Last accessed on 19/12/2023)
67. Conforti, M., Muto, F., Rago, V., & Critelli, S. (2014). Landslide inventory map of north-eastern Calabria (South Italy). Journal of maps, 10(1), 90-102. https://doi.org/10.1080/17445647.2013.852142
68. Confuorto, P., Casagli, N., Casu, F., De Luca, C., Del Soldato, M., Festa, D., ... & Raspini, F. (2023). Sentinel-1 P-SBAS data for the update of the state of activity of national landslide inventory maps. Landslides, 20(5), 1083-1097. https://doi.org/10.1007/s10346-022-02024-0
69. Corominas, J., van Westen, C., Frattini, P., Cascini, L., Malet, J. P., Fotopoulou, S., ... & Smith, J. T. (2014). Recommendations for the quantitative analysis of landslide risk. Bulletin of engineering geology and the environment, 73, 209-263. https://doi.org/10.1007/s10064-013-0538-8
70. Cosentino, A.; Brunetti, A.; Fiorio, M.; Gaeta, M.; Mazzanti, P. (2022). IRIS a new powerful tool for Geohazards Assessment by PhotoMonitoring. In Proceedings of Asita Conference, Genova, Italy, 20–24 June 2022
71. Costantini, M., Minati, F., Trillo, F., Ferretti, A., Novali, F., Passera, E., ... & Andersen, H. S. (2021, July). European ground motion service (EGMS). In 2021 IEEE International Geoscience and Remote Sensing Symposium IGARSS (pp. 3293-3296). IEEE. https://doi.org/10.1109/IGARSS47720.2021.9553562
72. Crippa, C., Franzosi, F., Zonca, M., Manconi, A., Crosta, G. B., Dei Cas, L., & Agliardi, F. (2020). Unraveling spatial and temporal heterogeneities of very slow rock-slope deformations with targeted DInSAR analyses. Remote Sensing, 12(8), 1329. https://doi.org/10.3390/rs12081329
73. Crippa, C., & Agliardi, F. (2021). Practical estimation of landslide kinematics using PSI data. Geosciences, 11(5), 214. https://doi.org/10.3390/geosciences11050214
74. Crippa, C., Valbuzzi, E., Frattini, P., Crosta, G. B., Spreafico, M. C., & Agliardi, F. (2021). Semi-automated regional classification of the style of activity of slow rock-slope deformations using PS InSAR and SqueeSAR velocity data. Landslides, 18, 2445-2463. https://doi.org/10.1007/s10346-021-01654-0
75. Crosta, G. B., & Agliardi, F. (2002). How to obtain alert velocity thresholds for large rockslides. Physics and Chemistry of the Earth, Parts A/B/C, 27(36), 1557-1565. https://doi.org/10.1016/S1474-7065(02)00177-8
76. Crosta, G. B., & Agliardi, F. (2003). A methodology for physically based rockfall hazard assessment. Natural Hazards and Earth System Sciences, 3(5), 407-422. https://doi.org/10.5194/nhess-3-407-2003
77. Crosta, G. B., Frattini, P., & Agliardi, F. (2013). Deep seated gravitational slope deformations in the European Alps. Tectonophysics, 605, 13-33. https://doi.org/10.1016/j.tecto.2013.04.028
78. Crosta, G. B., Di Prisco, C., Frattini, P., Frigerio, G., Castellanza, R., & Agliardi, F. (2014). Chasing a complete understanding of the triggering mechanisms of a large rapidly evolving rockslide. Landslides, 11, 747-764. https://doi.org/10.1007/s10346-013-0433-1
79. Crosta, G. B., Agliardi, F., Rivolta, C., Alberti, S., & Dei Cas, L. (2017). Long-term evolution and early warning strategies for complex rockslides by real-time monitoring. Landslides, 14, 1615-1632. https://doi.org/10.1007/s10346-017-0817-8
80. Cruden, D. (1991). A simple definition of a landslide. Bulletin of Engineering Geology & the Environment, 43(1).
81. Cruden, D. M., Krauter, E., Beltran, L., Lefebvre, G., Ter-Stepanian, G. I., & Zhang, Z. Y. (1994). Describing landslides in several languages: the multilingual landslide glossary. In International congress International Association of Engineering Geology (pp. 1325-1333).

82. Cruden, D. M., & Varnes, D. J. (1996). Landslides: investigation and mitigation. Chapter 3-Landslide types and processes. Transportation research board special report, (247).

83. Damm, B., & Klose, M. (2015). The landslide database for Germany: Closing the gap at national level. Geomorphology, 249, 82-93. https://doi.org/10.1016/j.geomorph.2015.03.021

84. Danneels, G., Pirard, E., & Havenith, H. B. (2007, July). Automatic landslide detection from remote sensing images using supervised classification methods. In 2007 IEEE international geoscience and remote sensing symposium (pp. 3014-3017). https://doi.org/IEEE. 10.1109/IGARSS.2007.4423479

85. Delchiaro, M., Della Seta, M., Martino, S., Dehbozorgi, M., & Nozaem, R. (2019). Reconstruction of river valley evolution before and after the emplacement of the giant Seymareh rock avalanche (Zagros Mts., Iran). Earth Surface Dynamics, 7(4), 929-947. https://doi.org/10.5194/esurf-7-929-2019

86. Delchiaro, M., Della Seta, M., Martino, S., Nozaem, R., & Moumeni, M. (2023). Tectonic deformation and landscape evolution inducing mass rock creep driven landslides: The Loumar case-study (Zagros Fold and Thrust Belt, Iran). Tectonophysics, 846, 229655. https://doi.org/10.1016/j.tecto.2022.229655

87. Della Seta, M., Esposito, C., Marmoni, G. M., Martino, S., Mugnozza, G. S., & Troiani, F. (2017). Morpho-structural evolution of the valley-slope systems and related implications on slope-scale gravitational processes: New results from the Mt. Genzana case history (Central Apennines, Italy). Geomorphology, 289, 60-77. https://doi.org/10.1016/j.geomorph.2016.07.003

88. Del Soldato, M., Di Martire, D., Bianchini, S., Tomás, R., De Vita, P., Ramondini, M., ... & Calcaterra, D. (2019). Assessment of landslide-induced damage to structures: the Agnone landslide case study (southern Italy). Bulletin of Engineering Geology and the Environment, 78, 2387-2408. https://doi.org/10.1007/s10064-018-1303-9

89. Del Ventisette, C., Casagli, N., Fortuny-Guasch, J., & Tarchi, D. (2012). Ruinon landslide (Valfurva, Italy) activity in relation to rainfall by means of GBInSAR monitoring. Landslides, 9, 497-509. https://doi.org/10.1007/s10346-011-0307-3

90. Devoto, S.; Macovaz, V.; Mantovani, M.; Soldati, M.; Furlani, S. (2020). Advantages of Using UAV Digital Photogrammetry in the Study of Slow-Moving Coastal Landslides. Remote Sensing, 12, 3566. https://doi.org/10.3390/rs12213566

91. Di Bucci, D., Buttinelli, M., D'Ambrogi, C., Scrocca, D., Anzidei, M., Basili, R., ... & Villani, F. (2021). RETRACE-3D project: a multidisciplinary collaboration to build a crustal model for the 2016-2018 central Italy seismic sequence. Bollettino di Geofisica Teorica e Applicata. https://doi.org/10.4430/bgta0343

92. Di Matteo, L., Cardinali, R., Cerboni, V., Guadagnano, F., Piagnani, G., Ribaldi, C., ... & Cencetti, C. (2023). Integrated Approaches for Field Mapping by Traditional Investigation and Satellite PSInSAR Data: Results from the Montemartano Landslide (Central Italy). Remote Sensing, 15(5), 1221. https://doi.org/10.3390/rs15051221

93. Di Martire, D., Paci, M., Confuorto, P., Costabile, S., Guastaferro, F., Verta, A., & Calcaterra, D. (2017). A nation-wide system for landslide mapping and risk management in Italy: The second Not-ordinary Plan of Environmental Remote Sensing. International journal of applied earth observation and geoinformation, 63, 143-157. https://doi.org/10.1016/j.jag.2017.07.018

94. Dikau, R., Cavallini, A., Jäger, S. (1996). Databases and GIS for landslide research in Europe. Geomorphology, 15(3-4), 95-116. https://doi.org/10.1016/0169-555X(95)00072-D

95. Ding, A., Zhang, Q., Zhou, X., & Dai, B. (2016, November). Automatic recognition of landslide based on CNN and texture change detection. In 2016 31st Youth Academic Annual Conference of Chinese Association of Automation (YAC) (pp. 444-448). IEEE. https://doi.org/10.1109/YAC.2016.7804935

96. Dini, B., Manconi, A., & Loew, S. (2019). Investigation of slope instabilities in NW Bhutan as derived from systematic DInSAR analyses. Engineering Geology, 259, 105111. https://doi.org/10.1016/j.enggeo.2019.04.008

97. Dong, J., Zhang, L., Li, M., Yu, Y., Liao, M., Gong, J., & Luo, H. (2018). Measuring precursory movements of the recent Xinmo landslide in Mao County, China with Sentinel-1 and ALOS-2 PALSAR-2 datasets. Landslides, 15, 135-144. https://doi.org/10.1007/s10346-017-0914-8

98. Dong, Y., Liao, Z., Wang, J., Liu, Q., & Cui, L. (2023). Potential failure patterns of a large landslide complex in the Three Gorges Reservoir area. Bulletin of Engineering Geology and the Environment, 82(1), 41. https://doi.org/10.1007/s10064-022-03062-7

99. Draebing, D. (2021). Identification of rock and fracture kinematics in high alpine rockwalls under the influence of elevation. Earth Surf. Dyn., 9, 977–994. https://doi.org/10.5194/esurf-9-977-2021.

100. Dragićević, S. (2004). Fuzzy sets for representing the spatial and temporal dimensions in GIS databases. In Spatio-Temporal Databases: Flexible Querying and Reasoning (pp. 11-27). Berlin, Heidelberg: Springer Berlin Heidelberg.

101. Dramis, F., Guida, D., & Cestari, A. (2011). Nature and aims of geomorphological mapping. In Developments in earth surface processes (Vol. 15, pp. 39-73). Elsevier. https://doi.org/10.1016/B978-0-444-53446-0.00003-3

102. Duman, T. Y., Çan, T., Emre, Ö., Keçer, M., Doğan, A., Ateş, Ş., & Durmaz, S. (2005). Landslide inventory of northwestern Anatolia, Turkey. Engineering geology, 77(1-2), 99-114. https://doi.org/10.1016/j.enggeo.2004.08.005

103. Dunrud, C.R. (1989). Geologic Map and Coal Stratigraphic Framework of the Paonia Area, Delta and Gunnison Counties, Colorado; (No. 115); USGA: Reston, VA, USA. https://doi.org/10.3133/coal115

104. EEA, E. (2010). Mapping the impacts of natural hazards and technological accidents in Europe. An overview of the last decade. EEA, Copenhagen.

105. El Bedoui, S., Guglielmi, Y., Lebourg, T., & Pérez, J. L. (2009). Deep-seated failure propagation in a fractured rock slope over 10,000 years: the La Clapière slope, the south-eastern French Alps. Geomorphology, 105(3-4), 232-238. https://doi.org/10.1016/j.geomorph.2008.09.025

106. El Hajj, M.; Baghdadi, N.; Zribi, M. (2019). Comparative analysis of the accuracy of surface soil moisture estimation from the C- and L-bands. Int. J. Appl. Earth Obs. Geoinf., 82, 101888. https://doi.org/10.1016/j.jag.2019.05.021.

107. Ellen, S. D., & Wieczorek, G. F. (1988). Landslides, floods, and marine effects of the storm of January 3-5, 1982, in the San Francisco Bay region, California (Vol. 1434). US Government Printing Office.

108. Ellis, M. S., & Gabaldo, V. (1989). Geologic map and cross sections of parts of the Grand Junction and Delta 30’x60’quadrangles. West-Central Colorado: US Geological Survey Coal Investigation Map C-124, scale, 1(100,000).

109. Eriksen, H. Ø., Lauknes, T. R., Larsen, Y., Corner, G. D., Bergh, S. G., Dehls, J., & Kierulf, H. P. (2017). Visualizing and interpreting surface displacement patterns on unstable slopes using multi-geometry satellite SAR interferometry (2D InSAR). Remote Sensing of Environment, 191, 297-312. https://doi.org/10.1016/j.rse.2016.12.024

110.Esposito, E., Porfido, S., Simonelli, A. L., Mastrolorenzo, G., & Iaccarino, G. (2000). Landslides and other surface effects induced by the 1997 Umbria–Marche seismic sequence. Engineering geology, 58(3-4), 353-376. https://doi.org/10.1016/S0013-7952(00)00035-1

111.Evans, S. G., Mugnozza, G. S., Strom, A., & Hermanns, R. L. (Eds.). (2007). Landslides from massive rock slope failure (Vol. 49). Springer Science & Business Media.

112.Fan, X., Scaringi, G., Korup, O., West, A. J., van Westen, C. J., Tanyas, H., ... & Huang, R. (2019). Earthquake-induced chains of geologic hazards: Patterns, mechanisms, and impacts. Reviews of geophysics, 57(2), 421-503. https://doi.org/10.1029/2018RG000626

113.Farina, P., Moretti, S., Colombo, D., Fumagalli, A., & Manunta, P. (2004, September). Landslide risk analysis by means of remote sensing techniques: results from the ESA/SLAM project. In IGARSS 2004. 2004 IEEE International Geoscience and Remote Sensing Symposium (Vol. 1). IEEE. https://doi.org/10.1109/IGARSS.2004.1368945

114.Farmakis, I.; Marinos, V.; Papathanassiou, G.; Karantanellis, E. (2020). Automated 3D Jointed Rock Mass Structural Analysis and Characterization Using LiDAR Terrestrial Laser Scanner for Rockfall Susceptibility Assessment: Perissa Area Case (Santorini). Geotech. Geol. Eng., 38, 3007–3024. https://doi.org/10.1007/s10706-020-01203-x.

115.Ferretti, A., Prati, C., & Rocca, F. (2000). Nonlinear subsidence rate estimation using permanent scatterers in differential SAR interferometry. IEEE Transactions on geoscience and remote sensing, 38(5), 2202-2212. https://doi.org/10.1109/36.868878

116.Ferretti, A., Prati, C., & Rocca, F. (2001). Permanent scatterers in SAR interferometry. IEEE Transactions on geoscience and remote sensing, 39(1), 8-20. https://doi.org/10.1109/36.898661

117.Festa, D., Bonano, M., Casagli, N., Confuorto, P., De Luca, C., Del Soldato, M., ... & Casu, F. (2022). Nation-wide mapping and classification of ground deformation phenomena through the spatial clustering of P-SBAS InSAR measurements: Italy case study. ISPRS Journal of Photogrammetry and Remote Sensing, 189, 1-22. https://doi.org/10.1016/j.isprsjprs.2022.04.022

118.Fick, S.E. and R.J. Hijmans, 2017. WorldClim 2: new 1km spatial resolution climate surfaces for global land areas. International Journal of Climatology 37 (12): 4302-4315. Available at https://www.worldclim.org/data/worldclim21.html (last accessed on 19/12/2023).

119.Ficklin, D.L., Stewart I.T., & Maurer E.P. (2013) Climate Change Impacts on Streamflow and Subbasin-Scale Hydrology in the Upper Colorado River Basin. PLoS ONE 8(8): e71297. doi:10.1371/journal.pone.0071297

120.Filice, F.; Pezzo, A.; Lollino, P.; Perrotti, M.; Ietto, F. (2022). Multi-approach for the assessment of rock slope stability using in-field and UAV investigations. Bull. Eng. Geol. Environ., 81, 502. https://doi.org/10.1007/s10064-022-03007-0.

121.Fiorentino, G., Forte, A., Pagano, E., Sabetta, F., Baggio, C., Lavorato, D., ... & Santini, S. (2018). Damage patterns in the town of Amatrice after August 24th 2016 Central Italy earthquakes. Bulletin of Earthquake Engineering, 16, 1399-1423. https://doi.org/10.1007/s10518-017-0254-z

122.Fiorucci, F., Cardinali, M., Carlà, R., Rossi, M., Mondini, A. C., Santurri, L., ... & Guzzetti, F. (2011). Seasonal landslide mapping and estimation of landslide mobilization rates using aerial and satellite images. Geomorphology, 129(1-2), 59-70. https://doi.org/10.1016/j.geomorph.2011.01.013

123. Francioni, M.; Antonaci, F.; Sciarra, N.; Robiati, C.; Coggan, J.; Stead, D.; Calamita, F. (2020). Application of Unmanned Aerial Vehicle Data and Discrete Fracture Network Models for Improved Rockfall Simulations. Remote Sensing, 12, 2053. https://doi.org/10.3390/rs12122053.

124. Frattini, P., Crosta, G. B., & Allievi, J. (2013). Damage to buildings in large slope rock instabilities monitored with the PSInSAR™ technique. Remote sensing, 5(10), 4753-4773. https://doi.org/10.3390/rs5104753

125. Frattini, P., Crosta, G. B., Rossini, M., & Allievi, J. (2018). Activity and kinematic behaviour of deep-seated landslides from PS-InSAR displacement rate measurements. Landslides, 15, 1053-1070. https://doi.org/10.1007/s10346-017-0940-6

126. Freund, C. A., Clark, K. E., Curran, J. F., Asner, G. P., & Silman, M. R. (2021). Landslide age, elevation and residual vegetation determine tropical montane forest canopy recovery and biomass accumulation after landslide disturbances in the Peruvian Andes. Journal of Ecology, 109(10), 3555-3571. https://doi.org/10.1111/1365-2745.13737

127. Frodella, W., Gigli, G., Morelli, S., Lombardi, L., Casagli, N. (2017). Landslide Mapping and Characterization through Infrared Thermography (IRT): Suggestions for a Methodological Approach from Some Case Studies. Remote Sensing, 9, 1281. https://doi.org/10.3390/rs9121281.

128. Fukuoka H., Sassa K., & Scarascia Mugnozza G. (1997): Distribution of landslides triggered bythe 1995 Hyogo-ken Nanbu earthquake and long runout mechanism of the Takarazuka GolfCourse landslide. J. Phyis. of the Earth, 45, 83-90. https://doi.org/10.4294/jpe1952.45.83

129. Funning, G.J., Bürgmann, R., Ferretti, A., Novali, F., Fumagalli, A. (2007). Creep on the Rodgers Creek fault, northern San Francisco Bay area from a 10 year PS-InSAR dataset. Geophys. Res. Lett., 34. https://doi.org/10.1029/2007gl030836.

130. Fusco, F., Tufano, R., De Vita, P., Di Martire, D., Di Napoli, M., Guerriero, L., ... & Calcaterra, D. (2023). A revised landslide inventory of the Campania region (Italy). Scientific data, 10(1), 355. https://doi.org/10.1038/s41597-023-02155-6

131. Gaffney, S. P., White, J. L., & Ellis, W. L. (2002, October). Instrumentation of the DeBeque Canyon landslide at Interstate 70 in west central Colorado. In Abstracts with Programs, Geological Society of America (Vol. 34, No. 6, p. 48).

132. Galli, M., Ardizzone, F., Cardinali, M., Guzzetti, F., & Reichenbach, P. (2008). Comparing landslide inventory maps. Geomorphology, 94(3-4), 268-289. https://doi.org/10.1016/j.geomorph.2006.09.023

133. Gallo, I.G.; Martínez-Corbella, M.; Sarro, R.; Iovine, G.; López-Vinielles, J.; Hérnandez, M.; Robustelli, G.; Mateos, R.M.; García-Davalillo, J.C. (2021). An Integration of UAV-Based Photogrammetry and 3D Modelling for Rockfall Hazard Assessment: The Cárcavos Case in 2018 (Spain). Remote Sensing, 13, 3450. https://doi.org/10.3390/rs13173450.

134. Gama, F., Mura, J. C., R., Paradella, W., & G. de Oliveira, C. (2020). Deformations prior to the Brumadinho dam collapse revealed by Sentinel-1 InSAR data using SBAS and PSI techniques. Remote sensing, 12(21), 3664. https://doi.org/10.3390/rs12213664

135. Gantimurova, S.; Parshin, A.; Erofeev, V. (2021). GIS-Based Landslide Susceptibility Mapping of the Circum-Baikal Railway in Russia Using UAV Data. Remote Sensing, 13, 3629. https://doi.org/10.3390/rs13183629.

136. Gautam, P., Kubota, T., Sapkota, L. M., & Shinohara, Y. (2021). Landslide susceptibility mapping with GIS in high mountain area of Nepal: a comparison of four methods. Environ Earth Sci 80 (9): 1–18. https://doi.org/10.1007/s12665-021-09650-2

137. Ghorbanzadeh, O., Blaschke, T., Gholamnia, K., Meena, S. R., Tiede, D., & Aryal, J. (2019). Evaluation of different machine learning methods and deep-learning convolutional neural networks for landslide detection. Remote Sensing, 11(2), 196. https://doi.org/10.3390/rs11020196

138. Gischig, V., Amann, F., Moore, J. R., Loew, S., Eisenbeiss, H., & Stempfhuber, W. (2011). Composite rock slope kinematics at the current Randa instability, Switzerland, based on remote sensing and numerical modeling. Engineering Geology, 118(1-2), 37-53. https://doi.org/10.1016/j.enggeo.2010.11.006

139. Glade, T., & Crozier, M. (1996). Towards a national landslide information base for New Zealand. New Zealand Geographer, 52(1), 29-40. https://doi.org/10.1111/j.1745-7939.1996.tb00461.x

140. Glenn, N. F., Streutker, D. R., Chadwick, D. J., Thackray, G. D., & Dorsch, S. J. (2006). Analysis of LiDAR-derived topographic information for characterizing and differentiating landslide morphology and activity. Geomorphology, 73(1-2), 131-148. https://doi.org/10.1016/j.geomorph.2005.07.006

141. Godwin, L.H. (1968). Geologic Map of the Chair Mountain Quadrangle, Gunnison and Pitkin Counties, Colorado; (No. 704); USGA: Reston, VA, USA. https://doi.org/10.3133/gq704.

142. Gómez, D., García, E. F., & Aristizábal, E. (2023). Spatial and temporal landslide distributions using global and open landslide databases. Natural Hazards, 117(1), 25-55. https://doi.org/10.1007/s11069-023-05848-8

143. Google Earth Pro, v.7.3.6.9345, (2016). 39°12'23.02"N, 108°15'33.81"W, elevation 1536m

144. Gorum, T., Fan, X., van Westen, C. J., Huang, R. Q., Xu, Q., Tang, C., & Wang, G. (2011). Distribution pattern of earthquake-induced landslides triggered by the 12 May 2008 Wenchuan earthquake. Geomorphology, 133(3-4), 152-167. https://doi.org/10.1016/j.geomorph.2010.12.030

145. Graber, A.; Santi, P. (2023). UAV-photogrammetry rockfall monitoring of natural slopes in Glenwood Canyon, CO, USA: background activity and post-wildfire impacts. Landslides, 20, 229–248. https://doi.org/10.1007/s10346-022-01974-9.

146. Grechi, G., Fiorucci, M., Marmoni, G. M., & Martino, S. (2021). 3D thermal monitoring of jointed rock masses through infrared thermography and photogrammetry. Remote Sensing, 13(5), 957. https://doi.org/10.3390/rs13050957

147. Grøneng, G., Christiansen, H. H., Nilsen, B., & Blikra, L. H. (2011). Meteorological effects on seasonal displacements of the Åknes rockslide, western Norway. Landslides, 8, 1-15. https://doi.org/10.1007/s10346-010-0224-x

148. Guthrie, R. H., & Evans, S. G. (2007). Work, persistence, and formative events: the geomorphic impact of landslides. Geomorphology, 88(3-4), 266-275. https://doi.org/10.1016/j.geomorph.2006.11.010

149. Guzzetti, F., & Cardinali, M. (1989a, May). Digital elevation models for landslide susceptibility maps. In Proc. 20th Annual Pittsburg Conference on Modelling and Simulation, Pittsburgh, USA (pp. 1541-1544).

150. Guzzetti, F., & Cardinali, M. (1989b). Carta Inventario dei Fenomeni Franosi della Regione dell'Umbria ed aree limitrofe. CNR Gruppo Nazionale per la Difesa dalle Catastrofi Idrogeologiche Publication n. 204, 2 sheets, scale 1:100,000, (in Italian).

151. Guzzetti, F., Cardinali, M., & Reichenbach, P. (1994). The AVI project: a bibliographical and archive inventory of landslides and floods in Italy. Environmental management, 18, 623-633. https://doi.org/10.1007/BF02400865

152. Guzzetti, F. (2000). Landslide fatalities and the evaluation of landslide risk in Italy. Engineering Geology, 58(2), 89-107. https://doi.org/10.1016/s0013-7952(00)00047-8

153. Guzzetti, F., Cardinali, M., Reichenbach, P., & Carrara, A. (2000a). Comparing Landslide Maps: A Case Study in the Upper Tiber River Basin, Central Italy. Environmental management, 25(3). https://doi.org10.1007/s002679910020

154. Guzzetti, F., Cardinali, M., Reichenbach, P., Cipolla, F., Sebastiani, C., Galli, M., & Salvati, P. (2004). Landslides triggered by the 23 November 2000 rainfall event in the Imperia Province, Western Liguria, Italy. Engineering Geology, 73(3-4), 229-245. https://doi.org/10.1016/j.enggeo.2004.01.006

155. Guzzetti, F., Mondini, A. C., Cardinali, M., Fiorucci, F., Santangelo, M., & Chang, K. T. (2012). Landslide inventory maps: New tools for an old problem. Earth-Science Reviews, 112(1-2), 42-66. https://doi.org/10.1016/j.earscirev.2012.02.001

156. Handwerger, A. L., Fielding, E. J., Sangha, S. S., & Bekaert, D. P. (2022). Landslide sensitivity and response to precipitation changes in wet and dry climates. Geophysical research letters, 49(13), e2022GL099499.

157. Hansen, M. J. (1984a). Strategies for classification of landslides. Slope instability, 1-25.

158. Hansen, A. (1984b). Engineering geomorphology: the application of an evolutionary model of Hong Kong's terrain. Zeitschrift für Geomorphologie. Supplementband, 51, 39-50.

159. Hanssen, R. F. (2001). Radar interferometry: data interpretation and error analysis (Vol. 2). Springer Science & Business Media.

160. Harp, E. L., & Jibson, R. W. (1996). Landslides triggered by the 1994 Northridge, California, earthquake. Bulletin of the Seismological society of America, 86(1B), S319-S332. https://doi.org/10.1785/BSSA08601BS319

161. He, J.; Barton, I. (2019). Hyperspectral remote sensing for detecting geotechnical problems at Ray mine. Eng. Geol., 292, 106261. https://doi.org/10.1016/j.enggeo.2021.106261.

162. Herrera, G., Notti, D., García-Davalillo, J. C., Mora, O., Cooksley, G., Sánchez, M., ... & Crosetto, M. (2011). Analysis with C-and X-band satellite SAR data of the Portalet landslide area. Landslides, 8, 195-206. https://doi.org/10.1007/s10346-010-0239-3

163. Herrera, G., Mateos, R. M., García-Davalillo, J. C., Grandjean, G., Poyiadji, E., Maftei, R., ... & Jensen, O. A. (2018). Landslide databases in the Geological Surveys of Europe. Landslides, 15, 359-379. https://doi.org/10.1007/s10346-017-0902-z

164. Hervás, J., Barredo, J. I., Rosin, P. L., Pasuto, A., Mantovani, F., & Silvano, S. (2003). Monitoring landslides from optical remotely sensed imagery: the case history of Tessina landslide, Italy. Geomorphology, 54(1-2), 63-75. https://doi.org/10.1016/S0169-555X(03)00056-4

165. Hettinger, R. D., & Kirschbaum, M. A. (2002). Stratigraphy of the Upper Cretaceous Mancos Shale (upper part) and Mesaverde Group in the southern part of the Uinta and Piceance basins, Utah and Colorado (pp. 1-16). US Geological Survey.

166.Highland, L. M., & Bobrowsky, P. (2008). The landslide handbook-A guide to understanding landslides (No. 1325). US Geological Survey. http://pubsdata.usgs.gov/pubs/circ/1325/index.html (Last access on 19 Sep. 2023)

167.Hölbling, D., Füreder, P., Antolini, F., Cigna, F., Casagli, N., & Lang, S. (2012). A semi-automated object-based approach for landslide detection validated by persistent scatterer interferometry measures and landslide inventories. Remote Sensing, 4(5), 1310-1336. https://doi.org/10.3390/rs4051310

168.Hovius, N., Meunier, P., Lin, C. W., Chen, H., Chen, Y. G., Dadson, S., ... & Lines, M. (2011). Prolonged seismically induced erosion and the mass balance of a large earthquake. Earth and Planetary Science Letters, 304(3-4), 347-355. https://doi.org/10.1016/j.epsl.2011.02.005

169.Howell, D. G., Brabb, E. E., & Ramsey, D. W. (1999). How useful is landslide hazard information? Lessons learned in the San Francisco Bay region. International geology review, 41(4), 368-381. https://doi.org/10.1080/00206819909465147

170.Hu, S.; Qiu, H.; Wang, N.; Wang, X.; Ma, S.; Yang, D.; Wei, N.; Liu, Z.; Shen, Y.; Cao, M.; et al. (2022). Movement process, geomorphological changes, and influencing factors of a reactivated loess landslide on the right bank of the middle of the Yellow River, China. Landslides, 19, 1265–1295. https://doi.org/10.1007/s10346-022-01856-0.

171.Hung, J. J. (2000). Chi-Chi earthquake induced landslides in Taiwan. Earthquake Engineering and Engineering Seismology, 2(2), 25-33.

172.Hungr, O., Leroueil, S., & Picarelli, L. (2014). The Varnes classification of landslide types, an update. Landslides, 11, 167-194. https://doi.org/10.1007/s10346-013-0436-y

173.Hussain, M.; Chen, D.; Cheng, A.; Wei, H.; Stanley, D. (2013). Change detection from remotely sensed images: From pixel-based to object-based approaches. ISPRS J. Photogramm. Remote Sensing, 80, 91–106, doi:10.1016/j.isprsjprs.2013.03.006.

174.Hussain, M.A.; Chen, Z.; Wang, R.; Shoaib, M. (2021). PS-InSAR-Based Validated Landslide Susceptibility Mapping along Karakoram Highway, Pakistan. Remote Sensing, 13, 4129. https://doi.org/10.3390/rs13204129.

175.Ibsen, M. L., & Casagli, N. (2004). Rainfall patterns and related landslide incidence in the Porretta-Vergato region, Italy. Landslides, 1, 143-150. https://doi.org/10.1007/s10346-004-0018-0

176.Ismail, A.; Rashid, A.A.S.; Sa'ari, R.; Rasib, A.W.; Mustaffar, M.; Abdullah, R.A.; Kassim, A.; Mohd Yusof, N.; Abd Rahaman, N.; Mohd Apandi, N.; et al. (2022a). Application of UAV-based photogrammetry and normalised water index (NDWI) to estimate the rock mass rating (RMR): A case study. Phys. Chem. Earth, Parts A/B/C, 127. https://doi.org/10.1016/j.pce.2022.103161.

177.Ismail, A.; Ahmad Safuan, A.R.; Sa'ari, R.; Wahid Rasib, A.; Mustaffar, M.; Asnida Abdullah, R.; Kassim, A.; Mohd Yusof, N.; Abd Rahaman, N.; Kalatehjari, R. (2022b). Application of combined terrestrial laser scanning and unmanned aerial vehicle digital photogrammetry method in high rock slope stability analysis: A case study. Meas. J. Int. Meas. Confed., 195, 111161. https://doi.org/10.1016/j.measurement.2022.111161.

178.Istituto Geografico Militare Italiano (IGMI). Available at https://www.igmi.org/it/descrizione-prodotti/aerial-photography (Last accessed on 30 September 2023)

179.Intrieri, E., Raspini, F., Fumagalli, A., Lu, P., Del Conte, S., Farina, P., ... & Casagli, N. (2018). The Maoxian landslide as seen from space: detecting precursors of failure with Sentinel-1 data. Landslides, 15, 123-133. https://doi.org/10.1007/s10346-017-0915-7

180.Jaboyedoff, M., Oppikofer, T., Abellán, A., Derron, M. H., Loye, A., Metzger, R., & Pedrazzini, A. (2012). Use of LIDAR in landslide investigations: a review. Natural hazards, 61, 5-28. https://doi.org/10.1007/s11069-010-9634-2

181.Jebur, M. N., Pradhan, B., & Tehrany, M. S. (2014). Detection of vertical slope movement in highly vegetated tropical area of Gunung pass landslide, Malaysia, using L-band InSAR technique. Geosciences Journal, 18, 61-68. https://doi.org/10.1007/s12303-013-0053-8

182.Jensen, J. R. (2009). Remote sensing of the environment: An earth resource perspective 2/e. Pearson Education India.

183.Johnson, R.C. (1989). Geologic History and Hydrocarbon Potential of Late Cretaceous-Age, Low-Permeability Reservoirs, Piceance Basin, Western Colorado; (No. 1787-E); USGA: Reston, VA, USA. https://doi.org/10.3133/b1787e.

184.Johnson, R.C.; May, F. A study of the Cretaceous-Tertiary unconformity in the Piceance Creek Basin, Colorado: The underlying Ohio Creek Formation (Upper Cretaceous) redefined as a member of the Hunter Canyon or Mesaverde Formation. Geol. Surv. Bull. 1980, 1482-B.

185.Kallimogiannis, V., Saroglou, C., Zekkos, D., & Papadimitriou, A. (2022). Back-analyses of co-seismic landslides in carbonate fault rocks due to the Mw 6.5 earthquake (2015) in Lefkada island, Greece. Engineering Geology, 309, 106850. https://doi.org/10.1016/j.enggeo.2022.106850

186.Karir, D., Ray, A., Bharati, A. K., Chaturvedi, U., Rai, R., & Khandelwal, M. (2022). Stability prediction of a natural and man-made slope using various machine learning algorithms. Transportation Geotechnics, 34, 100745. https://doi.org/10.1016/j.trgeo.2022.100745.

187.Kasai, M., Ikeda, M., Asahina, T., & Fujisawa, K. (2009). LiDAR-derived DEM evaluation of deep-seated landslides in a steep and rocky region of Japan. Geomorphology, 113(1-2), 57-69. https://doi.org/10.1016/j.geomorph.2009.06.004

188.Kawagoe, S., Kazama, S., & Sarukkalige, P. R. (2009). Assessment of snowmelt triggered landslide hazard and risk in Japan. Cold Regions Science and Technology, 58(3), 120-129. https://doi.org/10.1016/j.coldregions.2009.05.004

189.Keefer, D. K. (2002). Investigating landslides caused by earthquakes–a historical review. Surveys in geophysics, 23, 473-510. https://doi.org/10.1023/A:1021274710840

190.Keyport, R. N., Oommen, T., Martha, T. R., Sajinkumar, K. S., & Gierke, J. S. (2018). A comparative analysis of pixel-and object-based detection of landslides from very high-resolution images. International journal of applied earth observation and geoinformation, 64, 1-11. https://doi.org/10.1016/j.jag.2017.08.015

191.Khorram, S., Nelson, S.A., Koch, F.H., Van der Wiele C.F. (2012). Remote Sensing; Springer Science & Business Media: Berlin, Germany. https://doi.org/10.1007/978-1-4614-3103-9

192.Kirschbaum, D. B., Adler, R., Hong, Y., Hill, S., & Lerner-Lam, A. (2010). A global landslide catalog for hazard applications: method, results, and limitations. Natural Hazards, 52, 561-575. https://doi.org/10.1007/s11069-009-9401-4

193.Kirschbaum, D., Stanley, T., & Zhou, Y. (2015). Spatial and temporal analysis of a global landslide catalog. Geomorphology, 249, 4-15. https://doi.org/10.1016/j.geomorph.2015.03.016

194.Konishi, T., & Suga, Y. (2019, October). Landslide detection with ALOS-2/PALSAR-2 data using convolutional neural networks: a case study of 2018 Hokkaido Eastern Iburi earthquake. In Active and passive microwave remote sensing for environmental monitoring III (Vol. 11154, pp. 21-28). SPIE. https://doi.org/10.1117/12.2531695

195.Konstantinidis, I.; Marinos, V.; Papathanassiou, G. (2021). UAV-Based Evaluation of Rockfall Hazard in the Cultural Heritage Area of Kipinas Monastery, Greece. Appl. Sci. 2021, 11, 8946. https://doi.org/10.3390/app11198946.

196.Kopytkovskiy, M., Geza, M., & McCray, J. E. (2015). Climate-change impacts on water resources and hydropower potential in the Upper Colorado River Basin. Journal of Hydrology: Regional Studies, 3, 473-493. https://doi.org/10.1016/j.ejrh.2015.02.014

197.Kromer, R.A.; Hutchinson, D.J.; Lato, M.J.; Gauthier, D.; Edwards, T. (2015). Identifying rock slope failure precursors using LiDAR for transportation corridor hazard management. Eng. Geol., 195, 93–103. https://doi.org/10.1016/j.enggeo.2015.05.012.

198.Kronfellner-Kraus, G. (1985). Torrent erosion and its control in Europe and some activities in this field in Austria. Quarterly Journal of the Japanese Torrent Control Society, Tokyo, Japan, 35(3), 33-44.

199.Lacroix, P., Zavala, B., Berthier, E., & Audin, L. (2013). Supervised method of landslide inventory using panchromatic SPOT5 images and application to the earthquake-triggered landslides of Pisco (Peru, 2007, Mw8. 0). Remote Sensing, 5(6), 2590-2616. https://doi.org/10.3390/rs5062590

200.Lanari, R., Mora, O., Manunta, M., Mallorquí, J. J., Berardino, P., & Sansosti, E. (2004). A small-baseline approach for investigating deformations on full-resolution differential SAR interferograms. IEEE transactions on geoscience and remote sensing, 42(7), 1377-1386. https://doi.org/10.1109/TGRS.2004.828196

201.Landslides 101 | U.S. Geological Survey. Available online: https://www.usgs.gov/programs/landslide-hazards/landslides-101 (accessed on 20 March 2023)

202.Lanteri, L., & Colombo, A. (2013). The integration between satellite data and conventional monitoring system in order to update the Arpa Piemonte landslide inventory. Landslide Science and Practice: Volume 1: Landslide Inventory and Susceptibility and Hazard Zoning, 135-140. https://doi.org/10.1007/978-3-642-31325-7_17

203.Lato, M. J., Gauthier, D., & Hutchinson, D. J. (2015). Rock slopes asset management: selecting the optimal three-dimensional remote sensing technology. Transportation Research Record, 2510(1), 7-14. https://doi.org/10.3141/2510-02

204.Lato, M.J.; Gauthier, D.; Hutchinson, D.J. (2015). Rock Slopes Asset Management: Selecting the Optimal Three-Dimensional Remote Sensing Technology. Transp. Res. Rec., 2510, 7–14. https://doi.org/10.3141/2510-02.

205.Lauknes, T. R., Shanker, A. P., Dehls, J. F., Zebker, H. A., Henderson, I. H. C., & Larsen, Y. (2010). Detailed rockslide mapping in northern Norway with small baseline and persistent scatterer interferometric SAR time series methods. Remote Sensing of Environment, 114(9), 2097-2109. https://doi.org/10.1016/j.rse.2010.04.015

206.Lazzari, M., Gioia, D., & Anzidei, B. (2018). Landslide inventory of the Basilicata region (Southern Italy). Journal of Maps, 14(2), 348-356. https://doi.org/10.1080/17445647.2018.1475309

207.Licata, V., Bonasera, M., D'Angiò, D., Fraccica, A., Perrotti, M., & Romeo, S. (2023, June). The Static and Seismic Behaviour of a Slow-Moving Landslide: The Case of Montemartano (Umbria, Central

Italy). In National Conference of the Researchers of Geotechnical Engineering (pp. 527-535). Cham: Springer Nature Switzerland. https://doi.org/10.1007/978-3-031-34761-0_64

208. Li, Y., Guo, C., Shi, R., Liu, X., & Mei, Y. (2015). Dbscan-m: an intelligent clustering algorithm based on mutual reinforcement. In Algorithms and Architectures for Parallel Processing: 15th International Conference, ICA3PP 2015, Zhangjiajie, China, November 18-20, 2015, Proceedings, Part II 15 (pp. 66-77). Springer International Publishing. https://doi.org/10.1007/978-3-319-27122-4_5

209. Li, Z., Shi, W., Myint, S. W., Lu, P., & Wang, Q. (2016). Semi-automated landslide inventory mapping from bitemporal aerial photographs using change detection and level set method. Remote Sensing of Environment, 175, 215-230. https://doi.org/10.1016/j.rse.2016.01.003

210. Lin, C. W., Shieh, C. L., Yuan, B. D., Shieh, Y. C., Liu, S. H., & Lee, S. Y. (2004). Impact of Chi-Chi earthquake on the occurrence of landslides and debris flows: example from the Chenyulan River watershed, Nantou, Taiwan. Engineering geology, 71(1-2), 49-61. https://doi.org/10.1016/S0013-7952(03)00125-X

211. Lin, J.; Wang, M.; Yang, J.; Yang, Q. (2016). Landslide identification and information extraction based on optical and multispectral uav remote sensing imagery. In Proceedings of the IOP Conference Series: Earth and Environmental Science; IOP Publishing: Beijing, China; Volume 57, p. 012017.

212. Ling, S., & Chigira, M. (2020). Characteristics and triggers of earthquake-induced landslides of pyroclastic fall deposits: An example from Hachinohe during the 1968 M7. 9 tokachi-Oki earthquake, Japan. Engineering Geology, 264, 105301. https://doi.org/10.1016/j.enggeo.2019.105301

213. Liu, Z.; Qiu, H.; Ma, S.; Yang, D.; Pei, Y.; Du, C.; Sun, H.; Hu, S.; Zhu, Y. (2019). Surface displacement and topographic change analysis of the Changhe landslide on September 14, China. Landslides 2021, 18, 1471–1483. https://doi.org/10.1007/s10346-021-01626-4

214. Liu, Z.; Qiu, H.; Zhu, Y.; Liu, Y.; Yang, D.; Ma, S.; Zhang, J.; Wang, Y.; Wang, L.; Tang, B. (2022). Efficient Identification and Monitoring of Landslides by Time-Series InSAR Combining Single- and Multi-Look Phases. Remote Sensing, 14, 1026. https://doi.org/10.3390/rs14041026.

215. Lopez Saez, J., Corona, C., Stoffel, M., Astrade, L., Berger, F., & Malet, J. P. (2012). Dendrogeomorphic reconstruction of past landslide reactivation with seasonal precision: the Bois Noir landslide, southeast French Alps. Landslides, 9, 189-203. https://doi.org/10.1007/s10346-011-0284-6

216. Lowry, B.W.; Baker, S.; Zhou, W. (2020). A Case Study of Novel Landslide Activity Recognition Using ALOS-1 InSAR within the Ragged Mountain Western Hillslope in Gunnison County, Colorado, USA. Remote Sensing, 12, 1969. https://doi.org/10.3390/rs12121969

217. Lu, P., Casagli, N., Catani, F., & Tofani, V. (2012). Persistent Scatterers Interferometry Hotspot and Cluster Analysis (PSI-HCA) for detection of extremely slow-moving landslides. International journal of remote sensing, 33(2), 466-489. https://doi.org/10.1080/01431161.2010.536185

218. Lucieer, A.; Jong, S.M.D.; Turner, D. (2013). Mapping landslide displacements using Structure from Motion (SfM) and image correlation of multi-temporal UAV photography. Prog. Phys. Geogr., 38, 97–116. https://doi.org/10.1177/0309133313515293.

219. Lv, Y., Ma, T., Tang, M., Cao, J., Tian, Y., Al-Dhelaan, A., & Al-Rodhaan, M. (2016). An efficient and scalable density-based clustering algorithm for datasets with complex structures. Neurocomputing, 171, 9-22. https://doi.org/10.1016/j.neucom.2015.05.109

220. Ma, S.; Qiu, H.; Hu, S.; Yang, D.; Liu, Z. (2018). Characteristics and geomorphology change detection analysis of the Jiangdingya landslide on July 12, China. Landslides 2021, 18, 383–396. https://doi.org/10.1007/s10346-020-01530-3.

221.Ma, Z., Mei, G., & Piccialli, F. (2021). Machine learning for landslides prevention: a survey. Neural Computing and Applications, 33, 10881-10907. https://doi.org/10.1007/s00521-020-05529-8

222.Malamud, B. D., Turcotte, D. L., Guzzetti, F., & Reichenbach, P. (2004). Landslide inventories and their statistical properties. Earth Surface Processes and Landforms, 29(6), 687-711. https://doi.org/10.1002/esp.1064

223.Marc, O., Hovius, N., Meunier, P., Uchida, T., & Hayashi, S. I. (2015). Transient changes of landslide rates after earthquakes. Geology, 43(10), 883-886. https://doi.org/10.1130/G36961.1

224.Marini, M., Milli, S., Ravnås, R., & Moscatelli, M. (2015). A comparative study of confined vs. semi-confined turbidite lobes from the Lower Messinian Laga Basin (Central Apennines, Italy): implications for assessment of reservoir architecture. Marine and Petroleum Geology, 63, 142-165. https://doi.org/10.1016/j.marpetgeo.2015.02.015

225.Marmoni, G. M., Martino, S., Censi, M., Menichetti, M., Piacentini, D., Mugnozza, G. S., ... & Troiani, F. (2023). Transition from rock mass creep to progressive failure for rockslide initiation at Mt. Conero (Italy). Geomorphology, 108750. https://doi.org/10.1016/j.geomorph.2023.108750

226.Martha, T. R., Kerle, N., Jetten, V., van Westen, C. J., & Kumar, K. V. (2010). Characterising spectral, spatial and morphometric properties of landslides for semi-automatic detection using object-oriented methods. Geomorphology, 116(1-2), 24-36. https://doi.org/10.1016/j.geomorph.2009.10.004

227.Martino, S., & Mugnozza, G. S. (2005). The role of the seismic trigger in the Calitri landslide (Italy): historical reconstruction and dynamic analysis. Soil Dynamics and Earthquake Engineering, 25(12), 933-950. https://doi.org/10.1016/j.soildyn.2005.04.005

228.Martino, S. (2017). Eartquake-induced landslides in Italy. From the distribution of effects to the hazard mapping. Italian Journal of Engineering Geology and Environment, 1, 53-67. https://doi.org/10.4408/IJEGE.2017-01.S-04

229.Martino, S., Prestininzi, A., & Romeo, R. W. (2014). Earthquake-induced ground failures in Italy from a reviewed database. Natural Hazards and Earth System Sciences, 14(4), 799-814. https://doi.org/10.5194/nhess-14-799-2014

230.Martino, S., Bozzano, F., Caporossi, P., Della Seta, M., Esposito, C., Fantini, A., ... & Varone, C. (2016). Landslides triggered by the August 24, 2016 (Mw 6.0) Amatrice earthquake (Italy): data survey and inventorying.[in:]. GNGTS 35 convegno nazionale, Riassunti estesi delle comunicazioni 2016, 22–24 November, 2016, Lecce, Italia, 55-58.

231.Martino, S., Bozzano, F., Caporossi, P., D'angiò, D., Della Seta, M., Esposito, C., ... & Varone, C. (2019). Impact of landslides on transportation routes during the 2016–2017 Central Italy seismic sequence. Landslides, 16, 1221-1241. https://doi.org/10.1007/s10346-019-01162-2

232.Martino, S., Battaglia, S., D'alessandro, F., Della Seta, M., Esposito, C., Martini, G., ... & Troiani, F. (2020). Earthquake-induced landslide scenarios for seismic microzonation: application to the Accumoli area (Rieti, Italy). Bulletin of Earthquake Engineering, 18, 5655-5673. https://doi.org/10.1007/s10518-019-00589-1

233.Martino, S., Fiorucci, M., Marmoni, G. M., Casaburi, L., Antonielli, B., & Mazzanti, P. (2022). Increase in landslide activity after a low-magnitude earthquake as inferred from DInSAR interferometry. Scientific reports, 12(1), 2686. https://doi.org/10.1038/s41598-022-06508-w

234.Martins, B. H., Suzuki, M., Yastika, P. E., & Shimizu, N. (2020). Ground surface deformation detection in complex landslide area—Bobonaro, Timor-Leste—Using SBAS DinSAR, UAV photogrammetry, and field observations. Geosciences, 10(6), 245. https://doi.org/10.3390/geosciences10060245

235.Mazzanti, P., Bozzano, F., Cipriani, I., & Prestininzi, A. (2015). New insights into the temporal prediction of landslides by a terrestrial SAR interferometry monitoring case study. Landslides, 12, 55-68. https://doi.org/10.1007/s10346-014-0469-x

236.Mazzanti, P., Scancella, S., Virelli, M., Frittelli, S., Nocente, V., & Lombardo, F. (2022). Assessing the Performance of Multi-Resolution Satellite SAR Images for Post-Earthquake Damage Detection and Mapping Aimed at Emergency Response Management. Remote Sensing, 14(9), 2210. https://doi.org/10.3390/rs14092210

237.McCalpin, J. (1984). Preliminary age classification of landslides for inventory mapping. In Proceedings of the Annual Symposium on Engineering Geology and Soil Engineering (Vol. 21, pp. 99-120).

238.Meisina, C., Zucca, F., Notti, D., Colombo, A., Cucchi, A., Savio, G., ... & Bianchi, M. (2008). Geological interpretation of PSInSAR data at regional scale. Sensors, 8(11), 7469-7492. https://doi.org/10.3390/s8117469

239.Mezaal, M. R., Pradhan, B., Sameen, M. I., Mohd Shafri, H. Z., & Yusoff, Z. M. (2017). Optimized neural architecture for automatic landslide detection from high-resolution airborne laser scanning data. Applied Sciences, 7(7), 730. https://doi.org/10.3390/app7070730

240.Miele, P., Di Napoli, M., Novellino, A., Calcaterra, D., Mallorqui, J. J., & Di Martire, D. (2022). SAR data and field surveys combination to update rainfall-induced shallow landslide inventory. Remote Sensing Applications: Society and Environment, 26, 100755. https://doi.org/10.1016/j.rsase.2022.100755

241.Migliazza, M., Carriero, M.T., Lingua, A., Pontoglio, E., Scavia, C. (2021). Rock Mass Characterization by UAV and Close-Range Photogrammetry: A Multiscale Approach Applied along the Vallone dell'Elva Road (Italy). Geosciences, 11, 436. https://doi.org/10.3390/geosciences11110436.

242.Mirus, B. B., Jones, E. S., Baum, R. L., Godt, J. W., Slaughter, S., Crawford, M. M., ... & McCoy, K. M. (2020). Landslides across the USA: occurrence, susceptibility, and data limitations. Landslides, 17, 2271-2285. https://doi.org/10.1007/s10346-020-01424-4

243.Mohammadi, A., Shahabi, H., & Bin Ahmad, B. (2018). Integration of InSAR technique, Google Earth images and extensive field survey for landslide inventory in a part of Cameron Highlands, Pahang, Malaysia. Applied Ecology & Environmental Research, 16(6). http://dx.doi.org/10.15666/aeer/1606_80758091

244.Mohan, A., Singh, A. K., Kumar, B., & Dwivedi, R. (2021). Review on remote sensing methods for landslide detection using machine and deep learning. Transactions on Emerging Telecommunications Technologies, 32(7), e3998. https://doi.org/10.1002/ett.3998

245.Mondini, A. C., Viero, A., Cavalli, M., Marchi, L., Herrera, G., & Guzzetti, F. (2014). Comparison of event landslide inventories: the Pogliaschina catchment test case, Italy. Natural Hazards and Earth System Sciences, 14(7), 1749-1759. https://doi.org/10.5194/nhess-14-1749-2014

246.Mondini, A. C., Guzzetti, F., Chang, K. T., Monserrat, O., Martha, T. R., & Manconi, A. (2021). Landslide failures detection and mapping using Synthetic Aperture Radar: Past, present and future. Earth-Science Reviews, 216, 103574. https://doi.org/10.1016/j.earscirev.2021.103574

247.Montalti, R., Solari, L., Bianchini, S., Del Soldato, M., Raspini, F., & Casagli, N. (2019). A Sentinel-1-based clustering analysis for geo-hazards mitigation at regional scale: a case study in Central Italy. Geomatics, Natural Hazards and Risk, 10(1), 2257-2275. https://doi.org/10.1080/19475705.2019.1690058

248. Moore, J. R., Sanders, J. W., Dietrich, W. E., & Glaser, S. D. (2009). Influence of rock mass strength on the erosion rate of alpine cliffs. Earth Surface Processes and Landforms, 34(10), 1339-1352. https://doi.org/10.1002/esp.1821

249. Moosavi, V., Talebi, A., & Shirmohammadi, B. (2014). Producing a landslide inventory map using pixel-based and object-oriented approaches optimized by Taguchi method. Geomorphology, 204, 646-656. https://doi.org/10.1016/j.geomorph.2013.09.012

250. Moretto, S., Bozzano, F., & Mazzanti, P. (2021). The role of satellite InSAR for landslide forecasting: Limitations and openings. Remote sensing, 13(18), 3735. https://doi.org/10.3390/rs13183735

251. Napieralski, J., Barr, I., Kamp, U., & Kervyn, M. (2013). Remote sensing and GIScience in geomorphological mapping. Elsevier, 187–227

252. Nishii, R., Matsuoka, N., Daimaru, H., & Yasuda, M. (2013). Precursors and triggers of an alpine rockslide in Japan: the 2004 partial collapse during a snow-melting period. Landslides, 10, 75-82. https://doi.org/10.1007/s10346-012-0353-5

253. Nishiguchi, T., Tsuchiya, S., & Imaizumi, F. (2017). Detection and accuracy of landslide movement by InSAR analysis using PALSAR-2 data. Landslides, 14, 1483-1490. https://doi.org/10.1007/s10346-017-0821-z

254. Novellino, A., Cigna, F., Sowter, A., Ramondini, M., & Calcaterra, D. (2017). Exploitation of the Intermittent SBAS (ISBAS) algorithm with COSMO-SkyMed data for landslide inventory mapping in north-western Sicily, Italy. Geomorphology, 280, 153-166. https://doi.org/10.1016/j.geomorph.2016.12.009

255. Núñez-Andrés, M.A., Prades-Valls, A., Matas, G., Buill, F., Lantada, N. (2023). New Approach for Photogrammetric Rock Slope Premonitory Movements Monitoring. Remote Sensing, 15, 293. https://doi.org/10.3390/rs15020293.

256. Oommen, T.; Vitton, S.; Escobar-Wolf, R.; Brooks, C. (2017). Rockfall Hazard Rating System: Benefits of Utilizing Remote Sensing. Environ. Eng. Geosci., 23, 165–177. https://doi.org/10.2113/gseegeosci.23.3.165.

257. OneGeology Portal. Available online at http://portal.onegeology.org/ (Last accessed on 27 September 2023)

258. Owen, L. A., Kamp, U., Khattak, G. A., Harp, E. L., Keefer, D. K., & Bauer, M. A. (2008). Landslides triggered by the 8 October 2005 Kashmir earthquake. Geomorphology, 94(1-2), 1-9. https://doi.org/10.1016/j.geomorph.2007.04.007

259. PAI - Piano stralcio di Assetto Idrogeologico (Hydrogeological Asset Plan), available at https://www.autoritadistrettoac.it/restart/glossario/PAI (Last accessed 16 October 2023).

260. Pašek, J. (1975). Landslide inventory. International Association Engineering Geologist Bulletin, 12, 73–74. https://doi.org/10.1007/BF02635432

261. Pawluszek, K. (2019). Landslide features identification and morphology investigation using high-resolution DEM derivatives. Natural Hazards, 96(1), 311-330. https://doi.org/10.1007/s11069-018-3543-1

262. Pawluszek-Filipiak, K., Borkowski, A., & Motagh, M. (2021). Multi-temporal landslide activity investigation by spaceborne SAR interferometry: The case study of the Polish Carpathians. Remote Sensing Applications: Society and Environment, 24, 100629. https://doi.org/10.1016/j.rsase.2021.100629

263.Pellicani, R., & Spilotro, G. (2015). Evaluating the quality of landslide inventory maps: comparison between archive and surveyed inventories for the Daunia region (Apulia, Southern Italy). Bulletin of Engineering Geology and the Environment, 74, 357-367. https://doi.org/10.1007/s10064-014-0639-z

264.Perissin, D.; Wang, Z.; Wang, T. (2011). The SARPROZ InSAR tool for urban subsidence/manmade structure stability monitoring in China. In Proceedings of 34th International Symposium of Remote Sensing of Environment, Sidney, Australia, 10-15 April 2011.

265.Peruccacci, S., Gariano, S. L., Melillo, M., Solimano, M., Guzzetti, F., & Brunetti, M. T. (2023). ITALICA, an extensive and accurate spatio-temporal catalogue of rainfall-induced landslides in Italy. Earth System Science Data Discussions, 2023, 1-24. https://doi.org/10.5194/essd-15-2863-2023

266.Petley, D. N., Dunning, S. A., Rosser, N. J., & Hungr, O. (2005). The analysis of global landslide risk through the creation of a database of worldwide landslide fatalities. Landslide risk management, 52, 367-373.

267.Petley, D. N., Hearn, G. J., Hart, A., Rosser, N. J., Dunning, S. A., Oven, K., & Mitchell, W. A. (2007). Trends in landslide occurrence in Nepal. Natural hazards, 43, 23-44.https://doi.org/10.1007/s11069-006-9100-3

268.Photomonitoring.com. Available online: https://www.photomonitoring.com/iris/ (accessed on 25/04/2023)

269.Piacentini, D., Ercolessi, G., Pizziolo, M., & Troiani, F. (2015). Rockfall runout, Mount Cimone area, Emilia-Romagna region, Italy. Journal of Maps, 11(4), 598-605. https://doi.org/10.1080/17445647.2014.956154

270.Piacentini, D., Troiani, F., Daniele, G., & Pizziolo, M. (2018). Historical geospatial database for landslide analysis: the Catalogue of Landslide OCcurrences in the Emilia-Romagna Region (CLOCkER). Landslides, 15(4), 811-822. https://doi.org/10.1007/s10346-018-0962-8

271.Pierantoni, P., Deiana, G., & Galdenzi, S. (2013). Stratigraphic and structural features of the Sibillini mountains (Umbria-Marche Apennines, Italy). Italian Journal of Geosciences, 132(3), 497-520. https://doi.org/10.3301/IJG.2013.08

272.Pike, R. J. (1988). The geometric signature: quantifying landslide-terrain types from digital elevation models. Mathematical geology, 20, 491-511. https://doi.org/10.1007/BF00890333

273.Pike, R. J., Evans, I. S., & Hengl, T. (2009). Geomorphometry: a brief guide. Developments in soil science, 33, 3-30. https://doi.org/10.1016/S0166-2481(08)00001-9

274.Pokharel, B., Alvioli, M., & Lim, S. (2021). Assessment of earthquake-induced landslide inventories and susceptibility maps using slope unit-based logistic regression and geospatial statistics. Scientific reports, 11(1), 21333. https://doi.org/10.3390/rs13102008

275.Polcari, M., Montuori, A., Bignami, C., Moro, M., Stramondo, S., & Tolomei, C. (2017). Using multi-band InSAR data for detecting local deformation phenomena induced by the 2016–2017 Central Italy seismic sequence. Remote sensing of environment, 201, 234-242. https://doi.org/10.1016/j.rse.2017.09.009

276.Popescu, M. E. (2002, July). Landslide causal factors and landslide remediatial options. In 3rd international conference on landslides, slope stability and safety of infra-structures (pp. 61-81). CI-Premier PTE LTD Singapore.

277.Preisig, G., Eberhardt, E., Smithyman, M., Preh, A., & Bonzanigo, L. (2016). Hydromechanical rock mass fatigue in deep-seated landslides accompanying seasonal variations in pore pressures. Rock Mechanics and Rock Engineering, 49, 2333-2351. https://doi.org/10.1007/s00603-016-0912-5

278. Pucci, S., De Martini, P. M., Civico, R., Nappi, R., Ricci, T., Villani, F., ... & Lancia, M. (2016). Coseismic effects of the 2016 Amatrice seismic sequence: First geological results. Annals of Geopysyscs. https://doi.org/10.4401/ag-7195

279. Rahmah, N., & Sitanggang, I. S. (2016). Determination of optimal epsilon (eps) value on dbscan algorithm to clustering data on peatland hotspots in sumatra. In IOP conference series: earth and environmental science (Vol. 31, No. 1, p. 012012). IoP Publishing. https://doi.org/10.1088/1755-1315/31/1/012012

280. Ramirez, R., Lee, S. R., & Kwon, T. H. (2020). Long-term remote monitoring of ground deformation using sentinel-1 interferometric synthetic aperture radar (InSAR): Applications and insights into geotechnical engineering practices. Applied Sciences, 10(21), 7447. https://doi.org/10.3390/app10217447

281. Rapporto Attività Linea A2 -Rischio gravitativo: mappatura post sisma e programma delle misure (February, 2023). Available at https://www.autoritadistrettoac.it/restart/rischio-gravitativo-mappatura-post-sisma-e-programma-delle-misure (Last accessed 30 September 2023)

282. Raska, P., Klimes, J., & Dubisar, J. (2015). Using local archive sources to reconstruct historical landslide occurrence in selected urban regions of the Czech Republic: examples from regions with different historical development. Land Degradation & Development, 26(2), 142-157. https://doi.org/10.1002/ldr.2192

283. Raso, E., Cevasco, A., Di Martire, D., Pepe, G., Scarpellini, P., Calcaterra, D., & Firpo, M. (2019). Landslide-inventory of the Cinque Terre National Park (Italy) and quantitative interaction with the trail network. Journal of Maps, 15(2), 818-830. https://doi.org/10.1080/17445647.2019.1657511

284. Raspini, F., Bardi, F., Bianchini, S., Ciampalini, A., Del Ventisette, C., Farina, P., ... & Casagli, N. (2017). The contribution of satellite SAR-derived displacement measurements in landslide risk management practices. Natural hazards, 86, 327-351. https://doi.org/10.1007/s11069-016-2691-4

285. Raspini, F., Bianchini, S., Ciampalini, A., Del Soldato, M., Solari, L., Novali, F., ... & Casagli, N. (2018). Continuous, semi-automatic monitoring of ground deformation using Sentinel-1 satellites. Scientific reports, 8(1), 7253. https://doi.org/10.1038/s41598-018-25369-w

286. Reichenbach, P., Guzzetti, & F., Cardinali, M. (1998). Map of sites historically affected by landslides and floods in Italy, 2nd edition. CNR, Gruppo Nazionale per la Difesa dalle Catastrofi Idrogeologiche, Publication n. 1786, scale 1:1,200,000.

287. Reyes-Carmona, C., Galve, J. P., Pérez-Peña, J. V., Moreno-Sánchez, M., Alfonso-Jorde, D., Ballesteros, D., ... & Mateos, R. M. (2023). Improving landslide inventories by combining satellite interferometry and landscape analysis: the case of Sierra Nevada (Southern Spain). Landslides, 1-21. https://doi.org/10.1007/s10346-023-02071-1

288. Righini, G., Pancioli, V., & Casagli, N. (2012). Updating landslide inventory maps using Persistent Scatterer Interferometry (PSI). International Journal of Remote Sensing, 33(7), 2068-2096. https://doi.org/10.1080/01431161.2011.605087

289. Riva, F., Agliardi, F., Amitrano, D., & Crosta, G. B. (2018). Damage-based time-dependent modeling of paraglacial to postglacial progressive failure of large rock slopes. Journal of Geophysical Research: Earth Surface, 123(1), 124-141. https://doi.org/10.1002/2017JF004423

290.Robiati, C.; Eyre, M.; Vanneschi, C.; Francioni, M.; Venn, A.; Coggan, J. (2019). Application of Remote Sensing Data for Evaluation of Rockfall Potential within a Quarry Slope. ISPRS Int. J. Geo-Information, 8, 367. https://doi.org/10.3390/ijgi8090367.

291.Robiati, C.; Mastrantoni, G.; Francioni, M.; Eyre, M.; Coggan, J.; Mazzanti, P. (2023). Contribution of High-Resolution Virtual Outcrop Models for the Definition of Rockfall Activity and Associated Hazard Modelling. Land, 12, 191. https://doi.org/10.3390/land12010191.

292.Rocca, A., Mazzanti, P., Bozzano, F., & Perissin, D. (2015). Advanced characterization of a landslide-prone area by satellite a-DInSAR. In Engineering Geology for Society and Territory-Volume 5: Urban Geology, Sustainable Planning and Landscape Exploitation (pp. 177-181). Springer International Publishing. https://doi.org/10.1007/978-3-319-09048-1_35

293.“Rockfall in Colorado”. Rock Talk 11.2 (2008): 19. Web.

294.Rodriguez, J.; Macciotta, R.; Hendry, M.T.; Roustaei, M.; Gräpel, C.; Skirrow, R. (2020). UAVs for monitoring, investigation, and mitigation design of a rock slope with multiple failure mechanisms—A case study. Landslides, 17, 2027–2040. https://doi.org/10.1007/s10346-020-01416-4.

295.Romeo, S.; Cosentino, A.; Giani, F.; Mastrantoni, G.; Mazzanti, P. (2021). Combining Ground Based Remote Sensing Tools for Rockfalls Assessment and Monitoring: The Poggio Baldi Landslide Natural Laboratory. Sensors, 21, 2632. https://doi.org/10.3390/s21082632.

296.Rosi, A., Tofani, V., Tanteri, L., Tacconi Stefanelli, C., Agostini, A., Catani, F., & Casagli, N. (2018). The new landslide inventory of Tuscany (Italy) updated with PS-InSAR: geomorphological features and landslide distribution. Landslides, 15, 5-19. https://doi.org/10.1007/s10346-017-0861-4

297.Rosin, P. L., & Hervás, J. (2005). Remote sensing image thresholding methods for determining landslide activity. International Journal of Remote Sensing, 26(6), 1075-1092. https://doi.org/10.1080/01431160512331330481

298.Royán, M.J., Abellán, A., Jaboyedoff, M., Vilaplana, J.M., Calvet, J. (2014). Spatio-temporal analysis of rockfall pre-failure deformation using Terrestrial LiDAR. Landslides, 11, 697–709. https://doi.org/10.1007/s10346-013-0442-0.

299.Salvati, P., Balducci, V., Bianchi, C., Guzzetti, F., & Tonelli, G. (2009). A WebGIS for the dissemination of information on historical landslides and floods in Umbria, Italy. Geoinformatica, 13, 305-322. https://doi.org/10.1007/s10707-008-0072-1

300.Samia, J., Temme, A., Bregt, A., Wallinga, J., Guzzetti, F., Ardizzone, F., & Rossi, M. (2017) Do landslides follow landslides ? Insights in path dependency from a multi-temporal landslide inventory. Landslides 14:547–558. https://doi.org/10.1007/s10346-016-0739-x

301.Santangelo, M., Marchesini, I., Bucci, F., Cardinali, M., Fiorucci, F., & Guzzetti, F. (2015). An approach to reduce mapping errors in the production of landslide inventory maps. Natural Hazards and Earth System Science, 15(9), 2111-2126. https://doi.org/10.5194/nhess-15-2111-2015

302.Santi, P.M., Russell, C.P., Higgins, J.D., Spriet, J.I. (2009). Modification and statistical analysis of the Colorado Rockfall Hazard Rating System. Eng. Geol., 104, 55–65. https://doi.org/10.1016/j.enggeo.2008.08.009.

303.Sarro, R., Riquelme, A., García-Davalillo, J.C., Mateos, R.M., Tomás, R., Pastor, J.L., Herrera, G. (2018). Rockfall Simulation Based on UAV Photogrammetry Data Obtained during an Emergency Declaration: Application at a Cultural Heritage Site. Remote Sensing, 10, 1923. https://doi.org/10.3390/rs10121923.

304. Scaioni, M., Longoni, L., Melillo, V., & Papini, M. (2014). Remote sensing for landslide investigations: An overview of recent achievements and perspectives. Remote Sensing, 6(10), 9600-9652. https://doi.org/10.3390/rs6109600

305. Scheevel, C. R., Baum, R. L., Mirus, B. B., & Smith, J. B. (2017). Precipitation thresholds for landslide occurrence near Seattle, Mukilteo, and Everett, Washington (No. 2017-1039). US Geological Survey. https://doi.org/10.3133/ofr20171039

306. Schmidt, J., Andrew, R. (2005). Multi-scale landform characterization. Area, 37, 341–350. https://doi.org/10.1111/j.1475-4762.2005.00638.x.

307. Schulz, W. H. (2004). Landslides mapped using LIDAR imagery, Seattle, Washington. US Geological Survey Open-File Report, 1396(11).

308. Scikit-learn.org: https://scikit-learn.org/stable/about.html#citing-scikit-learn (last accessed on 09/09/2023)

309. Sekiguchi, T., & Sato, H. P. (2004). Mapping of micro topography using airborne laser scanning. Landslides, 1, 195-202. https://doi.org/10.1007/s10346-004-0021-5

310. Sentinels.copernicus.eu: https://sentinels.copernicus.eu/web/sentinel/technical-guides/sentinel-1-sar (last accessed on 09 September 2023)

311. Shafique, M., van der Meijde, M., & Khan, M. A. (2016). A review of the 2005 Kashmir earthquake-induced landslides; from a remote sensing prospective. Journal of Asian Earth Sciences, 118, 68-80. https://doi.org/10.1016/j.jseaes.2016.01.002

312. Si, A., Zhang, J., Tong, S., Lai, Q., Wang, R., Li, N., & Bao, Y. (2018). Regional landslide identification based on susceptibility analysis and change detection. ISPRS International Journal of Geo-Information, 7(10), 394. https://doi.org/10.3390/ijgi7100394

313. Singhroy, V., & Molch, K. (2004). Characterizing and monitoring rockslides from SAR techniques. Advances in Space Research, 33(3), 290-295. https://doi.org/10.1016/S0273-1177(03)00470-8

314. Siyahghalati, S., Saraf, A. K., Pradhan, B., Jebur, M. N., & Tehrany, M. S. (2016). Rule-based semi-automated approach for the detection of landslides induced by 18 September 2011 Sikkim, Himalaya, earthquake using IRS LISS3 satellite images. Geomatics, Natural Hazards and Risk, 7(1), 326-344. https://doi.org/10.1080/19475705.2014.898702

315. Smail, T., Abed, M., Mebarki, A., & Lazecky, M. (2022). Earthquake-induced landslide monitoring and survey by means of InSAR. Natural Hazards and Earth System Sciences, 22(5), 1609-1625. https://doi.org/10.5194/nhess-22-1609-2022

316. Soeters, R., & Van Westen, C. J. (1996). Slope instability recognition, analysis and zonation. Landslides: investigation and mitigation, 247, 129-177.

317. Solari, L., Del Soldato, M., Montalti, R., Bianchini, S., Raspini, F., Thuegaz, P., ... & Casagli, N. (2019). A Sentinel-1 based hot-spot analysis: landslide mapping in north-western Italy. International Journal of Remote Sensing, 40(20), 7898-7921. https://doi.org/10.1080/01431161.2019.1607612

318. Solari, L., Del Soldato, M., Raspini, F., Barra, A., Bianchini, S., Confuorto, P., ... & Crosetto, M. (2020). Review of satellite interferometry for landslide detection in Italy. Remote Sensing, 12(8), 1351. https://doi.org/10.3390/rs12081351

319. Sousa, J. J., Ruiz, A. M., Hanssen, R. F., Bastos, L., Gil, A. J., Galindo-Zaldívar, J., & de Galdeano, C. S. (2010). PS-InSAR processing methodologies in the detection of field surface deformation—Study of

the Granada basin (Central Betic Cordilleras, southern Spain). Journal of Geodynamics, 49(3-4), 181-189. https://doi.org/10.1016/j.jog.2009.12.002

320. Starczewski, A., Goetzen, P., & Er, M. J. (2020). A new method for automatic determining of the DBSCAN parameters. Journal of Artificial Intelligence and Soft Computing Research, 10(3), 209-221. https://doi.org/10.2478/jaiscr-2020-0014

321. Stead, D., Donati, D., Wolter, A., Sturzenegger, M. (2019). Application of Remote Sensing to the Investigation of Rock Slopes: Experience Gained and Lessons Learned. ISPRS Int. J. Geo-Information, 8, 296. https://doi.org/10.3390/ijgi8070296.

322. Steger, S., Moreno, M., Crespi, A., Zellner, P. J., Gariano, S. L., Brunetti, M. T., ... & Pittore, M. (2022). Deciphering seasonal effects of triggering and preparatory precipitation for improved shallow landslide prediction using generalized additive mixed models. Natural Hazards and Earth System Sciences Discussions, 2022, 1-38. https://doi.org/10.5194/nhess-23-1483-2023

323. Stover, B.K. (1986). Surficial-geologic map of the Muddy Creek landslide complex, Gunnison County, Colorado, April 15, 1986. Surface Geologic. Open File Report. Denver. CO: Colorado Geological Survey, Department of Natural Resources. https://coloradogeologicalsurvey.org/publications/surficial-geologic-map -muddy-creek-landslide-complex-gunnison-colorado-1986/ (accessed on 08 June 2023).

324. Stumpf, A., & Kerle, N. (2011). Object-oriented mapping of landslides using Random Forests. Remote sensing of environment, 115(10), 2564-2577. https://doi.org/10.1016/j.rse.2011.05.013

325. Swanston, D. N., & Schuster, R. L. (1989). Long-term landslide hazard mitigation programs: structure and experience from other countries. Bulletin of the Association of Engineering Geologists, 26(1), 109-133. https://doi.org/10.2113/gseegeosci.xxvi.1.109

326. Tang, C., Van Westen, C. J., Tanyas, H., & Jetten, V. G. (2016). Analysing post-earthquake landslide activity using multi-temporal landslide inventories near the epicentral area of the 2008 Wenchuan earthquake. Natural Hazards and Earth System Sciences, 16(12), 2641-2655. https://doi.org/10.5194/nhess-16-2641-2016

327. Tarchi, D., Casagli, N., Moretti, S., Leva, D., & Sieber, A. J. (2003). Monitoring landslide displacements by using ground-based synthetic aperture radar interferometry: Application to the Ruinon landslide in the Italian Alps. Journal of Geophysical Research: Solid Earth, 108(B8). https://doi.org/10.1029/2002JB002204

328. Tarolli, P. (2014). High-resolution topography for understanding Earth surface processes: Opportunities and challenges. Geomorphology, 216, 295-312. https://doi.org/10.1016/j.geomorph.2014.03.008

329. Tarquini, S., Isola, I., Favalli, M., Battistini, A., & Dotta, G. (2023). TINITALY, a digital elevation model of Italy with a 10 meters cell size (Version 1.1). Istituto Nazionale di Geofisica e Vulcanologia (INGV). https://doi.org/10.13127/tinitaly/1.1)

330. Taylor, F., & Brabb, E. E. (1986). Map showing landslides in California that have caused fatalities or at least $1,000,000 in damages from 1906 to 1984 (No. 1867). US Geological Survey. https://doi.org/10.3133/mf1867

331. Tehrani, F. S., Calvello, M., Liu, Z., Zhang, L., & Lacasse, S. (2022). Machine learning and landslide studies: recent advances and applications. Natural Hazards, 114(2), 1197-1245. https://doi.org/10.1007/s11069-022-05423-7

332. Tomás, R., Pagán, J. I., Navarro, J. A., Cano, M., Pastor, J. L., Riquelme, A., ... & Casagli, N. (2019). Semi-automatic identification and pre-screening of geological–geotechnical deformational processes using persistent scatterer interferometry datasets. Remote Sensing, 11(14), 1675. https://doi.org/10.3390/rs11141675
333. Torre, A., & Capece, P. (2011, June). COSMO-SkyMed: The advanced SAR instrument. In Proceedings of 5th International Conference on Recent Advances in Space Technologies-RAST2011 (pp. 865-868). IEEE.
334. Trigila, A., Iadanza, C., & Spizzichino, D. (2010). Quality assessment of the Italian Landslide Inventory using GIS processing. Landslides, 7, 455-470. https://doi.org/10.1007/s10346-010-0213-0
335. Trigila, A., Iadanza, C., Lastoria, B., Bussettini, M., and Barbano, A. (2021). Dissesto idrogeologico in Italia: pericolosità e indicatori di rischio – Edizione 2021, Rapporti 356/2021, ISPRA. (in Italian). Available at https://www.isprambiente.gov.it/files2022/pubblicazioni/rapporti/rapporto_dissesto_idrogeologico_italia_ispra_356_2021_finale_web.pdf (Last accessed 30 September 2023).
336. Trimble Germany GmbH. Trimble Documentation eCognition Developer 10.1 User Guide; Trimble Germany GmbH: Munich, Germany, 2022.
337. Troiani, F., Vergari, F., Capolongo, D., Della Seta, M., Fredi, P., Melelli, L., ... & Del Monte, M. (2014). The role of quantitative geomorphology in natural hazards assessment: a review on methods developed by the AIGeo's Working Group "Quantitative and Theoretic Geomorphology".
338. Tsai, F., Hwang, J. H., Chen, L. C., & Lin, T. H. (2010). Post-disaster assessment of landslides in southern Taiwan after 2009 Typhoon Morakot using remote sensing and spatial analysis. Natural Hazards and Earth System Sciences, 10(10), 2179-2190. https://doi.org/10.5194/nhess-10-2179-2010
339. Udin, W.S., Norazami, N.A.S., Sulaiman, N., Zaudin, N.C., Ma'ail, S., Nor, A.M. (2019). UAV based multi-spectral imaging system for mapping landslide risk area along Jeli-Gerik highway, Jeli, Kelantan. In Proceedings of the 2019 IEEE 15th International Colloquium on Signal Processing & Its Applications (CSPA), Pulau Pinang, Malaysia, 8–9 March 2019; pp. 162–167. https://doi.org/10.1109/CSPA.2019.8695995
340. U.S. Geological Survey, 2019, 3D Elevation Program 1-Meter Resolution Digital Elevation Model (published 20200606). Available online: https://www.usgs.gov/the-national-map-data-delivery (24/04/ 2023)
341. Valiante, M., Bozzano, F., & Guida, D. (2016). The Sant'Andrea-Molinello landslide system (Mt. Pruno, Roscigno, Italy). Rendiconti Online della Società Geologica Italiana, 41, 214-217. https://doi.org/10.3301/ROL.2016.132
342. Valiante, M., Guida, D., Della Seta, M., & Bozzano, F. (2021). A spatiotemporal object-oriented data model for landslides (LOOM). Landslides, 18(4), 1231-1244. https://doi.org/10.1007/s10346-020-01591-4
343. Van Den Eeckhaut, M., Poesen, J., Verstraeten, G., Vanacker, V., Nyssen, J., Moeyersons, J., ... & Vandekerckhove, L. (2007). Use of LIDAR-derived images for mapping old landslides under forest. Earth Surface Processes and Landforms, 32(5), 754-769. https://doi.org/10.1002/esp.1417
344. Van Den Eeckhaut, M., & Hervás, J. (2012). State of the art of national landslide databases in Europe and their potential for assessing landslide susceptibility, hazard and risk. Geomorphology, 139, 545-558. https://doi.org/10.1016/j.geomorph.2011.12.006
345. Van Den Eeckhaut, M., Hervás, J., Jaedicke, C., Malet, J. P., Montanarella, L., & Nadim, F. (2012). Statistical modelling of Europe-wide landslide susceptibility using limited landslide inventory data. Landslides, 9, 357-369. https://doi.org/10.1007/s10346-011-0299-z

346. Van Westen, C. J., Van Asch, T. W., & Soeters, R. (2006). Landslide hazard and risk zonation—why is it still so difficult?. Bulletin of Engineering geology and the Environment, 65, 167-184. https://doi.org/10.1007/s10064-005-0023-0
347. Van Westen, C. J., Castellanos, E., & Kuriakose, S. L. (2008). Spatial data for landslide susceptibility, hazard, and vulnerability assessment: An overview. Engineering geology, 102(3-4), 112-131. https://doi.org/10.1016/j.enggeo.2008.03.010
348. Varnes, D.J. (1954). Landslide types and processes. In: Eckel EB (ed) Landslides and engineering practice, special report 28. Highway research board. National Academy of Sciences, Washington, DC, pp 20–47
349. Varnes, D. J. (1978). Slope movement types and processes. Special report, 176, 11-33.
350. Vick, L. M., Böhme, M., Rouyet, L., Bergh, S. G., Corner, G. D., & Lauknes, T. R. (2020). Structurally controlled rock slope deformation in northern Norway. Landslides, 17, 1745-1776. https://doi.org/10.1007/s10346-020-01421-7
351. Wang, Z., Bovik, A.C., Sheikh, H.R., Simoncelli, E.P. (2004). Image Quality Assessment: From Error Visibility to Structural Similarity. IEEE Trans. Image Process., 13, 600–612. https://doi.org/10.1109/tip.2003.819861.
352. Wang, J., Xiao, L., Zhang, J., & Zhu, Y. (2020). Deformation characteristics and failure mechanisms of a rainfall-induced complex landslide in Wanzhou County, Three Gorges Reservoir, China. Landslides, 17, 419-431. https://doi.org/10.1007/s10346-019-01317-1
353. Wasowski, J., & Bovenga, F. (2014). Investigating landslides and unstable slopes with satellite Multi Temporal Interferometry: Current issues and future perspectives. Engineering Geology, 174, 103-138. https://doi.org/10.1016/j.enggeo.2014.03.003
354. Wang, S., Zhang, Z., Wang, C., Zhu, C., Ren, Y. (2019). Multistep rocky slope stability analysis based on unmanned aerial vehicle photogrammetry. Environ. Earth Sci., 78, 260. https://doi.org/10.1007/s12665-019-8145-z.
355. Wang, W., Zhao, W., Chai, B., Du, J., Tang, L., Yi, X. (2022). Discontinuity interpretation and identification of potential rockfalls for high-steep slopes based on UAV nap-of-the-object photogrammetry. Comput. Geosci., 166. https://doi.org/10.1016/j.cageo.2022.105191.
356. Weatherwx.com. Available online: https://www.weatherwx.com/climate-averages/co/paonia+reservoir.html (accessed on 24/04/2023)
357. Weidner, L., & Walton, G. (2020, June). Monitoring and modeling of the DeBeque Canyon landslide complex in three dimensions. In ARMA US Rock Mechanics/Geomechanics Symposium (pp. ARMA-2020). ARMA.
358. White, J., L., (2000). Photogrammetric analysis of Debeque Canyon Landslide from 1950 to present, Mesa County, Colorado. Colorado Geological Survey Technical Report.
359. White, J. L., Ellis, W. L., Higgins, J. D., Dessenberger, N. C., Gaffney, S., & Coe, J. A. (2003). Geology, instrumentation, and movement history of the DeBeque Canyon Landslide, Mesa County, West-central Colorado. Engineering geology in Colorado: contributions, trends, and case histories: Association of Engineering Geologists Special Publication, 14.
360. White J.L., Dessenberger N.C., Ellis W.L., Higgins J., Gaffney S. (2007). The DeBeque Canyon Landslide at interstate 70, Mesa county, West Central Colorado. 1ST North American Landslide Conference, Field Trips.
361. White J.L. (2014). Annual Report of Instrumentation Monitoring Results from the DeBeque Canyon landslide, Interstate 70, milepost 51.

362. White, J., L. (2005). The Debeque Canyon landslide at Interstate 70, Mesa County, West-central Colorado. Rocky Mountain Section, Geological Society of America, Field Trip Guidebook (2005), pp. 1-8.

363. Wieczorek, G. F. (1984). Preparing a detailed landslide-inventory map for hazard evaluation and reduction. Bulletin of the Association of Engineering Geologists, 21(3), 337-342. https://doi.org/10.2113/gseegeosci.xxi.3.337

364. Wills, C. J., & McCrink, T. P. (2002). Comparing landslide inventories: The map depends on the method. Environmental & Engineering Geoscience, 8(4), 279-293. https://doi.org/10.2113/8.4.279

365. Xu, Q., Guo, C., Dong, X., Li, W., Lu, H., Fu, H., & Liu, X. (2021). Mapping and characterizing displacements of landslides with InSAR and airborne LiDAR technologies: A case study of Danba County, southwest China. Remote Sensing, 13(21), 4234. https://doi.org/10.3390/rs13214234

366. Yang, X., & Chen, L. (2010). Using multi-temporal remote sensor imagery to detect earthquake-triggered landslides. International Journal of Applied Earth Observation and Geoinformation, 12(6), 487-495. https://doi.org/10.1016/j.jag.2010.05.006

367. Yazici, B. V., & Tunc Gormus, E. (2022). Investigating persistent scatterer InSAR (PSInSAR) technique efficiency for landslides mapping: a case study in Artvin dam area, in Turkey. Geocarto International, 37(8), 2293-2311. https://doi.org/10.1080/10106049.2020.1818854

368. Yin, Y., Wang, F., & Sun, P. (2009). Landslide hazards triggered by the 2008 Wenchuan earthquake, Sichuan, China. Landslides, 6, 139-152. https://doi.org/10.1007/s10346-009-0148-5

369. Yu, B., & Chen, F. (2017). A new technique for landslide mapping from a large-scale remote sensed image: A case study of Central Nepal. Computers & Geosciences, 100, 115-124. https://doi.org/10.1016/j.cageo.2016.12.007

370. Yuan, R., Chen, J. (2022). A hybrid deep learning method for landslide susceptibility analysis with the application of InSAR data. Nat. Hazards, 114, 1393–1426. https://doi.org/10.1007/s11069-022-05430-8.

371. Žabota, B., Berger, F., Kobal, M. (2023). The Potential of UAV-Acquired Photogrammetric and LiDAR-Point Clouds for Obtaining Rock Dimensions as Input Parameters for Modeling Rockfall Runout Zones. Drones, 7, 104. https://doi.org/10.3390/drones7020104.

372. Zepner, L., Karrasch, P., Wiemann, F., & Bernard, L. (2020) ClimateCharts.net – an interactive climate analysis web platform, International Journal of Digital Earth, DOI: 10.1080/17538947.2020.1829112. Accessed 29 August 2023

373. Zhao, W., Li, A., Nan, X., Zhang, Z., & Lei, G. (2017). Postearthquake landslides mapping from Landsat-8 data for the 2015 Nepal earthquake using a pixel-based change detection method. IEEE Journal of Selected Topics in Applied Earth Observations and Remote Sensing, 10(5), 1758-1768. https://doi.org/10.1109/JSTARS.2017.2661802

374. Zhao, K., Wulder, M. A., Hu, T., Bright, R., Wu, Q., Qin, H., ... & Brown, M. (2019). Detecting change-point, trend, and seasonality in satellite time series data to track abrupt changes and nonlinear dynamics: A Bayesian ensemble algorithm. Remote sensing of Environment, 232, 111181. https://doi.org/10.1016/j.rse.2019.04.034

375. Zhao, B., Wang, Y., Feng, Q., Guo, F., Zhao, X., Ji, F., ... & Ming, W. (2020). Preliminary analysis of some characteristics of coseismic landslides induced by the Hokkaido Iburi-Tobu earthquake (September 5, 2018), Japan. Catena, 189, 104502. https://doi.org/10.1016/j.catena.2020.104502

376. Zhong, C., Liu, Y., Gao, P., Chen, W., Li, H., Hou, Y., ... & Ma, H. (2020). Landslide mapping with remote sensing: challenges and opportunities. International Journal of Remote Sensing, 41(4), 1555-1581. https://doi.org/10.1080/01431161.2019.1672904